

Hydrogen- and halogen-bond driven supramolecular architectures from small molecules to
cavitands, and applications in energetic materials

by

Janaka Chaminda Gamekkanda Gamaethige

B.S., University of Colombo, 2010

AN ABSTRACT OF A DISSERTATION

submitted in partial fulfillment of the requirements for the degree

DOCTOR OF PHILOSOPHY

Department of Chemistry
College of Arts and Sciences

KANSAS STATE UNIVERSITY
Manhattan, Kansas

2018

Abstract

A family of six β -diketone based ligands capable of simultaneously acting as halogen-bond (XB) donors (each of para and meta substituted chloro, bromo and iodo functionalities) and chelating ligands was synthesized. Four ligands were characterized by X-ray diffraction to identify the structural behavior of the ligand itself. The free ligands bearing bromine and iodine show XB interactions ($C-X \cdots O$) whereas the ligand containing chlorine did not show XB interactions. The corresponding Cu(II) complexes for ligands were also synthesized in different solvents such as acetonitrile, ethyl acetate and nitromethane. Both acetonitrile and ethyl acetate participate in XB interactions with XB donors (Br or I) although nitromethane does not participate in such interaction. Metal-ligand complexes with iodine as XB donor in the para position engage in XB interactions to make extended supramolecular architecture when the solvent is nitromethane. When the XB donor attached in the meta position of the ligand, formation of extended supramolecular architecture was seen even in the presence of a strongly coordinating solvent such as acetonitrile.

Two tetra functionalized molecules bearing hydrogen-bond (HB) donors (-OH) and XB donors (-C≡C-I) and one tetra functionalized molecule which has only HB donors (-OH and -C≡C-H) were synthesized. The donor molecules themselves show potential for making HB and XB interactions with the available acceptor sites present in the system. The competition between intermolecular HB and XB was explored by co-crystallizing with suitable nitrogen based acceptors. HB and XB donors showed equal competitiveness toward common acceptors when making HB/ XB interactions. Furthermore, the geometry and relative positioning of the donor sites can, in certain cases, change the balance between the competing interactions by favoring HB interactions.

A series of cavitands functionalized with XB donors, HB/XB donors and β -diketone have been synthesized. Binding preferences of XB and HB/XB cavitands towards a series of suitable HB/XB acceptors were studied in solid state and they have confirmed the presence of interactions between donor and acceptors. Cavitands with β -diketone functionality were subjected to binding studies with metal ions in solution as well as in the solid state. Successful metal-ligand complexation in solid state as well as in solution state based on UV/Vis titrations have been confirmed.

In order to stabilize chemically unstable energetic compound, pentaerythritol tetranitrocaramate (**PETNC**), a co-crystallization approach targeting the acidic protons was employed. A co-crystal, a salt and a solvate were obtained and the acceptors were identified as supramolecular protecting groups leading to reduced chemical reactivity and improved stability of **PETNC** with minimal reduction of desirable energetic properties.

Several potential tetrazole based explosives which are thermal and impact sensitive and solid propellants which are impact sensitive were subjected to co-crystallization experiment to stabilize and enhance their properties. Co-crystals and salts of the explosives were obtained with suitable nitrogen based and oxygen based acceptors. The impact sensitivity and thermal instability of the explosives were improved with the introduction of co-formers. Oxygen based acceptors have shown more favorable explosive property improvements compared to nitrogen based acceptors with significant retention of explosive nature of the parent explosives.

Hydrogen- and halogen-bond driven supramolecular architectures from small molecules to
cavitands, and applications in energetic materials

by

Janaka Chaminda Gamekkanda Gamaethige

B.S., University of Colombo, 2010

A DISSERTATION

submitted in partial fulfillment of the requirements for the degree

DOCTOR OF PHILOSOPHY

Department of Chemistry
College of Arts and Sciences

KANSAS STATE UNIVERSITY
Manhattan, Kansas

2018

Approved by:

Major Professor
Christer B. Aakeröy

Copyright

© Janaka Chaminda Gamekkanda Gamaethige 2018.

Abstract

A family of six β -diketone based ligands capable of simultaneously acting as halogen-bond (XB) donors (each of para and meta substituted chloro, bromo and iodo functionalities) and chelating ligands was synthesized. Four ligands were characterized by X-ray diffraction to identify the structural behavior of the ligand itself. The free ligands bearing bromine and iodine show XB interactions ($C-X \cdots O$) whereas the ligand containing chlorine did not show XB interactions. The corresponding Cu(II) complexes for ligands were also synthesized in different solvents such as acetonitrile, ethyl acetate and nitromethane. Both acetonitrile and ethyl acetate participate in XB interactions with XB donors (Br or I) although nitromethane does not participate in such interaction. Metal-ligand complexes with iodine as XB donor in the para position engage in XB interactions to make extended supramolecular architecture when the solvent is nitromethane. When the XB donor attached in the meta position of the ligand, formation of extended supramolecular architecture was seen even in the presence of a strongly coordinating solvent such as acetonitrile.

Two tetra functionalized molecules bearing hydrogen-bond (HB) donors (-OH) and XB donors (-C≡C-I) and one tetra functionalized molecule which has only HB donors (-OH and -C≡C-H) were synthesized. The donor molecules themselves show potential for making HB and XB interactions with the available acceptor sites present in the system. The competition between intermolecular HB and XB was explored by co-crystallizing with suitable nitrogen based acceptors. HB and XB donors showed equal competitiveness toward common acceptors when making HB/ XB interactions. Furthermore, the geometry and relative positioning of the donor sites can, in certain cases, change the balance between the competing interactions by favoring HB interactions.

A series of cavitands functionalized with XB donors, HB/XB donors and β -diketone have been synthesized. Binding preferences of XB and HB/XB cavitands towards a series of suitable HB/XB acceptors were studied in solid state and they have confirmed the presence of interactions between donor and acceptors. Cavitands with β -diketone functionality were subjected to binding studies with metal ions in solution as well as in the solid state. Successful metal-ligand complexation in solid state as well as in solution state based on UV/Vis titrations have been confirmed.

In order to stabilize chemically unstable energetic compound, pentaerythritol tetranitrocaramate (**PETNC**), a co-crystallization approach targeting the acidic protons was employed. A co-crystal, a salt and a solvate were obtained and the acceptors were identified as supramolecular protecting groups leading to reduced chemical reactivity and improved stability of **PETNC** with minimal reduction of desirable energetic properties.

Several potential tetrazole based explosives which are thermal and impact sensitive and solid propellants which are impact sensitive were subjected to co-crystallization experiment to stabilize and enhance their properties. Co-crystals and salts of the explosives were obtained with suitable nitrogen based and oxygen based acceptors. The impact sensitivity and thermal instability of the explosives were improved with the introduction of co-formers. Oxygen based acceptors have shown more favorable explosive property improvements compared to nitrogen based acceptors with significant retention of explosive nature of the parent explosives.

Table of Contents

List of Figures	xv
List of Tables	xxiv
Acknowledgements.....	xxv
Dedication.....	xxvii
Preface.....	xxviii
Chapter 1 Introduction	1
1.1 Supramolecular chemistry and self-assembly.....	1
1.1.1 Metal-ligand interactions (coordinate bond).....	2
1.1.2 The hydrogen bond (HB)	3
1.1.3 The halogen bond (XB).....	4
1.2 Crystal engineering	5
1.2.1 Supramolecular synthons “Is the communicating part ready?”	6
1.2.2 Co-crystallization “Finding the best match”	6
1.2.3 Hydrogen bond in co-crystallization “A glue to bring things together”	7
1.2.4 Halogen bond in co-crystallization “An alternative glue”	8
1.2.5 Applications of co-crystallization	9
1.3 Host-guest chemistry	9
1.4 Goals of the thesis.....	12
1.5 References.....	14
Chapter 2 The Role of Halogen Bonding in Controlling Assembly and Organization of Cu(II)-Acac Based Coordination Complexes	17
2.1 Introduction.....	17
2.1.1 Goals of this study	20
2.2 Experimental	21
2.2.1 General	21
2.2.2 Synthesis of ligands	21
2.2.2.1 Synthesis of 4-(trimethylsilylethynyl)benzaldehyde	22
2.2.2.2 Synthesis of 4-(chloroethynyl)benzaldehyde.....	23
2.2.2.3 Synthesis of 4-(bromoethynyl)benzaldehyde	24

2.2.2.4	Synthesis of 4-(iodoethynyl)benzaldehyde	24
2.2.2.5	Synthesis of 3-(4-(chloroethynyl)phenyl)-4-hydroxypent-3-en-2-one, L1.....	25
2.2.2.6	Synthesis of 3-(4-(bromoethynyl)phenyl)-4-hydroxypent-3-en-2-one, L2	26
2.2.2.7	Synthesis of 3-(4-(iodoethynyl)phenyl)-4-hydroxypent-3-en-2-one, L3.....	26
2.2.2.8	Synthesis of 3-(trimethylsilylethynyl)benzaldehyde	27
2.2.2.9	Synthesis of 3-(chloroethynyl)benzaldehyde.....	27
2.2.2.10	Synthesis of 3-(bromoethynyl)benzaldehyde	28
2.2.2.11	Synthesis of 4-(iodoethynyl)benzaldehyde	28
2.2.2.12	Synthesis of 3-(3-(chloroethynyl)phenyl)-4-hydroxypent-3-en-2-one, L4...	28
2.2.2.13	Synthesis of 3-(3-(bromoethynyl)phenyl)-4-hydroxypent-3-en-2-one, L5 ..	29
2.2.2.14	Synthesis of 3-(3-(iodoethynyl)phenyl)-4-hydroxypent-3-en-2-one, L6.....	30
2.2.3	Metal-ligand complexes synthesis	30
2.2.3.1	Synthesis of $[\text{Cu}(\text{L}1)_2]$	30
2.2.3.2	Synthesis of $[\text{Cu}(\text{L}2)_2].2\text{CH}_3\text{CN}$	31
2.2.3.3	Synthesis of $[\text{Cu}(\text{L}2)_2].2\text{C}_4\text{H}_8\text{O}_2$	31
2.2.3.4	Synthesis of $[\text{Cu}(\text{L}2)_2].2\text{CH}_3\text{NO}_2$	31
2.2.3.5	Synthesis of $[\text{Cu}(\text{L}3)_2].4\text{CH}_3\text{CN}$	31
2.2.3.6	Synthesis of $[\text{Cu}(\text{L}3)_2].2\text{C}_4\text{H}_8\text{O}_2$	32
2.2.3.7	Synthesis of $[\text{Cu}(\text{L}3)_2]$	32
2.2.3.8	Synthesis of $[\text{Cu}(\text{L}5)_2]$	32
2.3	Results.....	33
2.3.1	Single crystals of ligands	33
2.3.2	FTIR spectroscopy of metal-ligand complexes	36
2.3.3	Single crystals of metal-ligand complexes	38
2.3.4	Thermal gravimetric analyses (TGA) of metal-ligand complexes	46
2.4	Discussion	46
2.4.1	Halogen-bond donor/acceptor ability of ligands.....	46
2.4.2	Halogen-bond donor/acceptor ability of metal-ligand complexes.....	47
2.4.3	Density functional theory (DFT) calculations	49
2.4.4	TGA data analysis.....	50
2.5	Conclusions.....	51

2.6 References	53
Chapter 3 Competition between hydrogen bonds and halogen bonds	55
3.1 Introduction.....	55
3.1.1 Objectives of this study.....	60
3.2 Experimental	60
3.2.1 General.....	60
3.2.2 Computational studies.....	61
3.2.3 Synthesis of D1-D3	61
3.2.3.1 Synthesis of trans- and cis -1,4-bis((trimethylsilyl)ethynyl)cyclohexane-1,4-diol	62
3.2.3.2 Synthesis of trans-1,4-bis(iodoethynyl)cyclohexane-1,4-diol.H ₂ O (D1.H ₂ O)	63
3.2.3.3 Synthesis of cis-1,4-bis(iodoethynyl)cyclohexane-1,4-diol (D2)	63
3.2.3.4 Synthesis of trans-1,4-diethynylcyclohexane-1,4-diol.H ₂ O (D3.H ₂ O).....	64
3.2.4 Crystal growth of D1-D3 and synthesis of co-crystals	64
3.3 Results.....	64
3.3.1 Molecular electrostatic potential of donors and acceptors.....	64
3.3.2 Differential scanning calorimetry (DSC) and thermogravimetric analysis (TGA) of donors.....	66
3.3.3 Single X-ray structures of donors	68
3.3.4 IR spectroscopy of co-crystals	70
3.3.5 Single X-ray structures of co-crystals.....	72
3.4 Discussion	77
3.4.1 Analysis of X-ray structures of donors	77
3.4.2 IR spectroscopy analysis of co-crystals	77
3.4.3 MEPs analysis	79
3.4.4 Structural analysis of co-crystals	80
3.4.5 Analysis of HB and XB geometries.....	83
3.5 Conclusions.....	84
3.6 References.....	86
Chapter 4 Functionalization of cavitands	88
4.1 Introduction.....	88

4.1.1 Upper rim functionalization	90
4.1.1.1 Metal coordinating cavitands	90
4.1.1.2 Hydrogen bonded cavitands	90
4.1.1.3 Halogen bonded cavitands	91
4.1.1.4 Host-guest chemistry of cavitands	91
4.1.2 Objectives of the study.....	93
4.2 Experimental	96
4.2.1 General	96
4.2.2 Synthesis of L7-L8 and D4-D6.....	96
4.2.2.1 Synthesis of C-hexylcalix[4]resorcinarene	98
4.2.2.2 Synthesis of C-hexyltetrabromocalix[4]resorcinarene	99
4.2.2.3 Synthesis of C-hexyltetrabromocavatand	100
4.2.2.4 Synthesis of C-hexyltetra(4-phenylformyl)cavatand.....	101
4.2.2.5 Synthesis of C-hexyltetra(3-phenylformyl)cavatand.....	102
4.2.2.6 Synthesis of C-hexyltetra(4-(2-hydroxy-4-oxopent-2-en-3-yl))cavatand (L7) ...	103
4.2.2.7 Synthesis of C-hexyltetra(3-(2-hydroxy-4-oxopent-2-en-3-yl))cavatand (L8) ...	103
4.2.2.8 Synthesis of C-hexyltetra(4-(iodoethynyl))cavatand (D4)	104
4.2.2.9 Synthesis of C-hexyltetra(3-(idoethynyl))cavatand (D5)	106
4.2.2.10 Synthesis of C-hexyltetra(4-(1-hydroxy-3-(trimethylsilyl)prop-2-yn-1-yl))cavatand	107
4.2.2.11 Synthesis of C-hexyltetra(4-(1-hydroxy-3-iodoprop-2-yn-1-yl))cavatand (D6) ...	108
4.2.3 Metal-ligand complex, host-guest complex and co-crystal synthesis.....	109
4.2.4 UV/ Vis titrations	109
4.3 Results and discussion	110
4.3.1 Metal-ligand complex formation	110
4.3.1.1 Solid state study	110
4.3.1.2 Solution state study	111
4.3.1.3 Host-guest inclusion studies	114
4.3.1.4 HB/ XB donor capability of cavitands.....	116
4.4 Conclusions.....	118
4.5 References.....	119

Chapter 5 Crystal engineering of energetic materials: Co-crystals of nitrocarbamates with modified performance.....	121
5.1 Introduction.....	121
5.1.1 Objectives of this study.....	124
5.2 Experimental	125
5.2.1 General	125
5.2.2 Safety	125
5.2.3 Synthesis of energetic material	125
5.2.3.1 Synthesis of 2,2-bis((carbamoyloxy)methyl)propane-1,3-diyl dicarbamate	125
5.2.3.2 Synthesis of 2,2-bis(((nitrocarbamoyl)oxy)methyl)propane-1,3-diyl bis(nitrocarbamate) or Pentaerythritol tetranitrocaramate (D9)	126
5.2.4 Synthesis of co-crystals.....	127
5.2.5 Oxygen balance calculation	127
5.2.6 Detonation velocity and pressure calculations.....	127
5.2.7 Impact sensitivity test (Drop test)	128
5.2.8 Reactivity analysis	129
5.3 Results.....	129
5.3.1 IR analysis.....	129
5.3.2 Crystal structures	130
5.3.3 Thermal properties	134
5.3.4 Oxygen balance of the energetic materials	135
5.3.5 Detonation pressure and detonation velocity	135
5.3.6 Impact sensitivity test	136
5.3.7 Reactivity	136
5.4 Discussion	137
5.4.1 IR spectroscopy analysis.....	137
5.4.2 Structural analysis	137
5.4.3 Thermal analysis	141
5.4.4 Detonation performance analysis.....	142
5.4.5 Improvement of impact sensitivity	142
5.4.6 Chemical reactivity/ instability modifications	143

5.5 Conclusions.....	143
5.6 References.....	144
Chapter 6 Co-crystals and salts of tetrazole based energetic materials with modified performance	146
6.1 Introduction.....	146
6.1.1 Objectives of this study.....	152
6.2 Experimental	152
6.2.1 General	152
6.2.2 Safety	152
6.2.3 Synthesis of energetic material	153
6.2.3.1 Synthesis of 5-(nitrimino)-1 <i>H</i> -tetrazole (D10)	153
6.2.3.2 Synthesis of 1-methyl-5-(nitrimino)-1 <i>H</i> -tetrazole (D11)	153
6.2.3.3 Synthesis of 2-methyl-5-(nitramino)-2 <i>H</i> -tetrazole (D12).....	154
6.2.3.4 Synthesis of bis(1-methyltetrazolyl)triazene (D13).....	154
6.2.3.5 Synthesis of bis(2-methyltetrazolyl)triazene (D14).....	155
6.2.4 Synthesis of co-crystals.....	155
6.2.5 Energy optimization.....	155
6.2.6 Explosive properties determination	156
6.3 Results.....	156
6.3.1 Geometry optimizations.....	156
6.3.2 IR analysis.....	157
6.3.3 Crystal structures	159
6.3.4 Thermal properties	164
6.3.5 Oxygen balance, detonation pressure and detonation velocity of the energetic materials	165
6.3.6 Impact sensitivity test	166
6.4 Discussion	167
6.4.1 Geometry optimization	167
6.4.2 IR spectroscopy analysis.....	167
6.4.3 Structural analysis	167
6.4.4 Acidity of energetics	168

6.4.5 Thermal stability analysis	169
6.4.6 Detonation property analysis	169
6.4.7 Impact sensitivity analysis	170
6.5 Conclusions.....	172
6.6 References.....	174
Chapter 7 Summary	175
7.1 Manipulation of halogen bonding and metal-ligand coordination in supramolecular chemistry.....	175
7.2 Finding alternative supramolecular forces.....	176
7.3 Host-guest chemistry in supramolecular chemistry.....	177
7.4 Applications of supramolecular chemistry	178
7.5 Future works	179
7.6 References.....	181
Appendix A – NMR spectra	182
Appendix B – Crystallographic data.....	204

List of Figures

Figure 1.1 Molecular recognition event by (a) intra-molecular, (b) intermolecular supramolecular forces.....	1
Figure 1.2 Covalent synthesis Vs. supramolecular synthesis	2
Figure 1.3 Schematic diagram that shows the formation of 0D, 1D, 2D and 3D coordination polymers or metal-ligand complexes	3
Figure 1.4 Schematics show the formation of hydrogen bond	4
Figure 1.5 Typical examples for hydrogen bonding (a) base pair of DNA helix, (b) carboxylic homodimer, (c) amide homodimer (d) acid-amide heterodimer.....	4
Figure 1.6 Schematics show the formation of hydrogen bond	5
Figure 1.7 Anisotropic distribution of positive and negative potential on halogen and change of strength of σ -hole with halogen atom	5
Figure 1.8 Examples for supramolecular synthons, (a) dimer in acids, (b) catemer in acids, (d) nitro···amino HB interaction and (d) nitro···iodo XB interaction.....	6
Figure 1.9 Re-crystallization vs co-crystallization	7
Figure 1.10 A binary co-crystal formed between 4,4'-bipyridine and hydroquinone via two heterosynthons	8
Figure 1.11 A binary co-crystal formed between 4,4'-bipyridine and 1,4-diiodobenzene via halogen bonds	8
Figure 1.12 Different geometries in halogen···halogen contacts (a) type I and (b) type II.....	9
Figure 1.13 Accidental synthesis of the first supramolecular host	10
Figure 1.14 Examples for supramolecular hosts, (a) [2,2,2]cryptand, (b) cavitand and (c) β -cyclodextrin.....	10
Figure 1.15 Molecular capsule based on cavitand constructed by multiple hydrogen bonds.....	11
Figure 2.1 Counter anion interference of metal-ligand coordination; L-ligand; M-metal ion; A- counter anion.....	17
Figure 2.2 Chelation of metal ions by β -diketone (acac) ligand.....	18
Figure 2.3 Hydrogen bond-donor group interference to metal-acac ligand coordination; M-metal ion; A-counter anion; H-hydrogen-bond donor	18

Figure 2.4 Newly designed molecules that can act as chelating ligands (through the acac site) decorated with activated halogen bond donors	19
Figure 2.5 Possible halogen–bond acceptor sites; (a) ligand itself, (b) metal-ligand complex	20
Figure 2.6 General pathway to the synthesis of ligands L1-L6	22
Figure 2.7 Part of the crystal structure of L1 (color codes: red-oxygen; green-chlorine).	33
Figure 2.8 Part of the crystal structure of L2 (color codes: red-oxygen; gold-bromine).	34
Figure 2.9 Part of the crystal structure of L3 (color codes: red-oxygen; purple-iodine).	34
Figure 2.10 Halogen bonded 1-D chain in L5 (color codes: red-oxygen; gold-bromine).	35
Figure 2.11 Part of the crystal structure of L5 showing short interactions (color codes: red-oxygen; gold-bromine).....	36
Figure 2.12 FTIR spectra of L2 (red) and the metal-ligand complex between L2 and Cu(II) in CH ₃ CN (blue).....	37
Figure 2.13 FTIR spectra of L5 (red) and the metal-ligand complex between L5 and Cu(II) in CH ₃ CN (blue).....	37
Figure 2.14 The geometry of the metal-ligand complex ion in the crystal structure of [Cu(L1) ₂] (color codes: red-oxygen; green-chlorine; orange-copper).....	38
Figure 2.15 The relative orientation of metal-ligand complex within an infinite stack in the structure of [Cu(L1) ₂] (color codes: red-oxygen; green-chlorine; orange-copper).....	38
Figure 2.16 Part of the crystal structure of [Cu(L2) ₂].2CH ₃ CN showing the geometry around the metal ion and the ligand-solvent halogen bond (color codes: red-oxygen; blue-nitrogen; gold-bromine; orange-copper).	39
Figure 2.17 Crystal packing of [Cu(L2) ₂].2CH ₃ CN (solvent molecules are omitted, color codes: red-oxygen; gold-bromine; orange-copper).....	39
Figure 2.18 Part of the crystal structure of [Cu(L2) ₂].2C ₄ H ₈ O ₂ showing the geometry around the metal ion and the ligand-solvent halogen bond (color codes: red-oxygen; gold-bromine; orange-copper).	40
Figure 2.19 Crystal packing of [Cu(L2) ₂].2C ₄ H ₈ O ₂ (solvent molecules are omitted, color codes: red-oxygen; gold-bromine; orange-copper).....	40
Figure 2.20 Part of the crystal structure of [Cu(L2) ₂].2CH ₃ NO ₂ showing the geometry around the metal ion and the packing of ligand and solvent (color codes: red-oxygen; blue-nitrogen; gold-bromine; orange-copper).	41

Figure 2.21 Crystal packing of $[\text{Cu}(\text{L2})_2] \cdot 2\text{CH}_3\text{NO}_2$ (solvent molecules are omitted, color codes: red-oxygen; gold-bromine; orange-copper).....	41
Figure 2.22 Part of the crystal structure of $[\text{Cu}(\text{L3})_2] \cdot 4\text{CH}_3\text{CN}$ showing the geometry around the metal ion and the ligand-solvent halogen bond (color codes: red-oxygen; blue-nitrogen; purple-iodine; orange-copper).....	42
Figure 2.23 Part of the crystal structure of $[\text{Cu}(\text{L3})_2] \cdot 2\text{C}_4\text{H}_8\text{O}_2$ showing the geometry around the metal ion and the ligand-solvent halogen bond (color codes: red-oxygen; purple-iodine; orange-copper).....	42
Figure 2.24 A stack of complex ions in the structure of $[\text{Cu}(\text{L3})_2] \cdot 2\text{C}_4\text{H}_8\text{O}_2$ (solvent molecules are omitted, color codes: red-oxygen; purple-iodine; orange-copper).....	43
Figure 2.25 Bifurcated halogen···oxygen halogen-bond interactions in $[\text{Cu}(\text{L3})_2]$ (color codes: red-oxygen; purple-iodine; orange-copper).....	43
Figure 2.26 Halogen··· π interactions in the structure of $[\text{Cu}(\text{L3})_2]$ (color codes: red-oxygen; purple-iodine; orange-copper).....	44
Figure 2.27 The halogen-bond driven assembly of metal-ligand complexes in the crystal structure of $[\text{Cu}(\text{L3})_2]$ (color codes: red-oxygen; purple-iodine; orange-copper).....	44
Figure 2.28 The geometry of the metal-ligand complexes in the crystal structure of $[\text{Cu}(\text{L5})_2]$ (color codes: red-oxygen; gold-bromine; orange-copper).....	45
Figure 2.29 The halogen-bond driven assembly of metal-ligand complexes in the crystal structure of $[\text{Cu}(\text{L5})_2]$ (color codes: red-oxygen; gold-bromine; orange-copper).....	45
Figure 2.30 Comparison of TGA traces: $[\text{Cu}(\text{L1})_2]$ (Green), $[\text{Cu}(\text{L2})_2] \cdot 2\text{CH}_3\text{CN}$ (Blue), $[\text{Cu}(\text{L3})_2] \cdot 4\text{CH}_3\text{CN}$ (Violet) and $[\text{Cu}(\text{L5})_2]$ (Red).....	46
Figure 2.31 Summary of the involvement of the halogen-bond acceptors and donors in the crystal structures of L1-L3 and L5.	47
Figure 2.32 Summary of the involvement of the potential halogen-bond acceptor and donor sites on metal-ligand complexes of L1-L3 and L5.	48
Figure 2.33 Interlocked 2-D bilayer self-assembled architecture of $[\text{Cu}(\text{L5})_2]$ (color codes: Green- and red – two different halogen-bonded 2-D assemblies).....	49
Figure 2.34 HOMO orbitals in $[\text{Cu}(\text{L3})_2]$ (color codes: red and blue- two phases of HOMO orbitals)	50
Figure 2.35 Part of TGA traces; $[\text{Cu}(\text{L2})_2] \cdot \text{C}_4\text{H}_8\text{O}_2$ (Red) and $[\text{Cu}(\text{L3})_2] \cdot \text{C}_4\text{H}_8\text{O}_2$ (Blue).	51

Figure 2.36 Solvent free supramolecular assembly formation	52
Figure 2.37 Proposed metallosupramolecular architecture formation when halogen-bond acceptor linkers are introduced.....	53
Figure 3.1 (a) HB interaction between 4.4'-bypyridine and hydroquinone, (b) XB interaction between 4.4'-bypyridine and 1,4-diiodobenzene.....	55
Figure 3.2 Supramolecular outcome of the mixture of 1,2-bis(4-pyridyl)-ethane, 1,4-diiodotetrafluorobenzene and hydroquinone	56
Figure 3.3 Supramolecular outcome of the mixture of N,N,N',N'-tetramethylethylenediamine, 1,2-diido-tetrafluoroethane and ethylene glycol	56
Figure 3.4 Molecules with competing halogen- and hydrogen-bond donors (D1/D2) and competing hydrogen-bond donors (D3).....	57
Figure 3.5 Ditopic nitrogen based XB/ HB acceptors (A1-A6).....	58
Figure 3.6 Hypothesized primary intermolecular interactions in co-crystals of D1/D2:A1-A6... ..	58
Figure 3.7 Hypothesized intermolecular interactions in co-crystals of D3:A1-A6	59
Figure 3.8 Synthesis pathway to D1, D2 and D3.....	61
Figure 3.9 Electrostatic potential surfaces of (a) XB/HB donors and acceptors of D1, (b) HB donors and acceptors of D3.....	65
Figure 3.10 Electrostatic potential surfaces of (a) XB donors, (b) HB donors and XB/HB acceptors of D2.	65
Figure 3.11 Electrostatic potential surfaces of acceptor atoms in A1-A6.	66
Figure 3.12 TGA traces comparison of D1.H ₂ O (Blue), D2 (Red) and D3.H ₂ O (Green)	67
Figure 3.13 DSC traces comparison of D1.H ₂ O (Blue), D2 (Red) and D3.H ₂ O (Green).....	67
Figure 3.14 Hydrogen bonding and halogen bonding in the crystal structure of D1.H ₂ O (color codes: red-oxygen; violet-iodine).	69
Figure 3.15 Hydrogen bonds (a) and halogen bonds (b) in the crystal structure of D2 (color codes: red-oxygen; violet-iodine).	69
Figure 3.16 (a) Water bridged hydrogen bonding and (b) C-H···C≡C hydrogen bond in the crystal structure of D3.H ₂ O (color codes: red-oxygen)	70
Figure 3.17 IR comparison of D1.H ₂ O, A3 and D1.H ₂ O: A3 ground mixture.....	71
Figure 3.18 IR comparison of D2, A3 and D2: A3 ground mixture	71
Figure 3.19 IR comparison of D1.H ₂ O, A3 and D1.H ₂ O: A3 ground mixture.....	72

Figure 3.20 Major HBs and XBs in the crystal structure of D1:A3 (color codes: red-oxygen; violet-iodine; blue-nitrogen)	74
Figure 3.21 Major HBs and XBs in the crystal structure of D1:A4 (color codes: red-oxygen; violet-iodine; blue-nitrogen)	74
Figure 3.22 Main HBs and XBs in the crystal structure of D1:A5 (color codes: red-oxygen; violet-iodine; blue-nitrogen)	75
Figure 3.23 Major HBs and XBs in the crystal structure of D2:A3 (color codes: red-oxygen; violet-iodine; blue-nitrogen)	75
Figure 3.24 Major HBs in the crystal structure of D3:A3 (color codes: red-oxygen; blue-nitrogen)	76
Figure 3.25 Major HBs in the crystal structure of D3:A5 (color codes: red-oxygen; blue-nitrogen)	76
Figure 3.26 HB/ XB donor and acceptor sites observed in single crystals of D1, D2 and D3	77
Figure 3.27 Comparison of ethynyl IR spectroscopy peak (-C≡C-) of D3.H ₂ O, D3:A3, D3:A5.	79
Figure 3.28 HB bond distances and MEP values of D2:A3	80
Figure 3.29 Outcome of interactions between HB/ XB donors and nitrogen-based acceptors	81
Figure 3.30 Moderate to weak $\pi \cdots \pi$ interactions in the crystal structure of D1:A3.....	82
Figure 3.31 Competition of halogen bonding with hydrogen bonding in the presence of the same acceptor (<i>trans</i> -isomers: D1 and D3).....	82
Figure 3.32 XB distances between ethynyl iodine and aromatic nitrogen: reported in CSD (blue circles) and observed in this study (red hollow squares)	83
Figure 3.33. XB angles $\theta(\text{C-I} \cdots \text{N})$: reported in CSD (blue circles) and observed in this study (red hollow squares)	84
Figure 3.34 Outcome of co-crystallization experiments between D1-D2 and nitrogen based acceptors	85
Figure 4.1 Cavitand scaffold (a) top view, (b) side view, (c) main parts of the cavitand, (d) schematic representation of cavitand	89
Figure 4.2 Examples for metal ligand coordination by (a) acetylacetone, (b) pyridil group and (c) carboxylate group.....	90
Figure 4.3 Examples for hydrogen bond interactions present on functionalized cavitands	91
Figure 4.4 Examples for halogen bond interactions present on functionalized cavitands.....	91

Figure 4.5 Host-guest chemistry involved in cavitands.....	92
Figure 4.6 Functionalized cavitands, L7, L8- acac functionalized, D4, D5- ethynyl iodine XB donor functionalized, D6- ethynyl iodine XB donor and –OH HB donor functionalized.....	93
Figure 4.7 Anticipated discrete (capsule) or polymeric metallo-supramolecular architecture by L7 in the presence of divalent metal ions	94
Figure 4.8 Three possible modes of guest binding to the host (X= XB donor, G= XB acceptor (guest))	95
Figure 4.9 Ditopic nitrogen based XB/ HB acceptors (A1-A6).....	95
Figure 4.10 Competition between HB/XB towards common acceptor/ guest the multi-functional cavitand	96
Figure 4.11 Overview of synthesis of bromocavitand	97
Figure 4.12 Overview of synthesis of acac functionalized cavitands (L7 and L8).....	97
Figure 4.13 Overview of synthesis of HB and XB functionalized cavitands (D4-D6)	98
Figure 4.14 FTIR spectra of L7 (blue) and the metal-ligand complex between L7 and Cu(II) (red).....	110
Figure 4.15 FTIR spectra of L8 (blue) and the metal-ligand complex between L8 and Cu(II) (red).....	111
Figure 4.16 Continuous variation method using UV-visible spectroscopy (L7:Cu(II))	112
Figure 4.17 Job plot of UV/is titration (a) at $\lambda_{\text{max}} = 420$ nm and (b) at $\lambda_{\text{max}} = 392$ nm	113
Figure 4.18 Proposed discrete metallo-supramolecular complex at $\lambda_{\text{max}} = 420$ nm	114
Figure 4.19 Proposed polymeric metallo-supramolecular architecture at $\lambda_{\text{max}} = 392$ nm	114
Figure 4.20 Preliminary single crystal X-ray structure (a) side view (capped stick model), (b) top view (space filling model) of C-hexyltetrabromocavitand	114
Figure 4.21(a) IR spectra of dry D4 (violet), (b) IR spectra of D4:Dioxane	115
Figure 4.22(a) IR spectra of dry D5 (violet), (b) IR spectra of D4:Dioxane	115
Figure 4.23(a) TGA spectra of dry D4 (red) and D4:dioxane (green), (b) TGA spectra of dry D5 (red) and D5:dioxane (green)	116
Figure 4.24 IR spectroscopy of D6, A3 and ground mixture D3:A3.....	117
Figure 4.25 Examples for functionalized cavitands; metal-coordinating, HB/XB multi-functional and XB donor cavitands	118
Figure 5.1 Chemical structure of PETNC	122

Figure 5.2 Part of crystal structure of D9 with hydrogen bonds between acidic proton and carbonyl oxygen	122
Figure 5.3 Hydrogen-bond donor sites in D9	123
Figure 5.4 Ditopic nitrogen or oxygen based hydrogen bond acceptors (A1-A8).....	124
Figure 5.5 (a) Schematic diagram of impact sensitivity test apparatus, (b) Impact sensitivity test apparatus with 5 lbs weight (c) explosion of an energetic material	128
Figure 5.6 IR comparison between D9, A8 and the D9:A8.....	130
Figure 5.7 Part of the crystal structure of D9 ³⁻ :A3H ₂ ²⁺ : A3H ⁺ that shows the interactions originates from D9 ³⁻	131
Figure 5.8 Part of the crystal structure of D9 ³⁻ :A3H ₂ ²⁺ : A3H ⁺ that shows additional interactions	131
Figure 5.9 Part of the crystal structure of D9:2A7:CH ₃ OH that shows the HB interactions and stoichiometry between D9: A7: methanol (1:2:1).....	132
Figure 5.10 Part of the crystal structure of D9:A8 that shows HBs originate from D9.....	133
Figure 5.11 Part of the crystal structure of D9:A8 that shows bifurcated nature of HB interactions	133
Figure 5.12 DSC traces comparison of D9 and co-crystal/salt/solvate.	134
Figure 5.13 On left; D9 and all three newly formed energetics placed on copper strip and on the right; after 1 hour with the addition of a drop of methanol.....	136
Figure 5.14. ¹ H NMR spectra comparison between D9, A4 and D9:A4	138
Figure 5.15. ¹ H NMR spectra comparison between D9, A5 and D9:A5	139
Figure 5.16. ¹ H NMR spectra comparison between D9, A7 and D9:2A7:CH ₃ OH	140
Figure 5.17. Heat plot of bifurcated HB distances between N-oxide and -NH proton.....	141
Figure 5.18. TGA trace of solvate D9:2A7:CH ₃ OH.....	142
Figure 5.19. Modification of explosive properties by co-crystallization.....	144
Figure 6.1 Basic structures of azoles	146
Figure 6.2 Chemical structures of some nitrated aminotetrazoles	147
Figure 6.3 Part of the crystal structure of D10 with hydrogen bonds between -NH protons and nitrogen atoms.....	147
Figure 6.4 Part of the crystal structure of D11 with hydrogen bonds between -NH protons and nitrogen and oxygen atoms	148

Figure 6.5 Part of the crystal structure of D12 with hydrogen bonds between -NH protons and nitrogen atoms	148
Figure 6.6 Hydrogen-bond donor sites in D10, D11 and D12	148
Figure 6.7 Chemical structures of bis-tetrazoles.....	149
Figure 6.8 Part of the crystal structure of D13.H ₂ O	150
Figure 6.9 Part of the crystal structure of D14 showing hydrogen bonding between the –NH protons and a nitrogen atom of the ring	150
Figure 6.10 Hydrogen-bond donor sites in D13 and D14.....	151
Figure 6.11 Ditopic nitrogen or oxygen based hydrogen-bond acceptors (A1-A8)	151
Figure 6.12 Geometry optimized structures and energy differences of different constitutional isomers of each tetrazole.....	156
Figure 6.13 MEPs surfaces of D10, D11, D12, D13, and D14 showing highest positive points of MEPs (All values are in kJ/mol)	157
Figure 6.14 IR spectroscopy comparison between D12, A3 and the D12:A3	159
Figure 6.15 Part of the crystal structure of D10:A8 showing main HB interactions and 1-D network	160
Figure 6.16 Part of the crystal structure of D10:A9 showing primary HB interactions and 1-D network	160
Figure 6.17 Crystal structure of trimeric salt, 2(D11 ⁻):A3H ₂ ²⁺ showing charge assisted HB interactions	160
Figure 6.18. Crystal structure of 2(D11):A8 showing primary HB interactions	161
Figure 6.19. Crystal structure of 2(D11):A9 showing main HB interactions	161
Figure 6.20 Crystal structure of 2(D12 ⁻):A3H ₂ ²⁺ showing main HB interactions	162
Figure 6.21 Part of the crystal structure of 2(D12 ⁻):A4H ₂ ²⁺ showing main HB interactions	162
Figure 6.22 Part of the crystal structure of 2(D12 ⁻):A6H ₂ ²⁺ showing main HB interactions	163
Figure 6.23. Part of the crystal structure of 2(D12):A8	163
Figure 6.24. DSC traces comparison of D10 and co-crystals.....	164
Figure 6.25. DSC traces comparison of D11 and co-crystals/salt.....	164
Figure 6.26. DSC traces comparison of D12 and co-crystal/salts.....	165
Figure 6.27 Salts formation of D11 and D12 with aquous ammonia	168

Figure 6.28 Melting point/ decomposition temperature comparison of explosives, co-formers and co-crystals	169
Figure 6.29 H ₅₀ values comparison for the explosives and their salts/ co-crystals.....	170
Figure 6.30 (a) HB interactions in D12, (b) HB interactions and short non-covalent interactions in D12:A3.....	171
Figure 6.31 (a) Packing of D10, (b) layered packing of salt.....	172
Figure 6.32 π-stacked interactions in a crystal buffer against external mechanical stimuli	172
Figure 6.33 Use of supramolecular chemistry and crystal engineering to balance the power and safety of explosives.....	173
Figure 7.1 Donor (red arrows) and acceptor (blue arrows) sites utilized by non-covalent interactions (a) in a 1,4-substituted metal ligand complex, (b) in a 1,3-substituted metal ligand complex ¹	176
Figure 7.2 Formation of equal number of HB and XB interactions between a donor and an acceptor molecules ²	177
Figure 7.3 Schematic representation of (a) metal-ligand coordination and (b) HB/XB interactions in cavitands	178
Figure 7.4 Use of co-crystallization to improve chemical, thermal stability and impact sensitivity of explosives	179
Figure 7.5 Formation of XB interactions between metal-ligand complex and acceptors.....	180
Figure 7.6 Capsule formation between (a) XB donor cavitands and ditopic acceptors (b) XB donor cavitand and XB acceptor cavitand	180
Figure 7.7 Formation of HB interaction driven co-crystal between two energetic materials	181

List of Tables

Table 3.1 HB distances and angles in D1-D3	68
Table 3.2 HB distances and angles in D1-D2	68
Table 3.3 HB distances and angles in the structures of six co-crystals.	73
Table 3.4 XB distances and angles in the structures of four co-crystals	73
Table 3.5 IR frequency changes of selected peaks of HB/ XB donors when form co-crystals	78
Table 4.1 UV-visible data for the Job plot at $\lambda_{\max} = 420$ nm.....	112
Table 4.2 UV-visible data for the Job plot at $\lambda_{\max} = 392$ nm.....	113
Table 4.3 IR analysis of attempted co-crystallization experiments	117
Table 5.1. Nitrogen equivalent indices of detonation products	128
Table 5.2 IR analysis of attempted co-crystallization experiments	130
Table 5.3 Hydrogen bond parameters of newly formed energetic materials	134
Table 5.4 Thermal properties of energetic materials	135
Table 5.5 Oxygen balance of energetic materials	135
Table 5.6 Detonation velocity and detonation pressure of energetic materials	135
Table 5.7. IR peak shift of pyridine derivatives.....	137
Table 6.1. IR analysis of attempted co-crystallization experiments	158
Table 6.2. Hydrogen bond parameters of co-crystals and salts	163
Table 6.3. Thermal properties of D10, D11, D12 and their co-crystals/ salts.	165
Table 6.4. Oxygen balance, detonation velocity and detonation pressure of energetic materials	166
Table 6.5. H ₅₀ values of energetic materials	166

Acknowledgements

First and foremost, I would like to express my sincere gratitude to my advisor, Professor Christer B. Aakeröy for his frequent guidance, encouragement, patience and motivation throughout these five years. You have been supportive since the days I joined your group. I cannot adequately express how much I appreciate the time, wisdom, and mentorship you have given me. It has been a great privilege to work with you and I am a better writer, presenter and scientist because of you.

Thank you to Dr. Christine Aikens, Dr. Tendai Gadzikwa, Dr. Keith Hohn and Dr. Meena Kumari for serving on my dissertation committee. Thank you for your guidance and expertise. My work is greatly improved because of your suggestions and guidance.

I also like to thank Dr. Eric Maatta for being on my committee for three years and for all his support and encouragement.

I'm grateful to Dr. John Desper, Dr. Abhijeet Sinha, Dr. Victor Day and Dr. Marijana Đaković for solving all the nice crystal structures and without them most of the chapters in this dissertation would not have been possible.

I would like to extend my gratitude to Dr. Eric Maatta, Dr. Duy Hua, Dr. Christopher Levy and Dr. Emily McLaurin for being wonderful teachers and increasing my interest towards chemistry. A special thanks to Dr. Amarasiri Fernando who was my undergraduate research mentor for his guidance and advises to continue chemistry research.

Thank you all Aakeröy group members, past and present, for all the support and all the fun time in the lab and in the travelling we had together. Special thanks to everyone for all the help in conducting drop impact tests. It was always a nice place and great group of people to work with.
“The best research group ever”

I want to acknowledge Department of Chemistry, Kansas State University, Dane Hansen Foundation, US Army Research Office and US Army Research Laboratory for funding throughout my Ph.D. life. I would like to extend my gratitude to Dr. Adam Matzger at University of Michigan and the Multidisciplinary University Research Initiative (MURI) team for all the knowledge and opportunities given.

A special gratitude is extended to Dr. Yasmin Patel, Dr. Leila Maurmann, Mr. Jim Hodgson, Mr. Ron Jackson, Mr. Tobe Eggers, Ms. Mary Dooley, Ms. Kimberly Ross and Ms. Lisa Percival for making my life at K-State a memorable and easy at K-State. Thanks to Mr. Michael Hinton for helping and guiding me to become a better teacher.

A special thanks to Dr. Dhanushi Welideniya for all the support, suggestions, motivation and mentoring me in the lab. I owe special thanks to my good friends Dr. Amendra Fernando and Dr. Tharanga Wijethunga for their great support from the K-State admission and making my life memorable and easy in the USA.

I am very thankful to all my friends in Manhattan and K-State for their support and being there for me and taking care of me during hard times. Among you I never felt alone or away from my home and the time we spend together was really enjoyable and memorable.

Finally, I would like to thank my mother for unconditional love, all of the sacrifices that she has made, all the blessings and for giving me strength to achieve all the success. She is the strongest and bravest women I have ever met in my life and her courage to raise me without a father was incredible. Thanks again “Amma” for your endless love and you made me become a strong man today.

Dedication

To my amazing mother...!

Preface

Research carried out at Aakeröy group in the Kansas State University for this dissertation led to the following publications in peer-reviewed scientific journals and more will be coming soon...

- **Gamekkanda, J.C.**; Sinha, A.S.; Desper, J.; Dakovic, M.; Aakeröy, C.B., Competition between hydrogen bonds and halogen bonds: a structural study. *New J. Chem.*, **2018**, 42, 10539-10547.
- **Gamekkanda, J.C.**; Sinha, A.S.; Desper, J.; Đaković, M.; Aakeröy, C. B., The Role of Halogen Bonding in Controlling Assembly and Organization of Cu(II)-Acac Based Coordination Complexes. *Crystals* **2017**, 7 (7), 226.

Chapter 1 Introduction

In the early 1980s, the phrase “Molecular recognition” became popular as it was highly relevant to crucial phenomena in biological systems.¹ Molecular recognition includes both intra- and intermolecular occurrences (Figure 1.1) even though “supramolecular chemistry,” “host-guest chemistry” and “self-assembly” are mostly concerned with intermolecular interactions. In this thesis, we are going to focus on structural chemistry and properties of chemical systems that involve intermolecular interaction.

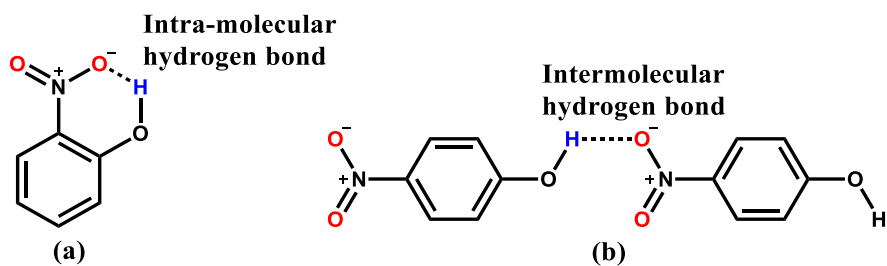


Figure 1.1 Molecular recognition event by (a) intra-molecular, (b) intermolecular supramolecular forces.

1.1 Supramolecular chemistry and self-assembly

Supramolecular chemistry focuses on designing and implementing functional chemical systems based on molecular components held together by noncovalent interactions. According to Jean-Marie Lehn, supramolecular chemistry is defined as “chemistry beyond the molecule”.²⁻³ Moreover, supramolecular chemistry is all about intermolecular bonds which cover the structures and functions of the chemical units held together.³ The Nobel Prize for Chemistry in 1987 was awarded jointly to Jean-Marie Lehn, Donald J. Cram, and Charles J. Pedersen "for their development and use of molecules with structure-specific interactions of high selectivity". Since supramolecular synthesis goes beyond the scope of using covalent bonds to build molecular architectures, the specific set of intermolecular interactions that are used to achieve controlled and

directional supramolecular assembly can result in a superior manipulation of the macroscopic properties of the targeted material (Figure 1.2).

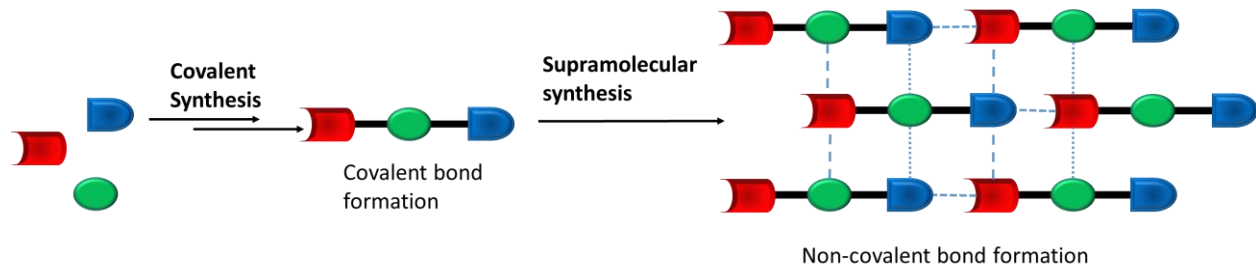


Figure 1.2 Covalent synthesis Vs. supramolecular synthesis

The key interactions of supramolecular synthesis are reversible intermolecular bonds such as: hydrogen-bonds,⁴⁻¹⁰ halogen-bonds,¹¹⁻¹⁵ π - π interactions,¹⁶⁻¹⁸ anion- π interactions,¹⁹ cation- π interactions²⁰, and dipole-dipole interactions.²¹⁻²² Metal-ligand interactions also play a significant role in supramolecular synthesis due to their reversible nature.²³⁻²⁴ Covalent synthesis can be one step or a multi-step process although non-covalent synthesis is a one-pot (one step) synthesis. Therefore, a better understanding about these non-covalent forces is necessary in order to design predictable supramolecular architectures or self-assemblies. We will discuss most significant and useful supramolecular driving forces, metal-ligand interactions, hydrogen bonds and halogen bonds in the following sections.

1.1.1 Metal-ligand interactions (coordinate bond)

Recently, it has been shown that coordination complexes of metal centers bridged by organic linkers can be engineered in order to get 0D, 1D, 2D or 3D architectures (Figure 1.3).²⁵⁻²⁷

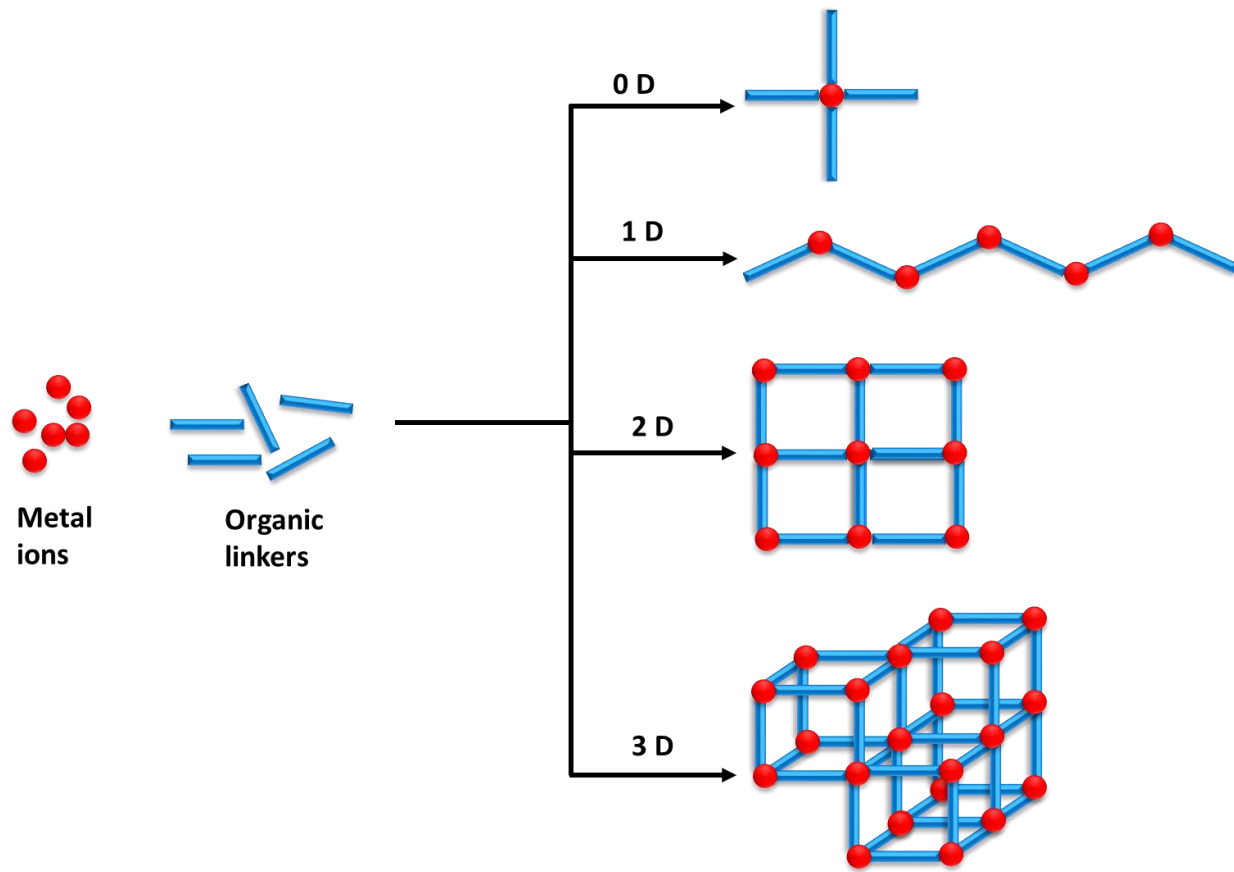


Figure 1.3 Schematic diagram that shows the formation of 0D, 1D, 2D and 3D coordination polymers or metal-ligand complexes

If we can assemble precise topologies and pre-determined connectivity we can make new functional materials which have several applications such as: gas adsorption, sensing, controlled release of molecules, water scavengers, electronics, magnetic materials, separations, and catalyst.²⁸⁻³²

1.1.2 The hydrogen bond (HB)

The hydrogen bond is the most common intermolecular interaction in molecular recognition due to its strength and directionality. A typical hydrogen bond may be shown as D–H \cdots A, where, D–H represents the hydrogen bond donor and A represents the acceptor which can be a neutral atom or anion (Figure 1.4).



Figure 1.4 Schematics show the formation of hydrogen bond

Hydrogen bonding is abundant in nature, and the best example is the DNA double helix composed of complementary base pairs.³³ Complementary hydrogen bonds may offer reliable tools for constructing supramolecular architectures³⁴ and there are many self-complementary dimers such as carboxylic acids and amides that can be used for making supramolecular architectures (Figure 1.5).

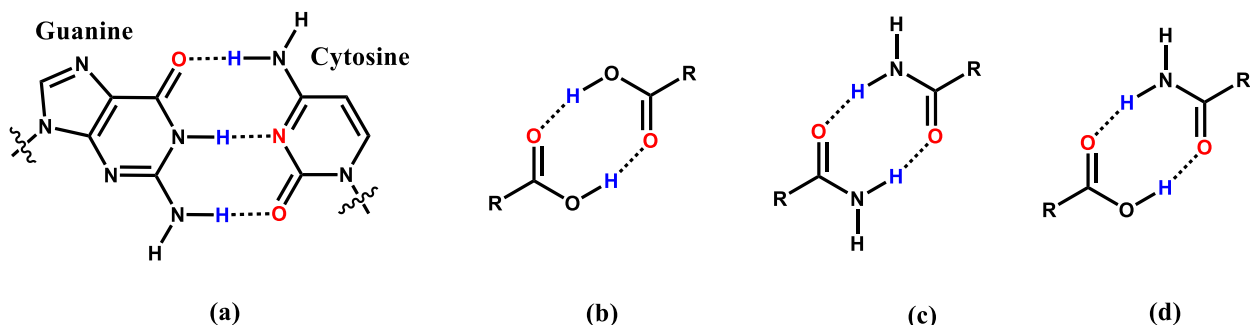


Figure 1.5 Typical examples for hydrogen bonding (a) base pair of DNA helix, (b) carboxylic homodimer, (c) amide homodimer (d) acid-amide heterodimer

1.1.3 The halogen bond (XB)

Halogen bonds have features that are similar to those of hydrogen bonds concerning both strength and directionality.³⁵ A typical halogen bond can be shown as D-X...A, where X represents the halogen-bond donor such as: iodine, bromine or chlorine and A represents the acceptor which can be a unit possessing at least one nucleophilic region. (Figure 1.6).



Figure 1.6 Schematics show the formation of hydrogen bond

The halogen atom can act as a halogen-bond donor or halogen-bond acceptor due to the anisotropic distribution of positive and negative electrostatic potential on halogen atom (Figure 1.7). The electropositive region is called sigma hole (σ -hole), and it becomes stronger from fluorine to iodine.

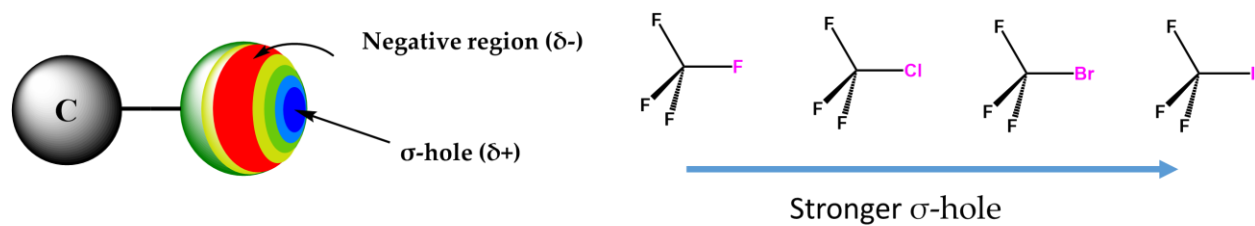


Figure 1.7 Anisotropic distribution of positive and negative potential on halogen and change of strength of σ -hole with halogen atom

The halogen bond has recently become an effective tool for supramolecular synthesis and it has shown the ability to make several functional materials in the fields of material science,³⁶⁻³⁷ catalyst,³⁸⁻³⁹ and biological sciences.⁴⁰⁻⁴¹

1.2 Crystal engineering

The basic goal of “crystal engineering” is to design periodic structures with a predictive supramolecular assembly that delivers desired property/ properties in the new material.⁴² The term crystal engineering was proposed by G. M. J. Schmidt in the 1970s with the research work on the photochemical reactions of cinnamic acids.⁴³ G.R. Desiraju, in 1989, defined crystal engineering as “*Understanding of intermolecular interactions in the context of crystal packing and the utilization of such understanding in the design of new solids with desired physical and chemical properties*”.⁴⁴ Crystal engineering can be considered as the supramolecular equivalent of organic

synthesis and the synthon (building block) approach is an effective approach of crystal engineering, which simplifies the complex problem of structure prediction.⁴⁵

1.2.1 Supramolecular synthons “Is the communicating part ready?”

A supramolecular synthon can be defined as “*A structural unit within a supermolecule which can be formed and/ or assembled by known or conceivable synthetic operations involving intermolecular interactions*”.⁴⁶ A supramolecular synthon plays a similar function in supramolecular synthesis as a molecular synthon does in a conventional synthesis, and the main difference is the role played by intermolecular interactions (Figure 1.8).

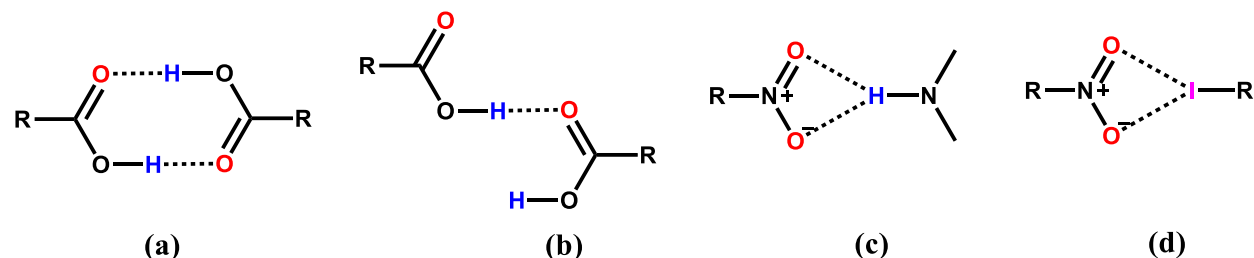


Figure 1.8 Examples for supramolecular synthons, (a) dimer in acids, (b) catemer in acids, (d) nitro···amino HB interaction and (d) nitro···iodo XB interaction

Supramolecular synthons can be categorized as homosynthons (occur between same complementary functional groups, Figure 1.8 (a) and (b)) and heterosynthons (occur between different functional groups, Figure 1.8 (c) and (d))

1.2.2 Co-crystallization “Finding the best match”

The process of bringing two or more different molecular species together inside one periodic crystalline lattice without breaking or making covalent bonds can be described as co-crystallization.⁴⁷⁻⁴⁸ Co-crystallization and re-crystallization can happen in parallel, but co-crystallization makes heteromeric products while the latter gives a homomeric product (Figure 1.9). The co-crystallization yields the co-crystals which is defined as “*Solids that are crystalline*

materials composed of two or more molecules in the same crystal lattice” according to a FDA guidance.⁴⁹

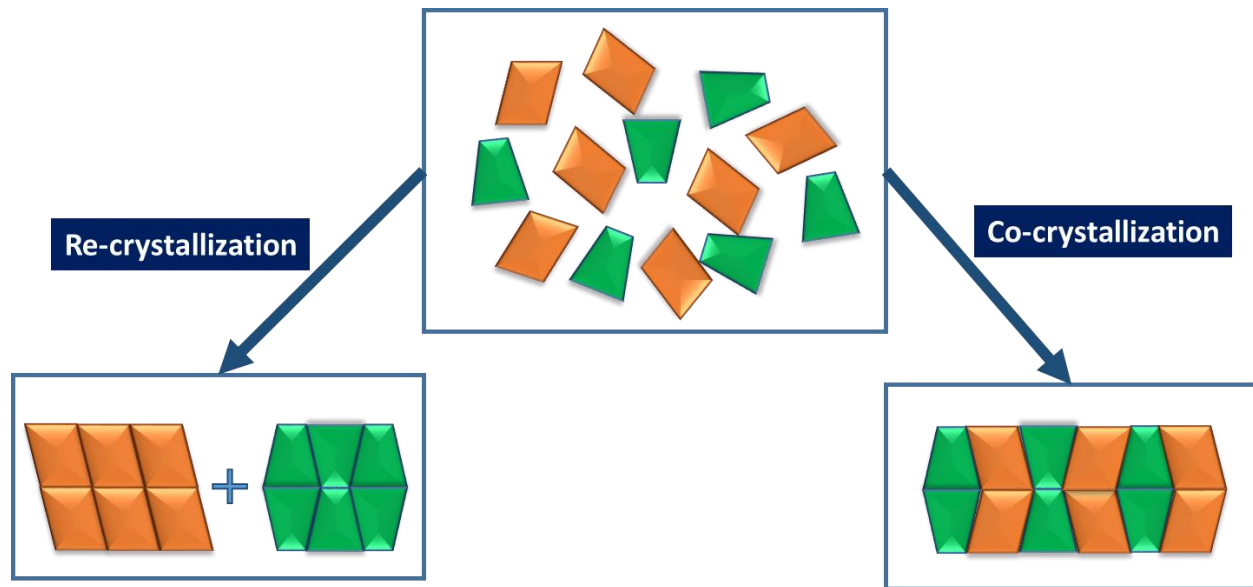


Figure 1.9 Re-crystallization vs co-crystallization

A co-crystallization attempt may give not only co-crystals but the outcome can be in a broad range including several solid forms such as: molecular salt, salt co-crystal, ionic liquid, solvate, sold dispersion, supramolecular gelator, eutectic and solid solution.⁵⁰ The non-covalent interactions can be identified as the driving force for co-crystal formation.

1.2.3 Hydrogen bond in co-crystallization “A glue to bring things together”

Hydrogen bonding can be used as a driving force for co-crystallization in order to bring supramolecular synthons together due to directionality and strength (Figure 1.10). Arguably, HB is the most studied intermolecular interaction in supramolecular chemistry and co-crystal design.⁵¹ Moreover, selectivity and interaction patterns play a major role in crystal engineering. Margaret C. Etter in 1990s published a particularly useful set of guidelines to identify possible preferences of hydrogen bonds in terms of selectivity and pattern of molecular aggregation.⁵² The following three Etter rules can be applied to neutral organic molecules in the formation of co-crystals.

1. All good proton donors and acceptors are used in hydrogen bonding.
2. Six-membered-ring intramolecular hydrogen bonds form in preference to intermolecular hydrogen bonds.
3. The best proton donors and acceptors remaining after intramolecular hydrogen-bond formation form intermolecular hydrogen bonds to one another.



Figure 1.10 A binary co-crystal formed between 4,4'-bipyridine and hydroquinone via two heterosynthons⁵³

1.2.4 Halogen bond in co-crystallization “An alternative glue”

The halogen bond is a relatively new addition to the toolbox of supramolecular chemistry and crystal engineering. It has gained widespread attraction due to its strong and directional nature comparable to hydrogen bonds (Figure 1.11).⁵⁴

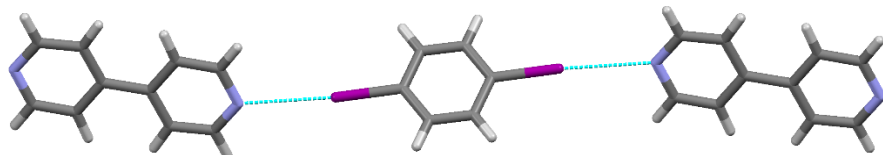


Figure 1.11 A binary co-crystal formed between 4,4'-bipyridine and 1,4-diiodobenzene via halogen bonds⁵⁵

Moreover, there are three types of XB interactions, namely: (i) a conventional halogen-bond between the electrophilic region (σ -hole) of a halogen atom and electronegative atom (such as N, O), (ii) type-I halogen-halogen bond occurs due to van der Waals interactions between two halogen atoms, and (iii) type-II halogen-halogen bond occurs between the nucleophilic region of

one halogen atom and electrophilic region on another (Figure 1.12). Type I ($\theta_1 \approx \theta_2$) and type II ($\theta_1 \approx 180^\circ$, $\theta_2 \approx 90^\circ$), where θ_1 and θ_2 are the C-X…X angles (X = Cl, Br, I).⁵⁶

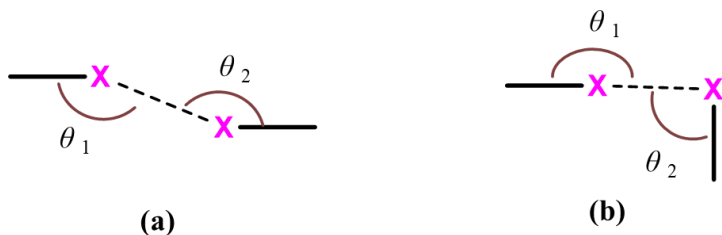


Figure 1.12 Different geometries in halogen...halogen contacts (a) type I and (b) type II

1.2.5 Applications of co-crystallization

Co-crystal technology can be applied to change the macroscopic properties of materials. For example, this technology can be used to overcome the non-solubility issue in pharmaceutical drugs. Agrochemicals industry can also benefit by co-crystallization addressing the high solubility problems which are common for fertilizer and pesticides.⁵⁷ Energetics/ explosives that suffer from instability and high sensitivity also can be improved by using this technology. Also, co-crystallization approaches have been applied in the areas of separation and purification processes, solid state solvent-free synthesis, and chiral resolution.⁵⁸⁻⁶¹ Further, applications of co-crystallization can be found in the areas of nutraceuticals, organic semiconductors, optoelectronic materials, ferroelectric materials, charge transfer complexes, non-linear optics, and liquid crystals.⁶²⁻⁶⁶

1.3 Host-guest chemistry

Despite of the predominance of noncovalent interactions in living nature, researchers did not explicitly investigate non-covalent interactions related to host-guest chemistry until the pioneering work on inclusion chemistry of molecular hosts such as crown ethers, cryptands, cavitands, and carcerands by Lehn, Cram, and Pedersen.⁶⁷ The first supramolecular host was a

crown ether which was synthesized accidentally by Pedersen.⁶⁸ The first cyclic host (cyclic hexaether) was obtained as a byproduct due to contaminations from an impurity in the synthesis process of bisphenol (Figure 1.13).

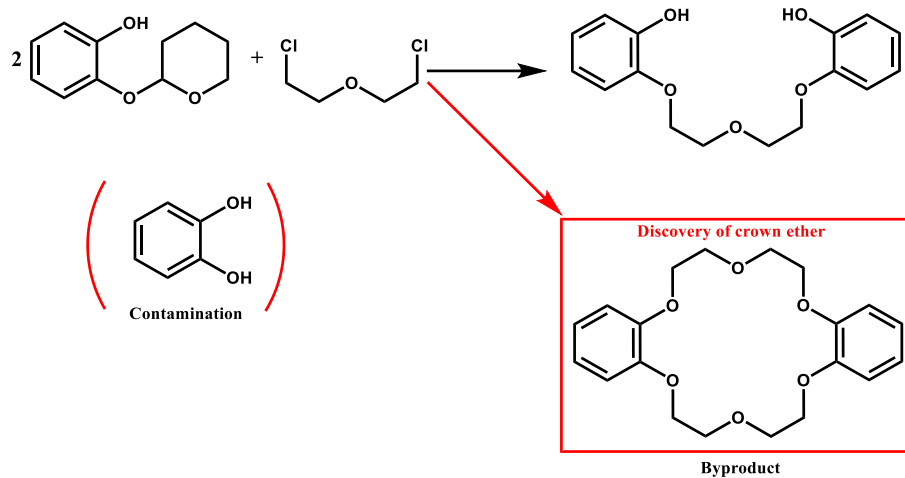


Figure 1.13 Accidental synthesis of the first supramolecular host

With the discovery of crown ethers, several other types of host molecules such as cryptands, spherands, pillararenes, cyclophanes, cryptophanes, calixarenes, cavitands, cyclodextrins, cucurbiturils and more have been discovered in past few decades (Figure 1.14).

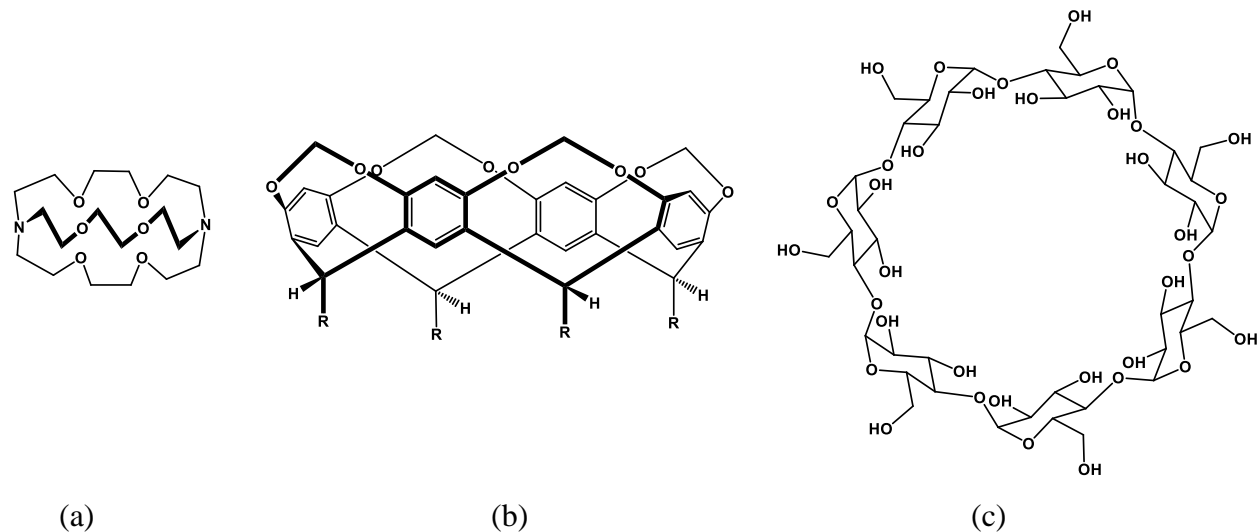


Figure 1.14 Examples for supramolecular hosts, (a) [2,2,2]cryptand, (b) cavitand and (c) β -cyclodextrin

Since these molecules have pre-organized binding pockets, they can be used for selective molecular recognition with high binding affinities for complementary guest molecules. In a binding event, several non-covalent interactions such as: hydrogen bonding, halogen bonding, π - π interactions, and hydrophobic forces play a major role as the driving forces. Further, functionalization of hosts such as: cucurbiturils,⁶⁹ cavitands,⁷⁰ calixarenes,⁷¹ and pillarines⁷² enables the more versatile use of host and multiple applications (Figure 1.14).

Self-assembled tetrafunctionalized calix[4]resorcinarene capsule cavitands have gained great attention due to their applications in detection of reactive intermediates and as microvesicles for drug delivery. The main driving forces that can be used to make such capsules are metal-ligand coordination, hydrogen bonding and halogen bonding. Figure 1.15 shows an example of a cavitand-based molecular capsule, where the driving force to make capsule is hydrogen bonding.⁷³

There are guest molecules incorporated inside the cavity of the capsule.

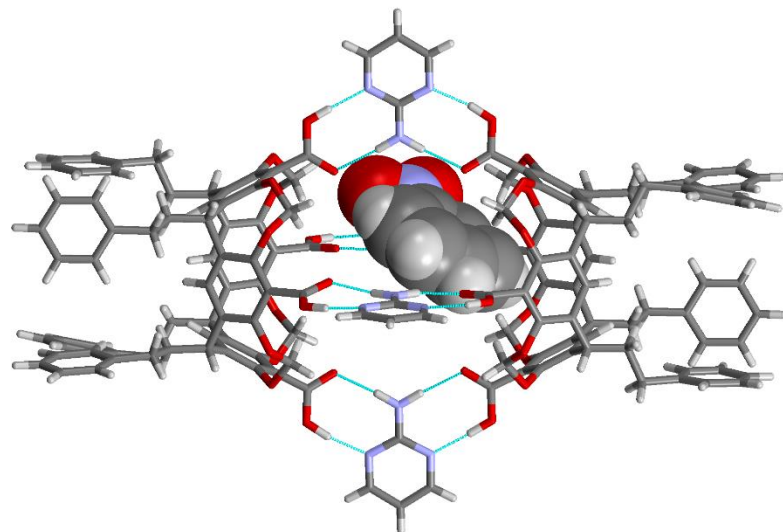


Figure 1.15 Molecular capsule based on cavitand constructed by multiple hydrogen bonds⁷³

1.4 Goals of the thesis

In order to better understand the supramolecular chemistry of synthons attached to small and large molecules, we have designed several research projects. In this study, major non-covalent interactions such as: metal-ligand interactions, hydrogen bonding and halogen bonding will be studied.

- **Construction of predictable supramolecular architectures⁷⁴**

Chapter 2 The acetylacetone (acac) ligand is considered as an excellent coordinating ligand in metal ion complexation. The anion of the acac ligand can exhibit with delocalized negative charges due to the two oxygen atoms which make acac as a bidentate ligand in binding with metal ions. The activated halogen-bond donor atoms such as Cl, Br and I are good candidates in making halogen bonds with suitable halogen-bond acceptor molecules. The ligands which have both the acac moiety and the activated halogen bond donor are advantageous in metal complexation as well as in halogen bonding. The halogen atoms are activated using ethynyl functionality as an effective way of strengthening the halogen bond formation. In this study, six different types of ligands which have acac sites and halogen donor sites have been synthesized (involved in multi-step synthesis) and characterized.

Characterization of these ligands was done by using proton ^1H NMR, IR, and X-ray diffraction when possible. Possibilities of halogen bonding sites were examined corresponding to each ligand, and further complexation of these ligands have been investigated using different metal ions. Ability to form organometallic supramolecular architectures based on halogen bonding were studied.

- **Understanding the competition between supramolecular forces by co-crystallization⁷⁵**

Chapter 3 The similarity in structural behavior and comparable strength of hydrogen bonding and halogen bonding enable opportunities to use them in similar applications. Combining these two interactions can produce more complex architectures. Due to the similar behavior of these interactions, there is significant competition between these donor molecules when forming noncovalent interactions with potential acceptors. Competition between hydrogen-bond (HB) donors and halogen-bond (XB) donors can be investigated by having them on one backbone. In this project, we designed and synthesized (multi-step synthesis) tetra-functional donor molecules having HB and XB donors attached to the same molecular backbone to study the competitiveness of these two types of interactions.

Co-crystallization of these donors with suitable acceptors was performed to gain a better understanding of structural behavior and competition to bind with acceptor molecules.

- **Study of the host-guest chemistry with enforced cavities**

Chapter 4 Cavitands are bowl-shaped molecules that are conformationally rigid. These molecules have enforced cavities which accommodate complementary guests, and they can assemble into molecular capsules. In this project, we functionalized the upper rim of the cavitands with different hydrogen and halogen bond donor/acceptor groups. Adding both halogen and hydrogen bond donors to the same cavitand molecule reveals opportunities to compare the relative competitiveness of those donors towards suitable acceptors as well. These cavitands can also be used for molecular recognition events via host-guest interactions. Another way of functionalization of the cavitand molecules is adding acac moiety to the cavitand. These types of functionalized cavitand can make capsules such as: discrete metal-ligand complexes or 1-D chains of metal-ligand

complexes with suitable metal ions. We have designed, and synthesized acac functionalized cavitands to study metal binding.

Suitable donors, acceptors, and metal ions were introduced to the functionalized cavitands in solid state and solution state.

- **Application of co-crystallization to enhance the properties and stability of known energetic compounds**

Chapter 5 and Chapter 6 Energetic/explosive materials contain a high amount of chemical energy that can be released in an explosion and produce high-temperature combustion products. Most of the energetic materials have limited use due to their high sensitivity towards impact and friction and also due to low melting/ decomposition points. Therefore, we need to improve those thermal and physical properties to make them more usable in the field.

Known unstable energetic materials such as nitrocarbamates, nitrated amino tetrazoles, bis-tetrazoles (synthesized in the lab in small scale) were co-crystallized with suitable donor/ acceptor molecules. Detonation properties such as detonation velocity and detonation pressure were also determined. The impact sensitivity of newly formed materials and parent explosives were investigated by drop test method and compared with parent explosive materials. Furthermore, the reactivity of some materials which have acidic nature was also studied.

1.5 References

1. Gellman, S. H., *Chem. Rev.* **1997**, 97 (5), 1231-1232.
2. Lehn, J.-M., *Chem. Soc. Rev.* **2017**, 46 (9), 2378-2379.
3. Jean-Marie, L., *Angew. Chem. Int. Ed. Engl.* **1988**, 27 (1), 89-112.
4. Slater, A. G.; Perdigão, L. M. A.; Beton, P. H.; Champness, N. R., *Acc. Chem. Res.* **2014**, 47 (12), 3417-3427.
5. Armstrong, G.; Buggy, M., *J Mater Sci* **2005**, 40 (3), 547-559.
6. Lin, X.; Suzuki, M.; Gushiken, M.; Yamauchi, M.; Karatsu, T.; Kizaki, T.; Tani, Y.; Nakayama, K.-i.; Suzuki, M.; Yamada, H.; Kajitani, T.; Fukushima, T.; Kikkawa, Y.; Yagai, S., *Sci Rep* **2017**, 7, 43098.
7. Seto, C. T.; Whitesides, G. M., *J. Am. Chem. Soc.* **1993**, 115 (3), 905-916.
8. González-Rodríguez, D.; Schenning, A. P. H. J., *Chem. Mater.* **2011**, 23 (3), 310-325.

9. Cheng, C.-C.; Wang, J.-H.; Chuang, W.-T.; Liao, Z.-S.; Huang, J.-J.; Huang, S.-Y.; Fan, W.-L.; Lee, D.-J., *Polym. Chem.* **2017**, 8 (21), 3294-3299.
10. Kyung, Y. S.; C., Z. S., *Isr. J. Chem.* **2013**, 53 (8), 511-520.
11. Gilday, L. C.; Robinson, S. W.; Barendt, T. A.; Langton, M. J.; Mullaney, B. R.; Beer, P. D., *Chem. Rev.* **2015**, 115 (15), 7118-7195.
12. Bertani, R.; Sgarbossa, P.; Venzo, A.; Lelj, F.; Amati, M.; Resnati, G.; Pilati, T.; Metrangolo, P.; Terraneo, G., *Coord. Chem. Rev.* **2010**, 254 (5), 677-695.
13. Metrangolo, P.; Meyer, F.; Pilati, T.; Resnati, G.; Terraneo, G., *Angew. Chem. Int. Ed.* **2008**, 47 (33), 6114-6127.
14. Meazza, L.; Foster, J. A.; Fucke, K.; Metrangolo, P.; Resnati, G.; Steed, J. W., *Nat. Chem* **2012**, 5, 42.
15. Aakeröy, C. B.; Spartz, C. L., *Top. Curr. Chem.* **2015**, 358, 155-182.
16. Chen, T.; Li, M.; Liu, J., *Cryst. Growth Des.* **2018**, 18 (5), 2765-2783.
17. Jethwa, S. J.; Kolsbjerg, E. L.; Vadapoo, S. R.; Cramer, J. L.; Lammich, L.; Gothelf, K. V.; Hammer, B.; Linderoth, T. R., *ACS Nano* **2017**, 11 (8), 8302-8310.
18. Hunter, C. A.; Sanders, J. K. M., *J. Am. Chem. Soc.* **1990**, 112 (14), 5525-5534.
19. Chifotides, H. T.; Dunbar, K. R., *Acc. Chem. Res.* **2013**, 46 (4), 894-906.
20. Dougherty, D. A., *Acc. Chem. Res.* **2013**, 46 (4), 885-893.
21. Würthner, F., *Acc. Chem. Res.* **2016**, 49 (5), 868-876.
22. Mu, Z.; Shao, Q.; Ye, J.; Zeng, Z.; Zhao, Y.; Hng, H. H.; Boey, F. Y. C.; Wu, J.; Chen, X., *Langmuir* **2011**, 27 (4), 1314-1318.
23. Beck, J. B.; Ineman, J. M.; Rowan, S. J., *Macromolecules* **2005**, 38 (12), 5060-5068.
24. Lanigan, N.; Wang, X., *Chem. Commun.* **2013**, 49 (74), 8133-8144.
25. Mendes, R. F.; Almeida Paz, F. A., *Inorg. Chem. Front.* **2015**, 2 (6), 495-509.
26. Jiang-Feng, S.; Rui-Sha, Z.; Jia, Z.; Chun-Yan, X.; Yan-Bing, L.; Biao-Bing, W., *Z. Anorg. Allg. Chem.* **2011**, 637 (5), 589-595.
27. Zhang, L.-P.; Ma, J.-F.; Yang, J.; Liu, Y.-Y.; Wei, G.-H., *Cryst. Growth Des.* **2009**, 9 (11), 4660-4673.
28. Ren, J.; Dyosiba, X.; Musyoka, N. M.; Langmi, H. W.; Mathe, M.; Liao, S., *Coord. Chem. Rev.* **2017**, 352, 187-219.
29. Falcaro, P.; Ricco, R.; Doherty, C. M.; Liang, K.; Hill, A. J.; Styles, M. J., *Chem. Soc. Rev.* **2014**, 43 (16), 5513-5560.
30. Chaemchuen, S.; Kabir, N. A.; Zhou, K.; Verpoort, F., *Chem. Soc. Rev.* **2013**, 42 (24), 9304-9332.
31. Yap, M. H.; Fow, K. L.; Chen, G. Z., *Green Energy & Environment* **2017**, 2 (3), 218-245.
32. Furukawa, H.; Cordova, K. E.; O'Keeffe, M.; Yaghi, O. M., *Science* **2013**, 341 (6149).
33. Célia, F. G.; Matthias, B. F.; G., S. J.; Jan, B. E., *Chem. Eur. J.* **1999**, 5 (12), 3581-3594.
34. Carsten, S.; Wolfgang, W., *Angew. Chem. Int. Ed.* **2001**, 40 (23), 4363-4369.
35. Aakeröy, C. B.; Fasulo, M.; Schultheiss, N.; Desper, J.; Moore, C., *J. Am. Chem. Soc.* **2007**, 129 (45), 13772-13773.
36. Meyer, F.; Dubois, P., *CrystEngComm* **2013**, 15 (16), 3058-3071.
37. Pierangelo, M.; Giuseppe, R.; Tullio, P.; Rosalba, L.; Franck, M., *J. Polym. Sci., Part A: Polym. Chem.* **2007**, 45 (1), 1-15.
38. David, B.; M., H. S., *Chem. Eur. J.* **2016**, 22 (41), 14434-14450.
39. Gliese, J.-P.; Jungbauer, S. H.; Huber, S. M., *Chem. Commun.* **2017**, 53 (88), 12052-12055.
40. Wilcken, R.; Zimmermann, M. O.; Lange, A.; Joerger, A. C.; Boeckler, F. M., *J. Med. Chem.* **2013**, 56 (4), 1363-1388.
41. Erdélyi, M., *Biochemistry* **2017**, 56 (22), 2759-2761.
42. Soldatov, D. V.; Terekhova, I. S., *J. Struct. Chem.* **2005**, 46 (1), S1-S8.
43. Schmidt, G. M. J., Photodimerization in the solid state. In *Pure Appl. Chem.*, 1971; Vol. 27, p 647.

44. Desiraju, G. R., *IUCrJ* **2016**, 3 (Pt 1), 1-2.
45. Desiraju, G. R., *J. Am. Chem. Soc.* **2013**, 135 (27), 9952-9967.
46. Thalladi, V. R.; Goud, B. S.; Hoy, V. J.; Allen, F. H.; Howard, J. A. K.; Desiraju, G. R., *Chem. Commun.* **1996**, (3), 401-402.
47. Dunitz, J. D., *CrystEngComm* **2003**, 5 (91), 506-506.
48. Aakeröy, C. B.; Salmon, D. J., *CrystEngComm* **2005**, 7 (72), 439-448.
49. Aitipamula, S.; Banerjee, R.; Bansal, A. K.; Biradha, K.; Cheney, M. L.; Choudhury, A. R.; Desiraju, G. R.; Dikundwar, A. G.; Dubey, R.; Duggirala, N.; Ghogale, P. P.; Ghosh, S.; Goswami, P. K.; Goud, N. R.; Jetti, R. R. K. R.; Karpinski, P.; Kaushik, P.; Kumar, D.; Kumar, V.; Moulton, B.; Mukherjee, A.; Mukherjee, G.; Myerson, A. S.; Puri, V.; Ramanan, A.; Rajamannar, T.; Reddy, C. M.; Rodriguez-Hornedo, N.; Rogers, R. D.; Row, T. N. G.; Sanphui, P.; Shan, N.; Shete, G.; Singh, A.; Sun, C. C.; Swift, J. A.; Thaimattam, R.; Thakur, T. S.; Kumar Thaper, R.; Thomas, S. P.; Tothadi, S.; Vangala, V. R.; Variankaval, N.; Vishweshwar, P.; Weyna, D. R.; Zaworotko, M. J., *Cryst. Growth Des.* **2012**, 12 (5), 2147-2152.
50. Cherukuvada, S.; Kaur, R.; Guru Row, T. N., *CrystEngComm* **2016**, 18 (44), 8528-8555.
51. Desiraju, G. R., *Cryst. Growth Des.* **2011**, 11 (4), 896-898.
52. Etter, M. C., *Acc. Chem. Res.* **1990**, 23 (4), 120-126.
53. Oswald, I. D. H.; Motherwell, W. D. S.; Parsons, S., *Acta Cryst. B* **2005**, 61 (1), 46-57.
54. Mukherjee, A.; Tothadi, S.; Desiraju, G. R., *Acc. Chem. Res.* **2014**, 47 (8), 2514-2524.
55. Walsh, R. B.; Padgett, C. W.; Metrangolo, P.; Resnati, G.; Hanks, T. W.; Pennington, W. T., *Cryst. Growth Des.* **2001**, 1 (2), 165-175.
56. Metrangolo, P.; Resnati, G., *IUCrJ* **2014**, 1 (Pt 1), 5-7.
57. Honer, K.; Pico, C.; Baltrusaitis, J., *ACS Sustainable Chem. Eng.* **2018**, 6 (4), 4680-4687.
58. Jiang, S.; Patil, R. S.; Barnes, C. L.; Atwood, J. L., *Cryst. Growth Des.* **2017**, 17 (8), 4060-4063.
59. Billot, P.; Hosek, P.; Perrin, M.-A., *Org. Process Res. Dev.* **2013**, 17 (3), 505-511.
60. Braga, D.; Grepioni, F.; Maini, L.; Mazzeo, P. P.; Rubini, K., *Thermochim. Acta* **2010**, 507-508, 1-8.
61. Harmsen, B.; Leyssens, T., *Cryst. Growth Des.* **2018**, 18 (1), 441-448.
62. Sinha, A. S.; Maguire, A. R.; Lawrence, S. E., *Cryst. Growth Des.* **2015**, 15 (2), 984-1009.
63. Khan, M.; Enkelmann, V.; Brunklaus, G., *J. Am. Chem. Soc.* **2010**, 132 (14), 5254-5263.
64. Chen, T.; Sun, Z.; Zhao, S.; Ji, C.; Luo, J., *J. Mater. Chem. C* **2016**, 4 (2), 266-271.
65. Golovanov, D. G.; Lyssenko, K. A.; Antipin, M. Y.; Vygodskii, Y. S.; Lozinskaya, E. I.; Shaplov, A. S., *Cryst. Growth Des.* **2005**, 5 (1), 337-340.
66. D'silva, E. D.; Podagatlapalli, G. K.; Rao, S. V.; Rao, D. N.; Dharmaprakash, S. M., *Cryst. Growth Des.* **2011**, 11 (12), 5362-5369.
67. J., C. D., *Angew. Chem. Int. Ed. Engl.* **1988**, 27 (8), 1009-1020.
68. The Chemistry of Molecular Recognition — Host Molecules and Guest Molecules. In *Supramolecular Chemistry — Fundamentals and Applications: Advanced Textbook*, Ariga, K.; Kunitake, T., Eds. Springer Berlin Heidelberg: Berlin, Heidelberg, 2006; pp 7-44.
69. Kim, K.; Selvapalam, N.; Ko, Y. H.; Park, K. M.; Kim, D.; Kim, J., *Chem. Soc. Rev.* **2007**, 36 (2), 267-279.
70. Hooley, R. J.; Rebek, J., *Chem. Biol.* **2009**, 16 (3), 255-264.
71. Roy, L.; Sara, Z.; Gaël, D. L.; Alex, I.; Alice, M.; Michel, L.; Olivia, R.; Ivan, J., *Asian J. Org. Chem.* **2015**, 4 (8), 710-722.
72. Strutt, N. L.; Zhang, H.; Schneebeli, S. T.; Stoddart, J. F., *Acc. Chem. Res.* **2014**, 47 (8), 2631-2642.
73. Kobayashi, K.; Shirasaka, T.; Yamaguchi, K.; Sakamoto, S.; Horn, E.; Furukawa, N., *Chem. Commun.* **2000**, (1), 41-42.
74. Gamekkanda, J.; Sinha, A.; Desper, J.; Đaković, M.; Aakeröy, C., *Crystals* **2017**, 7 (7), 226.
75. Gamekkanda, J. C.; Sinha, A. S.; Desper, J.; Dakovic, M.; Aakeroy, C. B., *New J. Chem.* **2018**, 42 (13), 10539-10547.

Chapter 2 The Role of Halogen Bonding in Controlling Assembly and Organization of Cu(II)-Acac Based Coordination Complexes

2.1 Introduction

Directed self-assembly of structurally and compositionally complex architectures require a thorough understanding of the design strategy. One way of constructing stable solid-state architectures is to use crystal engineering and by introducing structural preferences of building blocks, which lead to predictable and programmable assemblies.¹⁻² Making stable and programmable coordination complexes can be challenging in the presence of negatively charged counter anions that come with metal salts. These anions may coordinate with the metal center and disrupt metal-ligand interactions (Figure 2.1).

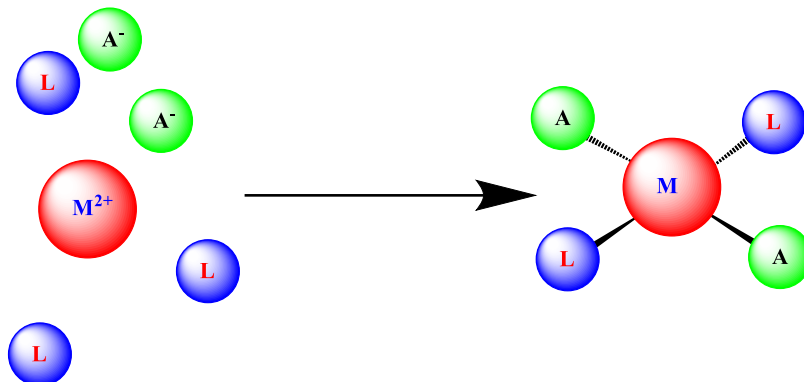


Figure 2.1 Counter anion interference of metal-ligand coordination; L-ligand; M-metal ion; A- counter anion

To avoid the structural interferences of anions, charged ligands that balance the oxidation state of the metal can be employed and by using a chelating ligand further increases the chance of formation of stable metal-ligand complex. With this in mind, the β -diketone (acac) moiety is a good candidate for making metal-ligand complexes. The removal of the acidic hydrogen atom of acac moiety by treating it with a base makes it a negatively charged chelating ligand that can overcome the interference from counter anions (Figure 2.2).

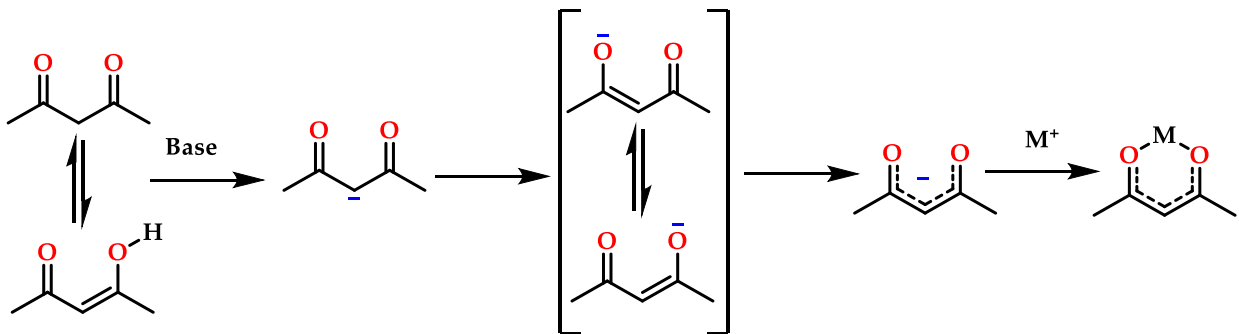


Figure 2.2 Chelation of metal ions by β -diketone (acac) ligand

There are several reported coordination complexes which act as reliable building blocks for supramolecular assemblies in 1-D,³ 2-D,³⁻⁵ and 3-D.^{4, 6} These building blocks may contain cation $\cdots\pi$,⁷ anion $\cdots\pi$,⁸⁻¹⁰ lone-pair $\cdots\pi$,^{8, 10-11} $\pi\cdots\pi$,^{8, 12-13} or metal $\cdots\pi$ ¹⁴⁻¹⁵ interactions as non-covalent interactions between building blocks. The hydrogen bond is one of the most frequently used non-covalent interactions for making these assemblies.¹⁶⁻²⁰ However, use of the hydrogen bond is not always ideal since most hydrogen-bond donor moieties such as: amines, oximes, and carboxylic acids may make unwanted coordination to the metal ion which leads to unpredictable assemblies and architectures. (Figure 2.3)

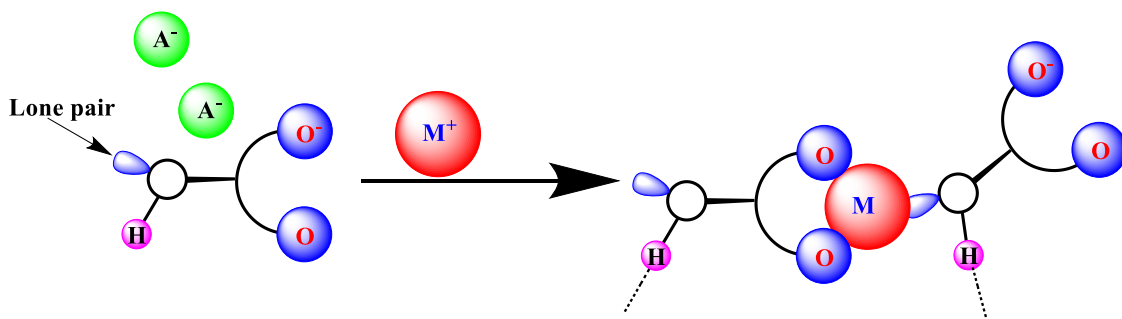


Figure 2.3 Hydrogen bond-donor group interference to metal-acac ligand coordination; M-metal ion; A-counter anion; H-hydrogen-bond donor

To avoid the interference from hydrogen-bond donor moieties, we have to find an alternative functionality that can make non-covalent interaction which has ability to build assemblies and architectures. Halogen bonding may be a possible alternative. According to the IUPAC recommendation from 2013,²¹ “a halogen bond occurs when there is evidence of a net

attractive interaction between an electrophilic region associated with a halogen atom in a molecular entity and a nucleophilic region in another, or the same, molecular entity.” This non-covalent interaction has been used for applications in material science, synthetic chemistry, polymer science, and in bi-molecular systems.²²⁻²⁵ Moreover, metallosupramolecular systems also constructed by combining halogen bonding with metal-containing systems were discovered²⁶⁻²⁷ with a variety of properties such as redox, magnetic, non-linear optical, gas adsorption, and catalytic properties.²⁸⁻²⁹

A previous study used the acac moiety and halogen-bond donors together to make a building block capable of self-assembly with the addition of Cu(II) metal ions.³⁰ Unfortunately, directed self-assemblies were not observed due to the use of un-activated halogen-bond donors. The “activation” of halogen-bond donors can be achieved by placing electron withdrawing groups³¹⁻³⁴ or *sp*-hybridized carbon next to the halogen atom.³⁵⁻³⁶ In order to improve upon this early study, we designed and synthesized six ligands (**L1-6**) which contain an acac moiety and a haloethynyl group (halogen: Cl, Br or I) (Figure 2.4).

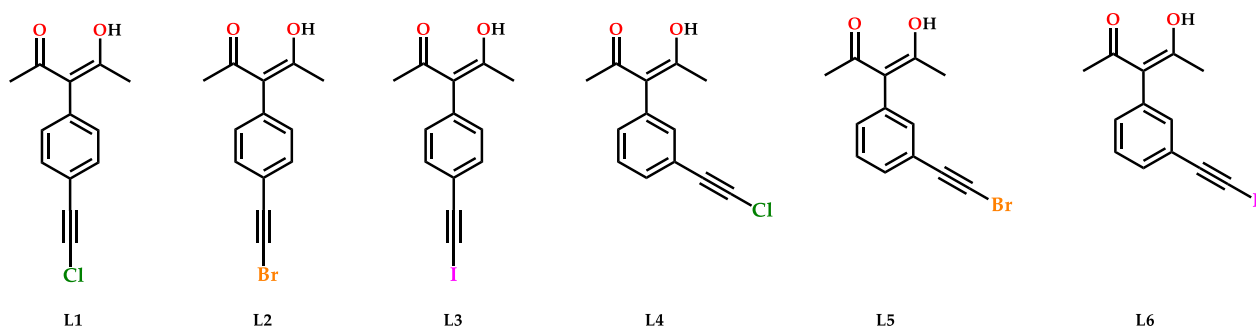


Figure 2.4 Newly designed molecules that can act as chelating ligands (through the acac site) decorated with activated halogen bond donors

In **L1-3**, the haloethynyl group is attached to the para position of the phenyl group while in **L4-6**, it is attached to the meta position in order to study the geometrical effect on making self-assembled architectures. In these ligands, there are four competing halogen-bond acceptor sites:

the hydroxyl oxygen, the keto oxygen, the π -electron cloud on the ethynyl group and the equatorial region on the halogen atom (Figure 2.5). Once the metal-ligand complex is formed, the number of acceptor types is reduced to 3 namely: oxygen of deprotonated acac moiety, the π -electron cloud on the ethynyl group and the equatorial region on the halogen atom.

In this study, we want to establish which acceptor site is going to be dominant in the making of solid-state architectures.

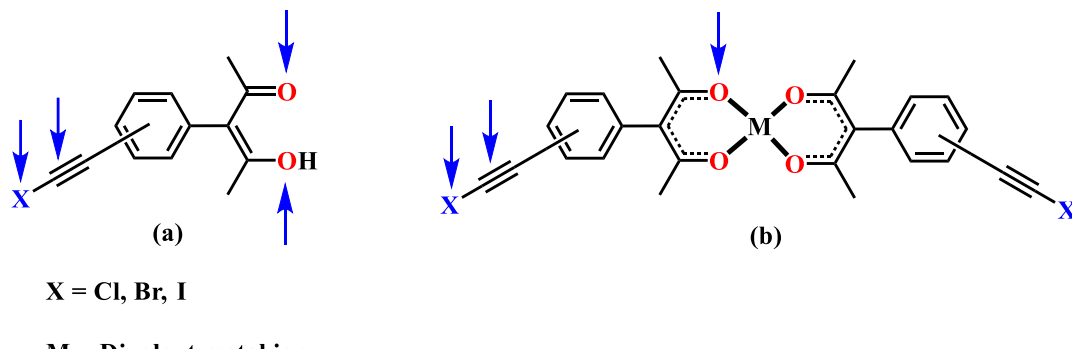


Figure 2.5 Possible halogen–bond acceptor sites; (a) ligand itself, (b) metal-ligand complex

2.1.1 Goals of this study

This study is carried out to achieve specific goals that are listed below.

1. Synthesis of six newly designed ligands and corresponding metal-ligand complexes with suitable divalent metal ions.
2. Modulating the coordination environment around the metal ions by exclusion of competing counter anions or solvent molecules that may interact with metal center.
3. Exploring halogen-bond donor capabilities of Cl, Br and I to form supramolecular architecture in the free ligands and metal-ligand complexes.
4. Investigating the halogen-bond acceptor abilities of free ligand and metal-ligand complexes.

5. Examining the effect of the geometry changes of ligands on formation of supramolecular architectures in free ligands and metal-ligand complexes.
6. Classifying the different types of non-covalent interactions that may appear in the resulting supramolecular assemblies.

2.2 Experimental

2.2.1 General

All chemicals were purchased from commercial sources and used without further purifications. The synthesis of biacetyl-trimethyl phosphite (**1**)³⁷ was carried out according to the previously reported procedure. ¹H NMR and ¹³C NMR spectra were recorded on a Varian Unity plus 400 MHz spectrometer in CDCl₃. Melting points were determined on a Fisher-Johns melting point apparatus and are uncorrected. Infrared spectroscopy (IR) was done on a Nicolet 380 FT-IR (Spectra were recorded by placing small amount of compounds on ZnSe crystal). DSC traces were obtained on a TA Q20. TGA traces were taken on a TA Q50.

2.2.2 Synthesis of ligands

Synthesis of ligands were started by converting corresponding bromobenzaldehyde to TMS protected compound using Sonogashira coupling reaction. It was then halogenated by corresponding halogen source. Finally, the aldehyde group was converted to acac functionality (Figure 2.6).

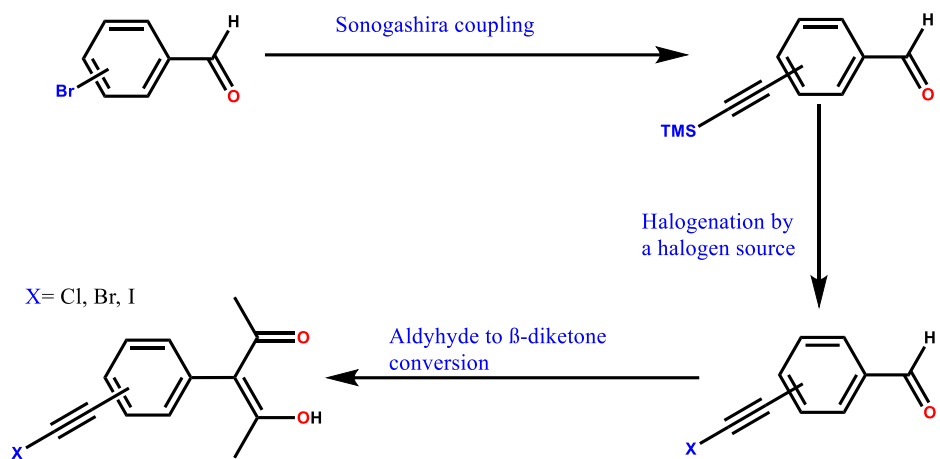
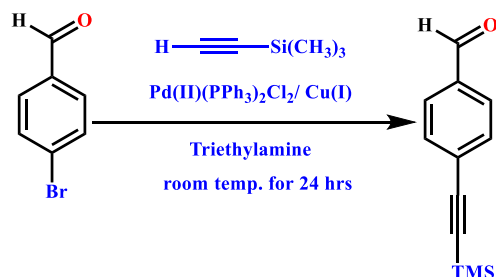


Figure 2.6 General pathway to the synthesis of ligands **L1-L6**

Synthesis of 4-(trimethylsilyl ethynyl)benzaldehyde, 4-(bromoethynyl)benzaldehyde, and 4-(iodoethynyl)benzaldehyde were carried out using literature methods.^{36, 38} Synthesis of 4-(chloroethynyl)benzaldehyde was carried out by using a modified literature method. Synthesis of 3-(trimethylsilyl ethynyl)benzaldehyde, 3-(chloroethynyl)benzaldehyde, 3-bromoethynylbenzaldehyde, and 4-(iodoethynyl)benzaldehyde, **L1**, **L2**, and **L3** were carried out based on literature reported methods.^{36, 38}

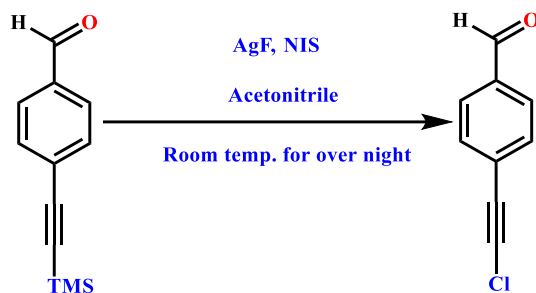
2.2.2.1 Synthesis of 4-(trimethylsilyl ethynyl)benzaldehyde



A stirred solution of 4.50 g (19.40 mmol) 4-bromobenzaldehyde, 83 mg (0.46 mmol) of CuI, and 163 mg (0.23 mmol) of Pd(PPh₃)₂Cl₂ in 80 mL of trimethylamine was degassed with N₂ for 20 minutes. A solution of 2.28 g (23.28 mmol) of trimethylsilylacetylene was added to the stirred solution. The mixture was refluxed overnight under N₂. Upon completion of the reaction, the

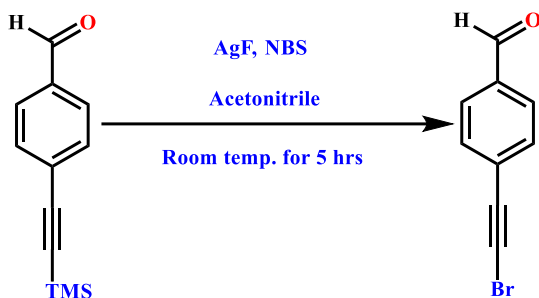
solvent was evaporated by rotavap. The residue was dissolved in ethyl acetate and washed three times with water followed by a saturated NaCl solution. The organic layer was dried with MgSO₄ and the solvent was evaporated by rotavap. The residue was chromatographed on a silica column with hexanes as the eluent to obtain the pure product. Yield: 4.08 g (93%); m.p. 59-61 °C (Lit, 57–58 °C)³⁶; ¹H NMR (δ _H, CDCl₃, 400 MHz): 10.01 (1H, s), 7.83 (2H, d), 7.61 (2H, d), 0.28 (9H, s).

2.2.2.2 Synthesis of 4-(chloroethynyl)benzaldehyde



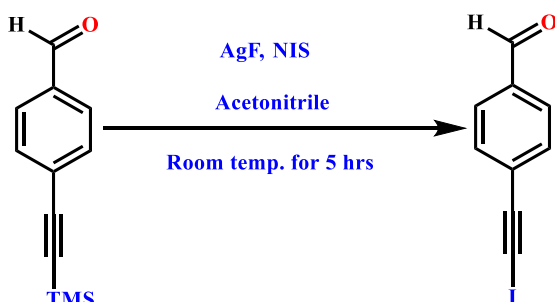
In 60 ml of acetonitrile, 2.00 g (9.80 mmol) of 4-(trimethylsilylethynyl)benzaldehyde and 1.86 g (14.6 mmol) of AgF were dissolved and degassed with N₂ for 20 mins. 1.94 g (14.6 mmol) of N-chlorosuccinimide was added to the stirred solution and the reaction vessel was covered with aluminium foil. The reaction mixture was stirred under N₂ at room temperature overnight. Upon completion of the reaction, the mixture was passed through a short pad of silica. The solvent was evaporated and the residue was dissolved in diethyl ether and washed three times with water. The organic layer was dried over MgSO₄ and the solvent was evaporated to get the pure product. Yield: 1.10 g (67%); m.p. 77-80 °C; ¹H NMR (δ _H, CDCl₃, 400 MHz): 10.01 (1H, s), 7.83 (2H, d), 7.59 (2H, d).

2.2.2.3 Synthesis of 4-(bromoethynyl)benzaldehyde



In 50 ml of acetonitrile, 1.50 g (7.40 mmol) of 4-(trimethylsilylethynyl)benzaldehyde and 940 mg of AgF (7.4 mmol) were dissolved and degassed with N₂ for 20 mins. 1.32 g (7.42 mmol) of N-bromosuccinimide was added to the stirred solution and the reaction vessel was covered with aluminium foil. The reaction mixture was stirred under N₂ at room temperature for 5 hours. Upon completion of the reaction, the mixture was passed through a short pad of silica. The solvent was evaporated and the residue was dissolved in diethyl ether and washed three times with water. The organic layer was dried over MgSO₄ and the solvent was evaporated to get the pure product. Yield: 1.49 g (96%); m.p. 99-102 °C (Lit, 96-98 °C)³⁹; ¹H NMR (δ_{H} , CDCl₃, 400 MHz): 10.02 (1H, s), 7.84 (2H, d), 7.61 (2H, d).

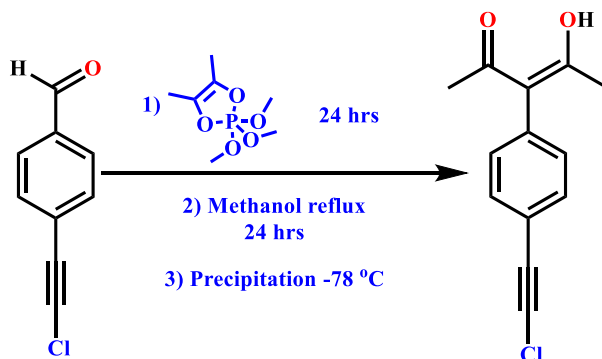
2.2.2.4 Synthesis of 4-(iodoethynyl)benzaldehyde



4-(Iodoethynyl)benzaldehyde was prepared according to the preparation of 4-(bromoethynyl)benzaldehyde from 1.50 g (7.40 mmol) of 4-(trimethylsilylethynyl)benzaldehyde, 940 mg (7.4 mmol) of AgF and 1.67 g of N-iodosuccinimide (7.42 mmol) in 50 ml of acetonitrile.

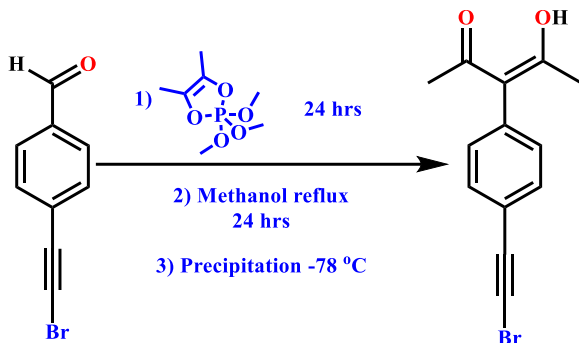
Yield: 1.86 g (98%); m.p. 141–143 °C (Lit, 120–121 °C)⁴⁰; ¹H NMR (δ_{H} , CDCl₃, 400 MHz): 10.02 (1H, s), 7.84 (2H, d), 7.59 (2H, d).

2.2.2.5 Synthesis of 3-(4-(chloroethynyl)phenyl)-4-hydroxypent-3-en-2-one, L1



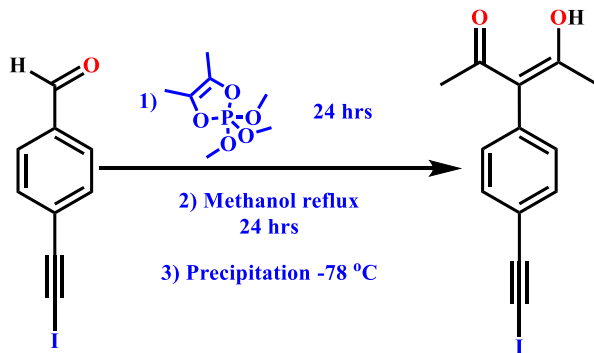
4-(Chloroethynyl)benzaldehyde (1.00 g, 6.00 mmol) was placed in a 100 mL round bottom flask under a N₂ atmosphere. **1** (1.53 g, 7.3 mmol) was added to the flask with continuous stirring. The resulting slurry was stirred for 24 h at room temperature under a N₂ atmosphere to obtain an oil. Then 50 ml of methanol was added, and the mixture was heated under reflux overnight under a N₂ atmosphere. Upon cooling the solution to room temperature, methanol was evaporated by rotavap to obtain a yellow oil. The residue was dissolved in 50 mL methanol and cooled to -78 °C to yield a white crystalline solid. The precipitate was filtered and washed with cold methanol to obtain the pure product. Colourless prism-shaped crystals suitable for single-crystal X-ray diffraction were grown using slow evaporation from methanol. Yield: 0.57 g (40%); m.p. 139–141 °C; ¹H NMR (δ_{H} , CDCl₃, 400 MHz): 16.68 (1H, s), 7.47 (2H, d), 7.14 (2H, d), 1.89 (6H, s); ¹³C NMR (δ_{c} , CDCl₃, 400 MHz) 190.72, 137.37, 132.40, 131.19, 121.44, 114.59, 68.93, 68.70, 24.13.

2.2.2.6 Synthesis of 3-(4-(bromoethynyl)phenyl)-4-hydroxypent-3-en-2-one, L2



3-(4-(Bromoethynyl)phenyl)-4-hydroxypent-3-en-2-one was prepared according to the preparation of 3-(4-(chloroethynyl)phenyl)-4-hydroxypent-3-en-2-one from 1.00 g (4.80 mmol) of 4-(bromoethynyl)benzaldehyde and 1.20 g (5.8 mmol) of **1**. Brown color prism-shaped crystals suitable for single-crystal X-ray diffraction were grown using slow evaporation from methanol. Yield: 0.72 g (56%); m.p. 155-158 °C; ¹H NMR (δ_{H} , CDCl₃, 400 MHz): ¹H NMR (δ_{H} , CDCl₃, 400 MHz): 16.67 (1H, s), 7.48 (2H, d), 7.14 (2H, d), 1.89 (6H, s); ¹³C NMR (δ_{c} , CDCl₃, 400 MHz): 190.70, 137.46, 132.43, 131.16, 121.98, 114.59, 79.58, 50.50, 24.13.

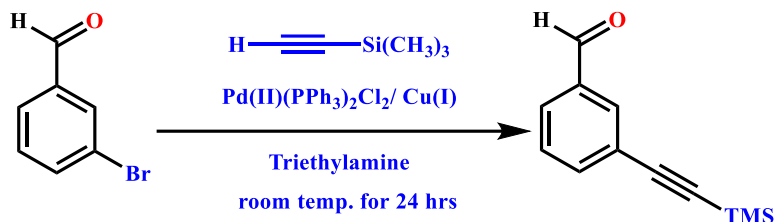
2.2.2.7 Synthesis of 3-(4-(iodoethynyl)phenyl)-4-hydroxypent-3-en-2-one, L3



3-(4-(Iodoethynyl)phenyl)-4-hydroxypent-3-en-2-one was prepared according to the preparation of 3-(4-(chloroethynyl)phenyl)-4-hydroxypent-3-en-2-one from 1.00 g (3.90 mmol) of 4-(chlorooethynyl)benzaldehyde and 0.98 g (4.70 mmol) of **1**. Yellow color plate-shaped crystals suitable for single-crystal X-ray diffraction were grown using slow evaporation from methanol.

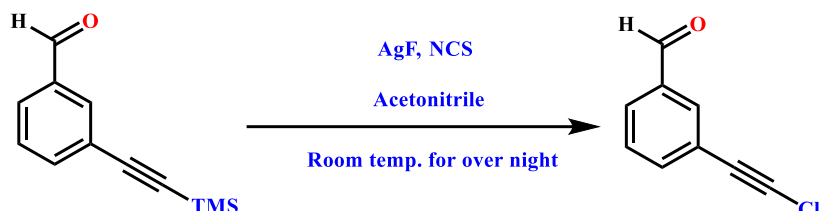
Yield: 0.65 g (51%); m.p. 164-167 °C ^1H NMR (δ_{H} , CDCl_3 , 400 MHz): 16.67 (1H, s), 7.47 (2H, d), 7.14 (2H, d), 1.88 (6H, s); ^{13}C NMR (δ_{c} , CDCl_3 , 400 MHz) 190.72, 137.58, 132.76, 131.05, 122.66, 114.59, 93.64, 24.13.

2.2.2.8 Synthesis of 3-(trimethylsilyl)ethynylbenzaldehyde



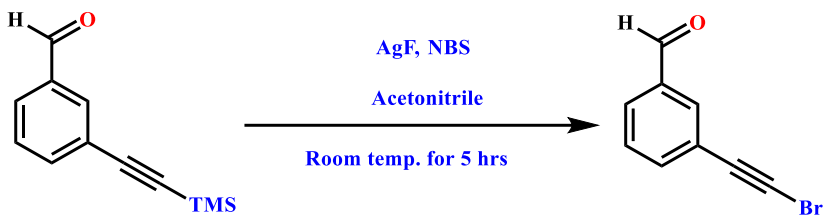
3-(Trimethylsilyl)ethynylbenzaldehyde was prepared according to the preparation of 4-(trimethylsilyl)ethynylbenzaldehyde from 5.00 g (27.02 mmol) 3-bromobenzaldehyde, 123 mg (0.65 mmol) of CuI, and 227 mg (0.32 mmol) of $\text{Pd}(\text{PPh}_3)_2\text{Cl}_2$ and 3.18 g (32.40 mmol) of trimethylsilylacetylene in 80 mL of trimethylamine. An oil was obtained as the product. Yield: 5.02 g (92%); b.p. 145-148 °C (Lit, 144-146 °C)⁴¹; ^1H NMR (δ_{H} , CDCl_3 , 400 MHz): 9.99 (1H, s), 7.97 (1H, s), 7.82 (1H, d), 7.70 (1H, d), 7.48 (1H, t), 0.27 (9H, s).

2.2.2.9 Synthesis of 3-(chloroethynyl)benzaldehyde



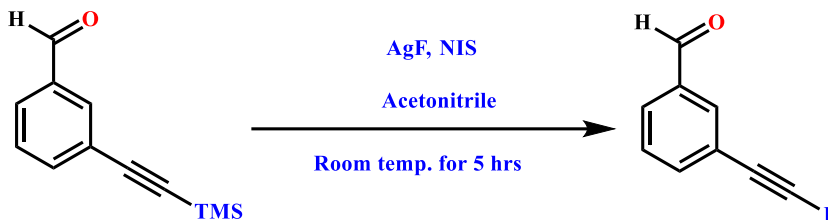
3-(Chloroethynyl)benzaldehyde was prepared according to the preparation of 4-(chloroethynyl)benzaldehyde from 3.00 g (14.80 mmol) of 4-(trimethylsilyl)ethynylbenzaldehyde and 3.80 g (30.00 mmol) of AgF and 1.98 g (14.80 mmol) of N-chlorosuccinimide in 60 ml of acetonitrile. Yield: 1.54 g (64%); m.p. 72-76 °C; ^1H NMR (δ_{H} , CDCl_3 , 400 MHz): 9.99 (1H, s), 7.94 (1H, s), 7.84 (1H, d), 7.68 (1H, d), 7.50 (1H, t).

2.2.2.10 Synthesis of 3-(bromoethynyl)benzaldehyde



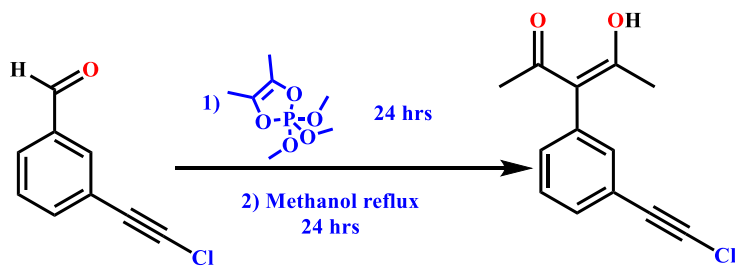
3-(Bromoethynyl)benzaldehyde was prepared according to the preparation of 4-(bromoethynyl)benzaldehyde from 2.00 g (9.9 mmol) of 4-(trimethylsilyl)ethynylbenzaldehyde and 1.26 g (9.9 mmol) of AgF and 1.76 g (9.9 mmol) of N-bromosuccinimide in 50 ml of acetonitrile. Yield: 1.86 g (90%); m.p. 73-76 °C; ^1H NMR (δ_{H} , CDCl_3 , 400 MHz): 10.00 (1H, s), 7.96 (1H, s), 7.85 (1H, d), 7.69 (1H, d), 7.50 (1H, t).

2.2.2.11 Synthesis of 4-(iodoethynyl)benzaldehyde



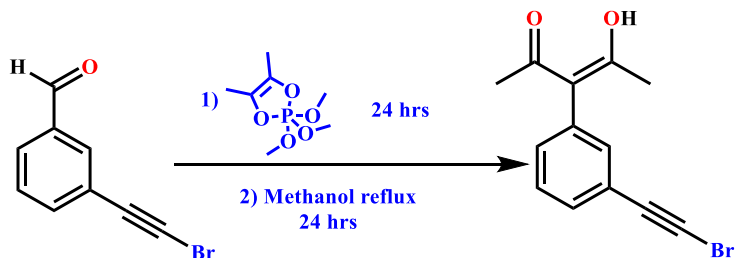
3-(Iodoethynyl)benzaldehyde was prepared according to the preparation of 4-(iodoethynyl)benzaldehyde from 2.00 g (9.9 mmol) of 4-(trimethylsilyl)ethynylbenzaldehyde and 1.26 g (9.9 mmol) of AgF and 2.23 g (9.9 mmol) of N-iodosuccinimide in 50 ml of acetonitrile. Yield: 2.20 g (82%); m.p. 107-111 °C; ^1H NMR (δ_{H} , CDCl_3 , 400 MHz): 9.99 (1H, s), 7.94 (1H, s), 7.84 (1H, d), 7.67 (1H, d), 7.50 (1H, t).

2.2.2.12 Synthesis of 3-(3-(chloroethynyl)phenyl)-4-hydroxypent-3-en-2-one, L4



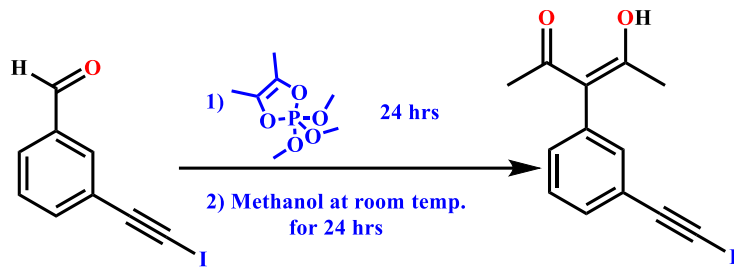
3-(Chloroethynyl)benzaldehyde (1.00 g, 6.0 mmol) was placed in a 100 mL round bottom flask under a N₂ atmosphere. **1** (1.53 g, 7.3 mmol) was added to the flask with continuous stirring. The resulting slurry was stirred for 24 hours at room temperature under a N₂ atmosphere to obtain an oil. Then, 50 ml of methanol was added and the mixture was heated under reflux overnight under a N₂ atmosphere. Upon cooling the solution to room temperature, methanol was evaporated by rotavap to obtain a yellow oil. The residue was chromatographed on a silica column with hexanes as the eluent to obtain the pure product. Yield: 0.55 g (40%); m.p. 48-52 °C, Dec. 129 °C (DSC 5 °C/min); ¹H NMR (δ_{H} , CDCl₃, 400 MHz): 16.66 (1H, s), 7.42 (1H, d), 7.34 (1H, t) 7.28 (1H, s), 7.16 (1H, d), 1.88 (6H, s); ¹³C NMR (δ_{c} , CDCl₃, 400 MHz) 190.87, 137.17, 134.46, 131.43, 131.07, 128.96, 122.76, 114.31, 68.74, 24.12.

2.2.2.13 Synthesis of 3-(3-(bromoethynyl)phenyl)-4-hydroxypent-3-en-2-one, L5



3-(4-(Bromoethynyl)phenyl)-4-hydroxypent-3-en-2-one was prepared according to the preparation of 3-(4-(chloroethynyl)phenyl)-4-hydroxypent-3-en-2-one from 1.00 g (4.80 mmol) of 4-(bromoethynyl)benzaldehyde and 1.20 g (5.80 mmol) of **1**. Gold color plate crystals suitable for single-crystal X-ray diffraction were grown using slow evaporation from methanol. Yield: 0.52 g (39%); m.p. 71-73 °C, Dec. 97 °C (DSC 5 °C/min); ¹H NMR (δ_{H} , CDCl₃, 400 MHz): 16.69 (1H, s), 7.43 (1H, d), 7.35 (1H, t) 7.29 (1H, s), 7.17 (1H, d), 1.88 (6H, s); ¹³C NMR (δ_{c} , CDCl₃, 400 MHz) 190.85, 137.46, 134.53, 131.55, 131.11, 128.96, 123.33, 114.32, 79.54, 50.63, 24.15.

2.2.2.14 Synthesis of 3-(3-(iodoethyl)phenyl)-4-hydroxypent-3-en-2-one, L6



4-(Iodoethyl)benzaldehyde (1.00 g, 3.90 mmol) was placed in a 100 mL round bottom flask under a N_2 atmosphere. **1** (0.98 g, 4.70 mmol) was added to the flask with continuous stirring. The resulting slurry was stirred for 24 h at room temperature under a N_2 atmosphere to obtain an oil. Then, 50 ml of methanol was added and the mixture was stirred at room temperature overnight under a N_2 atmosphere. After completion of the reaction, methanol was evaporated under room temperature to obtain a yellow oil. The residue was chromatographed on a silica column with hexanes as the eluent to obtain the pure product as yellow sticky solid. Yield: 0.66 g (52%); Dec. 196 °C (DSC 5 °C/min); ^1H NMR (δ_{H} , CDCl_3 , 400 MHz): 16.68 (1H, s), 7.42 (1H, d), 7.35 (1H, t) 7.28 (1H, s), 7.16 (1H, d), 1.88 (6H, s); ^{13}C NMR (δ_{c} , CDCl_3 , 400 MHz) 190.86, 137.10, 134.86, 131.66, 131.44, 128.86, 124.00, 114.33, 93.59, 24.16, 7.32.

2.2.3 Metal-ligand complexes synthesis

2.2.3.1 Synthesis of $[\text{Cu}(\text{L1})_2]$

L1 (0.010g, 0.04 mmol) was dissolved in 1.0 mL of acetonitrile and a drop of triethylamine was added to the solution in a vial and stirred. Copper(II) tetrafluoroborate hydrate (0.006 g, 0.0025 mmol) in 1.0 mL of acetonitrile was added. The solution was mixed and kept for slow evaporation at room temperature. After two days, green needle-shaped crystals were obtained and subjected to single-crystal X-ray diffraction. Dec. 309 °C (DSC 5 °C /min).

2.2.3.2 Synthesis of [Cu(L2)2].2CH₃CN

L2 (0.010g, 0.0036 mmol) was dissolved in 1.0 mL of acetonitrile and a drop of triethylamine was added in a vial and stirred well. Copper(II) tetrafluoroborate hydrate (0.005 g, 0.002 mmol) in 1.0 mL of acetonitrile was added to the above mixture. The resulting mixture was mixed well and kept for slow evaporation at room temperature. After one day, green plate-shaped crystals were obtained and subjected to single-crystal X-ray diffraction. Dec. 276 °C (DSC 5 °C /min).

2.2.3.3 Synthesis of [Cu(L2)2].2C₄H₈O₂

L2 (0.010g, 0.0036 mmol) was dissolved in 1.0 mL of ethyl acetate and a drop of triethylamine was added in a vial and stirred well. Copper(II) tetrafluoroborate hydrate (0.005 g, 0.002 mmol) in 1.0 mL of ethyl acetate was added to the mixture. The resulting solution was mixed and kept for slow evaporation at room temperature. After one day, blue prism-shaped crystals were obtained and subjected to single-crystal X-ray diffraction. Dec. 263 °C (DSC 5 °C /min).

2.2.3.4 Synthesis of [Cu(L2)2].2CH₃NO₂

L2 (0.010g, 0.0036 mmol) was dissolved in 1.0 mL of nitro methane and a drop of triethylamine was added in a vial and stirred. Copper(II) tetrafluoroborate hydrate (0.005 g, 0.002 mmol) in 1.0 mL of nitro methane was added to the mixture. The resulting solution was mixed and kept for slow evaporation at room temperature. After two days, green plate-shaped crystals were obtained and subjected to the single-crystal X-ray diffraction. Dec. 274 °C (DSC 5 °C /min).

2.2.3.5 Synthesis of [Cu(L3)2].4CH₃CN

L3 (0.010g, 0.003 mmol) was dissolved in 1.0 mL of acetonitrile and a drop of triethylamine was added in a vial and stirred. Copper(II) tetrafluoroborate hydrate (0.004 g, 0.0017 mmol) in 1.0 mL of acetonitrile was added to the mixture. The resulting solution was mixed and kept for slow

evaporation at room temperature. After one day, blue plate-shaped crystals were obtained and subjected to single-crystal X-ray diffraction. Dec. 182 °C (DSC 5 °C /min).

2.2.3.6 Synthesis of [Cu(L3)₂].2C₄H₈O₂

L3 (0.010g, 0.003 mmol) was dissolved in 1.0 mL of ethyl acetate and a drop of triethylamine was added to a vial and stirred. Copper(II) tetrafluoroborate hydrate (0.004 g, 0.0017 mmol) in 1.0 mL of ethyl acetate was added to the mixture. The resulting solution was mixed and kept for slow evaporation at room temperature. After one day, green needle-shaped crystals were obtained and subjected to single-crystal X-ray diffraction. Dec. 205 °C (DSC 5 °C /min).

2.2.3.7 Synthesis of [Cu(L3)₂]

L3 (0.010g, 0.003 mmol) was dissolved in 1.0 mL of nitro methane and a drop of triethylamine was added in a vial and stirred. Copper(II) tetrafluoroborate hydrate (0.004 g, 0.0017 mmol) in 1.0 mL of nitro methane was added to the mixture. The resulting solution was mixed and kept for slow evaporation at room temperature. After three days green needle-shaped crystals were obtained and subjected to single-crystal X-ray diffraction. Dec. 180 °C (DSC 5 °C /min).

2.2.3.8 Synthesis of [Cu(L5)₂]

L5 (0.010g, 0.0036 mmol) was dissolved in 1.0 mL of acetonitrile and a drop of triethylamine was added in a vial and stirred. Copper(II) tetrafluoroborate hydrate (0.005 g, , 0.002 mmol) in 1.0 mL of acetonitrile was added to the mixture. The resulting solution was mixed and kept for slow evaporation at room temperature. After five days prism-shaped crystals were obtained and subjected to single-crystal X-ray diffraction. Dec. 176 °C (DSC 5 °C /min).

2.3 Results

2.3.1 Single crystals of ligands

X-ray quality single crystals are obtained for **L1-L3** and **L5**. Keto-enol tautomerism is observed in the crystal structure of **L1**. (Figure 2.7) The hydrogen on acac moiety is equally distributed on two oxygen. Adjacent **L1** molecules are close-packed and no significant halogen bonding interactions are present. The acac moiety is almost perpendicular with respect to the phenyl ring and it also accepts a C-H \cdots O hydrogen bond from an adjacent ligand, $r(\text{O}\cdots\text{H})$ ca. 2.649 Å, (Fig. 1). The X-C≡C bond is linear with a 180° angle.

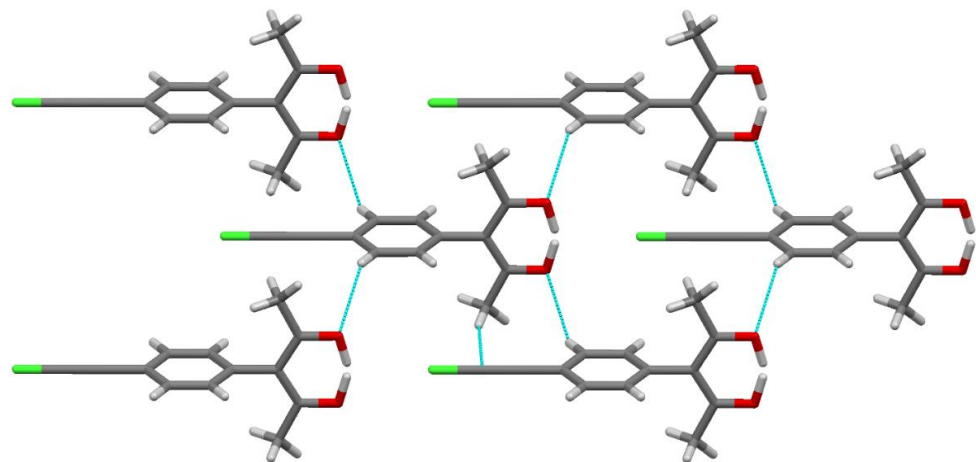


Figure 2.7 Part of the crystal structure of **L1** (color codes: red-oxygen; green-chlorine).

Both crystal structures, **L2** (Figure 2.8) and **L3** (Figure 2.9) contain intermolecular interactions between their keto oxygen atom of the acac group and respective haloethynyl moieties. These halogen bonding interactions have created 1-D chains in both structures, **L2** $r(\text{O}\cdots\text{Br})$ 2.976 Å, and **L3** $r(\text{O}\cdots\text{I})$ 3.040 Å. A slightly higher reduction in combined van der Waals radii (13% reduction) is observed in the more polarizable iodine atom involved halogen bonding compared to corresponding bromo species (11.6% reduction). In addition to halogen bonding, there are C-H \cdots O hydrogen bonds between acac-O and phenyl-H. In both structures, oxygen makes bifurcated

hydrogen bonding with phenyl-H and in **L3** symmetric hydrogen bonds are observed with $r(\text{O}\cdots\text{H})$ ca. 2.81 Å. Bifurcated hydrogen bonding distances in **L2** are $r(\text{O}\cdots\text{H})$ ca. 2.70 Å and 2.79 Å.

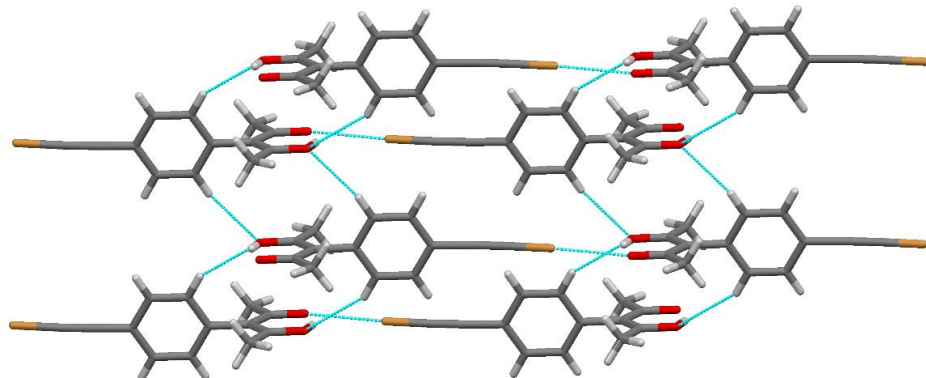


Figure 2.8 Part of the crystal structure of **L2** (color codes: red-oxygen; gold-bromine).

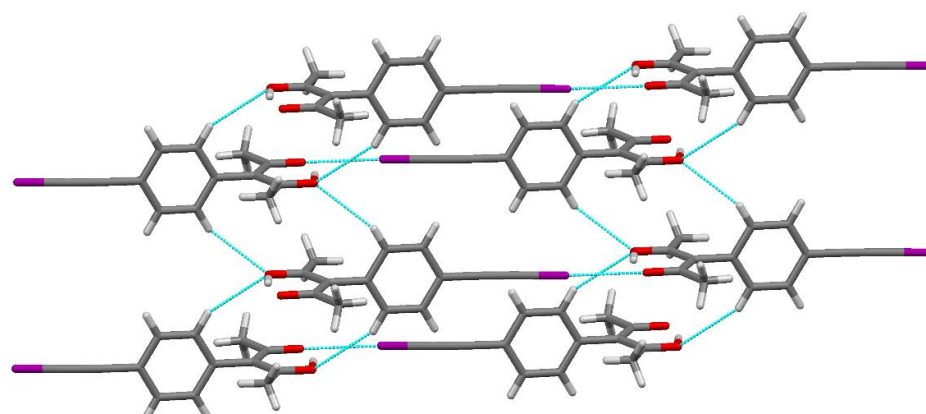


Figure 2.9 Part of the crystal structure of **L3** (color codes: red-oxygen; purple-iodine).

The C-X \cdots O halogen-bond angle is less linear in both **L1** and **L2** compared to **L3**. Higher linearity is observed when the halogen is iodine (178.0°) than when bromine (170.8°). The torsion angle of the acac moiety with respect to the phenyl ring is close to 90° for both **L2** and **L3**. The X-C≡C bond angles in **L2** and **L3** deviate slightly from linear at 174.14° and 172.44°, respectively.

When it comes to the **L5** (an isomer of **L2**), a similar type of 1-D chain is formed by intermolecular interactions between its keto oxygen atom of the acac group and bromoethynyl group (Figure 2.10). Halogen bonding distance in the structure of **L5** $r(\text{O}\cdots\text{Br})$ 3.082 Å, has 8.6%

vdW reduction. This reduction is slightly less than in the case of **L2**. The C-Br \cdots O halogen-bond angle is 149.5° in **L5**, which is less linear compared to the angle in **L2**.

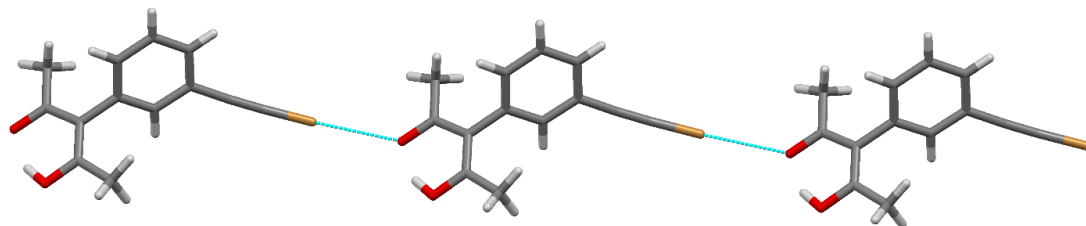


Figure 2.10 Halogen bonded 1-D chain in **L5** (color codes: red-oxygen; gold-bromine).

In addition to the halogen-bond interaction in the 1-D chain, several other interactions are also observed in **L5** (Figure 2.11). There is a short contact between ethynyl bromine and triple bond $r(\text{Br}\cdots\text{triple bond})$ 4.08 Å, θ (C-Br \cdots triple bond) 167.33°. There are several C-H \cdots O hydrogen bonds between acac-O and phenyl-H. Bifurcated interactions originated from keto oxygen of acac moiety to phenyl-H $r(\text{O}\cdots\text{H})$ ca. 2.49 Å, 2.65 Å are the prominent non-covalent interactions. These prominent short contacts connect halogen bonded 1-D chains (Figure 2.11).

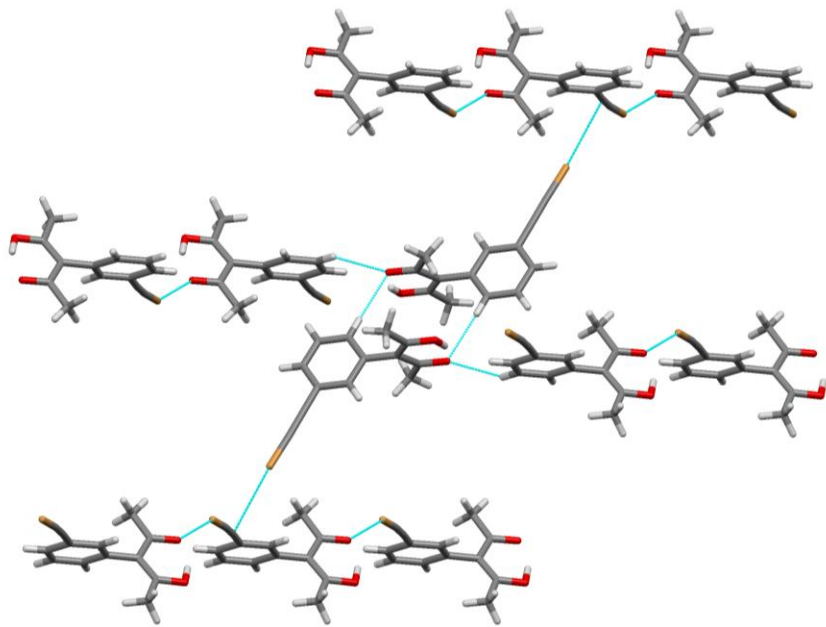


Figure 2.11 Part of the crystal structure of **L5** showing short interactions (color codes: red-oxygen; gold-bromine).

2.3.2 FTIR spectroscopy of metal-ligand complexes

FTIR spectroscopy analysis of crystal formed provides an initial clue about the formation of metal ligand complexes (Figure 2.12 and Figure 2.13). A red shift of the peak corresponding to the triple bond is observed with the formation of metal-ligand complexes compared to the free ligand. Well resolved peaks are also observed in the region from $1,600\text{ cm}^{-1}$ to $1,300\text{ cm}^{-1}$ after the formation of a metal ligand complexes. Presence of solvent in the crystal lattice can also be identified by IR spectroscopy. For example, peaks correspond to acetonitrile (2319 cm^{-1} and 2362 cm^{-1}) can be seen in the metal-ligand complex between Cu(II) and **L2** obtained in acetonitrile solvent (Figure 2.12). In some cases, the solvent peaks are not observed in IR spectra which suggest the absence of the solvent in the crystal structure. For example, no indication of the presence of a solvent in the crystal of metal-ligand complex between Cu(II) and **L5** obtained in acetonitrile solvent (Figure 2.13).

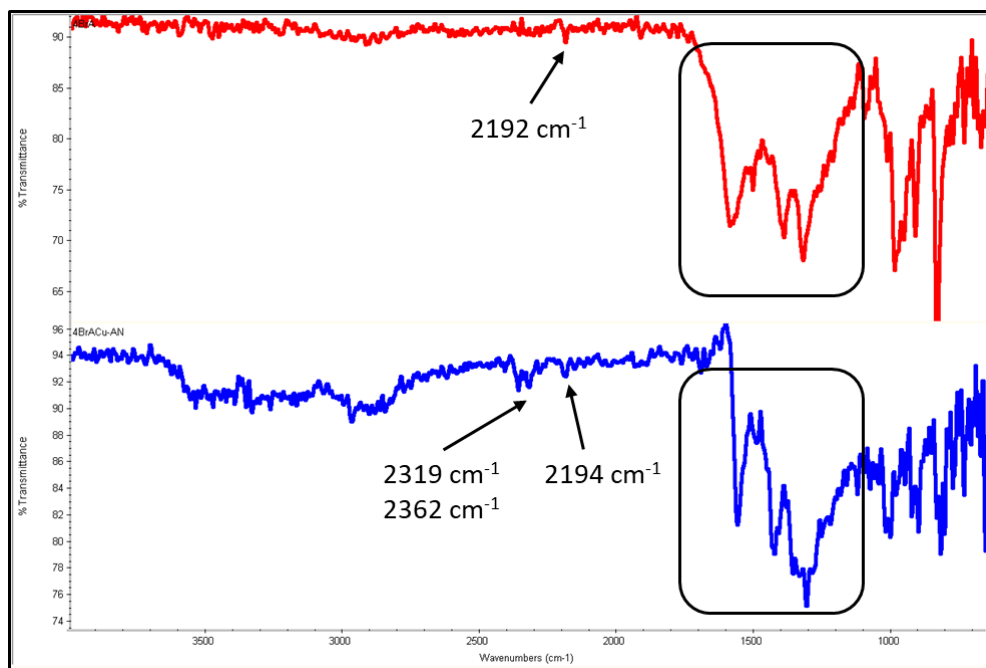


Figure 2.12 FTIR spectra of **L2** (red) and the metal-ligand complex between **L2** and Cu(II) in CH₃CN (blue).

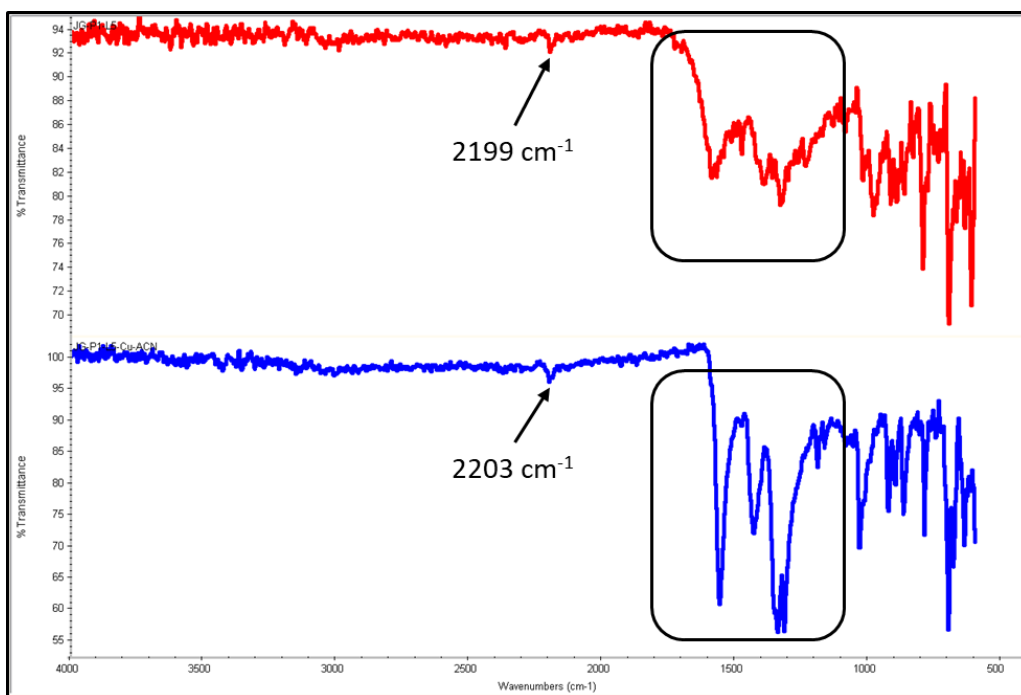


Figure 2.13 FTIR spectra of **L5** (red) and the metal-ligand complex between **L5** and Cu(II) in CH₃CN (blue).

2.3.3 Single crystals of metal-ligand complexes

As expected, neutral metal complex was obtained with a 1:2 metal to ligand stoichiometry from **L1** and Cu(II) salt with a square planar geometry around the metal ion (Figure 2.14). There are no significant halogen bonds from the ethynyl moiety.



Figure 2.14 The geometry of the metal-ligand complex ion in the crystal structure of $[\text{Cu}(\text{L1})_2]$ (color codes: red-oxygen; green-chlorine; orange-copper).

Several C-H \cdots O hydrogen bonds are present between the hydrogens of the phenyl group and the acac moiety (Figure 2.15) $r(\text{O}\cdots\text{H})$ ca 2.70 Å and 2.94 Å and these interactions create an infinite stack of metal-ligand complex.

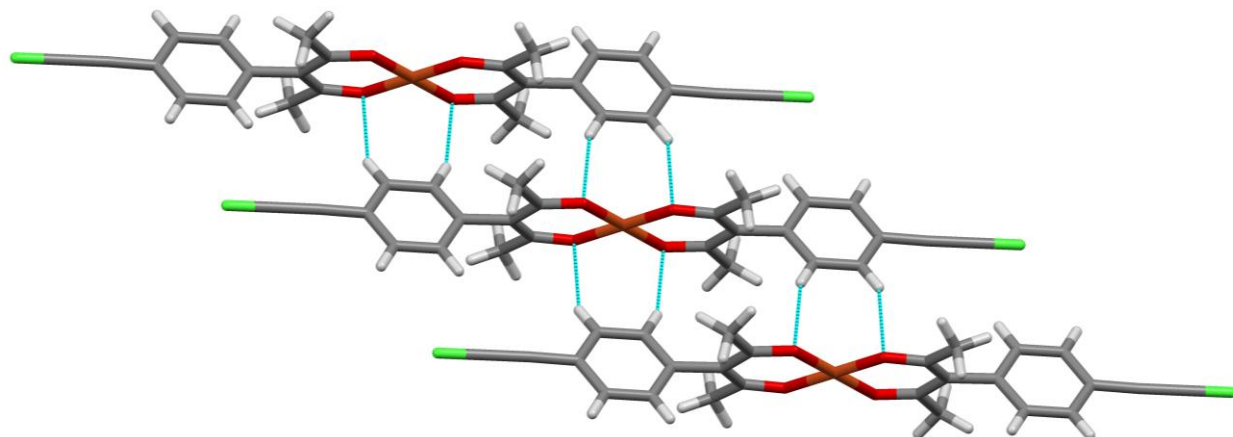


Figure 2.15 The relative orientation of metal-ligand complex within an infinite stack in the structure of $[\text{Cu}(\text{L1})_2]$ (color codes: red-oxygen; green-chlorine; orange-copper).

The reaction between **L2** and Cu(II) in acetonitrile gives a complex, $[\text{Cu}(\text{L2})_2] \cdot 2\text{CH}_3\text{CN}$ and a square planar geometry. In this structure, acetonitrile forms halogen bonding with the

‘activated’ bromine; $r(\text{Br}\cdots\text{N})$ 3.070 Å (a 9.7% vdW reduction), θ ($\text{C}-\text{Br}\cdots\text{N}$) 172.05°, θ ($\text{Br}\cdots\text{N}\equiv\text{C}$) 144.48° (Figure 2.16).



Figure 2.16 Part of the crystal structure of $[\text{Cu}(\text{L2})_2] \cdot 2\text{CH}_3\text{CN}$ showing the geometry around the metal ion and the ligand-solvent halogen bond (color codes: red-oxygen; blue-nitrogen; gold-bromine; orange-copper).

There are several $\text{C}-\text{H}\cdots\text{O}$ hydrogen bonds between the hydrogens of the phenyl ring and the acac group (Figure 2.17) $r(\text{O}\cdots\text{H})$ ca. 2.57 Å and 2.73 Å and these interactions create an infinite stack of metal-ligand complexes.

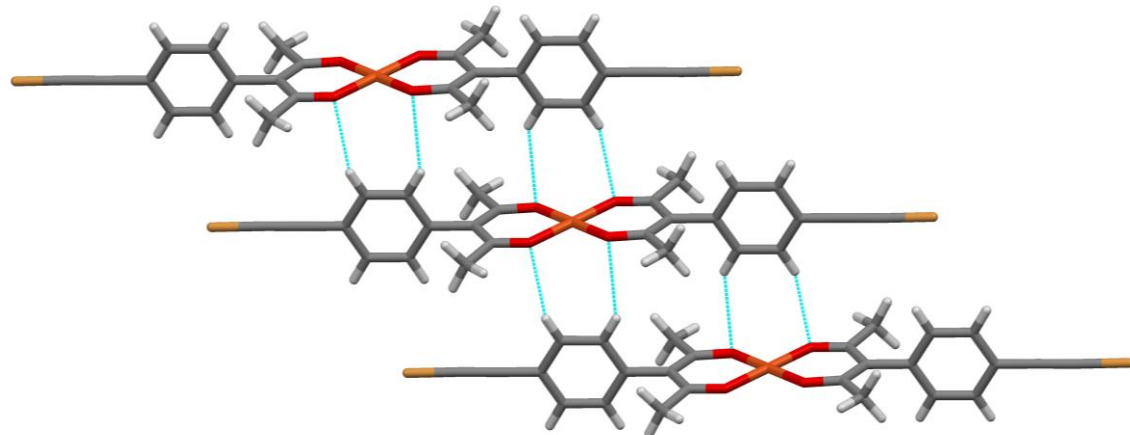


Figure 2.17 Crystal packing of $[\text{Cu}(\text{L2})_2] \cdot 2\text{CH}_3\text{CN}$ (solvent molecules are omitted, color codes: red-oxygen; gold-bromine; orange-copper).

When the reaction between **L2** and Cu(II) salt was performed in ethyl acetate, a 1:2 metal-ligand solvate is observed. The geometry around the metal ion is square planar and the activated bromine forms halogen bonds with oxygen of ethyl acetate; ; $r(\text{Br}\cdots\text{O})$ 2.88 Å (a 14.5% vdW reduction), θ ($\text{C}-\text{Br}\cdots\text{O}$) 171.07°, θ ($\text{Br}\cdots\text{O}=\text{C}$) 126.47° (Figure 2.18) .

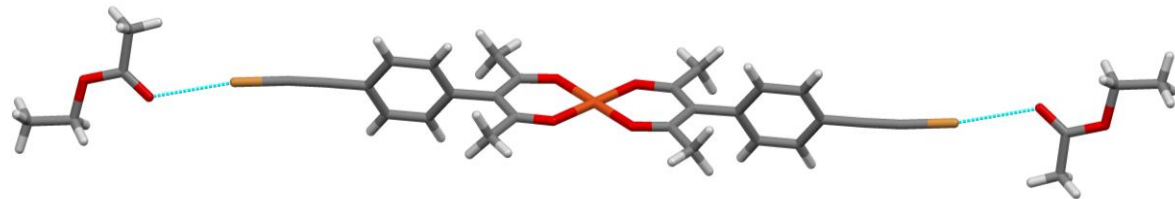


Figure 2.18 Part of the crystal structure of $[\text{Cu}(\text{L2})_2] \cdot 2\text{C}_4\text{H}_8\text{O}_2$ showing the geometry around the metal ion and the ligand-solvent halogen bond (color codes: red-oxygen; gold-bromine; orange-copper).

Infinite stacks of complex ions are created by the $\text{C}-\text{H}\cdots\text{O}$ hydrogen bonds between adjacent complex ions $r(\text{O}\cdots\text{H})$ ca. 2.61 \AA and 2.63 \AA (Figure 2.19).

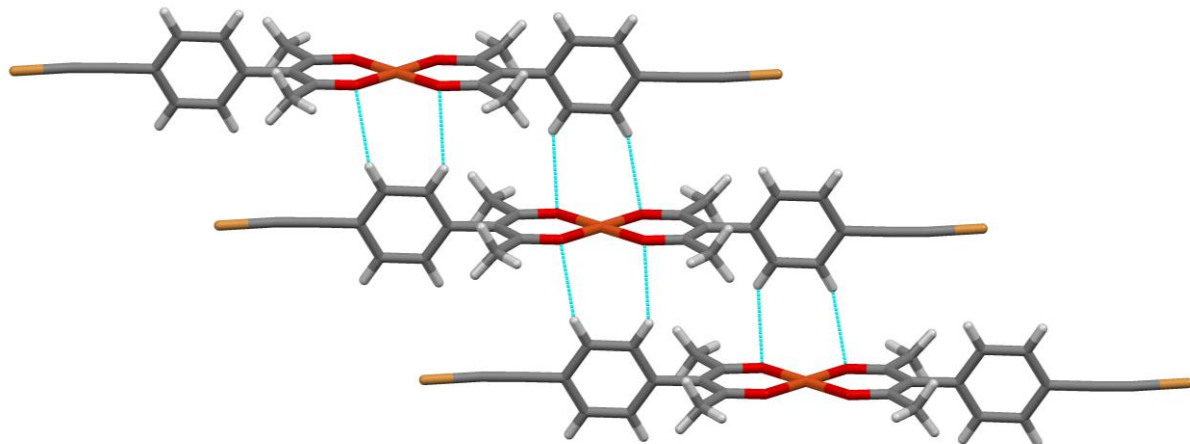


Figure 2.19 Crystal packing of $[\text{Cu}(\text{L2})_2] \cdot 2\text{C}_4\text{H}_8\text{O}_2$ (solvent molecules are omitted, color codes: red-oxygen; gold-bromine; orange-copper).

Nitromethane acts as a non-directional space filler in the crystal structure when the reaction between **L2** and Cu(II) is performed in nitromethane (Figure 2.20). Although halogen bonded iodo-nitromethane synthons are reported⁴²⁻⁴³, when it comes to relatively weak halogen donor such as bromine, interactions with nitromethane become weak as well.

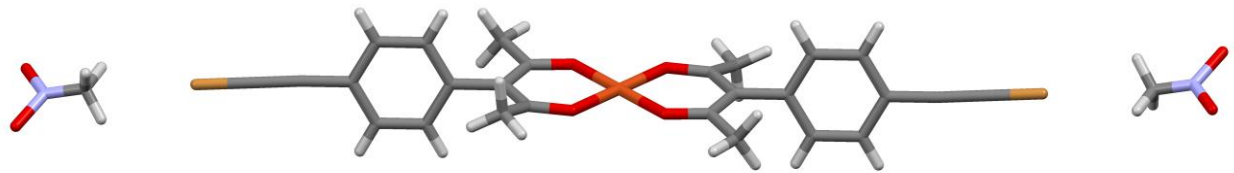


Figure 2.20 Part of the crystal structure of $[\text{Cu}(\text{L2})_2] \cdot 2\text{CH}_3\text{NO}_2$ showing the geometry around the metal ion and the packing of ligand and solvent (color codes: red-oxygen; blue-nitrogen; gold-bromine; orange-copper).

In the crystal packing, $\text{C}-\text{H}\cdots\text{O}$ hydrogen bonding between hydrogen atoms of the phenyl group and oxygen of acac moiety is observed as in the case of $[\text{Cu}(\text{L2})_2] \cdot 2\text{CH}_3\text{CN}$ and $[\text{Cu}(\text{L2})_2] \cdot 2\text{C}_4\text{H}_8\text{O}_2$ (Figure 2.21). This again forms a stack of complex ions $r(\text{O}\cdots\text{H})$ ca. 2.50 \AA and 2.57 \AA .

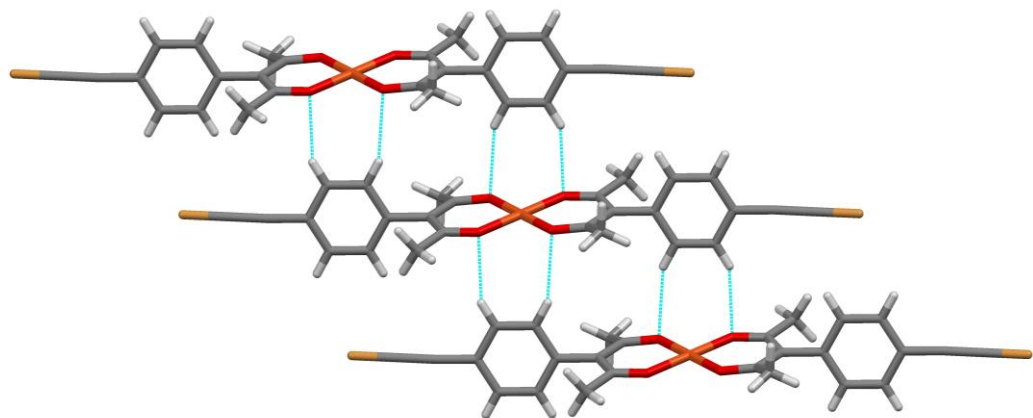


Figure 2.21 Crystal packing of $[\text{Cu}(\text{L2})_2] \cdot 2\text{CH}_3\text{NO}_2$ (solvent molecules are omitted, color codes: red-oxygen; gold-bromine; orange-copper).

The combination of **L3** and Cu(II) in acetonitrile produces a 1:2 metal-ligand complex with two solvent molecules included in the structure plus two solvent molecules that interact with iodine. Two acetonitrile molecules axially coordinated to the Cu(II) ion, change the overall geometry around metal center to octahedral. The activated iodine atom forms a halogen bond with the nitrogen of acetonitrile (Figure 2.22); $r(\text{I}\cdots\text{N})$ 2.98 \AA (a 15.6% vdW reduction), θ ($\text{C}-\text{I}\cdots\text{N}$) 174.28° , θ ($\text{I}\cdots\text{N}\equiv\text{C}$) 141.61° .

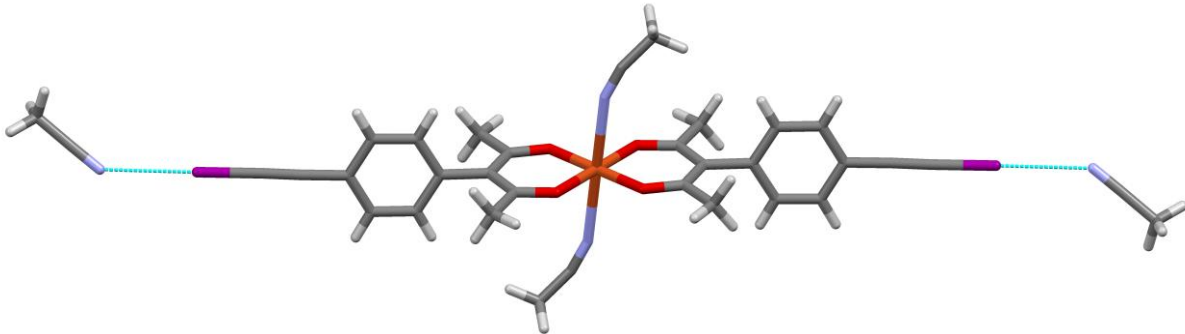


Figure 2.22 Part of the crystal structure of $[\text{Cu}(\text{L3})_2] \cdot 4\text{CH}_3\text{CN}$ showing the geometry around the metal ion and the ligand-solvent halogen bond (color codes: red-oxygen; blue-nitrogen; purple-iodine; orange-copper).

When the same reaction between **L3** and Cu(II) is performed in ethyl acetate solvent, a 1:2 metal-ligand complex is observed and this time there is no axial coordination of solvent molecules (Figure 2.23). The solvent molecules interact only with iodine atoms by making halogen bonds between the iodoethyl group and the O=C group of ethyl acetate, $r(\text{I}\cdots\text{O})$ 2.91 Å (a 20.0% vdW reduction), $\theta(\text{C-I}\cdots\text{O})$ 172.33°, $\theta(\text{I}\cdots\text{O=C})$ 128.19°.

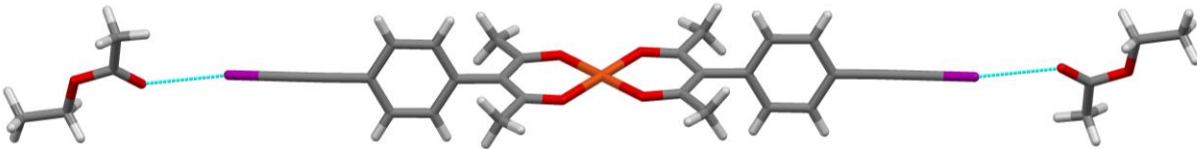


Figure 2.23 Part of the crystal structure of $[\text{Cu}(\text{L3})_2] \cdot 2\text{C}_4\text{H}_8\text{O}_2$ showing the geometry around the metal ion and the ligand-solvent halogen bond (color codes: red-oxygen; purple-iodine; orange-copper).

Since there is no axial coordination of solvent to the metal center, C-H...O hydrogen bonding between phenyl rings and acac moieties can be observed resulting in stacks of metal complexes. (Figure 2.24) ca. $r(\text{O}\cdots\text{H})$ 2.63 Å and 2.76 Å.

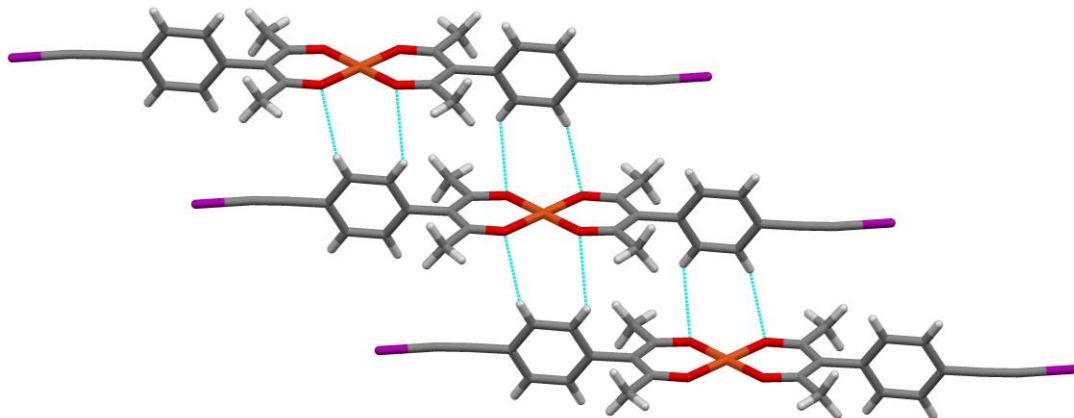


Figure 2.24 A stack of complex ions in the structure of $[\text{Cu}(\text{L3})_2] \cdot 2\text{C}_4\text{H}_8\text{O}_2$ (solvent molecules are omitted, color codes: red-oxygen; purple-iodine; orange-copper).

When the solvent is changed to nitromethane, which is a poor halogen-bond acceptor, it is not incorporated in the crystal structure of **L3** and Cu(II). In the absence of the solvent, the relatively strong halogen bond donor, iodoethynyl group finds alternative acceptor sites to interact with. The first interaction is a bifurcated bond between iodine and two oxygen atoms of the acac moiety (Figure 2.25) $r(\text{I}\cdots\text{O})$ 3.31 Å and 3.29 Å, $\theta (\text{C}-\text{I}\cdots\text{O})$ 153.02°, and 157.72°, $\theta (\text{I}\cdots\text{O}=\text{C})$ 128.19°.

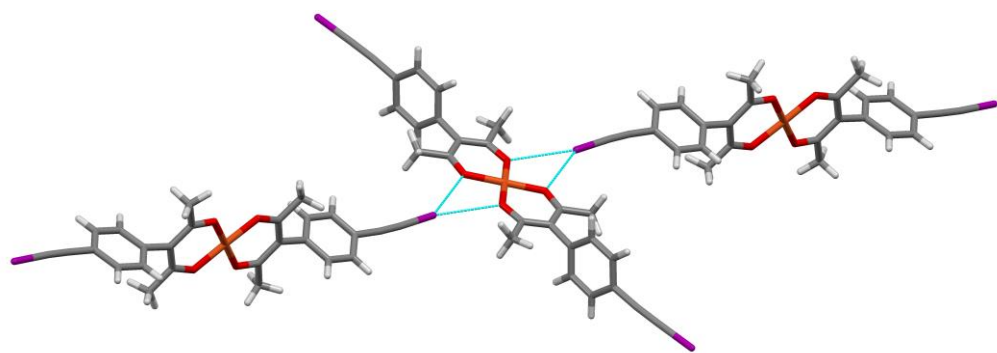


Figure 2.25 Bifurcated halogen...oxygen halogen-bond interactions in $[\text{Cu}(\text{L3})_2]$ (color codes: red-oxygen; purple-iodine; orange-copper).

The second interaction is the C-I...π bond (Figure 2.26) $r(\text{I}\cdots\text{triple bond})$ 3.63 Å, $\theta (\text{C}-\text{I}\cdots\text{triple bond})$ 153.84°, $\theta (\text{I}\cdots\text{triple bond}-\text{I})$ 80.58° (geometric parameters calculated with respect to the center of the $\text{C}\equiv\text{C}$ bond).

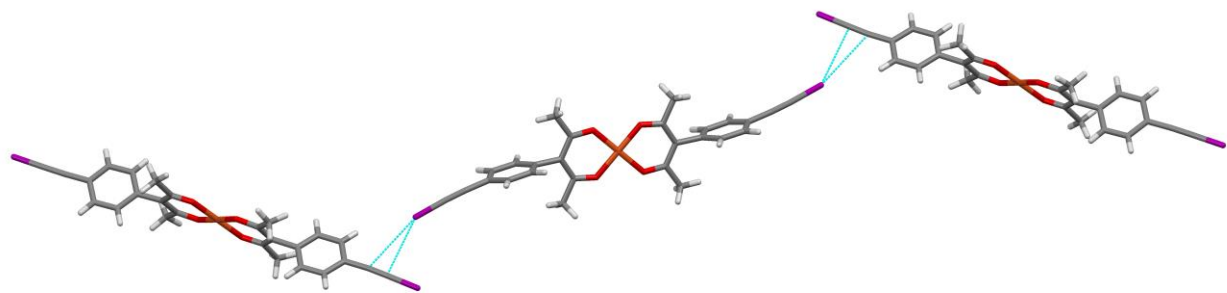


Figure 2.26 Halogen $\cdots\pi$ interactions in the structure of $[\text{Cu}(\text{L3})_2]$ (color codes: red-oxygen; purple-iodine; orange-copper).

There is another C-I $\cdots\pi$ interaction between an iodine atom and the aromatic ring in addition to the previous two halogen bonding interactions $r(\text{I}\cdots\text{centroid of phenyl ring})$ 3.58 Å, θ (C-I $\cdots\text{centroid of phenyl ring}$) 170.86°, $r(\text{I}\cdots\text{C=C})$ 3.29 Å $r(\text{I}\cdots\text{C}\equiv\text{C-I})$ 3.48 Å. These different types of halogen bonds combine to form a 3-D architecture in the structure of $[\text{Cu}(\text{L3})_2]$ (Figure 2.27).

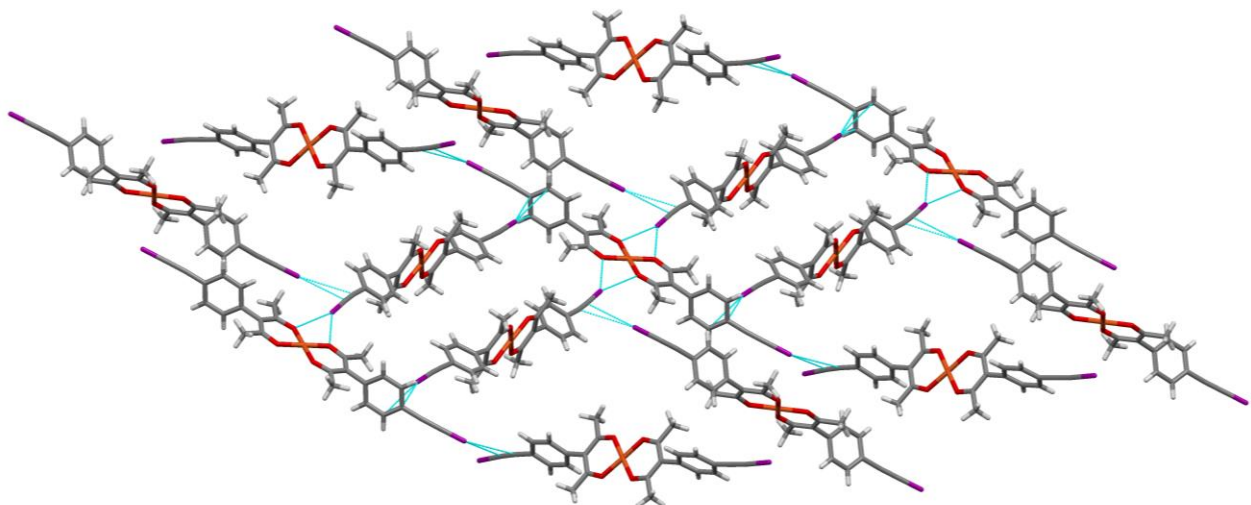


Figure 2.27 The halogen-bond driven assembly of metal-ligand complexes in the crystal structure of $[\text{Cu}(\text{L3})_2]$ (color codes: red-oxygen; purple-iodine; orange-copper).

When **L5** reacts with a metal ion in acetonitrile, an expected 1:2 metal-ligand complex is formed. Square planar geometry is observed and the bromo ethynyl groups are arranged in an anti-parallel manner (Figure 2.28).

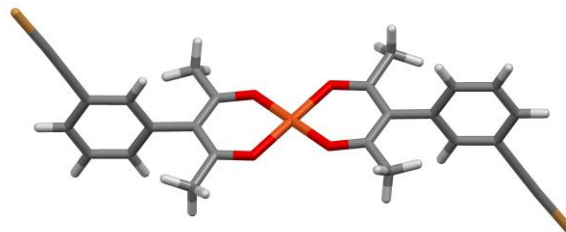


Figure 2.28 The geometry of the metal-ligand complexes in the crystal structure of $[\text{Cu}(\text{L5})_2]$ (color codes: red-oxygen; gold-bromine; orange-copper).

In the structure, there is only one halogen bonding and it is a bifurcated interaction between bromine and two oxygen atoms of the acac moiety (Figure 2.29) $r(\text{Br}\cdots\text{O})$ 3.13 Å and 3.16 Å, θ (C-I \cdots O) 158.30° and 143.70°, θ (I \cdots O=C) 122.37° and 115.11°. As a result, a completely different packing is observed compared to the complex ion formed when the ligand is **L2**, and it makes the 2-D self-assembled metal-ligand complexes.

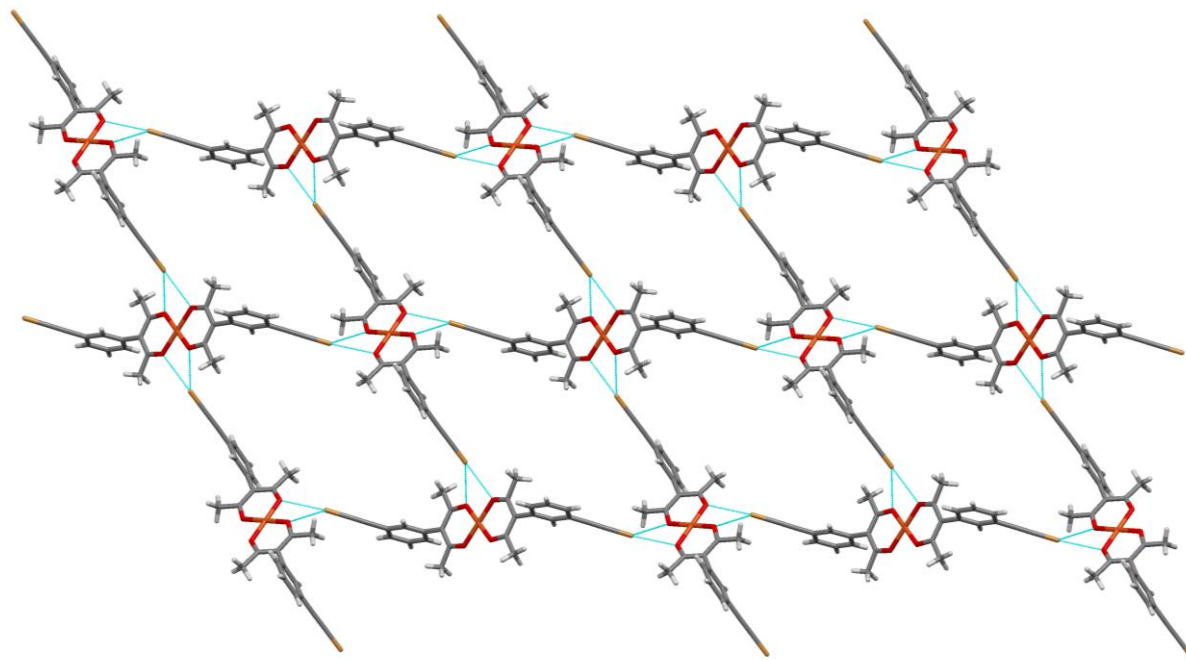


Figure 2.29 The halogen-bond driven assembly of metal-ligand complexes in the crystal structure of $[\text{Cu}(\text{L5})_2]$ (color codes: red-oxygen; gold-bromine; orange-copper).

2.3.4 Thermal gravimetric analyses (TGA) of metal-ligand complexes

TGA analysis of the metal-ligand complexes is performed to confirm the presence or absence of solvent in the crystal lattice. Figure 2.30 shows the selected TGA traces of metal-ligand complexes. The crystals were obtained in same solvent, acetonitrile.

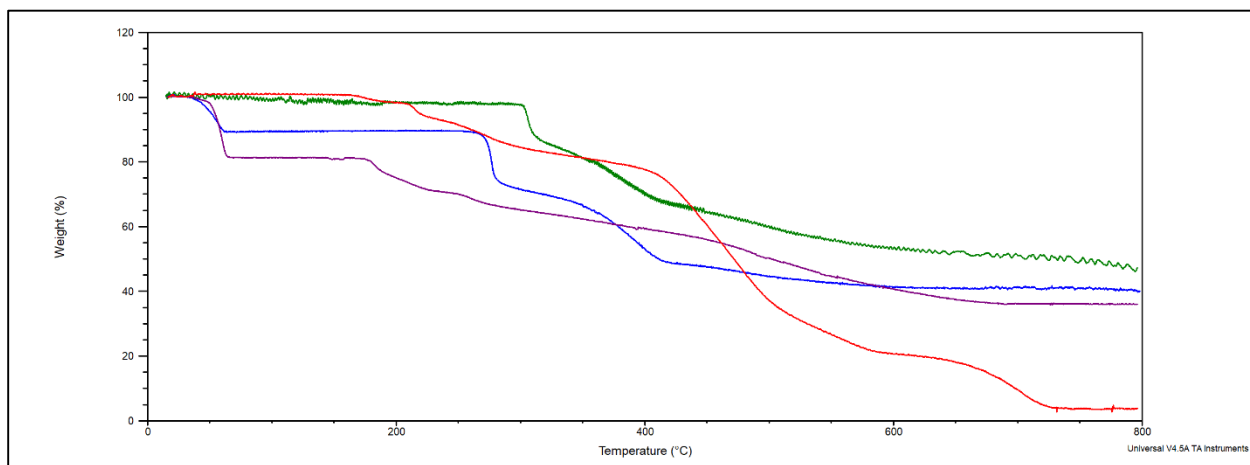


Figure 2.30 Comparison of TGA traces: $[\text{Cu}(\text{L1})_2]$ (Green), $[\text{Cu}(\text{L2})_2] \cdot 2\text{CH}_3\text{CN}$ (Blue), $[\text{Cu}(\text{L3})_2] \cdot 4\text{CH}_3\text{CN}$ (Violet) and $[\text{Cu}(\text{L5})_2]$ (Red).

Both $[\text{Cu}(\text{L2})_2] \cdot 2\text{CH}_3\text{CN}$ and $[\text{Cu}(\text{L3})_2] \cdot 4\text{CH}_3\text{CN}$ in which solvent are incorporated in the crystal show weight loss at lower temperatures in support of the findings from the XRD data.

2.4 Discussion

2.4.1 Halogen-bond donor/acceptor ability of ligands

Only bromo- and iodo substituted ligands, **L2**, **L5**, and **L3** show clear signs of halogen bonding in their crystal structures. In **L2** and **L3**, the acceptor site is the oxygen atom of the keto group, which carries a higher negative charge than the enolic oxygen atom. In the case of **L5**, different packing and several other short interactions are observed apart from familiar halogen 1-D chain due to the geometrical difference of the ligand compared to **L2**. Short contact between bromine and triple bond of **L5** gives a hint of geometrical change which enables the access of other acceptor sites in the molecule.

The chloro ligand **L1** does not show halogen bonding due to the absence of a big σ -hole with enough positive electrostatic potential even with the activation of chlorine through an adjacent ethynyl group. Out of four postulated probable halogen-bond acceptor sites, only 2 sites were exploited in the four structures of the ligands themselves (Figure 2.31). However, the only common structural feature among **L1**, **L2**, and **L3** is the intramolecular hydroxyl \cdots keto hydrogen bonding between the hydroxyl group and the oxygen of the keto group.

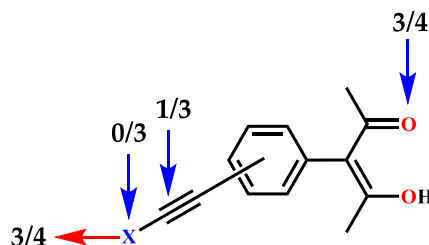


Figure 2.31 Summary of the involvement of the halogen-bond acceptors and donors in the crystal structures of **L1-L3** and **L5**.

Both **L2** and **L3** show isostructural halogen bonding with solvents, indicating that both bromine and iodine are adequately activated by the adjacent ethyl group to provide big enough positive charge on the tip of halogen to form halogen-bond interactions with structurally similar 1-D chains. Obviously, a greater reduction in the combined van der Waals radii of X \cdots O is observed in **L3** compared to that of **L2** due to the polarizability and large σ -hole in iodine. When it comes to the ligand **L3**, two best acceptor sites are utilized by halogen-bond donor due to the geometrical change of the ligand (meta isomer) compared to its para substituted isomer, **L2**.

2.4.2 Halogen-bond donor/acceptor ability of metal-ligand complexes

Unsurprisingly, metal-ligand complexes are obtained in a 1:2 stoichiometry when ligands are reacted with Cu(II) in all the cases. The relatively weak σ -hole in **L1** is continued in the metal-ligand complex $[\text{Cu}(\mathbf{L1})_2]$ and does not produce a notable halogen bonding in the complex. In the structures of metal-ligand complexes with **L2**, **L3**, and **L5**, halogen bonds become predominant

with more polarizable bromo, and iodo substituents respectively compared to chloro analog **L1**. Overall, prominent halogen-bond interactions are observed in six of the eight structures of metal-ligand complexes. In four cases, solvent molecules act as electron-pair donors for halogen-bond donors. One halogen-bond acceptor site is utilized in one case and in the other one, two different halogen-bond acceptors sites on the complex itself are utilized without the involvement of solvent (Figure 2.32).

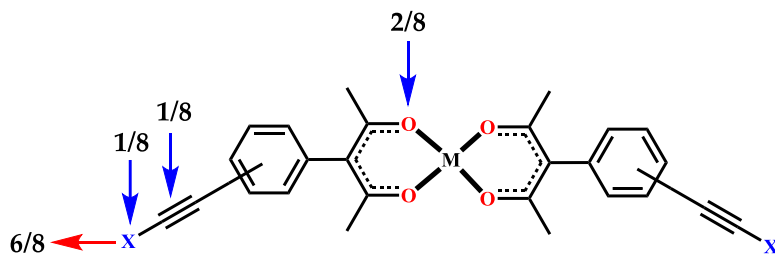


Figure 2.32 Summary of the involvement of the potential halogen-bond acceptor and donor sites on metal-ligand complexes of **L1-L3** and **L5**.

All metal complexes display square-planar geometries except $[\text{Cu}(\text{L3})_2] \cdot 4\text{CH}_3\text{CN}$ where an octahedral geometry is observed due to the axial coordination of two acetonitrile molecules. When the solvent is changed to weakly coordinating solvents such as: nitromethane, halogen bonding with solvent is not observed. When halogen atom is bromine in the para-substituted ligand (**L2**), activated bromine does not form any interactions with other acceptor sites of metal-ligand complex due to the relatively small σ -hole compared to iodine. However, activated iodine in the para-substituted ligand (**L3**) has shown the ability to form interactions with acac oxygen and the π -electron density of a triple bond which can act as a halogen bond acceptor.⁴⁴⁻⁴⁶

Bromo- analogue of meta substituted isomer (**L5**) prevents interaction of competitive acetonitrile solvent to the halogen atom. Bromine in this analogue is strong enough to find acac oxygen acceptor with the geometry change and forms 2-D self-assembled architecture. These 2-D architectures make interlocked 2-D bilayer type of sheets by combining two of halogen-boded

sheets (Figure 2.33). Furthermore, these bi-layers stack together on top of each other in the crystal packing.

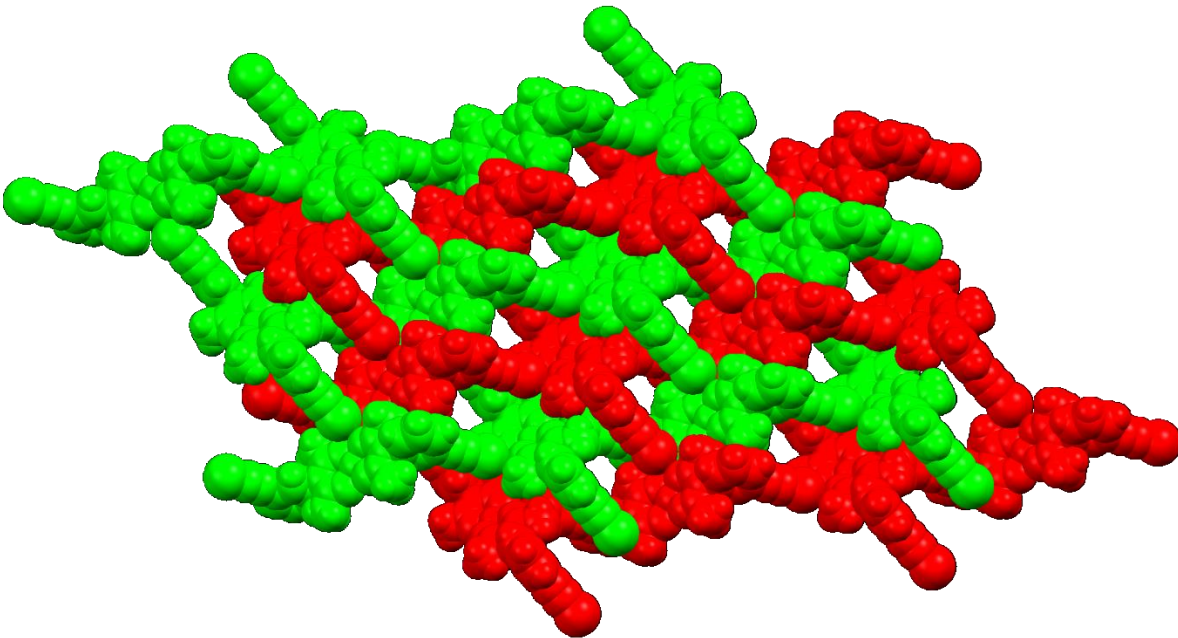


Figure 2.33 Interlocked 2-D bilayer self-assembled architecture of $[\text{Cu}(\text{L5})_2]$ (color codes: Green- and red – two different halogen-bonded 2-D assemblies).

In addition to the halogen bonding interactions, several C-H \cdots O hydrogen bonds produce a highly consistent structural feature, an infinite slipped stack, in five of the eight metal-ligand complexes. The exception are the octahedral $[\text{Cu}(\text{L3})_2] \cdot 4\text{CH}_3\text{CN}$ where steric hindrance caused by additional acetonitrile molecules that prevent the formation of C-H \cdots O hydrogen bonds and 2-D and 3-D metal-ligand self-assemblies produced by $[\text{Cu}(\text{L5})_2]$ and $[\text{Cu}(\text{L3})_2]$ respectively.

2.4.3 Density functional theory (DFT) calculations

A simple DFT calculation (B3LYP and basis set: 6-31G**) was performed for $\text{Cu}(\text{L3})_2$ system in order to account for the contribution of acac oxygen atoms in halogen bonding in the cases of $\text{Cu}(\text{L3})_2$ and $\text{Cu}(\text{L5})_2$. According to the results obtained, the HOMO orbitals of the complex are located around the acac oxygen atoms indicating their ability to act as partial electron donors in halogen-bond formation (Figure 2.34).

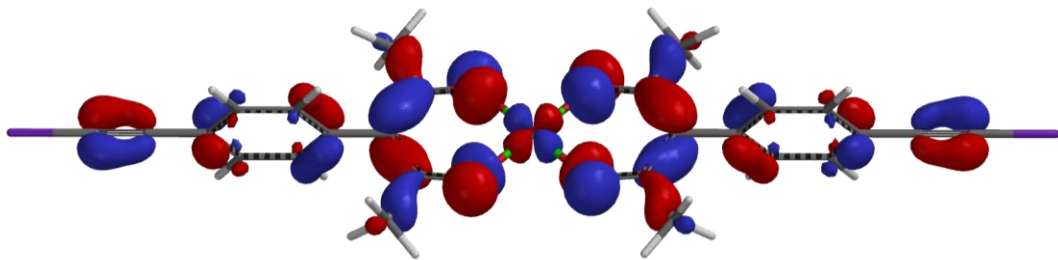


Figure 2.34 HOMO orbitals in $[\text{Cu}(\text{L3})_2]$ (color codes: red and blue- two phases of HOMO orbitals).

2.4.4 TGA data analysis

Early weight loss (below 100 °C) in $[\text{Cu}(\text{L2})_2] \cdot 2\text{CH}_3\text{CN}$ and $[\text{Cu}(\text{L3})_2] \cdot 4\text{CH}_3\text{CN}$ suggests the presence of loosely bound solvent molecules in the crystal lattice. Higher weight loss corresponds to the solvent in $[\text{Cu}(\text{L3})_2] \cdot 4\text{CH}_3\text{CN}$ (19%) compared to $[\text{Cu}(\text{L2})_2] \cdot 2\text{CH}_3\text{CN}$ (11%) demonstrate loss of all four acetonitrile molecules in $[\text{Cu}(\text{L3})_2] \cdot 4\text{CH}_3\text{CN}$. It suggests that the additional two acetonitrile molecules apart from two solvent molecules attached to halogen atoms, are poorly coordinated to the metal center of $[\text{Cu}(\text{L3})_2] \cdot 4\text{CH}_3\text{CN}$.

Higher van der Waals radii reduction of I···O bonds compared to Br···O bond in the structures $[\text{Cu}(\text{L3})_2] \cdot \text{C}_4\text{H}_8\text{O}_2$ and $[\text{Cu}(\text{L2})_2] \cdot \text{C}_4\text{H}_8\text{O}_2$ respectively, provides evidence for iodine as the better halogen-bond donor than bromine. This argument is further confirmed indirectly from the TGA data of the isostructural ethyl acetate solvates in which the loss of the halogen bound solvent molecule occurred at 50 °C in $[\text{Cu}(\text{L2})_2] \cdot \text{C}_4\text{H}_8\text{O}_2$. It was removed from the crystalline complex $[\text{Cu}(\text{L3})_2] \cdot \text{C}_4\text{H}_8\text{O}_2$ at 76 °C (Figure 2.35). It also indicates the stronger solvent···X-C bond formed when halogen-bond donor is iodine compared to bromine.

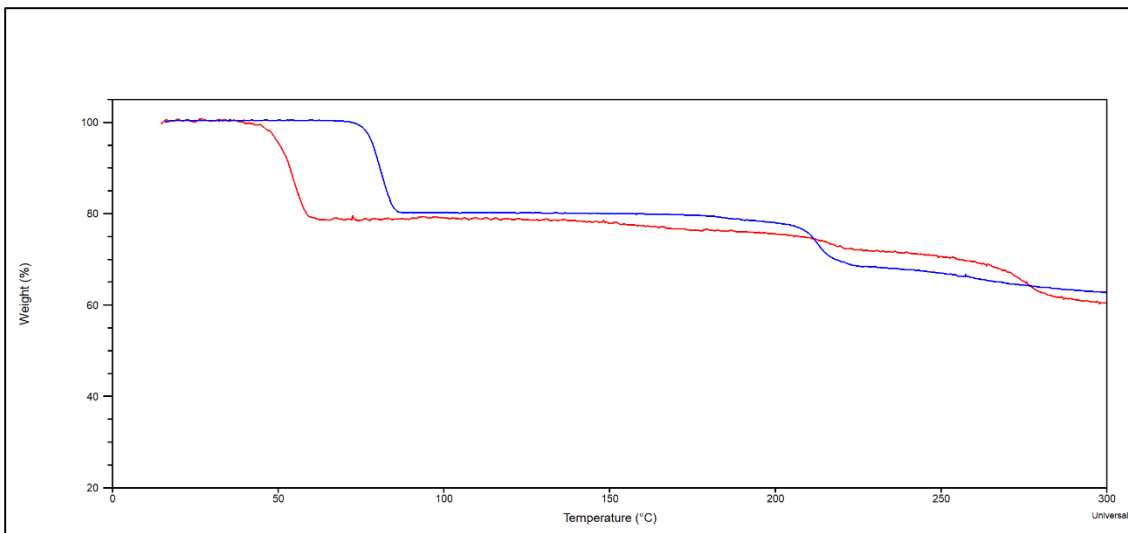


Figure 2.35 Part of TGA traces; $[\text{Cu}(\text{L}2)_2] \cdot \text{C}_4\text{H}_8\text{O}_2$ (Red) and $[\text{Cu}(\text{L}3)_2] \cdot \text{C}_4\text{H}_8\text{O}_2$ (Blue).

2.5 Conclusions⁴⁷

Novel metal-chelating ligands decorated with halogen-bond donors are designed and synthesized as new building blocks to utilize in predictable and programmable supramolecular architectures. The acac moiety shows the capability of efficiently chelate metal ions by avoiding counter anion binding. Furthermore, the acac ligand makes stable metal-ligand complexes which cannot be disrupted by metal coordinating solvents such as acetonitrile.

The bromo- and iodo substituted ligands are capable of forming halogen bonds with oxygen of the acac moiety. The chloro substituted ligand **L1** is incapable of forming any halogen-bond interactions with available acceptors. With the introduction of metal ions to the ligands (**L2**, **L3**), different solvent molecules such as: acetonitrile and ethyl acetate bind via halogen-bond interactions forming discrete assemblies.

With the absence of solvent that is capable of forming halogen-bond interactions, the halogen-bond donors find available acceptor sites on the metal-ligand complex ($\text{Cu}(\text{L}3)_2$) (Figure 2.36). With the geometric change of the ligand (from **L2** to **L5**), the metal-ligand complex

$(\text{Cu}(\text{L5})_2)$ has the ability to make extended architectures without forming any interactions with solvent (Figure 2.36).

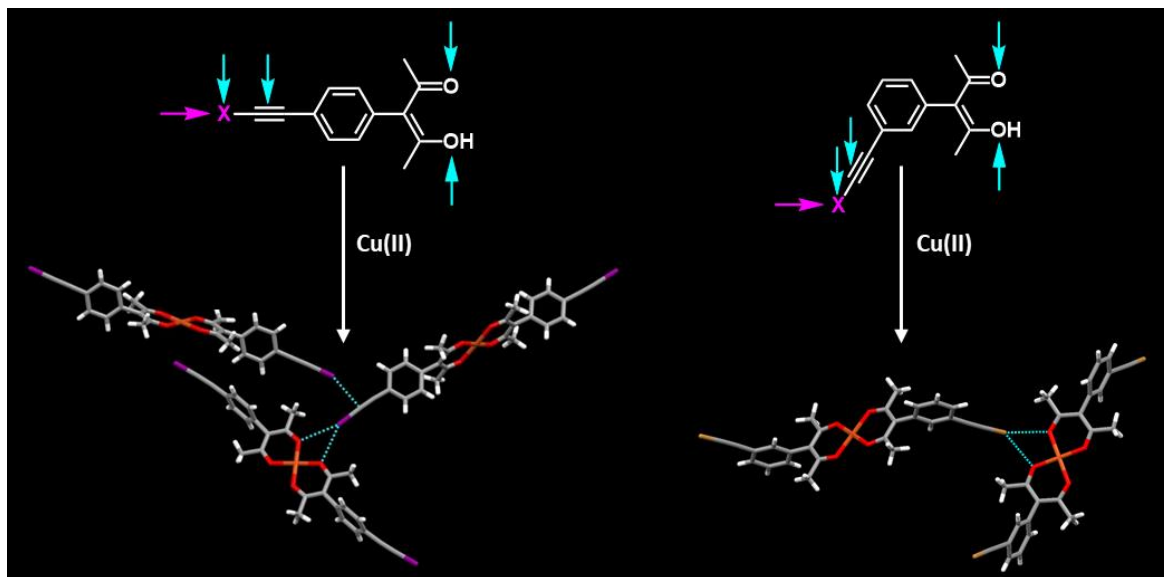


Figure 2.36 Solvent free supramolecular assembly formation

Overall, noticeable halogen-bond interactions were observed in six of the eight structures of metal-ligand complexes. Solvent molecules acted as electron-pair donors for halogen-bond donors in four cases. In one case, one halogen-bond acceptor site was utilized by the halogen bond donor and in the other case, two different halogen-bond acceptors sites on the complex itself were utilized without participation of solvent (Figure 2.36). The other weak non-covalent interaction such as, $\text{CH}\cdots\text{O}$ hydrogen bonds and $\text{I}\cdots\pi$ interactions play a big role in the propagation of the supramolecular assembly in 2D or 3D direction.

Finally, it can be concluded that the new ligands with bromo or iodo groups are capable of simultaneous metal-chelation and directional halogen bonding, and they show potential to make extended 1-D, 2-D, and 3-D architectures when halogen bonding linkers are introduced (Figure 2.37).

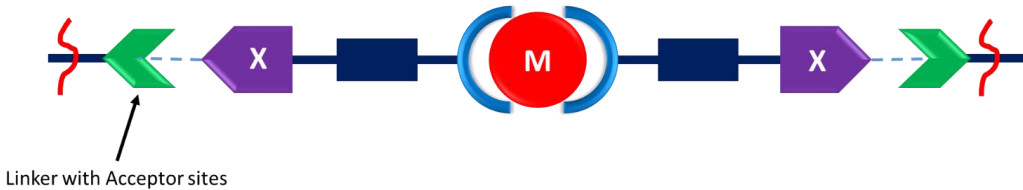


Figure 2.37 Proposed metallosupramolecular architecture formation when halogen-bond acceptor linkers are introduced

Furthermore, if we want to synthesize robust extended architectures by combining ligands with bridging linkers, we need to avoid solvents that can compete with the anticipated halogen bonds. The metal node can be used as an anchoring point for bound ligands while engaging the bromo- or iodo species as connectors to make more complex and predictable metallosupramolecular architectures.

2.6 References

1. Maugeri, L.; Lébl, T.; Cordes, D. B.; Slawin, A. M. Z.; Philp, D., *J. Org. Chem.* **2017**, 82 (4), 1986-1995.
2. Takemura, A.; McAllister, L. J.; Karadakov, P. B.; Pridmore, N. E.; Whitwood, A. C.; Bruce, D. W., *CrystEngComm* **2014**, 16 (20), 4254-4264.
3. Kukovec, B.-M.; Malik, M.; Kodrin, I.; Aakeröy, C. B.; Đaković, M., *Cryst. Growth Des.* **2016**, 16 (12), 7308-7317.
4. Béziau, A.; Baudron, S. A.; Rogez, G.; Hosseini, M. W., *Inorg. Chem.* **2015**, 54 (4), 2032-2039.
5. Durá, G.; Carrión, M. C.; Jalón, F. A.; Manzano, B. R.; Rodríguez, A. M.; Mereiter, K., *Cryst. Growth Des.* **2015**, 15 (7), 3321-3331.
6. Durá, G.; Carrión, M. C.; Jalón, F. A.; Manzano, B. R.; Rodríguez, A. M., *Eur. J. Inorg. Chem.* **2015**, 2015 (36), 5874-5885.
7. Kumari, H.; Jin, P.; Teat, S. J.; Barnes, C. L.; Dalgarno, S. J.; Atwood, J. L., *J. Am. Chem. Soc.* **2014**, 136 (49), 17002-17005.
8. Choudhury, S. R.; Dey, B.; Das, S.; Gamez, P.; Robertazzi, A.; Chan, K.-T.; Lee, H. M.; Mukhopadhyay, S., *J. Phys. Chem. A* **2009**, 113 (8), 1623-1627.
9. Safin, D. A.; Robeyns, K.; Babashkina, M. G.; Vande Velde, C. M. L.; Filinchuk, Y., *Cryst. Growth Des.* **2016**, 16 (7), 3763-3770.
10. Manna, P.; Seth, S. K.; Das, A.; Hemming, J.; Prendergast, R.; Helliwell, M.; Choudhury, S. R.; Frontera, A.; Mukhopadhyay, S., *Inorg. Chem.* **2012**, 51 (6), 3557-3571.
11. Seth, S. K.; Saha, I.; Estarellas, C.; Frontera, A.; Kar, T.; Mukhopadhyay, S., *Cryst. Growth Des.* **2011**, 11 (7), 3250-3265.
12. He, L.; Ma, D.; Duan, L.; Wei, Y.; Qiao, J.; Zhang, D.; Dong, G.; Wang, L.; Qiu, Y., *Inorg. Chem.* **2012**, 51 (8), 4502-4510.
13. Khavasi, H. R.; Kavand, S., *CrystEngComm* **2016**, 18 (25), 4760-4764.
14. Tiekink, E. R. T.; Zukerman-Schpector, J., *CrystEngComm* **2009**, 11 (7), 1176-1186.
15. Cheng, B.; Tehrani, A. A.; Hu, M.-L.; Morsali, A., *CrystEngComm* **2014**, 16 (38), 9125-9134.
16. Sommer, S. K.; Zakharov, L. N.; Pluth, M. D., *Inorg. Chem.* **2015**, 54 (4), 1912-1918.
17. Marshall, L. J.; de Mendoza, J., *Org. Lett.* **2013**, 15 (7), 1548-1551.

18. Piñón, V.; Weck, M., *Langmuir* **2012**, 28 (6), 3279-3284.
19. Wang, L.; Zhu, L.; Yin, P.; Fu, W.; Chen, J.; Hao, J.; Xiao, F.; Lv, C.; Zhang, J.; Shi, L.; Li, Q.; Wei, Y., *Inorg. Chem.* **2009**, 48 (19), 9222-9235.
20. Dong, H.; Wang, D.; Sun, G.; Hinestroza, J. P., *Chem. Mater.* **2008**, 20 (21), 6627-6632.
21. Desiraju Gautam, R.; Ho, P. S.; Kloo, L.; Legon Anthony, C.; Marquardt, R.; Metrangolo, P.; Politzer, P.; Resnati, G.; Rissanen, K., Definition of the halogen bond (IUPAC Recommendations 2013). In *Pure Appl. Chem.*, 2013; Vol. 85, p 1711.
22. Cavallo, G.; Metrangolo, P.; Milani, R.; Pilati, T.; Priimagi, A.; Resnati, G.; Terraneo, G., *Chem. Rev.* **2016**, 116 (4), 2478-2601.
23. Berger, G.; Soubhye, J.; Meyer, F., *Polym. Chem.* **2015**, 6 (19), 3559-3580.
24. Meyer, F.; Dubois, P., *CrystEngComm* **2013**, 15 (16), 3058-3071.
25. Priimagi, A.; Cavallo, G.; Metrangolo, P.; Resnati, G., *Acc. Chem. Res.* **2013**, 46 (11), 2686-2695.
26. Ivanov, D. M.; Novikov, A. S.; Ananyev, I. V.; Kirina, Y. V.; Kukushkin, V. Y., *Chem. Commun.* **2016**, 52 (32), 5565-5568.
27. Khavasi, H. R.; Ghanbarpour, A.; Tehrani, A. A., *RSC Advances* **2016**, 6 (3), 2422-2430.
28. Li, B.; Zang, S.-Q.; Wang, L.-Y.; Mak, T. C. W., *Coord. Chem. Rev.* **2016**, 308, 1-21.
29. Bertani, R.; Sgarbossa, P.; Venzo, A.; Lelj, F.; Amati, M.; Resnati, G.; Pilati, T.; Metrangolo, P.; Terraneo, G., *Coord. Chem. Rev.* **2010**, 254 (5), 677-695.
30. Aakeroy, C. B.; Sinha, A. S.; Chopade, P. D.; Desper, J., *Dalton Trans.* **2011**, 40 (45), 12160-12168.
31. Nguyen, S. T.; Rheingold, A. L.; Tschumper, G. S.; Watkins, D. L., *Cryst. Growth Des.* **2016**, 16 (11), 6648-6653.
32. Aakeröy, C. B.; Wijethunga, T. K.; Desper, J., *J. Mol. Struct.* **2014**, 1072, 20-27.
33. Riley, K. E.; Murray, J. S.; Fanfrlík, J.; Řezáč, J.; Solá, R. J.; Concha, M. C.; Ramos, F. M.; Politzer, P., *J. Mol. Model.* **2011**, 17 (12), 3309-3318.
34. Clark, T.; Hennemann, M.; Murray, J. S.; Politzer, P., *J. Mol. Model.* **2007**, 13 (2), 291-296.
35. Carlucci, L.; Gavezzotti, A., *PCCP* **2017**.
36. Aakeröy, C. B.; Baldridge, M.; Desper, J.; Metrangolo, P.; Resnati, G., *Chem. Eur. J.* **2013**, 19 (48), 16240-16247.
37. Ramirez, F.; Patwardhan, A. V.; Ramanathan, N.; Desai, N. B.; Greco, C. V.; Heller, S. R., *J. Am. Chem. Soc.* **1965**, 87 (3), 543-548.
38. Osowska, K.; Lis, T.; Szafert, S., *Eur. J. Org. Chem.* **2008**, 2008 (27), 4598-4606.
39. Aakeroy, C. B.; Sinha, A. S.; Epa, K. N.; Spartz, C. L.; Desper, J., *Chem. Commun.* **2012**, 48 (92), 11289-11291.
40. Dumele, O.; Schreib, B.; Warzok, U.; Trapp, N.; Schalley, C. A.; Diederich, F., *Angew. Chem. Int. Ed.* **2017**, 56 (4), 1152-1157.
41. Frixas, C.; Mahon, M. F.; Thompson, A. S.; Threadgill, M. D., *Org. Biomol. Chem.* **2003**, 1 (2), 306-317.
42. R. Desiraju, G., *Chem. Commun.* **1997**, (16), 1475-1482.
43. Thalladi, V. R.; Goud, B. S.; Hoy, V. J.; Allen, F. H.; Howard, J. A. K.; Desiraju, G. R., *Chem. Commun.* **1996**, (3), 401-402.
44. Aakeröy, C. B.; Welideniya, D.; Desper, J., *CrystEngComm* **2017**, 19 (1), 11-13.
45. Baldridge, M.; Bartesaghi, D.; Cavallo, G.; Chierotti, M. R.; Gobetto, R.; Metrangolo, P.; Pilati, T.; Resnati, G.; Terraneo, G., *CrystEngComm* **2014**, 16 (26), 5897-5904.
46. Dumele, O.; Wu, D.; Trapp, N.; Goroff, N.; Diederich, F., *Org. Lett.* **2014**, 16 (18), 4722-4725.
47. Gamekkanda, J. C.; Sinha, A. S.; Desper, J.; Dakovic, M.; Aakeroy, C. B., *New J. Chem.* **2018**, 42 (13), 10539-10547.

Chapter 3 Competition between hydrogen bonds and halogen bonds

3.1 Introduction

Intermolecular interactions that can provide hierarchical assembly are useful for developing practical and robust strategies needed for effective synthesis of co-crystals.¹⁻² By minimizing or avoiding synthon crossover³ (interactions that compete for the same binding site), we can produce predictable, more advance, and complex architectures.⁴⁻⁷ The hydrogen bond (HB) is recognized as one of the synthetic tools for making predictable architectures,⁸⁻¹¹ but sometimes HBs fail in the making of complex architectures that involve more than one competitive interaction.¹²⁻¹⁷ As an alternative to HBs, the halogen bond has received attention recently as a synthon for making predictable heteromeric architectures.

There are similarities in both interactions such as directionality and strength, and both have common dependence upon long-range electrostatic forces.^{15, 18-20} In the solid state, there are several examples regarding HB/XB “imitation” which show that HB and XB interactions make structurally similar interactions.²¹ The interaction between 4,4'-bypyridine (HB/XB acceptor) and hydroquinone²² (HB donor) is mimicked by the XB donor, 1,4-diiodobenzene²³ (Figure 3.1).

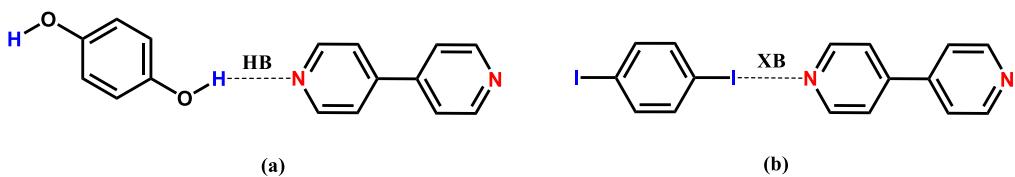


Figure 3.1 (a) HB interaction between 4,4'-bypyridine and hydroquinone, (b) XB interaction between 4,4'-bypyridine and 1,4-diiodobenzene

1,4-Diiodotetrafluorobenzene also makes the same interaction with 4,4'-bypyridine.²⁴

There are more examples of HB/XB mimicry such as: the formation of equivalent architectures between aminopyrimidine-based ethynyl and iodoethynyl donors with tetramethylpyrazine and 1,2-bis(4-pyridyl)ethylene.²⁵

In addition, there are some studies in the literature that address the competition between separate XB and HB donors for the same acceptor in experimentally²⁶⁻²⁸ and theoretical²⁹ manners. For example, HB/XB competition in mixtures of 1,2-bis(4-pyridyl)-ethane, 1,4-diiodotetrafluorobenzene and hydroquinone or of N,N,N',N'-tetramethylethylenediamine, 1,2-diido-tetrafluoroethane and ethylene glycol have been reported.^{24, 30} A dominating hydrogen bonding outcome was observed in mixtures of 1,2-bis(4-pyridyl)-ethane, 1,4-diiodotetrafluorobenzene and hydroquinone (Figure 3.2) while halogen bonding was the dominant non-covalent interaction in the latter system (Figure 3.3).

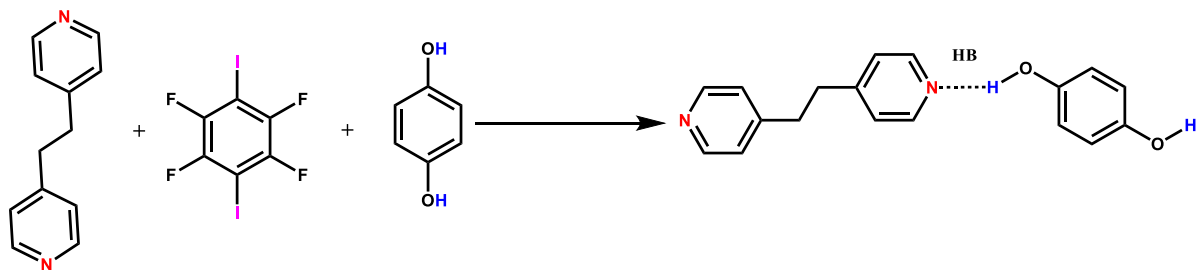


Figure 3.2 Supramolecular outcome of the mixture of 1,2-bis(4-pyridyl)-ethane, 1,4-diiodotetrafluorobenzene and hydroquinone

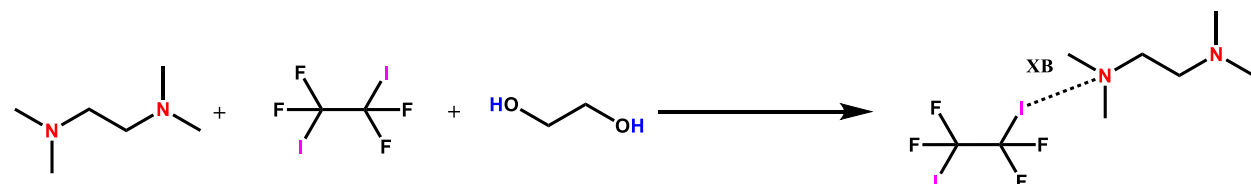


Figure 3.3 Supramolecular outcome of the mixture of N,N,N',N'-tetramethylethylenediamine, 1,2-diido-tetrafluoroethane and ethylene glycol

There are only a small number of studies that address competition between HB and XB by attaching both HB and XB donors to the same molecular backbone. Investigation of HB/XB competition towards 4,4'-azobipyridine from bi-functional molecules such as 4-iodotetrafluorobenzoic acid, 4-iodotetrafluorophenol or 4-iodotetrafluoroaldoxime are some notable examples.³¹ In order to advance supramolecular synthesis by using both HB and XB interactions in same system, we have to fully understand the balance between them.

Apart from activation of an XB donor by attaching electro withdrawing groups next to it, the same effect can be achieved by attaching the XB donor to an sp-hybridized carbon.^{23,32} So far very little research has been done on the competition between such XB donors and HB donors.²⁶ In order to remedy this, we have designed two tetra-functionalized molecules, *trans*-1,4-bis(iodoethynyl)cyclohexane-1,4-diol (**D1**) and *cis*-1,4-bis(iodoethynyl)cyclohexane-1,4-diol (**D2**) which are geometric isomers of each other with two HB donors and two XB donors (Figure 3.4). *Trans*-1,4-diethynylcyclohexane-1,4-diol (**D3**) which has only HB donors was also designed to study the structural chemistry (Figure 3.4).

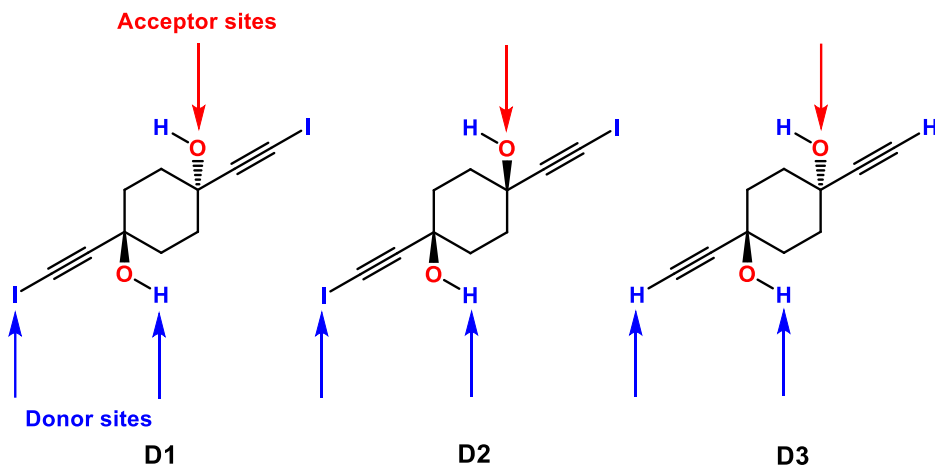


Figure 3.4 Molecules with competing halogen- and hydrogen-bond donors (**D1/D2**) and competing hydrogen-bond donors (**D3**)

The activation of XB donors in **D1** and **D2** were done by an sp-hybridized carbon atom, and **D3** is the control molecule which has an HB donor, R-C≡C-H instead of XB donor, R-C≡C-I and geometrically identical to **D1**. In order to study how synthon preferences may depend on the molecular geometry, two geometrical isomers **D1** and **D2** were designed. Six HB/XB nitrogen based symmetric ditopic acceptor molecules were selected in order to subject donors to co-crystallization experiments (Figure 3.5).

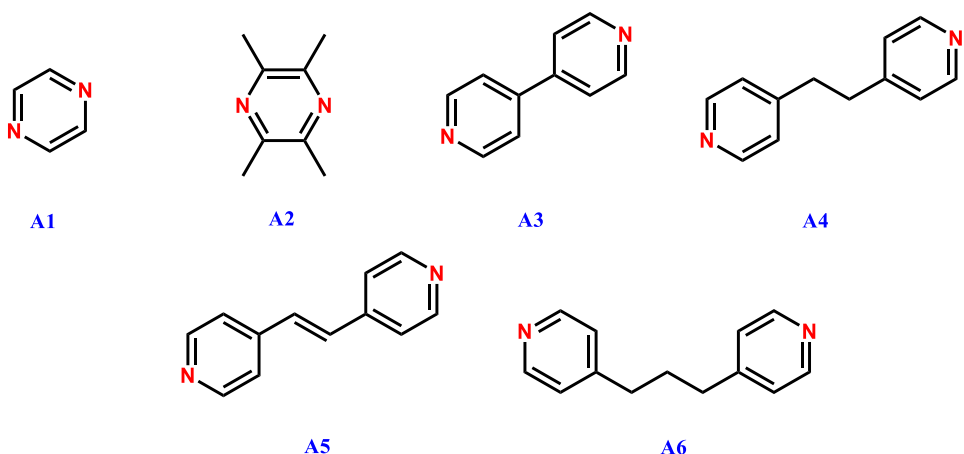


Figure 3.5 Ditopic nitrogen based XB/ HB acceptors (**A1-A6**)

Based on the donor- and acceptor molecules examined in this study, we postulated a series of different outcomes if **D1-D3** were to form co-crystals with the acceptors **A1-A6** (Figures 3.6 and 3.7).

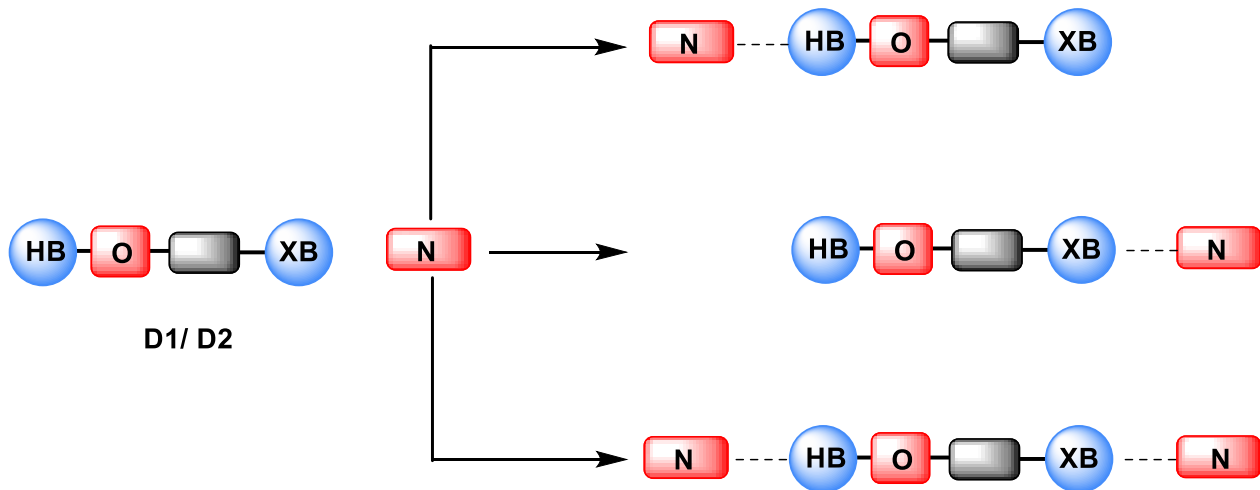


Figure 3.6 Hypothesized primary intermolecular interactions in co-crystals of D1/D2:A1-A6

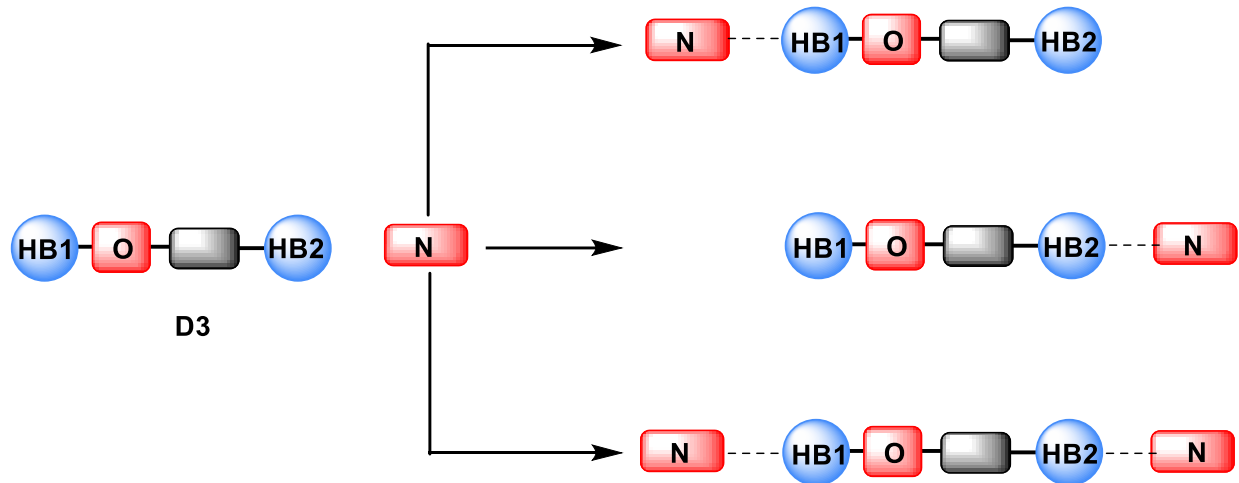


Figure 3.7 Hypothesized intermolecular interactions in co-crystals of **D3:A1-A6**

The main advantage of these molecules is that by having both XB and HB bond donors on the same backbone, the outcome is not going to be affected by possible solubility differences. We supplemented the structural study further with an analysis of calculated molecular electrostatic potential surfaces for **D1-D3** and acceptors in order to rationalize the outcome of the co-crystallizations.

3.1.1 Objectives of this study

This study is carried out to achieve specific goals stated below.

1. Synthesis of three newly designed HB/ XB donor molecules and subject them in co-crystallization experiments with suitable acceptors.
2. Exploring whether both hydrogen- and halogen-bond interactions behave structurally similar since both have shared dependence upon molecular electrostatic potentials.
3. Studying the possible competitiveness of HB and XB when interacting with a common acceptor since both interactions demonstrate comparable strength and directionality.
4. Investigating the impact of geometric changes of donor positioning on competitiveness of HB and XB interactions.
5. Comparison of the strength of both HB (C≡C-H) and XB (C≡C-I) donors which are activated similarly by *sp*-hybridized carbon.
6. Evaluating the capability of predicting outcome of a supramolecular architecture in the presence of competitive/ concurrent non-covalent forces.

3.2 Experimental

3.2.1 General

All solvents, reagents, precursors and acceptors (**A1-A6**) were purchased from commercial sources and used without further purification. Melting points were determined using a Fisher-Johns melting point apparatus and are uncorrected. Infrared spectra were obtained on a Nicolet 380 FT-

IR spectrometer. ^1H NMR spectra were obtained on a Varian unity plus 400 MHz spectrometer. DSC data were obtained on a TA instruments Q20 and TGA data on a TA instruments Q50.

3.2.2 Computational studies

All the calculations were carried out using B3LYP functional and 6-31G* basis set which employs LANL2DZ³³ under vacuum in Spartan'14 software. Molecular electrostatic potential surfaces (MEPs) were generated for the optimized structures on the electron isodensity surface of the 0.002 electrons/au³.

3.2.3 Synthesis of D1-D3

The three donors were synthesized using commercially available 1,4-cyclohexanedione. The ketone was converted to the propargyl alcohol with a TMS protected alkyne group³⁴ (the trans-cyclohexane being the major product). **D3** was obtained by deprotecting the ethynyl group and **D1** and **D2** were obtained through a reaction with N-iodosuccinimide, Figure 3.8.

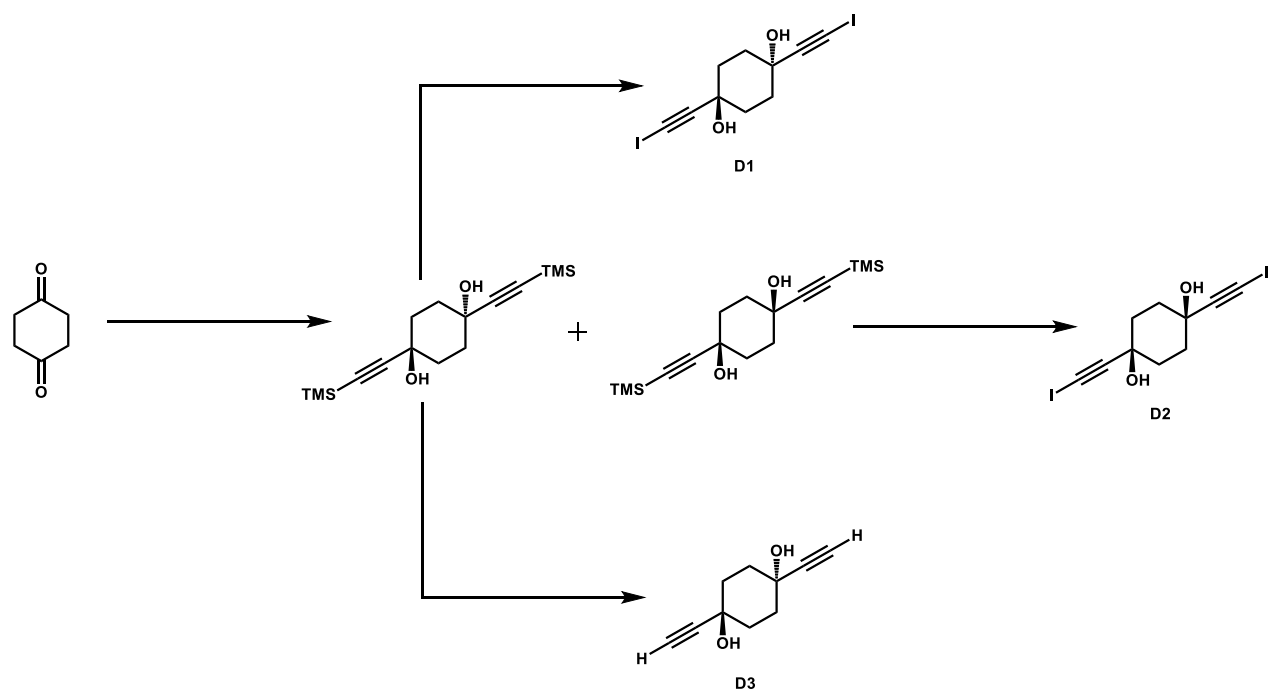
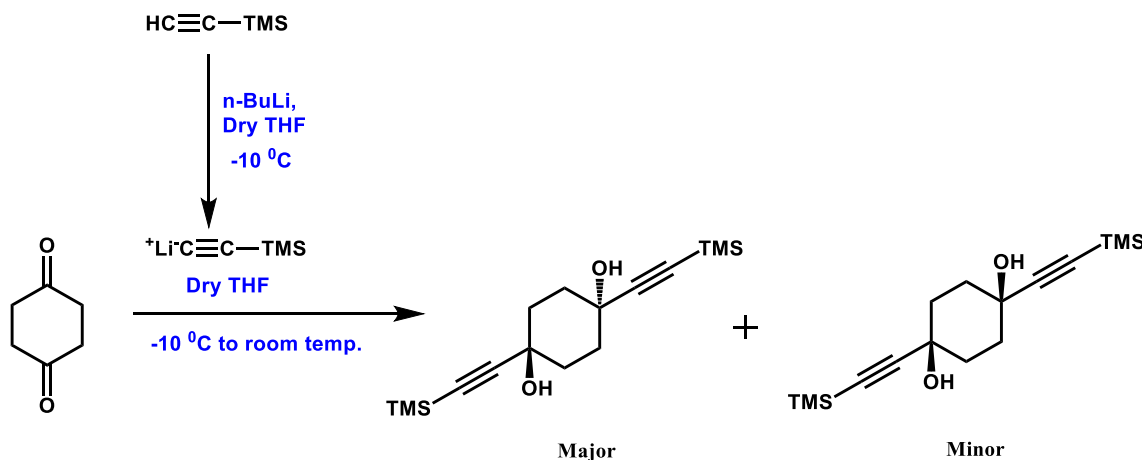


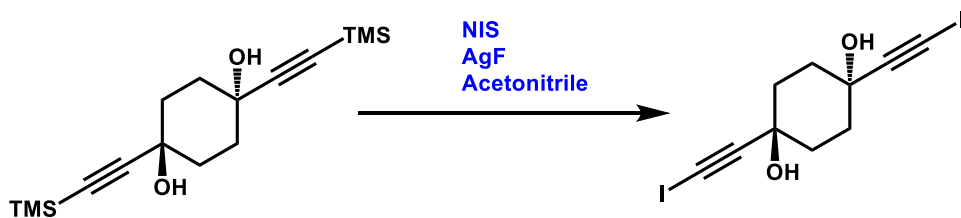
Figure 3.8 Synthesis pathway to **D1**, **D2** and **D3**

3.2.3.1 Synthesis of trans- and cis -1,4-bis((trimethylsilyl)ethynyl)cyclohexane-1,4-diol



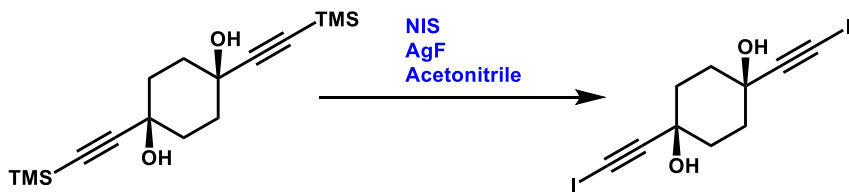
A solution of trimethylsilylacetylene (1.75 ml, 18 mmol) was stirred in 100 ml of dry THF and cooled to $-10\text{ }^\circ\text{C}$ under N_2 . A solution of $n\text{-BuLi}$ (4.9ml 18 mmol) was added slowly over 30 min. at $-10\text{ }^\circ\text{C}$ under N_2 . The mixture was stirred for an additional hour at the same temperature. Cyclohexane-1,4-dione (1.0 g, 8.9 mmol) was dissolved in 25 ml of dry THF and added dropwise to the resulting trimethylsilyl acetylide solution under N_2 at $-10\text{ }^\circ\text{C}$. The mixture was then allowed to reach room temperature and stirred overnight. After completion of the reaction, 100 ml of water was added and extracted with ethyl acetate ($3 \times 100\text{ml}$). The combined organic layers were dried over magnesium sulfate and the solution was concentrated to obtain a crude solid and purified by column chromatography. The *trans* isomer was obtained using hexane as the eluent and the *cis* isomer was obtained using a mixture of hexanes: ethyl acetate (8:2) as the eluent. Yield: *trans* isomer 1.43g, 52%, m.p.: 160-163 $^\circ\text{C}$, $^1\text{H NMR}$ (400 MHz in DMSO-d_6): 5.43 (2H, s), 1.77-1.62 (8H, m), 0.13 (18H, s) *cis* isomer 0.410g, 15%, m.p.: 123-125 $^\circ\text{C}$, $^1\text{H NMR}$ (400 MHz in DMSO-d_6): 5.31 (2H, s), 1.68-1.71 (8H, m), 0.12 (18H, s).

3.2.3.2 Synthesis of trans-1,4-bis(iodoethynyl)cyclohexane-1,4-diol.H₂O (D1.H₂O)



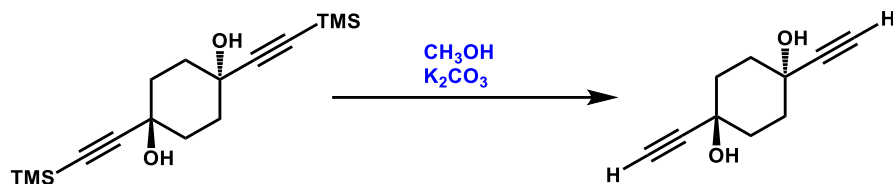
Silver fluoride (0.825g, 6.5 mmol) and trans-1,4-bis((trimethylsilyl)ethynyl)cyclohexane-1,4-diol (1.0 g, 3.24 mmol) were dissolved in 50ml of acetonitrile and N₂ was bubbled through the solution for 20 minutes. N-iodosuccinimide (1.46 g, 6.5 mmol) was added to the mixture and the flask was covered with aluminium foil. The reaction was stirred overnight under N₂. After completion of the reaction, the resulting mixture was passed through a short pad of silica and the resulting solution was evaporated under vacuum in order to get the crude product. It was dissolved in methanol and water was added to the mixture. The product crashed out and the precipitate was filtered and dried in air to give a light-yellow solid. Yield 1.23g, 87%, m.p.: 218-220 °C (dec.), ¹H NMR (400 MHz in DMSO-d₆): 5.57 (2H, s), 1.60-1.80 (8H, m).

3.2.3.3 Synthesis of cis-1,4-bis(iodoethynyl)cyclohexane-1,4-diol (D2)



The synthesis of cis-1,4-bis(iodoethynyl)cyclohexane-1,4-diol was carried out in the same way as the synthesis of D1 by using 0.250g (2.0 mmol) of silver fluoride, and 0.3g (9.7 mmol) of cis-1,4-bis((trimethylsilyl)ethynyl)cyclohexane-1,4-diol and 0.450g (2.0 mmol) of N-iodosuccinimide dissolved in 30 ml of acetonitrile. Yield: 0.360g, 89%, m.p.: 168-171 °C (dec.), ¹H NMR (400 MHz in DMSO-d₆): 5.40 (2H, s), 1.61-1.71 (8H, m).

3.2.3.4 Synthesis of trans-1,4-diethynylcyclohexane-1,4-diol.H₂O (D3.H₂O)



Trans-1,4-bis((trimethylsilyl)ethynyl)cyclohexane-1,4-diol (0.5g, 1.6mmol) and potassium carbonate (0.45g, 3.25 mmol) were dissolved in 50ml of methanol. The reaction mixture was stirred for 4 hrs and after completion of the reaction, the solvent was evaporated under vacuum. The solid mixture was dissolved in ethyl acetate and washed with brine. The organic layer was dried over magnesium sulfate and the solvent was evaporated to get a white powder as the product. Yield 0.22 g, 75%, m.p.: 175-178 °C, Yield 0.22 g, 75%, m.p.: 175-178 °C, ¹H NMR (400 MHz in DMSO-d6): 5.41 (2H, s), 3.28 (2H, s), 1.64-1.79 (8H, m).

3.2.4 Crystal growth of D1-D3 and synthesis of co-crystals

D1-D3 (10 mg) were individually combined with each acceptor (**A1-A6**) in a 1:1 stoichiometric ratio using solvent assisted grinding (methanol as the solvent). Eighteen experiments were performed and the resulting solids were analyzed using IR spectroscopy. The solid mixtures obtained from grinding experiments were dissolved in 2 ml of methanol or methanol/tetrahydrofuran and kept in small vials for slow evaporation at room temperature. Crystals suitable for single-crystal X-ray diffraction were obtained after 2-3 days.

3.3 Results

3.3.1 Molecular electrostatic potential of donors and acceptors

The maximum positive and negative MEPs values on the electrostatic potential surfaces for **D1** and **D3** are listed in Figure 3.9 (a) and Figure 3.9 (b) respectively. Figure 3.10 (a) and (b) shows them for **D2**.

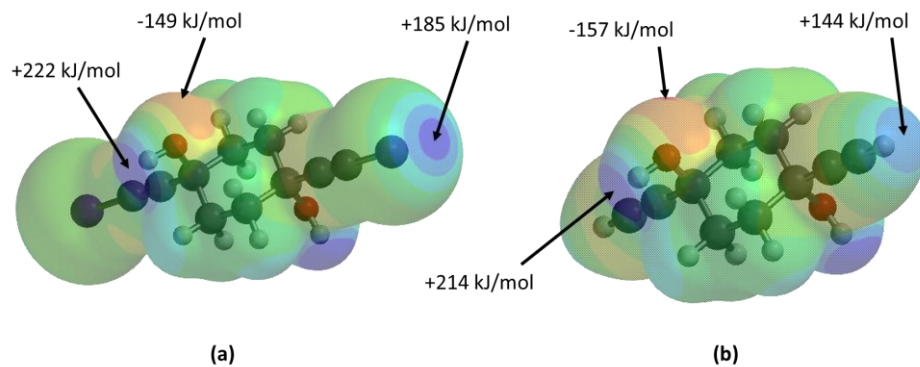


Figure 3.9 Electrostatic potential surfaces of (a) XB/HB donors and acceptors of **D1**, (b) HB donors and acceptors of **D3**.

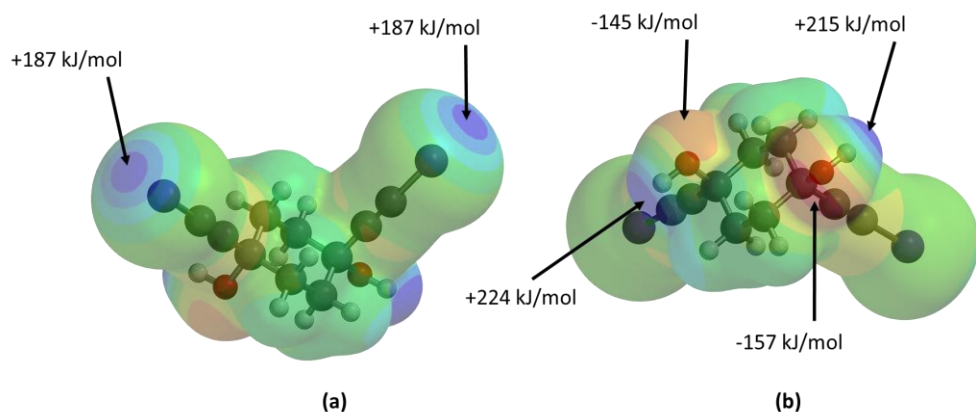


Figure 3.10 Electrostatic potential surfaces of (a) XB donors, (b) HB donors and XB/HB acceptors of **D2**.

Figure 3.11 shows MEPs of **A1-A6** which were calculated in order to rank the ability of these molecules to act as HB/XB acceptors.

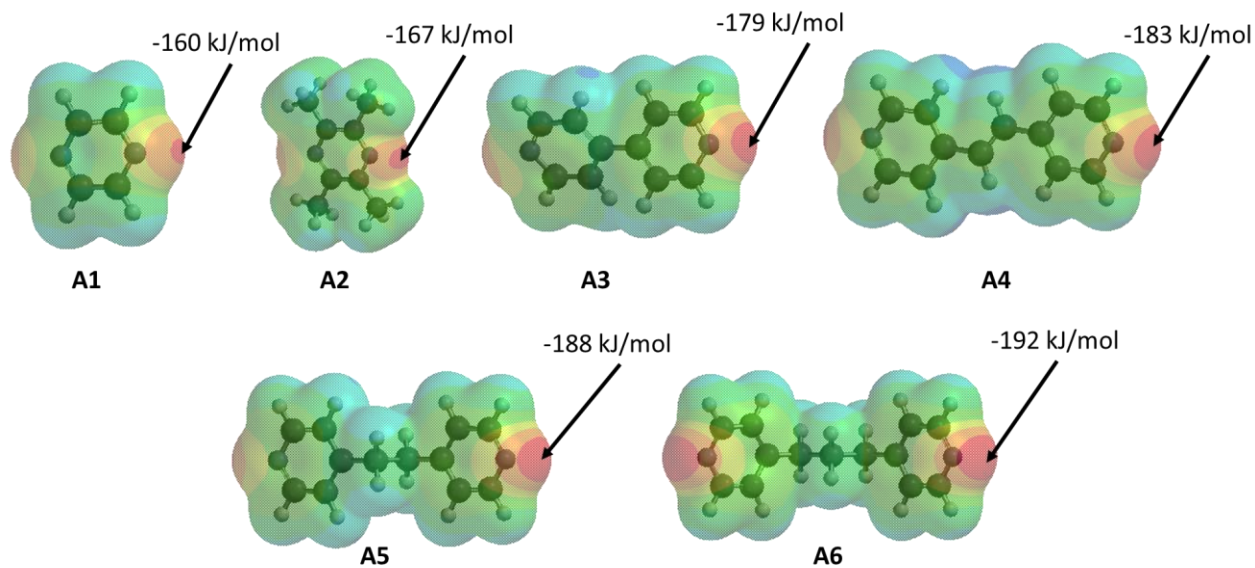


Figure 3.11 Electrostatic potential surfaces of acceptor atoms in **A1-A6**.

3.3.2 Differential scanning calorimetry (DSC) and thermogravimetric analysis (TGA) of donors

In crystals of **D1** and **D3**, water molecules are incorporated in the lattices and both crystallized as monohydrates, while **D2** does not include any solvent in its lattice. These results are confirmed by TGA which shows the loss of one equivalent of water only for **D1** and **D3** (Figure 3.12). DSC traces also indicate thermodynamic events at the matching temperatures for the loss of water in the lattices of **D1** and **D3** (Figure 3.13). There was no indication in the DSC or TGA for solvent in the structure of **D2**.

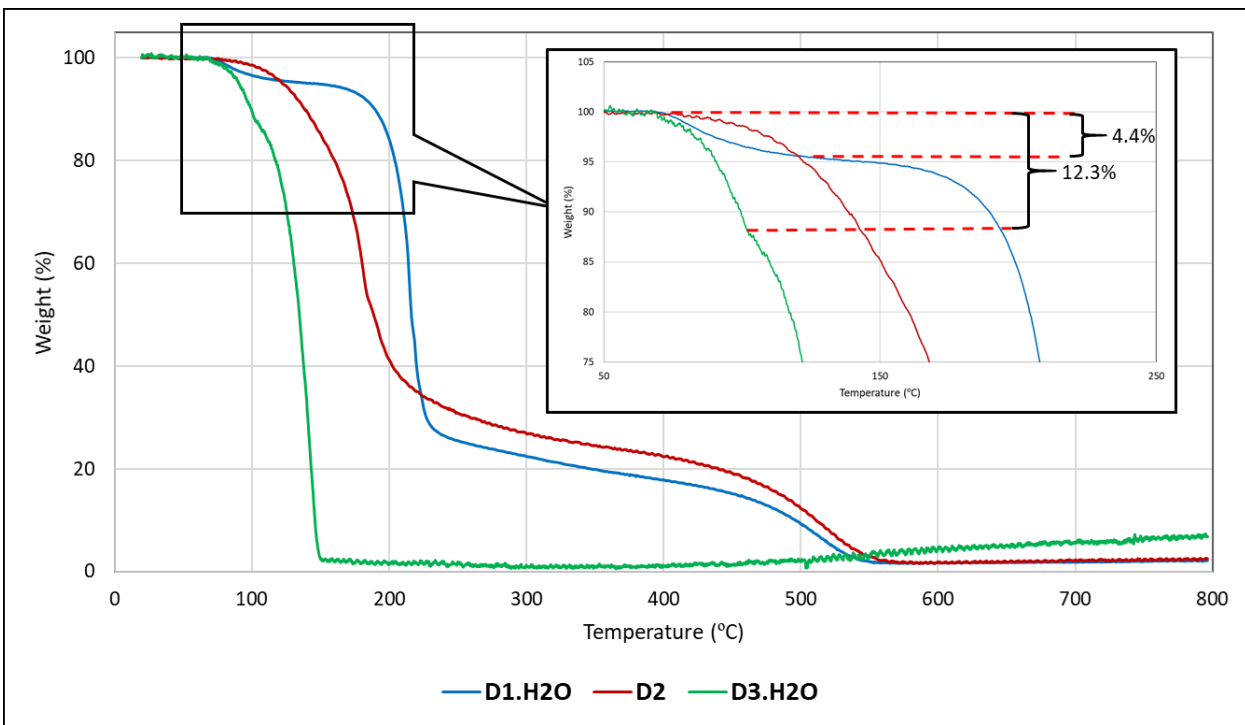


Figure 3.12 TGA traces comparison of **D1.H₂O** (Blue), **D2** (Red) and **D3.H₂O** (Green)

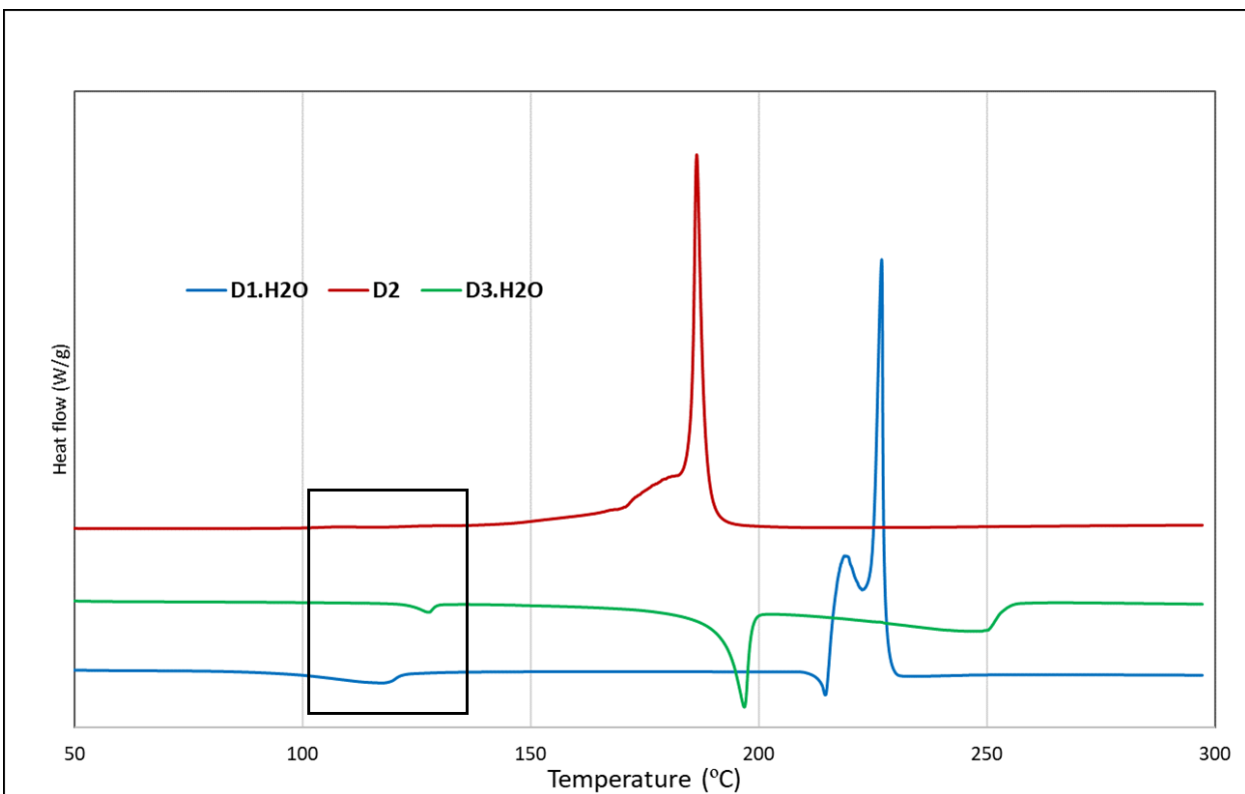


Figure 3.13 DSC traces comparison of **D1.H₂O** (Blue), **D2** (Red) and **D3.H₂O** (Green)

3.3.3 Single X-ray structures of donors

All donor molecules and six co-crystals between donors and acceptors produced crystals suitable for single-crystal X-ray diffraction, and the crystallographic data is provided in the appendix B. Geometric parameters (bond distances and angles) for hydrogen- and halogen bonds in the crystal structures of **D1-D3** are given in Table 1 and Table 2, respectively.

Table 3.1 HB distances and angles in **D1-D3**

Compound	D-H…A	D…A (Å)	∠(DHA) (°)
D1.H₂O	O(1)-H(1O)…O(2)	2.8239(19)	164(8)
	O(2)-H(2O)…O(1)	2.8239(19)	154(8)
D2	O(10)-H(10)…O(14)	2.806(2)	173(3)
	O(14)-H(14)…O(10)	2.922(2)	170(3)
D3.H₂O	O(4)-H(4)…O(13)	2.6333(11)	173.2(16)
	O(10)-H(10)…O(4)	2.7789(11)	160.8(17)
	O(13)-H(13A)…O(10)	2.7575(13)	168.9(16)
	O(13)-H(13B)…O(4)	2.9174(12)	169.3(18)

Table 3.2 HB distances and angles in **D1-D2**

Compound	D-X…A	X…A (Å)	∠(DXA) (°)
D1.H₂O	C(1)-I(1)…O(1)	3.146(3)	174.68(15)
	C(8)-I(9)…I(13)	3.9222(4)	140.69(7)
	C(12)-I(13)…I(9)	3.9222(4)	71.49(7)
	C(12)-I(13)…C(8)	3.296(2)	168.69(8)
	C(12)-I(13)…C(7)	3.354(2)	170.34(8)

In the crystal structure of **D1**, all four donors (2 x O-H and 2 x R-C≡C-I) participate in non-covalent interactions. The presence of a water molecule has made the crystal packing more complicated. This disordered water molecule acts as a hydrogen bond donor to the hydroxylic oxygen atoms and acceptor to the hydroxyl hydrogen of **D1**. Both XB donors interact with –OH groups of **D1** in a homomeric manner (Figure 3.14).

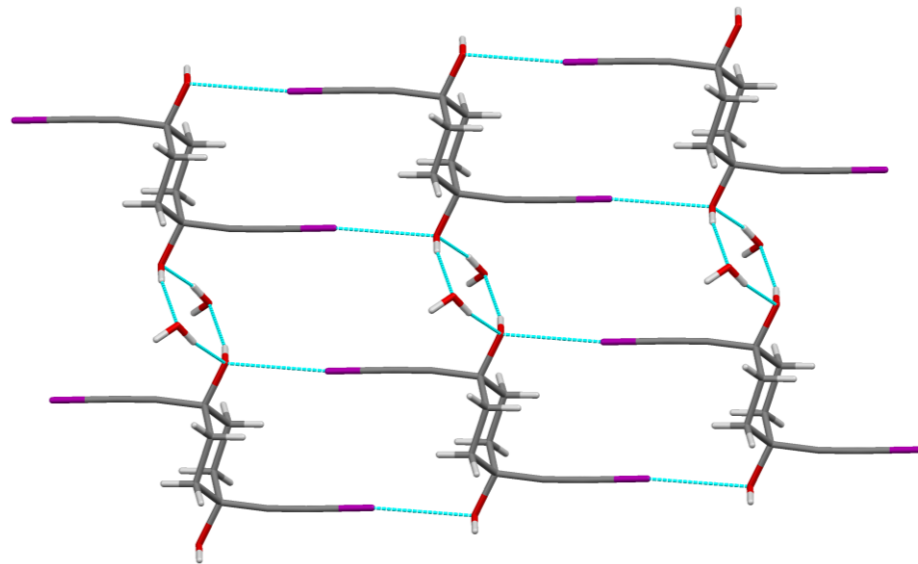


Figure 3.14 Hydrogen bonding and halogen bonding in the crystal structure of **D1**·H₂O (color codes: red-oxygen; violet-iodine).

When it comes to the crystal structure of **D2**, no water molecules are present in the lattice in agreement with DSC and TGA evidence. There are two intermolecular HB interactions between adjacent hydroxyl groups, (Figure 3.15 a). In addition, there is one XB interaction between the triple bond of **D2** as an acceptor site $r(I\cdots\text{centroid of triple bond}) ca. 3.27\text{\AA}$, $\theta(\text{centroid of triple bond}\cdots I-C) ca. 177.76^\circ$, and there is one iodine···iodine type II interaction, (Figure 3.15 b).

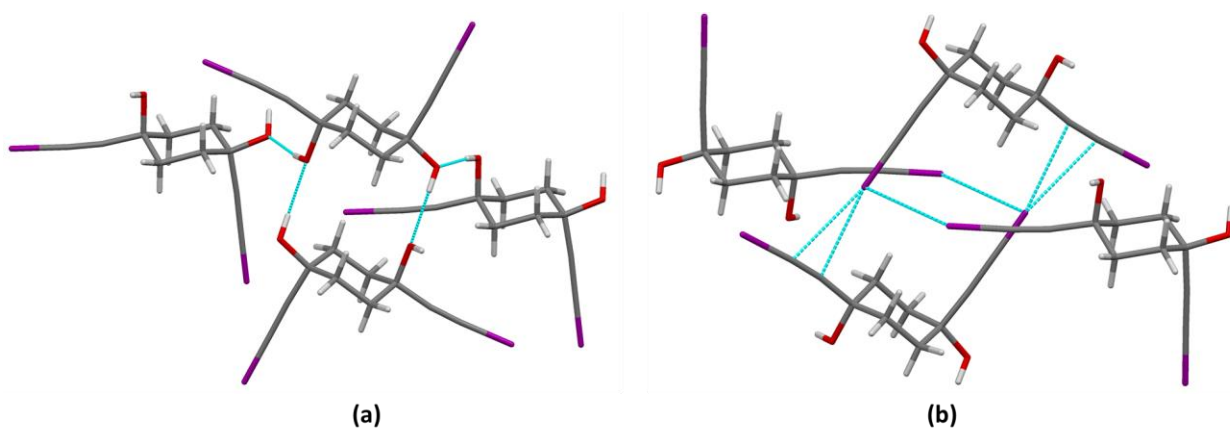


Figure 3.15 Hydrogen bonds (a) and halogen bonds (b) in the crystal structure of **D2** (color codes: red-oxygen; violet-iodine).

When water is incorporated into the crystal lattice of **D3**, **D3**···**D3** water-bridged interactions (Figure 3.16 a) can be seen in the packing. In addition, direct **D3**···**D3** hydrogen bonds (Figure 3.16 b), and a triple bond-ethynyl hydrogen atom interaction $r(C \cdots \text{centroid of triple bond})$ ca. 3.87 Å, $\theta(\text{centroid of triple bond} \cdots H-C)$ ca. 138° (Figure 3.16 b) are observed in the solid state.

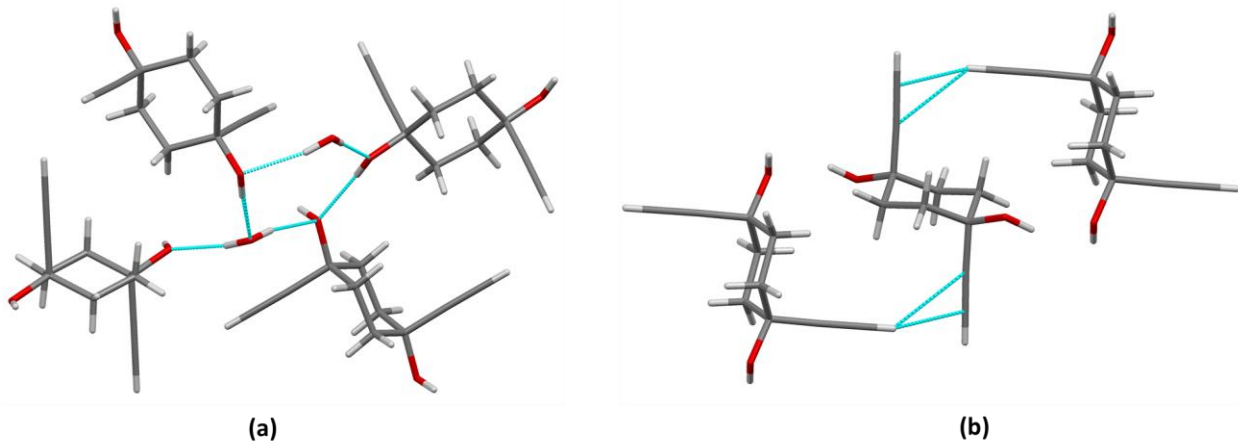


Figure 3.16 (a) Water bridged hydrogen bonding and (b) C-H \cdots C≡C hydrogen bond in the crystal structure of D3.H₂O (color codes: red-oxygen)

3.3.4 IR spectroscopy of co-crystals

IR spectroscopy analysis shows evidence for the formation of co-crystals for all sixteen attempted co-crystallization experiments. Peak shifts of major peaks of donors and acceptors can be seen in the ground mixtures of corresponding donor-acceptor pairs. For example, the peak shift corresponding to the triple bond in **D1** (from 2158 cm^{-1} to 2153 cm^{-1}) in Figure 3.17, in **D2** (from 2170 cm^{-1} to 2167 cm^{-1}) in Figure 3.18, in **D3** (from 2104 cm^{-1} to 2097 cm^{-1}) in Figure 3.19, a peak corresponding to the –OH group (broad peak $3600\text{-}3200\text{ cm}^{-1}$) in all three donors and characteristic acceptor peak (1586 cm^{-1}) shift in **A3** can be used as evidence for the formation of co-crystals.

Complementary blue-shift of a characteristic peak in 4,4'-bipyridine of **D1:A3** can be observed (from ca. 1586 cm^{-1} to 1590 cm^{-1}) with the formation of a co-crystal (Figure 3.17).

Similar red shifts corresponding peaks of **D2** and **D3** and blue shifts in peaks of 4,4'-bipyridine³⁵ revealed the formation of co-crystals (Figures 3.18 and 3.19).

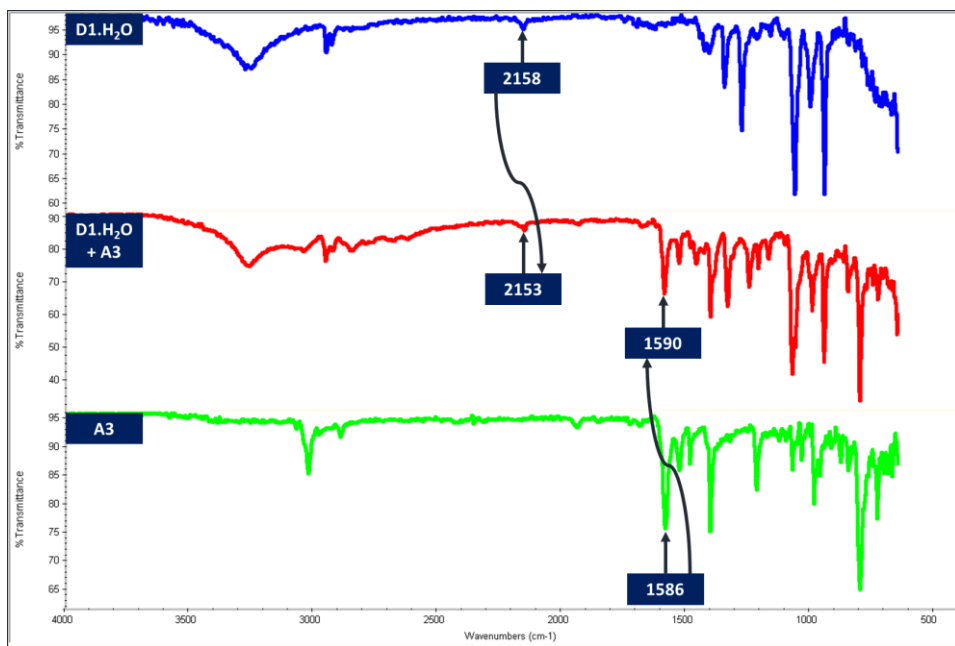


Figure 3.17 IR comparison of **D1.H₂O**, **A3** and **D1.H₂O: A3** ground mixture

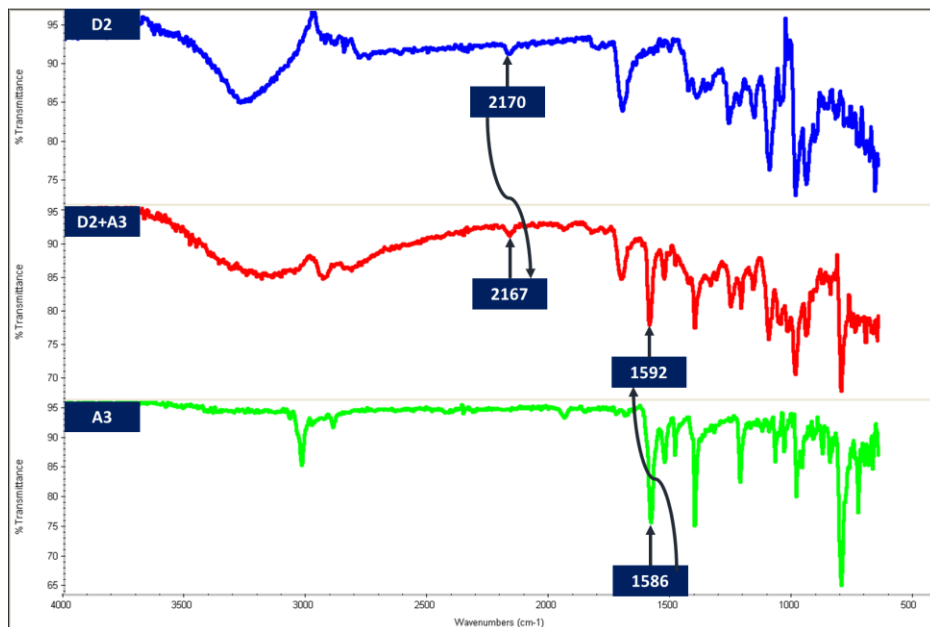


Figure 3.18 IR comparison of **D2**, **A3** and **D2: A3** ground mixture

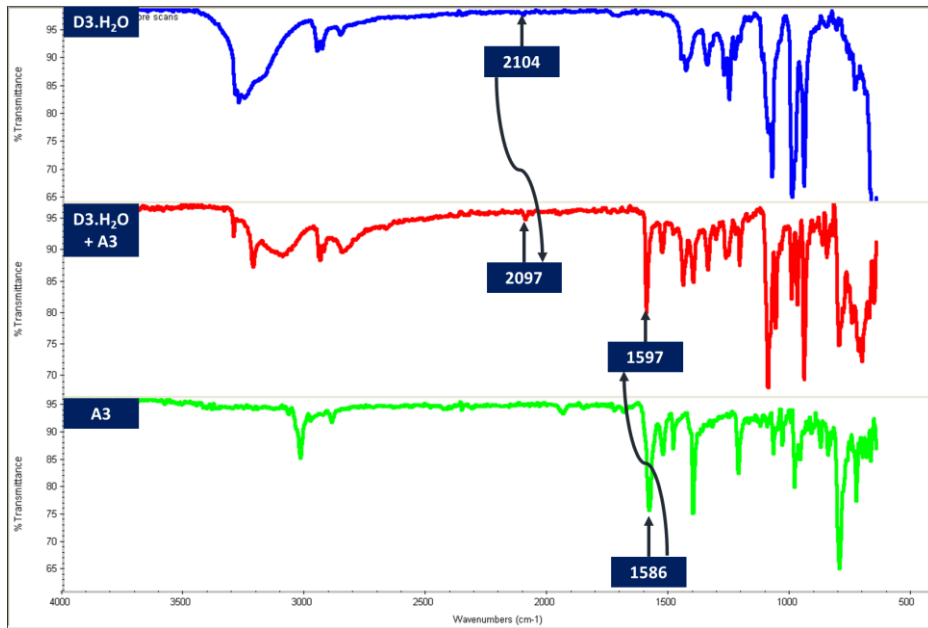


Figure 3.19 IR comparison of **D1.H₂O**, **A3** and **D1.H₂O: A3** ground mixture

3.3.5 Single X-ray structures of co-crystals

Out of sixteen positive outcomes, six co-crystals gave sample of X-ray quality and we were able to determine the structures by single crystals X-ray diffraction. All the XB and HB geometries are listed in Table 3.3 and Table 3.4 and the crystallographic data is provided in the appendix B.

Table 3.3 HB distances and angles in the structures of six co-crystals.

Compound	D-H…A	D…A (Å)	<(DHA) (°)
D1:A3	O(7)-H(7)…O(11)	2.758(5)	159(9)
	O(11)-H(11)…N(32)	2.809(5)	161(7)
	O(21)-H(21)…N(44)	2.786(6)	163(7)
	O(25)-H(25)…O(21)	2.717(5)	171.5*
D1:A4	O(7)-H(7)…N(20)	2.726(7)	172(3)
	O(11)-H(11)…O(7)	2.831(12)	169.(3)
D1:A5	O(11)-H(11)…N(51A)	2.726(7)	172.9*
	O(11)-H(11)…N(51B)	2.831(12)	174.7*
	O(14)-H(14)…O(11)	2.740(3)	168.7*
D2:A3	O(1)-H(1O)…N(1)	2.810(7)	165(9)
	O(11)-H(2O)…N(2)	2.791(7)	174(7)
D3:A3	O(1)-H(1O)…N(2)	2.7777(18)	170.5(19)
	O(2)-H(2O)…N(1)	2.8241(19)	170(2)
	C(10)-H(10)…O(1)	3.303(3)	173(2)
D3:A5	O(13)-H(13)…N(4)	2.7314(16)	171(2)
	C(12)-H(12)…O(13)	3.235(2)	160.7*

(* Some of the hydrogen atoms involved in hydrogen-bonding could not be located based on the difference electron density. Hence, they were placed in geometrically calculated positions and refined using a riding model)

Table 3.4 XB distances and angles in the structures of four co-crystals

Compound	D-X…A	X…A (Å)	<(DXA) (°)
D1:A3	C(9)-I(10)…N(50)	2.826(5)	178.30(19)
	C(13)-I(14)…O(25)	2.938(4)	175.19(19)
	C(23)-I(24)…O(7)	2.951(4)	173.60(19)
	C(27)-I(28)…N(38)	2.782(4)	178.97(19)
D1:A4	C(9)-I(10)…O(11)	2.9273(17)	174.73(8)
	C(13)-I(14)…N(26)	2.768(2)	177.81(9)
D1:A5	C(32)-I(2)…N(41B)	2.755(8)	173.2(5)
	C(32)-I(2)…N(41A)	2.761(4)	179.9(2)
	C(22)-I(1)…O(14)	2.901(2)	175.12(9)
D2:A3	C(1)-I(1)…O(2)	2.978(4)	154.6(2)
	C(10)-I(2)…O(1)	2.955(4)	159.0(2)

D1 and **A3** crystallize in a 1:1 stoichiometry and there are two XB interactions between I…N (a 20% combined vdW reduction) and between I…O (a 16% vdW reduction). These interactions are mirrored by two hydrogen bonds, O(H)…N and O(H)…O, respectively. They occupy the same type of acceptor sites that were used in the XB interactions (Figure 3.20).

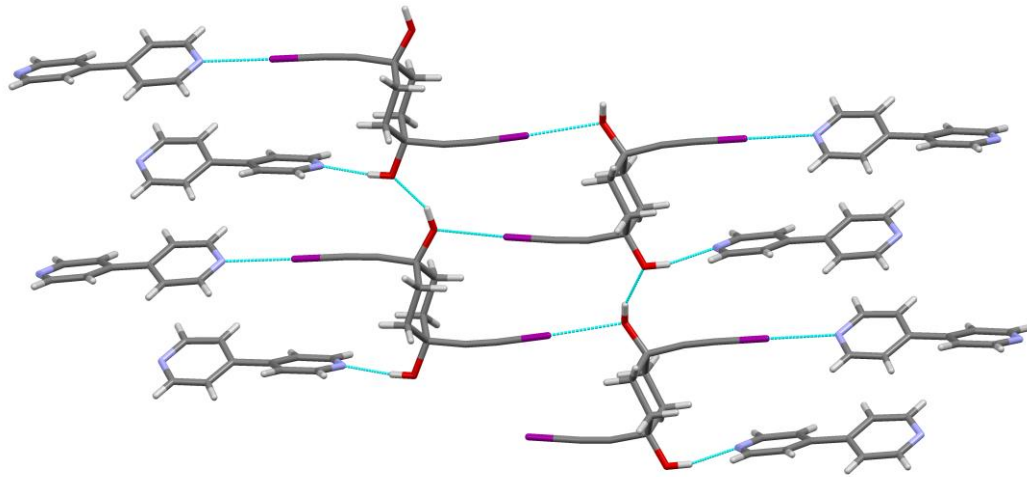


Figure 3.20 Major HBs and XB_s in the crystal structure of **D1:A3** (color codes: red-oxygen; violet-iodine; blue-nitrogen).

In the crystal structure of **D1:A4**, the same set of intermolecular interactions can be seen as were found in **D1:A3**. One XB between I···N (with a 22% vdW reduction) and one XB interaction between I···O (with a 16% vdW reduction) can be observed. Again, these two XB_s are mirrored by two HBs, O(H)···N and O(H)···O (Figure 3.21).

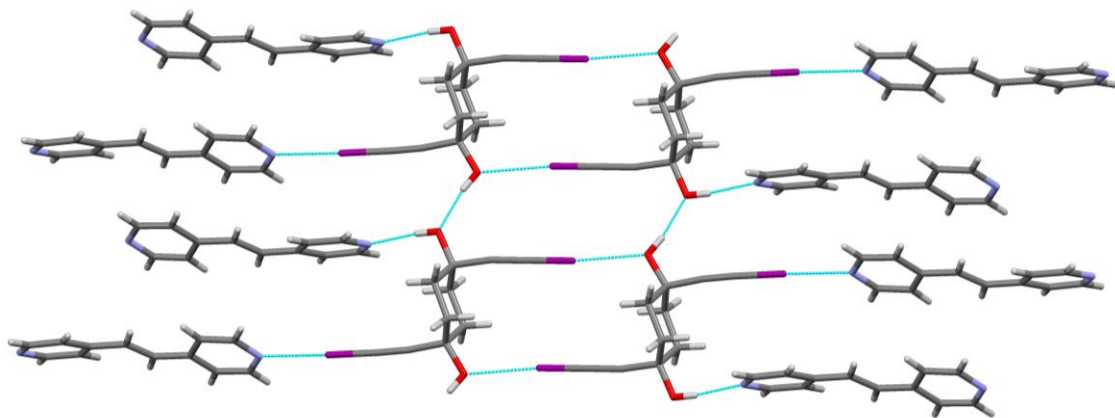


Figure 3.21 Major HBs and XB_s in the crystal structure of **D1:A4** (color codes: red-oxygen; violet-iodine; blue-nitrogen).

The crystal structure of **D1:A5** shows the same combination of two XB interactions (with a 22% and a 17% reduction in the combined vdW radii for I···N and I···O, respectively) and two structurally similar HB interactions between O(H)···N and O(H)···O (Figure 3.22).

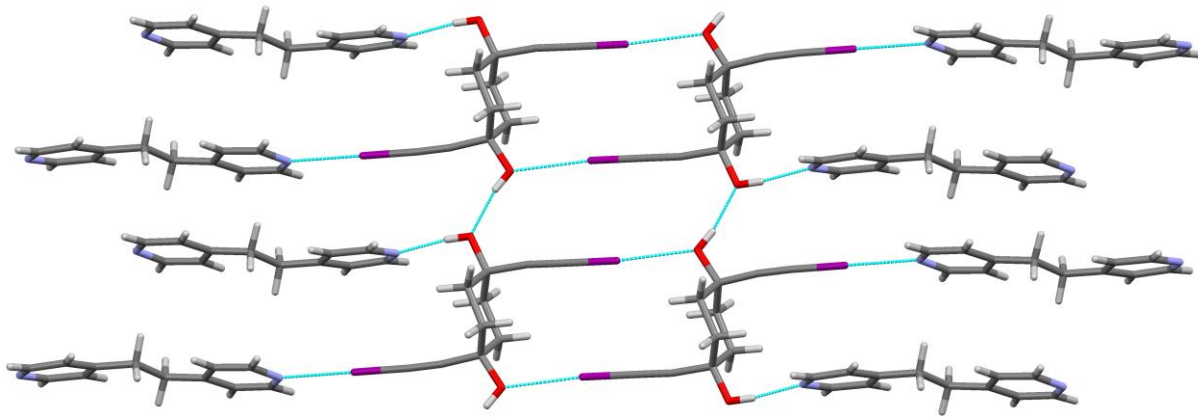


Figure 3.22 Main HBs and XBs in the crystal structure of **D1:A5** (color codes: red-oxygen; violet-iodine; blue-nitrogen).

When acceptor **A3** is combined with **D2** (a geometrical isomer of **D1**), different set of interactions are observed between **D2** and **A3**. Only two O(H) \cdots N hydrogen bond interactions are involved in the heteromeric co-crystallization. The remaining two C \equiv C-I moieties form XBs to the hydroxylic oxygen atoms (with a 15% vdW reduction) (Figure 3.23).

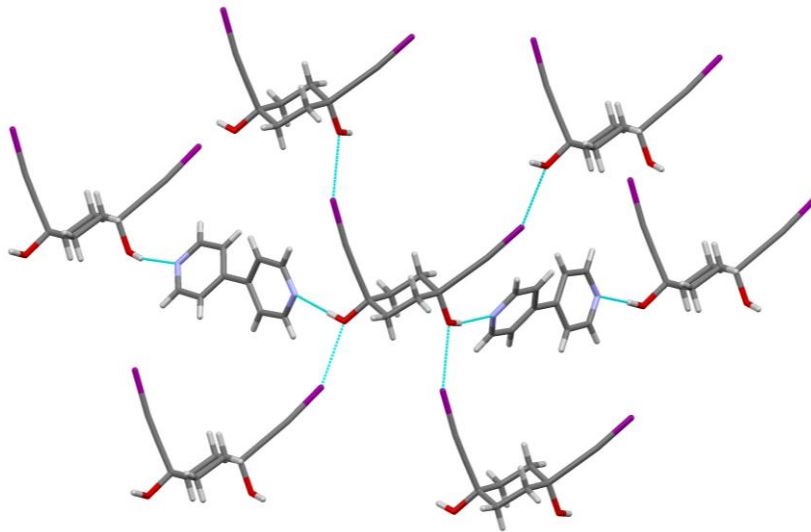


Figure 3.23 Major HBs and XBs in the crystal structure of **D2:A3** (color codes: red-oxygen; violet-iodine; blue-nitrogen).

When the C \equiv C-I moieties are replaced with C \equiv C-H groups in **D3**, the co-crystal is formed as a result of O-H \cdots N hydrogen-bonds. In the crystal structure of **D3:A3**, the ethynyl group forms

C-H \cdots O hydrogen bonds which drive the co-crystal formation. In addition, C≡C-H \cdots O hydrogen-bonds can be seen between hydroxylic oxygen atoms and ethynyl protons of **D3** (Figure 3.24).

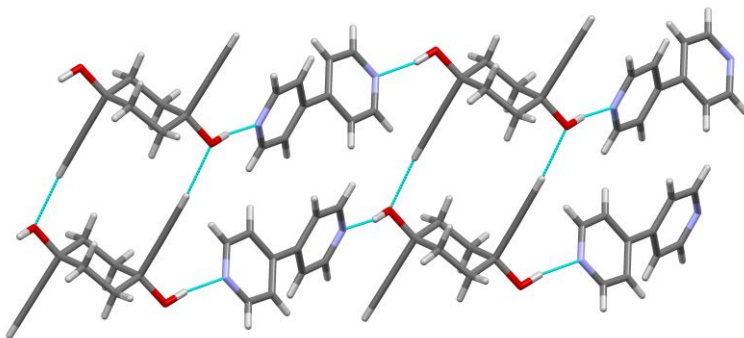


Figure 3.24 Major HBs in the crystal structure of **D3:A3** (color codes: red-oxygen; blue-nitrogen).

In the crystal structure of **D3:A5**, O-H \cdots N hydrogen bonds are responsible for the co-crystal formation, and this time both ethynyl group form hydrogen bonds with hydroxylic oxygen atoms (Figure 3.25).

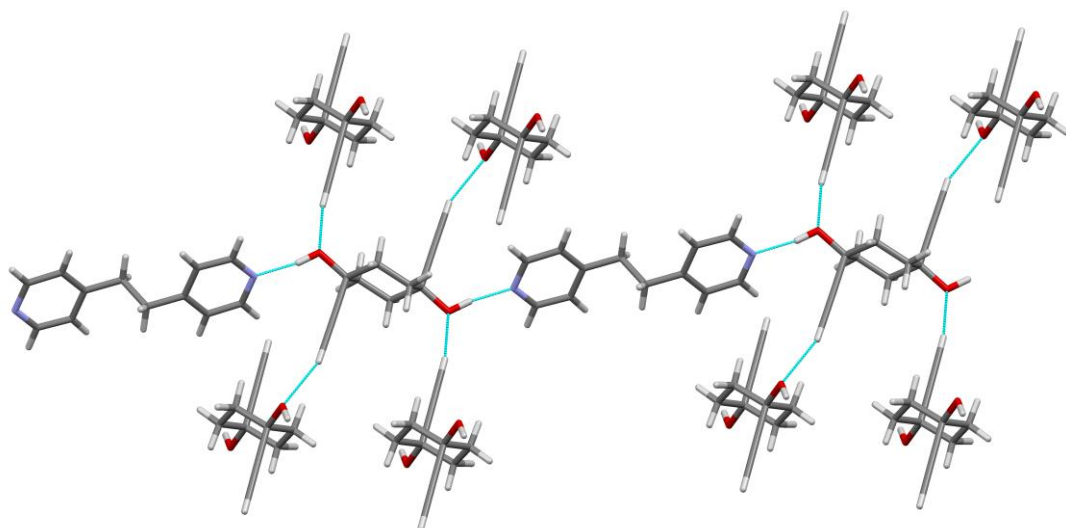


Figure 3.25 Major HBs in the crystal structure of **D3:A5** (color codes: red-oxygen; blue-nitrogen).

3.4 Discussion

3.4.1 Analysis of X-ray structures of donors

Due to the inclusion of water molecules in the structure of **D1**, it is possible for C-I \cdots O(hydroxyl) halogen bonds and O-H \cdots O(water) hydrogen bonds to occur side by side. In the absence of water molecules in **D2** causes a shortage of oxygen acceptor sites. Therefore, a competition arises between O-H and C-I and finally leads to O-H \cdots O hydrogen bonds. The C-I groups have to fulfil the requirement of acceptor by forming XB to triple bond³⁶ and type II halogen bonds³⁷ to the electron-rich equatorial region of a neighboring iodine atom (Figure 3.26).

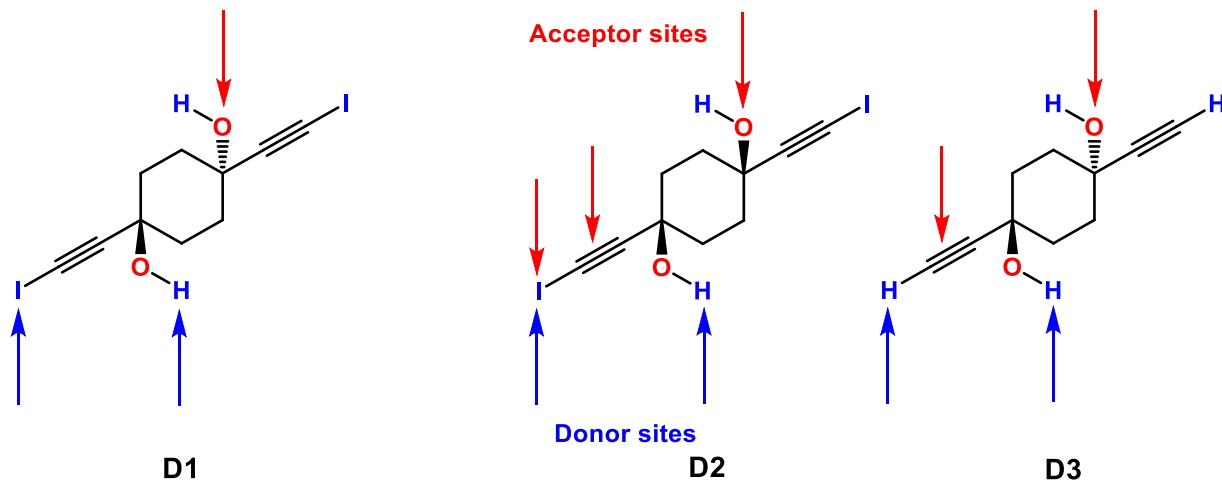


Figure 3.26 HB/ XB donor and acceptor sites observed in single crystals of **D1**, **D2** and **D3**

In the absence of strong XB donors in **D3.H₂O**, hydroxyl oxygen interacts only with water molecules. In addition, the ethynyl hydrogen atoms of **D3.H₂O** form hydrogen bonds through a side-ways interaction with an electron rich area of triple bond³⁸ in an adjacent molecule of **D3** similar to the behavior of iodine in **D2** (Figure 3.26).

3.4.2 IR spectroscopy analysis of co-crystals

In order to screen the formation of co-crystals, IR spectroscopy can be used as an effective and sensitive method.³⁹ Significant peak shifts of both donors and acceptors indicate successful

co-crystal formation. It is known that a red shift of IR frequency in the D-H/ D-X bonds are observed in a typical HB or XB formation respectively.⁴⁰ Small blue-shifts of a characteristic peak of the pyridyl moiety is observed when the pyridyl nitrogen act as the HB/XB acceptor.³⁵ One of the most sensitive IR peaks of donors **D1-D3** is the peak corresponding to the triple bond due to direct influence of the halogen/ hydrogen bond formation.⁴¹ This peak may show a red shift in a formation HB or XB between a donor attached to triple bond and an acceptor. In all the co-crystals that are structurally characterized in this study, a red shift of the triple bond of the XB donor (C≡C-I) and the HB donor (C≡C-H) due to the bond elongation was observed (Table 3.5).

Table 3.5 IR frequency changes of selected peaks of HB/ XB donors when form co-crystals

Co-crystal/ compound	XB peak (-C≡C- stretch) cm ⁻¹	HB peak (-C≡C- stretch) cm ⁻¹	Change of IR frequency cm ⁻¹	Shift
D1.H₂O	2158	-	-	-
D1:A3	2153	-	-5	Red
D1:A4	2156	-	-2	Red
D1:A5	2157	-	-1	Red
D2	2170	-	-	-
D2:A3	2167	-	-3	Red
D3.H₂O	2104	-	-	-
D3:A3	2097	-	-7	Red
D3:A5	2096	-	-8	Red

In addition, an enhanced intensity of the ethynyl peak was also observed with the formation of HB interactions in **D3:A3** and **D3:A5** (Figure 3.27). This phenomenon is common for typical HB interaction formations.⁴⁰

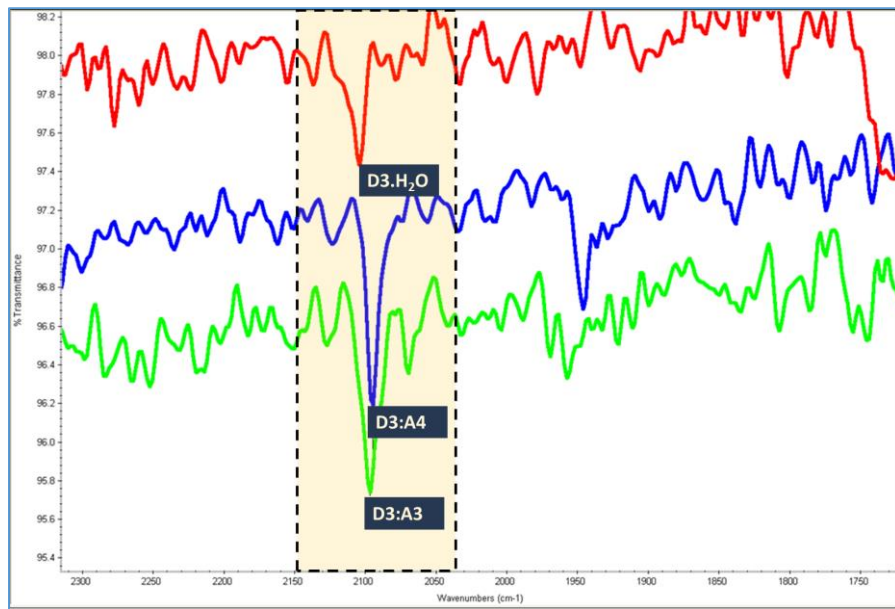


Figure 3.27 Comparison of ethynyl IR spectroscopy peak (-C≡C-) of **D3.H₂O**, **D3:A3**, **D3:A5**

3.4.3 MEPs analysis

Even though halogen-bond donor and hydrogen-bond donor of **D1** have different MEP values, based on the co-crystal formed between **D1** and acceptors, they are equally capable of competing for the acceptor sites. The XB donor (iodine atom) acts in a structurally similar way to the HB donor (hydrogen atom) demonstrating the competitiveness between the two and showing the difficulty in predicting the outcome purely based on MEP of individual donors.⁴² A previous study has shown that if the Q value ($Q = \text{HB electrostatic potential} - \text{XB electrostatic potential}$) is less than about 140 kJ/mol then the HB and XB donors tend to be competitive with each other.²⁶ The difference in MEP values of two donors is 37 kJ/mol in **D1** which is in agreement with earlier studies and supports the MEP argument for competitive nature of two donors.

Slightly different MEPs for hydrogen bond donors (axial OH; 224 kJ/mol, equatorial OH; 215 kJ/mol) of **D2** are due to the different setting of the hydroxyl groups in **D2** compared to **D1** (equatorial:equatorial in **D1** vs axial:equatorial in **D2**) (Figure 3.9 (a) and Figure 3.10 (b)). This

makes one hydroxyl group a slightly better HB donor than the other. Intermolecular HB bond distances in **D3:A3** ($r(\text{O axial}\cdots\text{N})$ 2.791(7) Å and $r(\text{O equatorial}\cdots\text{N})$ 2.810(7) Å) display only very minor differences that makes the slight difference of MEPs of the two O-H hydrogen bond donors unimportant (Figure 3.28). Even though the two iodine atoms in **D2** are in different geometric orientation (axial and equatorial) they show similar MEPs (187 kJ/mol).

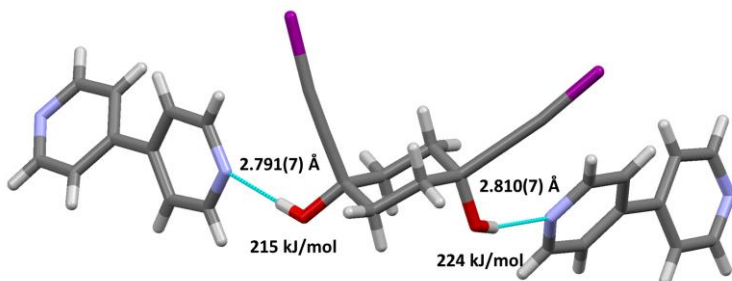


Figure 3.28 HB bond distances and MEP values of **D2:A3**

In the case of **D2:A3**, the Q values of the two pairs of XB and HB donors on **D2** are 37 kJ/mol and 28 kJ/mol, respectively which are also much lower than 140 kJ/mol. Hydrogen-bond donors dominate over the C-I donors which show that MEPs cannot be solely used for predicting the outcome.

3.4.4 Structural analysis of co-crystals

The competitive nature of XB and HB donors is illustrated in the three co-crystals of **D1**, (with **A3**, **A4**, and **A5**) since each donor is interacting with two nitrogen acceptor sites and two oxygen acceptors (Figure 3.29). **D2:A3** (**D2** has the cis-configuration of donor sites), the HB donor initiates the co-crystal synthesis by forming an O-H \cdots N hydrogen bond with **A3**. This leaves the C-I halogen-bond donors to interact with the only remaining acceptors, the hydroxylic oxygen atoms. This clearly indicates that relatively subtle changes in molecular geometry can change the balance in favor of one donor over another (Figure 3.29). Additionally, the polarity of the solvent

present in the crystallization can also play a role in shifting the balance between HB and XB interactions towards a particular acceptor in a competitive situation.²¹

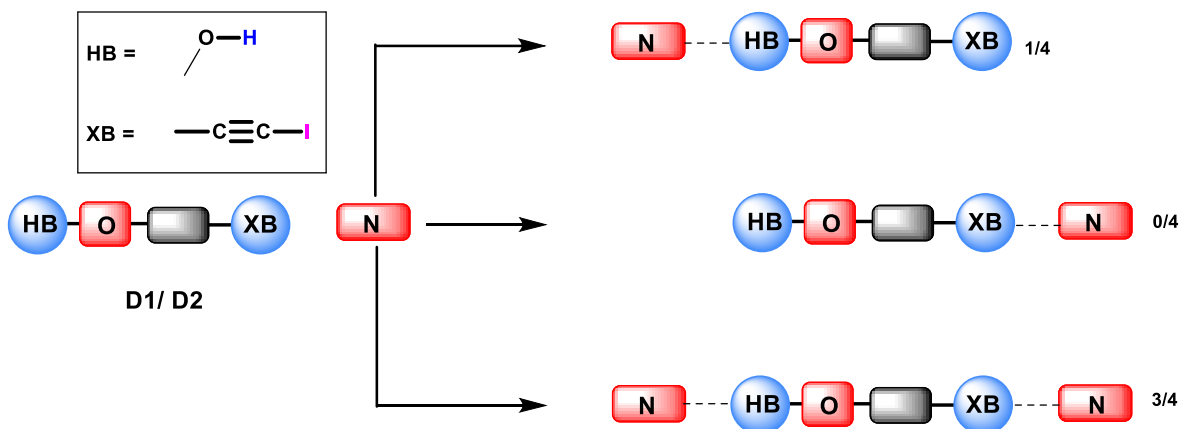


Figure 3.29 Outcome of interactions between HB/ XB donors and nitrogen-based acceptors

Due to the existence of moderate⁴³ to weak⁴⁴ $\pi \cdots \pi$ interactions ($r(\pi \cdots \pi)$ 3.83 Å and 3.94 Å) between rings of **A3** in the packing of **D1:A3**, the packing of **D1:A3** is different compared to packing of **D1:A4** and **D1:A5** (Figure 3.30). In **D1:A3**, the pyridyl rings are stacked on top of each other and thus it facilitates the formation of $\pi \cdots \pi$ interactions. In **D1:A4** and **D1:A5**, such arrangement is not possible due to the bridging groups between aromatic rings of **A4** and **A5** sit on top of the aromatic groups of **A4** and **A5** (Figure 3.21 and Figure 3.22). Since the structure directing hydrogen- and halogen bonds are present in the crystal arrangement, weak $\pi \cdots \pi$ interactions cannot overturn strong intermolecular interactions by bringing aromatic rings on top of each other.

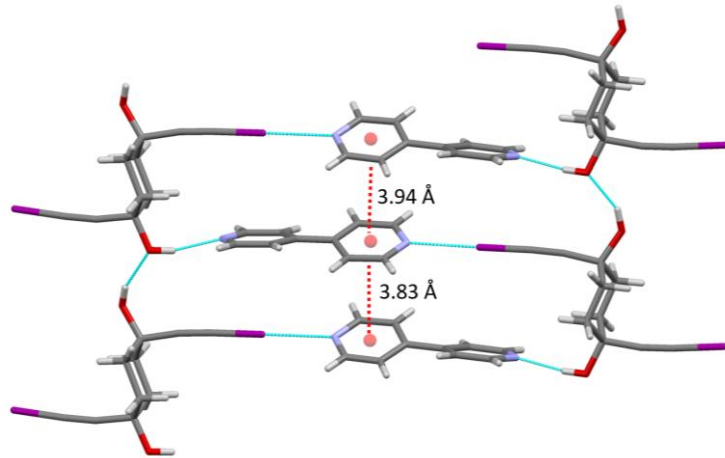


Figure 3.30 Moderate to weak $\pi \cdots \pi$ interactions in the crystal structure of **D1:A3**

The ethynyl hydrogen atom has the ability to make hydrogen bonds with nitrogen based or oxygen based acceptors in co-crystals.⁴⁵⁻⁴⁷ However, ethynyl donors in **D3** are unable to compete successfully with the hydroxyl hydrogen (Figure 3.31) due to the weaker donor ability of ethynyl hydrogen compared to ethynyl iodine. HB bond formation only one HB donor (HB1) and nitrogen acceptor was observed in **D3** (2 out of 2), although both donors (HB1 and XB) of **D1** interacted with nitrogen acceptor (3 out of 3) in all co-crystal formations between **D1** and acceptors (Figure 3.31).

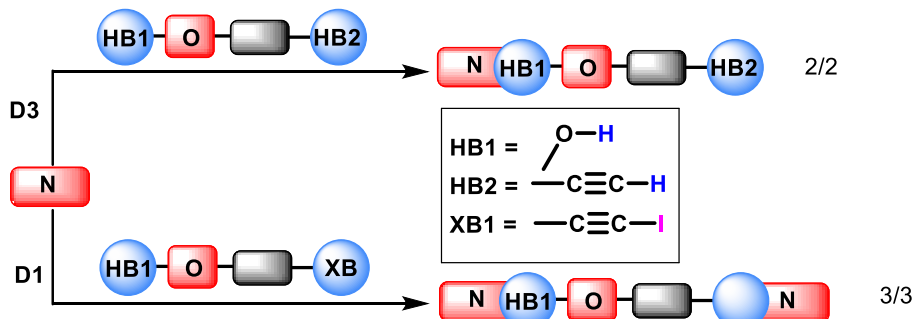


Figure 3.31 Competition of halogen bonding with hydrogen bonding in the presence of the same acceptor (*trans*-isomers: **D1** and **D3**)

3.4.5 Analysis of HB and XB geometries

Higher vdW reduction in XB bonding is noted when the acceptor is nitrogen instead of oxygen (average vdW radii reduction is 21% for I···N, average vdW reduction is 16% for I···O) in all co-crystals. All the XB distances and angles between nitrogen in aromatic ring and iodoethynyl functionality are in the range of values found among relevant structures in the Cambridge Structural Database (CSD) (Figure 3.32 and 3.34)⁴⁸.

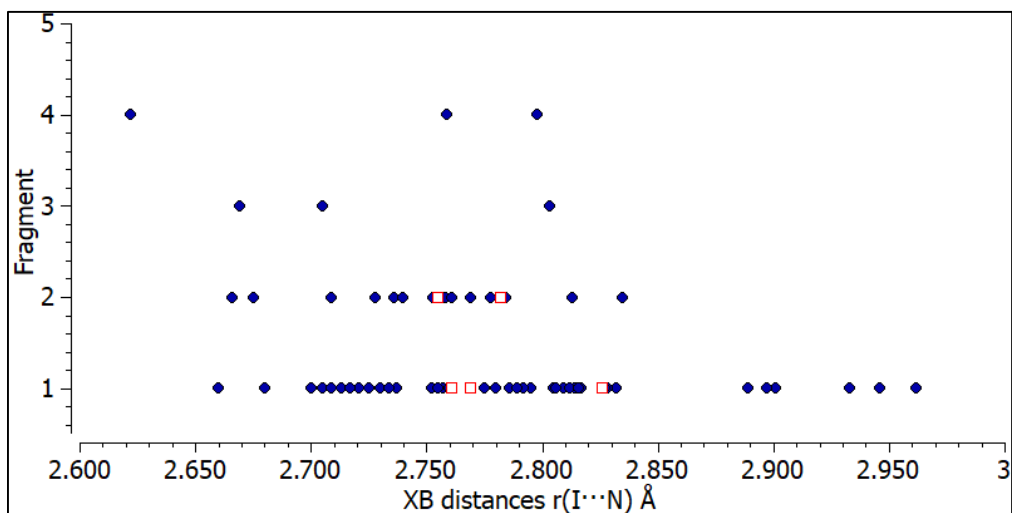


Figure 3.32 XB distances between ethynyl iodine and aromatic nitrogen: reported in CSD (blue circles) and observed in this study (red hollow squares)

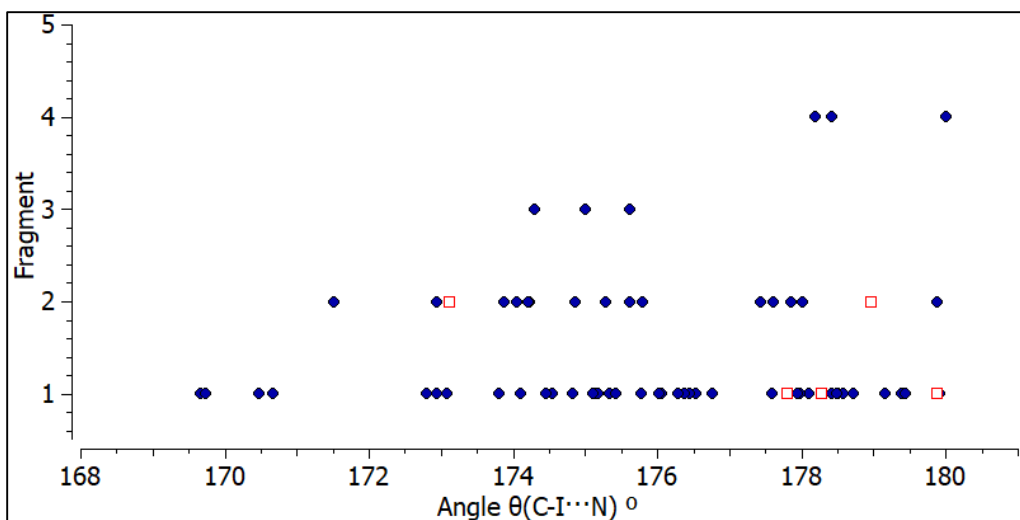


Figure 3.33. XB angles $\theta(\text{C-I}\cdots\text{N})$: reported in CSD (blue circles) and observed in this study (red hollow squares)

Halogen-bonds between ethynyl iodine and hydroxyl oxygen atom are reported only once in the literature⁴⁹ $r(\text{I}\cdots\text{O})$ ca.2.98 Å, $\theta(\text{C-I}\cdots\text{O})$ ca.178.5° and which is more linear than the most linear angle ($\theta(\text{C-I}\cdots\text{O})$ ca.175.2°) found in a co-crystal (**D1:A3**) of this study. In addition, halogen bonds are observed as more linear when nitrogen acceptors are involved (average $\theta(\text{C-I}\cdots\text{N})$ ca.178°), compared to when oxygen atoms act as acceptor sites (average $\theta(\text{C-I}\cdots\text{O})$ ca.169°).

3.5 Conclusions⁵⁰

Three tetra-functionalized HB/ XB donor molecules were synthesized and eighteen attempted co-crystallization experiments were performed. The single crystals of **D1-D3** show the desire of donors to find suitable acceptors in the crystal lattice by adopting water molecules (**D1.H₂O** and **D3.H₂O**) or finding acceptor sites itself (**D2**).

In **D1**, both HB and XB donors behave structurally similar way when making interactions with a common acceptor. This clearly demonstrates the similar directionality and strength of both interactions that have shared dependence upon molecular electrostatic potentials.

Based on the results, it can be concluded that the ability of R-O-H hydrogen-bond donors and R-C≡C-I halogen bond donors to involved in structure-directing interactions is very finely

balanced. Both hydroxylic groups and the iodo-ethynyl groups are equally capable of competing for nitrogen-based or oxygen-based acceptor sites.

The geometric isomers, trans-1,4-bis(iodoethynyl)cyclohexane-1,4-diol, **D1**, and cis-1,4-bis(iodoethynyl)cyclohexane-1,4-diol, **D2**, are different in the competing environment. This indicates that the balance between hydrogen- and halogen bonds can be altered by very small changes in molecular geometry (Figure 3.34).

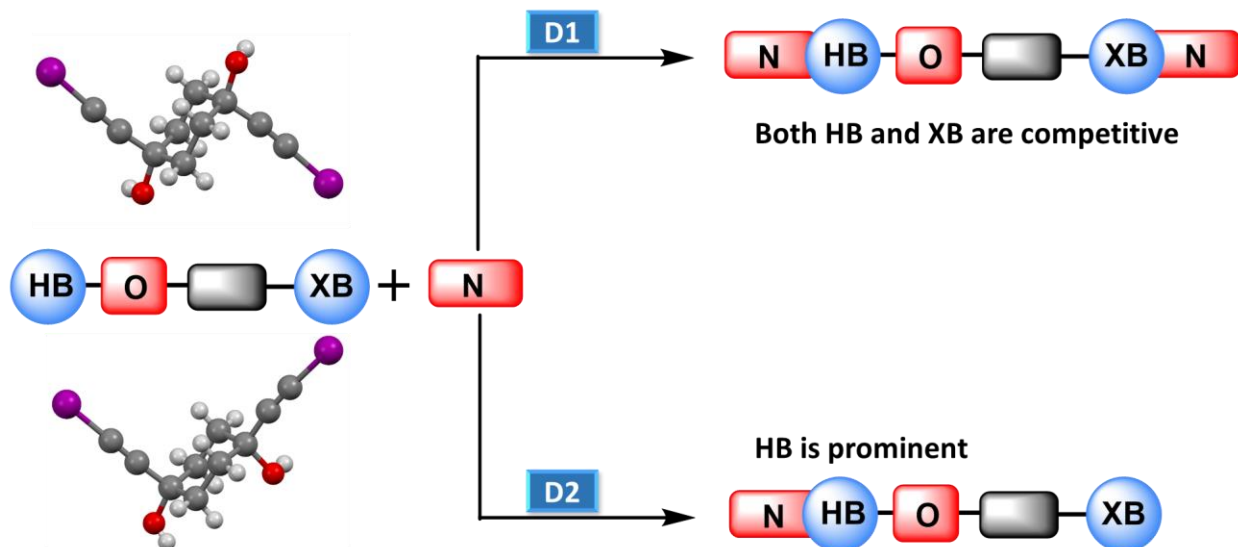


Figure 3.34 Outcome of co-crystallization experiments between **D1-D2** and nitrogen based acceptors

In the control molecule, *trans*-1,4-diethynylcyclohexane-1,4-diol, **D3**, the hydroxylic HB donor is stronger due to its significantly larger positive electrostatic potential on the proton when compared to weak HB donor, R-C≡C-H. The electrostatic potential analysis of XB and HB donors aid to rationalize the co-crystallization outcomes.

The outcome of a supramolecular synthesis experiment cannot be solely determined by MEPs when it comes to different geometrical positioning of donor atoms. However, the combination of MEPs study and the co-crystallization outcomes give valuable information that

can be used for the design and synthesis of multi-component solid-state architectures based on halogen- and hydrogen-bond interactions.

3.6 References

1. Rest, C.; Kandanelli, R.; Fernandez, G., *Chem. Soc. Rev.* **2015**, *44* (8), 2543-2572.
2. Webber, M. J.; Appel, E. A.; Meijer, E. W.; Langer, R., *Nat Mater* **2016**, *15* (1), 13-26.
3. Aakeröy, C. B.; Chopade, P. D.; Desper, J., *Cryst. Growth Des.* **2011**, *11* (12), 5333-5336.
4. Khavasi, H. R.; Tehrani, A. A., *CrystEngComm* **2013**, *15* (29), 5813-5820.
5. Adsmond, D. A.; Sinha, A. S.; Khandavilli, U. B. R.; Maguire, A. R.; Lawrence, S. E., *Cryst. Growth Des.* **2016**, *16* (1), 59-69.
6. Shirman, T.; Boterashvili, M.; Orbach, M.; Freeman, D.; Shimon, L. J. W.; Lahav, M.; van der Boom, M. E., *Cryst. Growth Des.* **2015**, *15* (10), 4756-4759.
7. Khavasi, H. R.; Ghanbarpour, A.; Tehrani, A. A., *CrystEngComm* **2014**, *16* (5), 749-752.
8. Gómez, P.; Más-Montoya, M.; da Silva, I.; Cerón-Carrasco, J. P.; Tárraga, A.; Curiel, D., *Cryst. Growth Des.* **2017**, *17* (6), 3371-3378.
9. Li, X.; Gao, Y.; Harniman, R.; Winnik, M.; Manners, I., *J. Am. Chem. Soc.* **2016**, *138* (39), 12902-12912.
10. Gao, Z.; Han, Y.; Chen, S.; Li, Z.; Tong, H.; Wang, F., *ACS Macro Letters* **2017**, *6* (5), 541-545.
11. Wang, H.; Bao, Z.; Wu, H.; Lin, R.-B.; Zhou, W.; Hu, T.-L.; Li, B.; Zhao, J. C.-G.; Chen, B., *Chem. Commun.* **2017**.
12. Liu, R.; Wang, H.; Jin, W. J., *Cryst. Growth Des.* **2017**, *17* (6), 3331-3337.
13. Gamekkanda, J.; Sinha, A.; Desper, J.; Daković, M.; Aakeröy, C., *Crystals* **2017**, *7* (7), 226.
14. Vanderkooy, A.; Taylor, M. S., *Faraday Discuss.* **2017**, *203* (0), 285-299.
15. Aakeröy, C. B.; Wijethunga, T. K.; Desper, J.; Đaković, M., *Cryst. Growth Des.* **2016**, *16* (5), 2662-2670.
16. Pfrunder, M. C.; Micallef, A. S.; Rintoul, L.; Arnold, D. P.; McMurtrie, J., *Cryst. Growth Des.* **2016**, *16* (2), 681-695.
17. Priimagi, A.; Cavallo, G.; Metrangolo, P.; Resnati, G., *Acc. Chem. Res.* **2013**, *46* (11), 2686-2695.
18. Perera, M. D.; Desper, J.; Sinha, A. S.; Aakeroy, C. B., *CrystEngComm* **2016**, *18* (44), 8631-8636.
19. Rowe, R. K.; Ho, P. S., *Acta Cryst. B* **2017**, *73* (2), 255-264.
20. Gunawardana, C. A.; Desper, J.; Sinha, A. S.; akovic, M.; Aakeroy, C. B., *Faraday Discuss.* **2017**.
21. Robertson, C. C.; Wright, J. S.; Carrington, E. J.; Perutz, R. N.; Hunter, C. A.; Brammer, L., *Chemical Science* **2017**, *8* (8), 5392-5398.
22. Oswald, I. D. H.; Motherwell, W. D. S.; Parsons, S., *Acta Cryst. B* **2005**, *61* (1), 46-57.
23. Walsh, R. B.; Padgett, C. W.; Metrangolo, P.; Resnati, G.; Hanks, T. W.; Pennington, W. T., *Cryst. Growth Des.* **2001**, *1* (2), 165-175.
24. Corradi, E.; Meille, S. V.; Messina, M. T.; Metrangolo, P.; Resnati, G., *Angew. Chem. Int. Ed.* **2000**, *39* (10), 1782-1786.
25. Aakeroy, C. B.; Welideniya, D.; Desper, J., *CrystEngComm* **2017**, *19* (1), 11-13.
26. Aakeroy, C. B.; Spartz, C. L.; Dembowski, S.; Dwyre, S.; Desper, J., *IUCrJ* **2015**, *2* (5), 498-510.
27. Montis, R.; Arca, M.; Aragoni, M. C.; Bauza, A.; Demartin, F.; Frontera, A.; Isaia, F.; Lippolis, V., *CrystEngComm* **2017**, *19* (30), 4401-4412.
28. Geboes, Y.; De Proft, F.; Herrebout, W. A., *Acta Cryst. B* **2017**, *73* (2), 168-178.
29. Ding, H.; Lu, Y.; Wu, W.; Liu, H., *Chem. Phys.* **2014**, *441* (Supplement C), 30-37.

30. Amico, V.; Meille, S. V.; Corradi, E.; Messina, M. T.; Resnati, G., *J. Am. Chem. Soc.* **1998**, *120* (32), 8261-8262.
31. Aakeroy, C. B.; Panikkattu, S.; Chopade, P. D.; Desper, J., *CrystEngComm* **2013**, *15* (16), 3125-3136.
32. Dumele, O.; Wu, D.; Trapp, N.; Goroff, N.; Diederich, F., *Org. Lett.* **2014**, *16* (18), 4722-4725.
33. Goud, N. R.; Bolton, O.; Burgess, E. C.; Matzger, A. J., *Cryst. Growth Des.* **2016**, *16* (3), 1765-1771.
34. Hosseinzadeh, R.; Abolfazli, M. K.; Mohseni, M.; Mohadjerani, M.; Lasemi, Z., *J. Heterocycl. Chem.* **2014**, *51* (5), 1298-1305.
35. González, L.; Gimeno, N.; Tejedor, R. M.; Polo, V.; Ros, M. B.; Uriel, S.; Serrano, J. L., *Chem. Mater.* **2013**, *25* (22), 4503-4510.
36. Mukherjee, A.; Tothadi, S.; Desiraju, G. R., *Acc. Chem. Res.* **2014**, *47* (8), 2514-2524.
37. Cavallo, G.; Metrangolo, P.; Milani, R.; Pilati, T.; Priimagi, A.; Resnati, G.; Terraneo, G., *Chem. Rev.* **2016**, *116* (4), 2478-2601.
38. Steiner, T., *J. Chem. Soc., Chem. Commun.* **1995**, (1), 95-96.
39. Joseph, J.; Jemmis, E. D., *J. Am. Chem. Soc.* **2007**, *129* (15), 4620-4632.
40. Wang, C.; Danovich, D.; Shaik, S.; Mo, Y., *J. Chem. Theory Comput.* **2017**, *13* (4), 1626-1637.
41. Aakeröy, C. B.; Baldrihi, M.; Desper, J.; Metrangolo, P.; Resnati, G., *Chem. Eur. J.* **2013**, *19* (48), 16240-16247.
42. Corpinot, M. K.; Stratford, S. A.; Arhangelskis, M.; Anka-Lufford, J.; Halasz, I.; Judas, N.; Jones, W.; Bucar, D.-K., *CrystEngComm* **2016**, *18* (29), 5434-5439.
43. Moradi, M.; Tulli, L. G.; Nowakowski, J.; Baljozovic, M.; Jung, T. A.; Shahgaldian, P., *Angew. Chem. Int. Ed.* **2017**, *56* (46), 14395-14399.
44. Avasthi, I.; Khanna, S.; Tripathi, S. K.; Verma, S., *CrystEngComm* **2017**, *19* (35), 5202-5213.
45. Bosch, E.; Bowling, N. P.; Darko, J., *Cryst. Growth Des.* **2015**, *15* (4), 1634-1641.
46. Bosch, E., *Acta Cryst. C* **2016**, *72* (10), 748-752.
47. Bosch, E., *Cryst. Growth Des.* **2010**, *10* (8), 3808-3813.
48. Groom, C. R.; Bruno, I. J.; Lightfoot, M. P.; Ward, S. C., *Acta Cryst. B* **2016**, *72* (2), 171-179.
49. Moss, D. K.; Spence, J. D.; Nantz, M. H., *J. Org. Chem.* **1999**, *64* (12), 4339-4343.
50. Gamekkanda, J. C.; Sinha, A. S.; Desper, J.; Dakovic, M.; Aakeroy, C. B., *New J. Chem.* **2018**, *42* (13), 10539-10547.

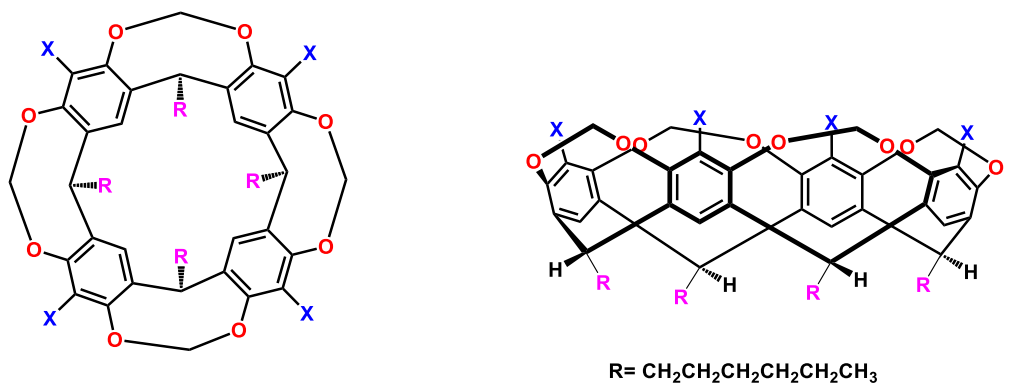
Chapter 4 Functionalization of cavitands

4.1 Introduction

Molecular recognition can be described as the process by which two or more molecules bind together in a specific geometry¹ via non-covalent interactions.² Specially, this event can be used for selective separation,³⁻⁶ and selective identification of component/s in multicomponent mixtures.⁷⁻⁸ The shape,⁹⁻¹⁰ and functional groups¹¹ of the receptors are responsible for their molecular recognition ability. One of most studied examples for such receptor is the resorcin[4]arene based cavitand which has a cavity that accommodates guest molecules.¹²

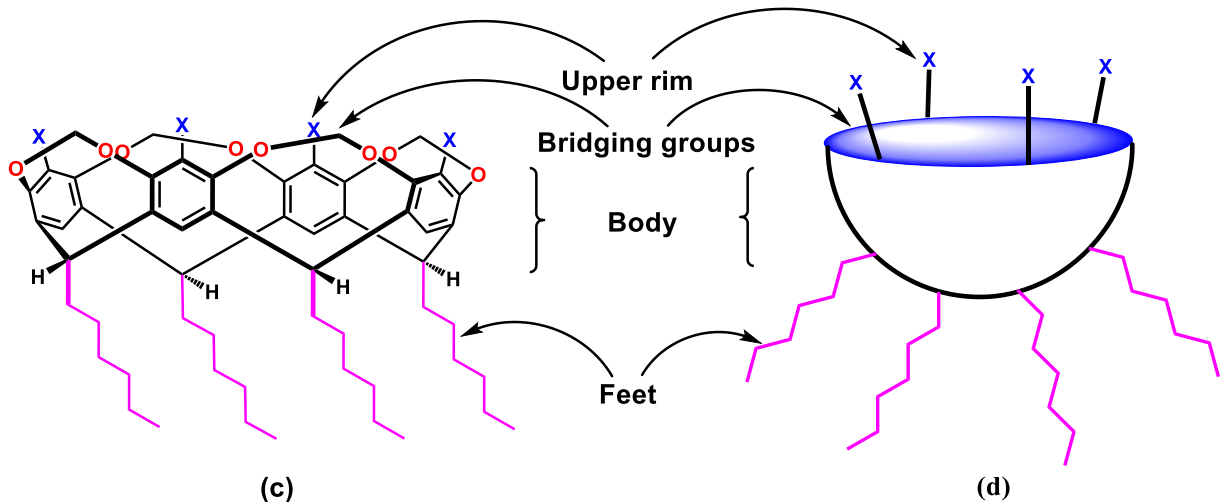
Cavitands are bowl shaped molecules which “contain enforced cavities large enough to accommodate simple molecules or ions”¹³ derived from resorcinarene.¹⁴ Cavitands were first synthesized by Cram in 1982.¹³ These molecules can be further functionalized in order to obtain molecular baskets,¹⁵⁻¹⁶ carcerands,¹⁷⁻¹⁸ self-assembled capsules,¹⁹⁻²¹ and nanotubes.²²⁻²³ Interest in cavitand based molecular receptors has increased due to their applications in host–guest chemistry,²⁴ separations,³ catalysis,²⁵ and coordination chemistry.²⁶⁻²⁷

The main components of a cavitand include bridging groups, upper rim, body and feet (Figure 4.1). The functional group attachments and modifications can be done on the upper rim in order to obtain cavitands which are selective towards particular guests. The bridging groups are the methylene groups that connect the adjacent aromatic rings. They are responsible for limiting the flexibility of the cavity, hence avoiding other possible conformations of the host. The middle part of the molecule, the body, can capture electron deficient guest molecules since it is made up of four phenyl rings which provide a π -electron rich interior. Finally, the aliphatic chains at the bottom are called feet and they can be altered in order to change solubility of the molecule.



(a)

(b)



(c)

(d)

Figure 4.1 Cavitand scaffold (a) top view, (b) side view, (c) main parts of the cavitand, (d) schematic representation of cavitand

The cavitand without the upper rim functionalization can hold particular guest/s inside the cavity only, but with the upper rim functionalization, four additional guest molecules can be bound per host molecule. On the other hand, by making the upper rim selective to a particular guest, the host can be used to selectively recognize/ bind a single guest in a multicomponent mixture. The functionalization can be done in order to achieve reversible recognition event via non-covalent interactions such as hydrogen bonding, halogen bonding and/ or metal-ligand coordination.

4.1.1 Upper rim functionalization

In order to get specific selectivity towards a guest molecule, the upper rim of the cavitand can be functionalized with appropriate supramolecular synthons. Furthermore, with complementary functionalities, cavitand based capsules can also be engineered.

4.1.1.1 Metal coordinating cavitands

Resorcin[4]arene based cavitands with different ligands can complex with soft and hard metal ions. In a cavitand, four ligands can be introduced at once and can be used as pre organized multidentate ligands due to the fixed geometry of the cavitand. Acetylacetone²⁸⁻²⁹, pyridyl²⁶ and carboxylic acid³⁰ functionalities are a few popular functionalities for the cavitand based metal-ligand complexes (Figure 4.2).

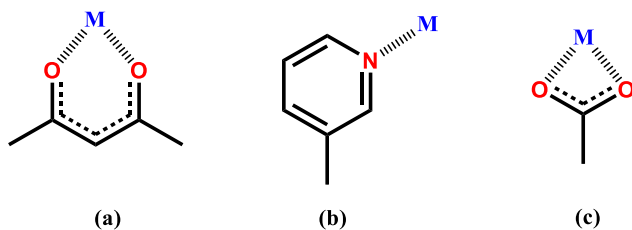


Figure 4.2 Examples for metal ligand coordination by (a) acetylacetone, (b) pyridil group and (c) carboxylate group

4.1.1.2 Hydrogen bonded cavitands

There are several examples of cavitands decorated with hydrogen-bond donors or acceptors which make capsules and supramolecular polymers. Hydrogen bond donors such as -OH, -COOH, -NH₂, -NH, -C(R)=NOH, -NHCOR and hydrogen bond acceptors such as -pyridyl, -pyrazole, and -C≡N functionalities are reported as O-H···O, O-H···N, N-H···N, N-H···O hydrogen bonding interactions (Figure 4.3).^{15, 19, 24-25, 31-32}

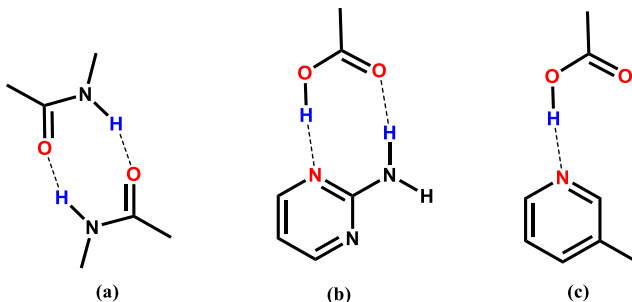


Figure 4.3 Examples for hydrogen bond interactions present on functionalized cavitands

4.1.1.3 Halogen bonded cavitands

The field of halogen bonding has recently witnessed a great deal of progress, thus cavitands with halogen-bond functionalities have also attracted attention in this arena. Cavitands functionalized by fluorinated iodine donors,^{12, 33} iodoethynyl donors³⁴⁻³⁶ have demonstrated ability to act as multivalent halogen bond donors towards acceptors and anions (Figure 4.4).

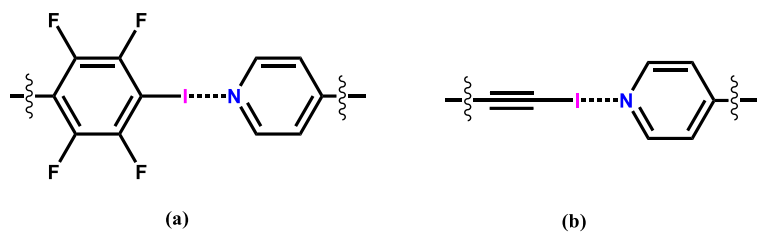


Figure 4.4 Examples for halogen bond interactions present on functionalized cavitands

4.1.1.4 Host-guest chemistry of cavitands

The cavitand has a concave cavity that can accommodate guest molecules selectively via non-covalent interactions such as π -interactions or hydrophobic interactions depending on the nature of the guest (e.g. cation can bind via cation- π interactions, anions by anion- π interactions) (Figure 4.5- path ‘A’). If the cavitand is functionalized by complementary supramolecular synthons, the formation of molecular capsules can be expected. However, host-guest binding on the rim of the cavitands is possible as well (Figure 4.5- path ‘B’).

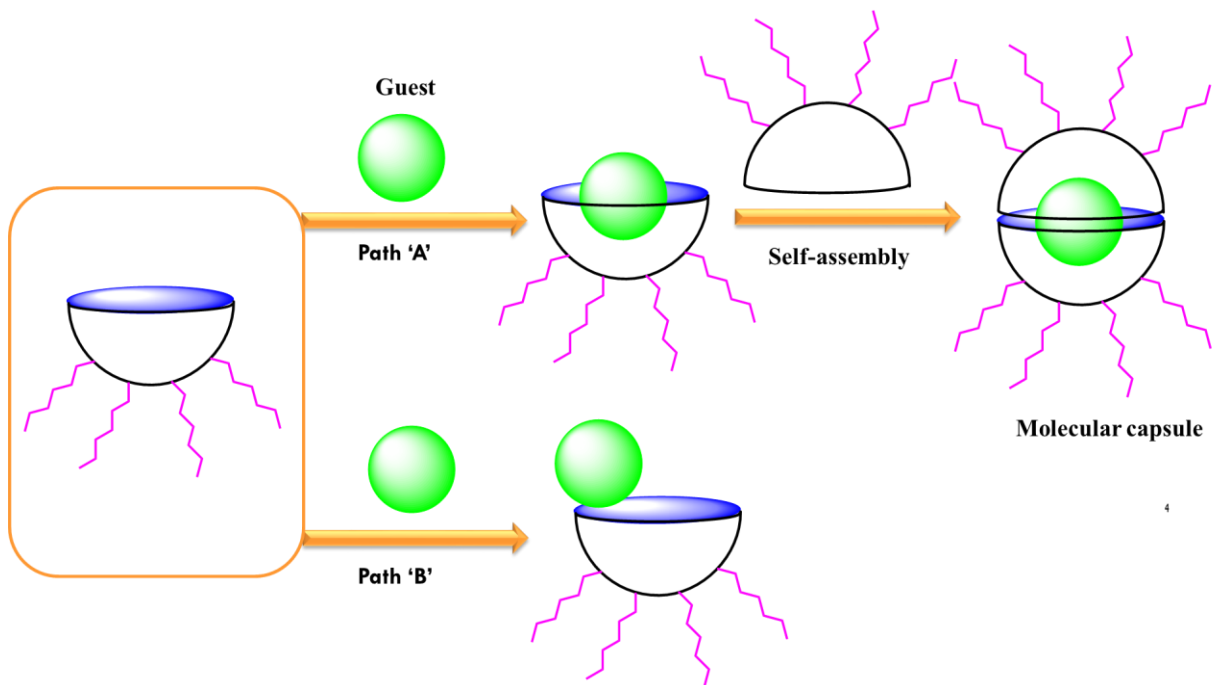


Figure 4.5 Host-guest chemistry involved in cavitands

The host-guest interactions can be qualitatively detected in solid state via FTIR spectroscopy due to the red-or blue-shift of corresponding peaks of both host and guest due to non-covalent interactions.³⁷ However, IR spectroscopy cannot be used to get binding stoichiometry of binding constants. Determination of binding stoichiometry can be achieved by analyzing crystal packing obtained by single X-ray diffraction in solid state. Quantification of binding constant and stoichiometry between host and guest in solution can be obtained via UV/Vis spectroscopic titrations, NMR titrations and ITC experiments.³⁸⁻³⁹

4.1.2 Objectives of the study

This study is divided into following areas.

1. Design and synthesis of resorcin[4]arene based bromo cavitand and rim functionalization with various functional groups such as metal coordinating groups (**L6, L7**), hydrogen bond donor groups and halogen bond donor groups (**D4, D5, D6**) (Figure 4.6).

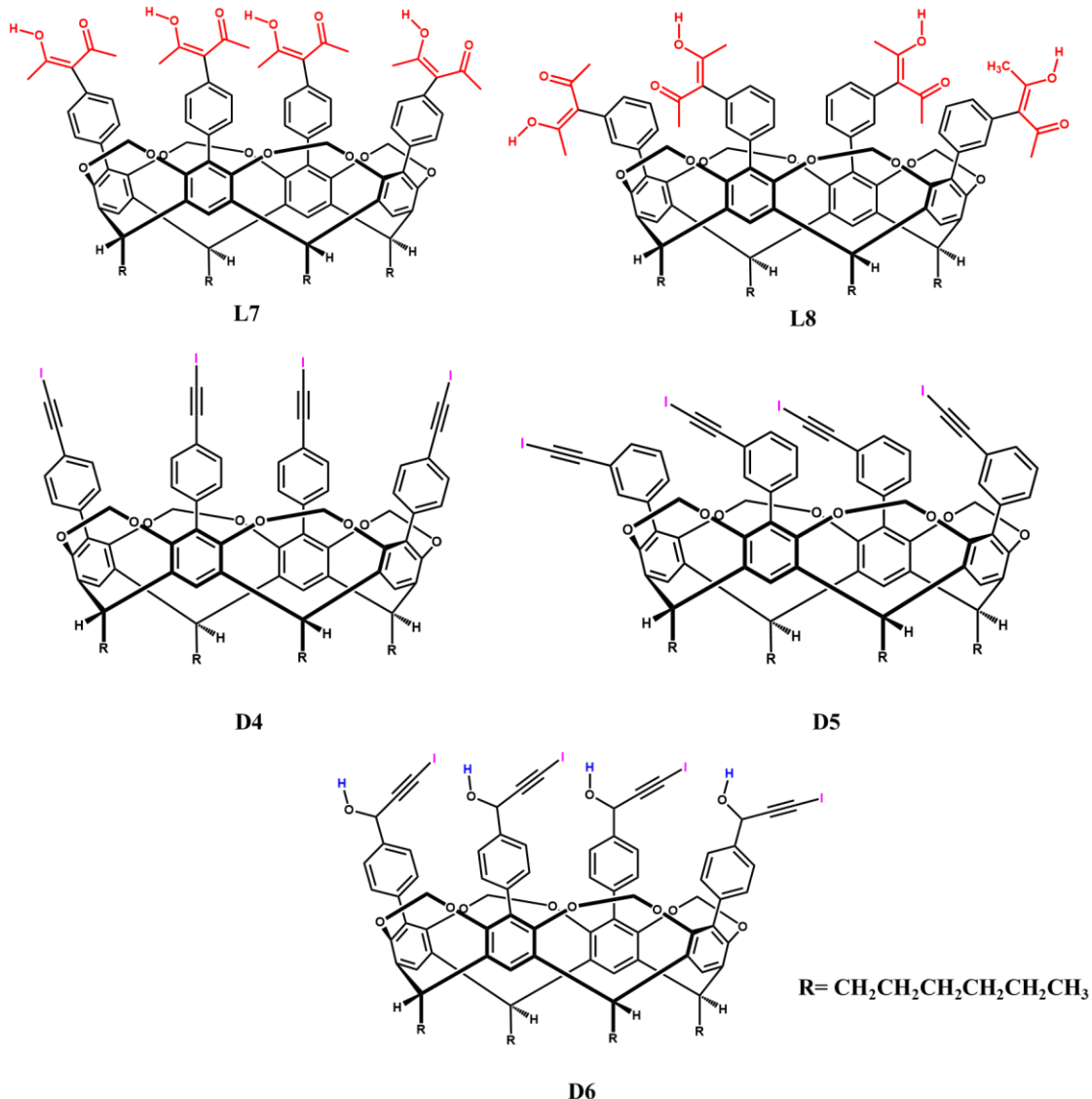


Figure 4.6 Functionalized cavitands, **L7, L8-** acac functionalized, **D4, D5-** ethynyliodine XB donor functionalized, **D6-** ethynyliodine XB donor and –OH HB donor functionalized

2. Study of the divalent metal ion binding (driven by metal-ligand coordination) ability of cavitands **L7** and **L8** in solid state and solution. Perform solution state binding studies by UV/Vis spectroscopy titration and use a Job plot to examine the structural behavior in solution.

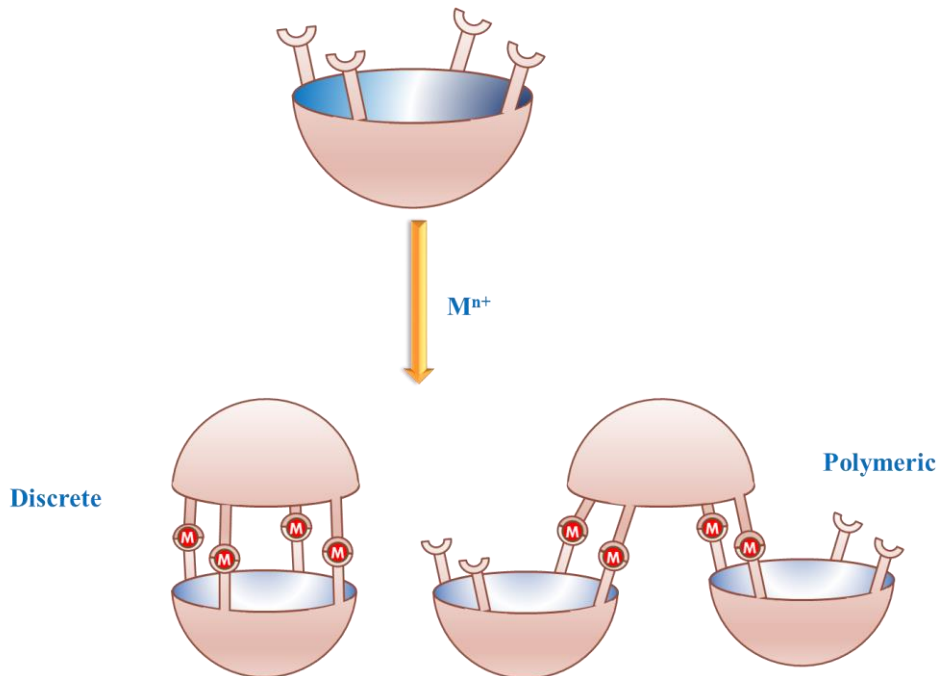


Figure 4.7 Anticipated discrete (capsule) or polymeric metallo-supramolecular architecture by **L7** in the presence of divalent metal ions

3. Examine the formation of halogen bond driven supramolecular architectures by **D4** and **D5** in the presence of suitable XB acceptors/ guest (Figure 4.8). Solvents such as THF and dioxane which have potential binding preference towards iodine are selected as XB acceptors for the binding studies.⁴⁰ FTIR and TGA experiments can be used to identify guest inclusion in to the cavitand. In addition, potential XB acceptors (Figure 4.9) can be used to study guest binding to the XB donor sites of the cavitands.

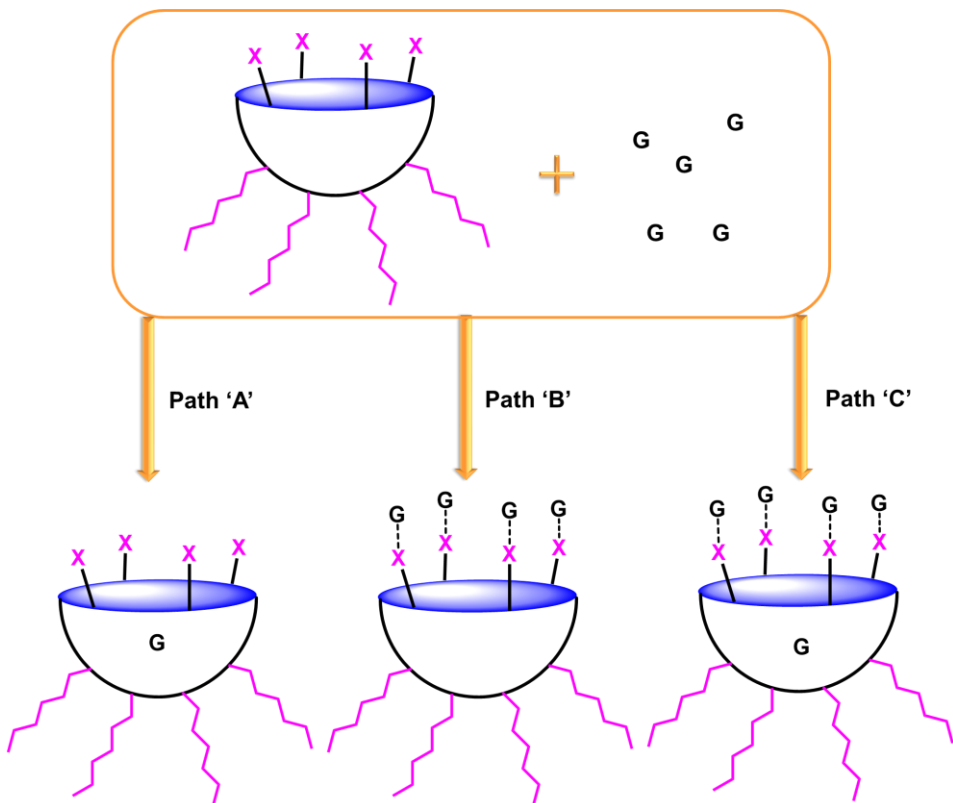


Figure 4.8 Three possible modes of guest binding to the host (X= XB donor, G= XB acceptor (guest))

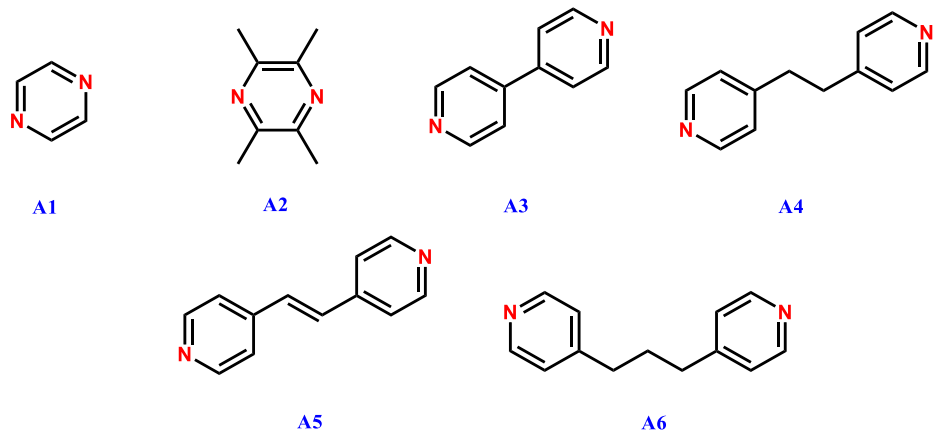


Figure 4.9 Ditopic nitrogen based XB/ HB acceptors (A1-A6)

4. Study the competition between HB and XB attached to same cavitand by introducing suitable nitrogen based acceptors (Figure 4.10). Six ditopic HB/ XB donors (Figure 4.9) can be used to co-crystallization/ host-guest chemistry study. Possibility of formation co-crystal/ host-guest complexes will be explored by FTIR.

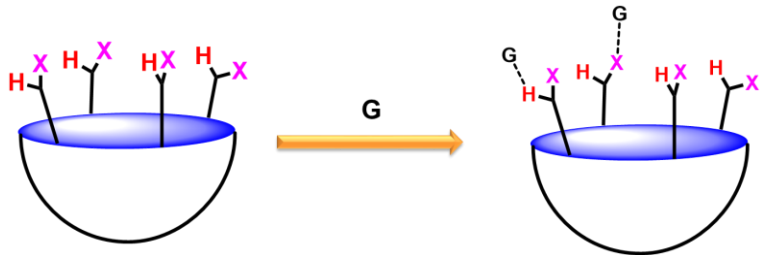


Figure 4.10 Competition between HB/XB towards common acceptor/ guest the multi-functional cavitand

4.2 Experimental

4.2.1 General

All solvents, reagents, precursors and acceptors (**A1-A6**) were purchased from commercial sources and used without further purification. For UV/Vis experiments, spectroscopic grade DMSO was used as the solvent. Melting points were determined using a Fisher-Johns melting point apparatus and are uncorrected. Infrared spectra were obtained on a Nicolet 380 FT-IR spectrometer. ^1H NMR and ^{13}C NMR spectra were obtained on a Varian unity plus 400 MHz spectrometer. DSC data were obtained on a TA instruments Q20 and TGA data on a TA instruments Q50. UV/Vis spectra were recorded by Shimadzu UV-Vis-1650PC spectrophotometer.

4.2.2 Synthesis of L7-L8 and D4-D6

Synthesis of bromo-cavitand was performed using literature methods starting with resorcinol (Figure 4.11).⁴¹ Synthesis of **L7** and **L8** were carried out by functionalizing the bromo cavitand by modified literature reported methods (Figure 4.12).⁴²⁻⁴³ HB/ XB donor cavitands (**D4-D6**) were synthesized by functionalizing bromo cavitands based on literature methods (Figure 4.13).⁴³⁻⁴⁵

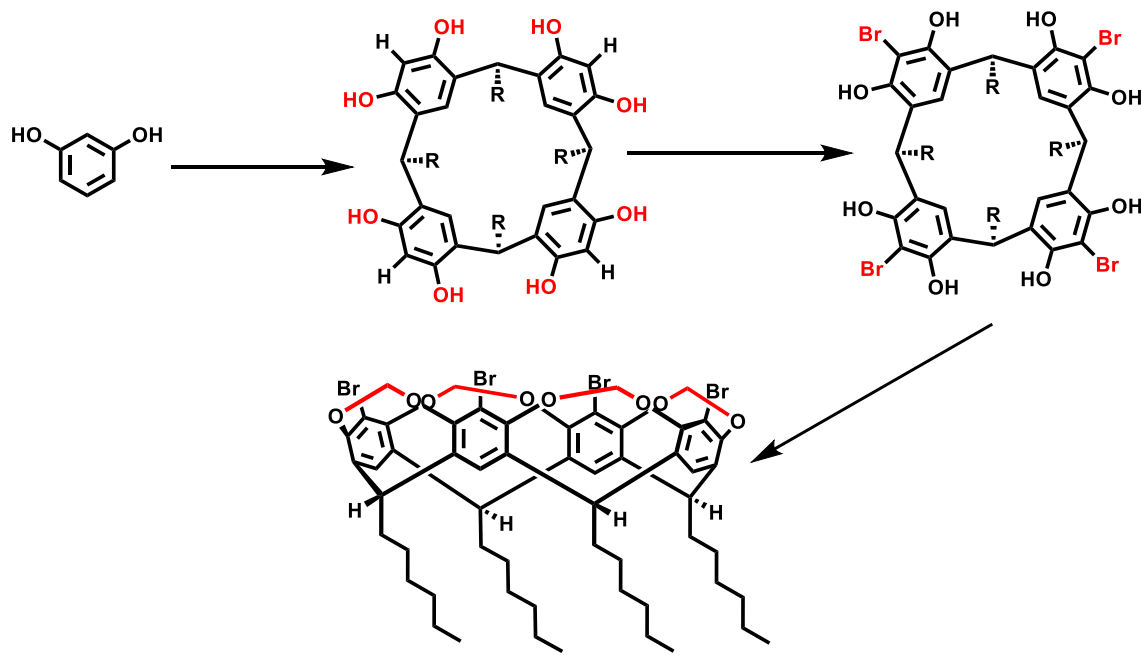


Figure 4.11 Overview of synthesis of bromocavitand

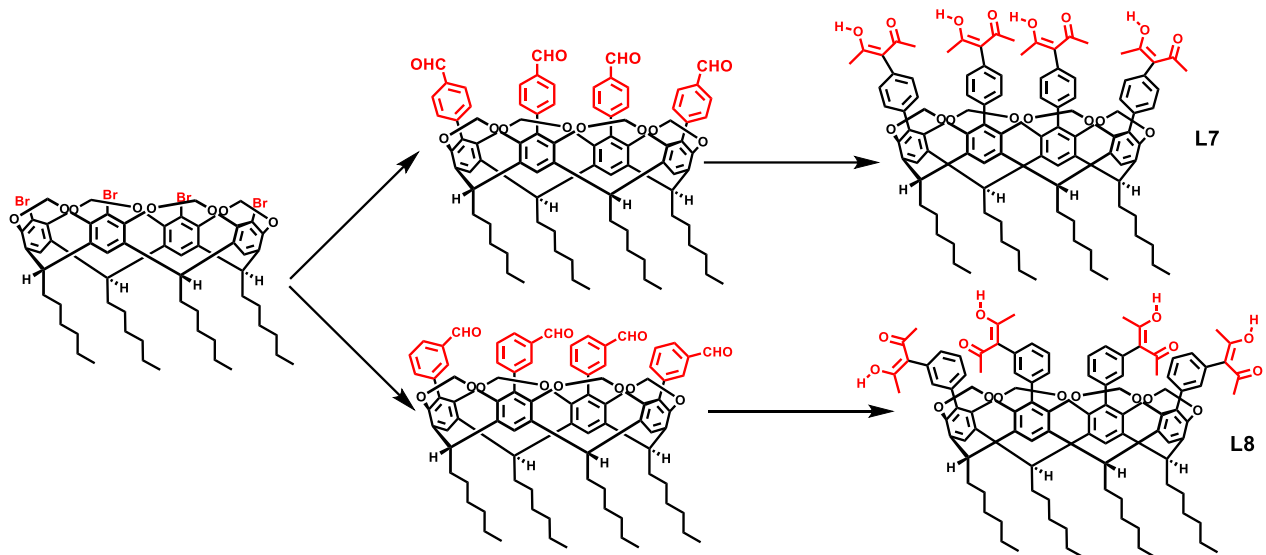


Figure 4.12 Overview of synthesis of acac functionalized cavitands (**L7** and **L8**)

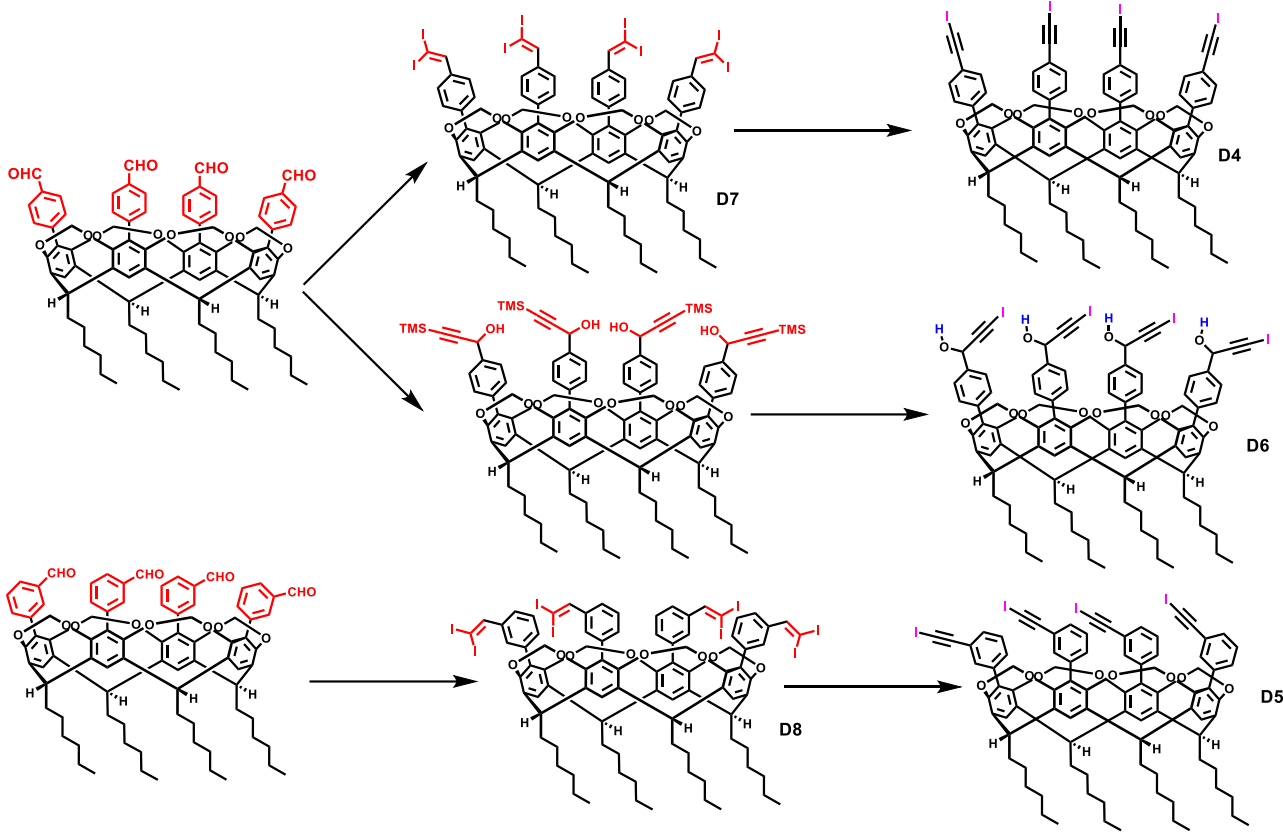
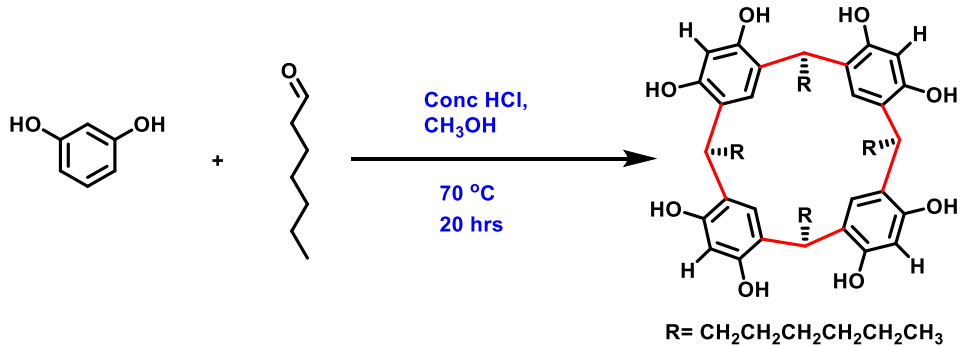


Figure 4.13 Overview of synthesis of HB and XB functionalized cavitands (**D4-D6**)

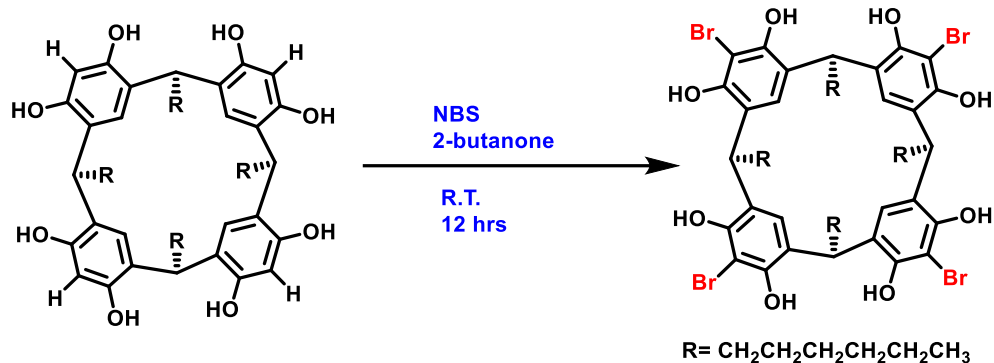
4.2.2.1 Synthesis of C-hexylcalix[4]resorcinarene



Resorcinol (50.0 g, 0.45 mol) was dissolved in ethanol (500 mL) and hexanal (51.4 g, 0.45 mol) was then added into the mixture. After cooling the mixture to 0 °C, conc. HCl (70 mL) was added dropwise under a nitrogen atmosphere. The mixture was refluxed at 70 °C for 20 hours under nitrogen. Then the reaction mixture was cooled to room temperature and diluted with water (500 mL). An orange color precipitate with a fruity smell was obtained upon completion. The

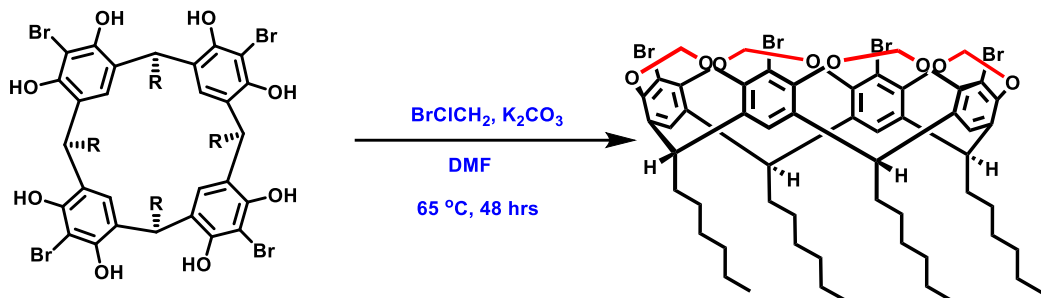
precipitate was filtered using a fritted Buchner funnel. The filtrate was washed with hot water until it became pH neutral. The solid was air dried to get the final product. Yield 90%; M.p. >280 °C; ¹H NMR (δ H; 400 MHz, DMSO-d6): 8.86 (s, 8H), 7.12 (s, 4H), 6.14 (s, 4H), 4.22 (t, 4H), 2.10 (m, 8H), 1.16 (m, 32H), 0.77 (m, 12H)

4.2.2.2 Synthesis of C-hexyltetrabromocalix[4]resorcinarene



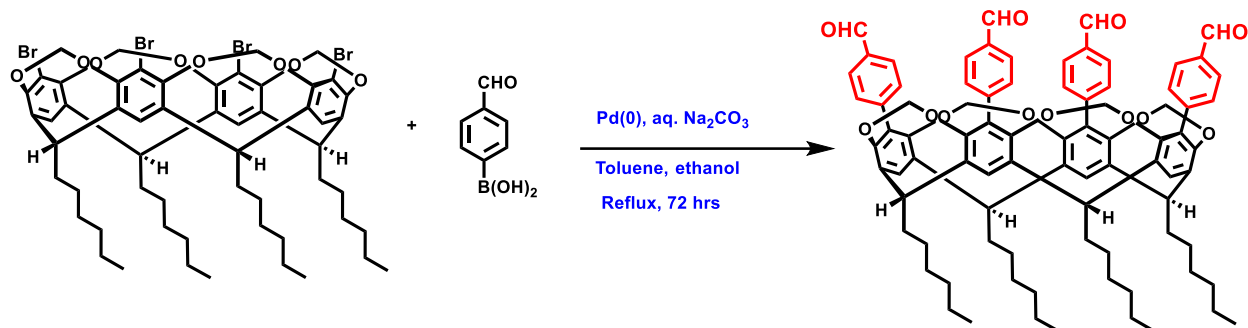
C-hexylcalix[4]resorcinarene, (50.0 g, 0.060 mol) was added to flask containing 2- butanone (375 mL). The mixture was stirred until all the solid was dissolved. After the mixture was cooled down to 0 °C, it was covered with an aluminium foil. N-bromosuccinamide (64.0 g, 0.36 mol) was added to the reaction mixture under the dark conditions over an hour. The reaction mixture was stirred for 16 hours at room temperature under a nitrogen atmosphere. After completion, a precipitate was formed. It was filtered and washed with cold 2- butanone (3 x 50 mL) followed by cold acetone (3 x 100 mL). The product was air dried followed by drying in the oven overnight 100 °C to produce off-white solid. Yield 84% M.p. >280 °C; ¹H NMR (δ H; 400 MHz, DMSO-d6): 9.10(s, 8H), 7.33 (s, 4H), 4.35 (t, 4H), 2.15 (m, 8H), 1.32-1.23 (m, 32H), 0.83 (m, 12H).

4.2.2.3 Synthesis of C-hexyltetrabromocavitan



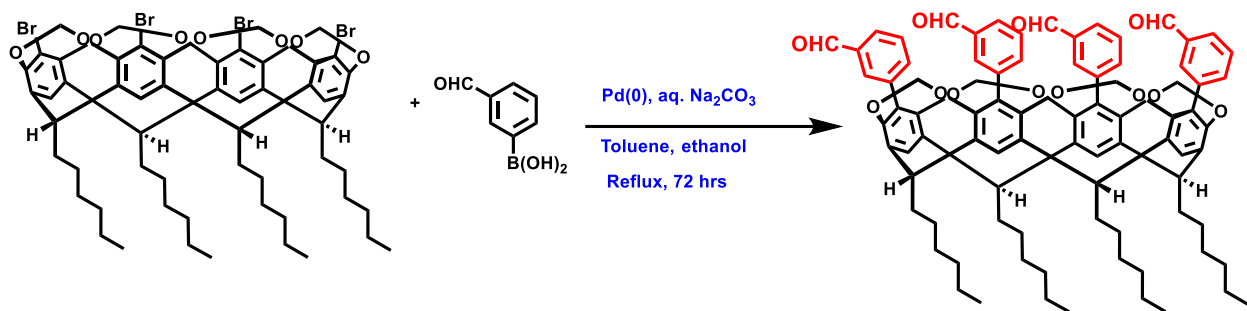
To a stirred solution of C-hexyltetrabromoresorcin[4]arene, (30.00 g, 26.3 mmol) dissolved in dry DMF (500 mL) was added K_2CO_3 (44.00 g, 318 mmol). The reaction mixture was purged with nitrogen for 20 minutes followed by the addition of CH_2BrCl (51.10 g, 395.0 mmol). A condenser was attached and the solution was heated at 65 °C for 24 h under a dinitrogen atmosphere. After 24 hours, an additional amount of CH_2BrCl (6.8 g, 52.6 mmol) was added, and the reaction mixture was stirred at 65 °C for a further 24 h. After completion, the reaction mixture was cooled to room temperature and poured into an aqueous HCl solution (2%, 600 mL). The solid, which contained mainly the product, was filtered off and washed with water until pH was neutral. The solid was air dried and then purified by column chromatography using hexanes: dichloromethane 1:1 mixture as the eluent. The product was isolated as a white solid. Yield 82%; M.p. >280 °C; ^1H NMR (δH ; 400 MHz, CDCl_3): 7.04 (s, 4H), 5.97 (d, 4H), 4.86 (t, 4H), 4.40 (d, 4H), 2.21 (m, 8H), 1.44-1.32 (m, 32H), 0.91 (m, 12H); ^{13}C NMR (δC ; 400 MHz, CDCl_3) : 152.01, 139.26, 119.03, 113.49, 98.45, 37.63, 31.80, 29.35, 27.68, 22.62, 14.05.

4.2.2.4 Synthesis of C-hexyltetra(4-phenylformyl)cavitand



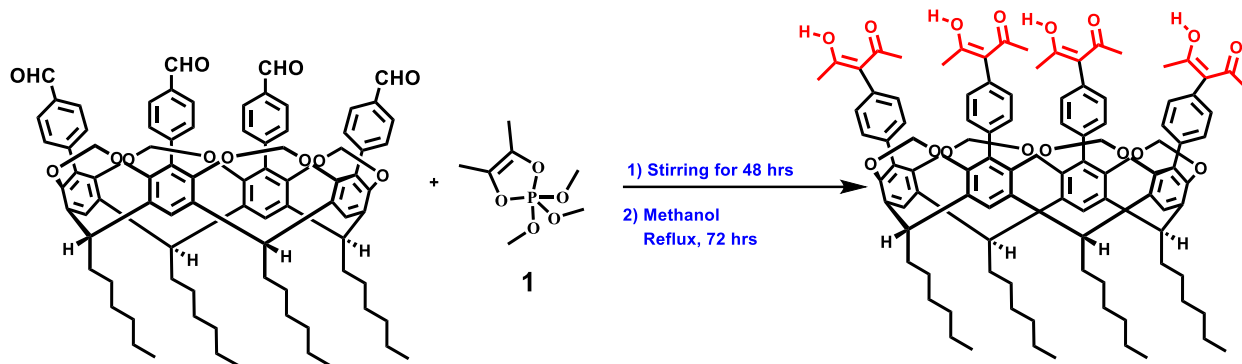
A mixture of tetrabromocavitand (6.0 g, 5.05 mmol) and tetrakis(triphenylphosphine)palladium(0) (1.17 g, 1.01 mmol) were added to a round-bottom flask under a stream of nitrogen. Toluene (80 mL), ethanol (60 mL), and aqueous sodium carbonate (6.00 g) were all purged with dinitrogen, then added to the round bottom flask along with 4-formylphenyl boronic acid (7.57 g, 50.5 mmol). The reaction mixture was refluxed for 72 hours under a dinitrogen atmosphere. Upon completion, the reaction was cooled to room temperature and diluted with water (300 mL). The aqueous phase was extracted with chloroform (3 x 100 mL). The combined organic phases were washed with saturated brine (3 x 100 mL), and dried over anhydrous magnesium sulfate. The solvent was removed on a rotary evaporator and the residue purified by column chromatography using a hexanes: ethyl acetate (6:4) mixture as the eluent. The product was isolated as a white powder. Yield 85%; M.p. >280 °C; ^1H NMR (δH ; 400 MHz, CDCl_3): 10.00 (s, 4H), 7.86 (d, 8H), 7.39 (s, 4H), 7.21 (d, 8H), 5.23 (d, 4H), 4.86(t, 4H), 4.24 (d, 4H), 2.38 (m, 8H), 1.52-1.36 (m, 32H), 0.94 (m, 12H); ^{13}C NMR (δC ; 400 MHz, CDCl_3) : 191.70, 152.32, 140.39, 138.52, 135.16, 130.60, 129.27, 128.30, 120.63, 100.46, 37.03, 31.86, 29.47, 27.89, 22.65, 14.06.

4.2.2.5 Synthesis of C-hexyltetra(3-phenylformyl)cavitand



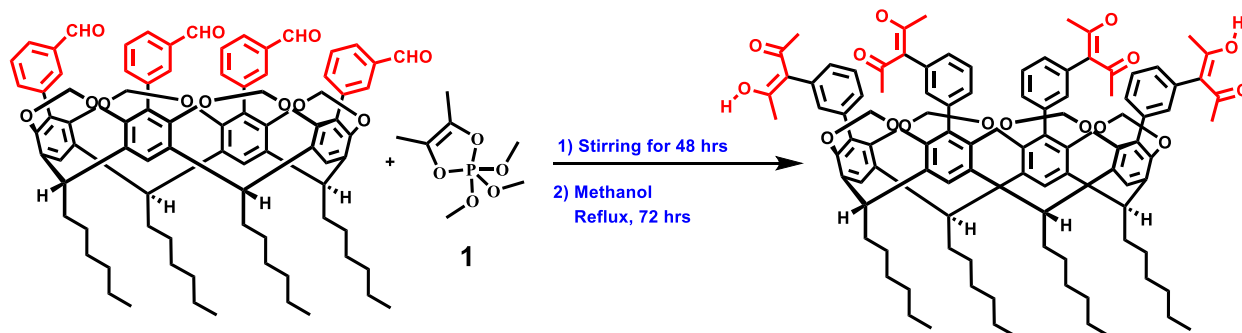
A mixture of tetrabromocavitand (6.0 g, 5.05 mmol) and tetrakis(triphenylphosphine)palladium(0) (1.17 g, 1.01 mmol) were added to a round-bottom flask under a stream of nitrogen. Toluene (80 mL), ethanol (60 mL), and aqueous sodium carbonate (6.00 g) were all purged with dinitrogen, then added to the round bottom flask along with 3-formylphenyl boronic acid (7.57 g, 50.5 mmol). The reaction mixture was refluxed for 72 hours under a dinitrogen atmosphere. Upon completion, the reaction was cooled to room temperature and diluted with water (300 mL). The aqueous phase was extracted with chloroform (3 x 100 mL) the combined organic phases were washed with saturated brine (3 x 100 mL), and dried over anhydrous magnesium sulfate. The solvent was removed on a rotary evaporator and the residue was purified by column chromatography using a hexanes: ethyl acetate (7:3) mixture as the eluent. The product was isolated as a white powder. Yield 58%; M.p. >280 °C; ¹H NMR (δ H; 400 MHz, CDCl₃): 10.01 (s, 4H), 7.78 (d, 4H), 7.55(s, 4H), 7.52 (t, 4H), 7.39 (m, 8H), 5.17(d, 4H), 4.86(t, 4H), 4.27(d, 4H), 2.38 (m, 8H), 1.52-1.37 (m, 32H), 0.94 (m, 12H); ¹³C NMR (δ C; 400 MHz, CDCl₃) : 192.09, 152.5, 138.37, 136.04, 129.11, 128.73, 128.20, 120.38, 100.45, 37.04, 31.87, 29.49, 27.92, 22.66, 14.07.

4.2.2.6 Synthesis of C-hexyltetra(4-(2-hydroxy-4-oxopent-2-en-3-yl))cavitand (L7)



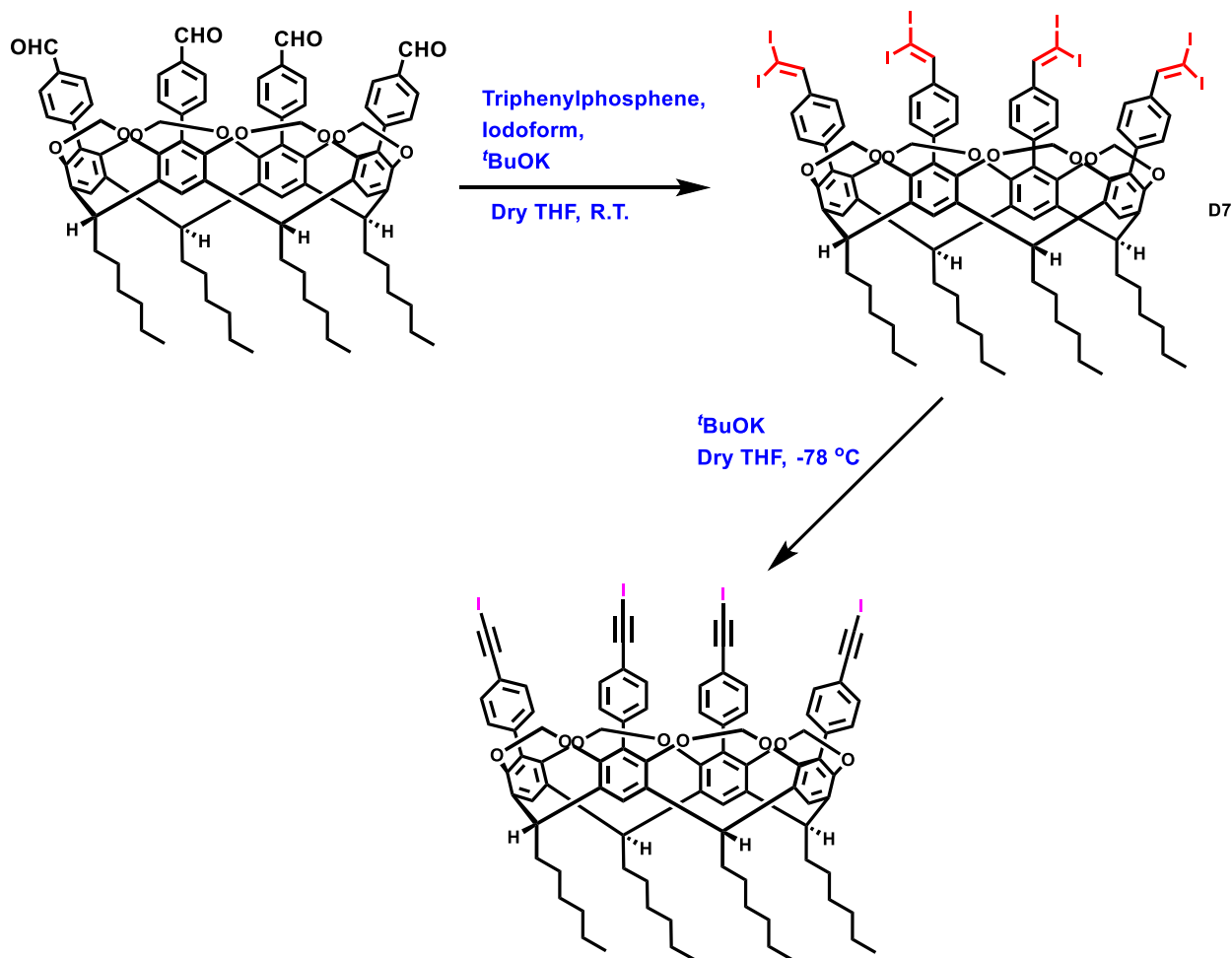
C-hexyltetra(4-phenylformyl)cavitand (0.5 g, 0.39 mmol) was placed in a 100 mL round bottom flask under a N₂ atmosphere. Compound, **1** (0.65 g, 3.12 mmol) was added to the flask with continuous stirring. The resulting slurry was stirred for 48 hrs at room temperature under a N₂ atmosphere to obtain an oil. Then 50 ml of methanol was added, and the mixture was heated under reflux 72 hrs under a N₂ atmosphere. Upon cooling the solution to room temperature, a precipitate was obtained. The precipitate was filtered and washed with methanol to obtain the pure product. Yield 55%; M.p. 260 °C; ¹H NMR (δ H; 400 MHz, CDCl₃): 16.68 (s, 4H), 7.37 (s, 4H), 7.17 (d, 8H), 7.09 (d, 8H), 5.25 (d, 4H), 4.87 (t, 4H), 4.30 (d, 4H), 2.36 (m, 8H), 1.87(s, 24H), 1.50-1.36 (m, 32H), 0.94 (m, 12H); ¹³C NMR (δ C; 400 MHz, CDCl₃) : 190.77, 152.62, 138.38, 135.73, 133.19, 130.56, 130.26, 128.75, 120.10, 114.62, 100.40, 37.14, 31.88, 30.49, 29.48, 27.94, 24.10, 22.66, 14.08.

4.2.2.7 Synthesis of C-hexyltetra(3-(2-hydroxy-4-oxopent-2-en-3-yl))cavitand (L8)



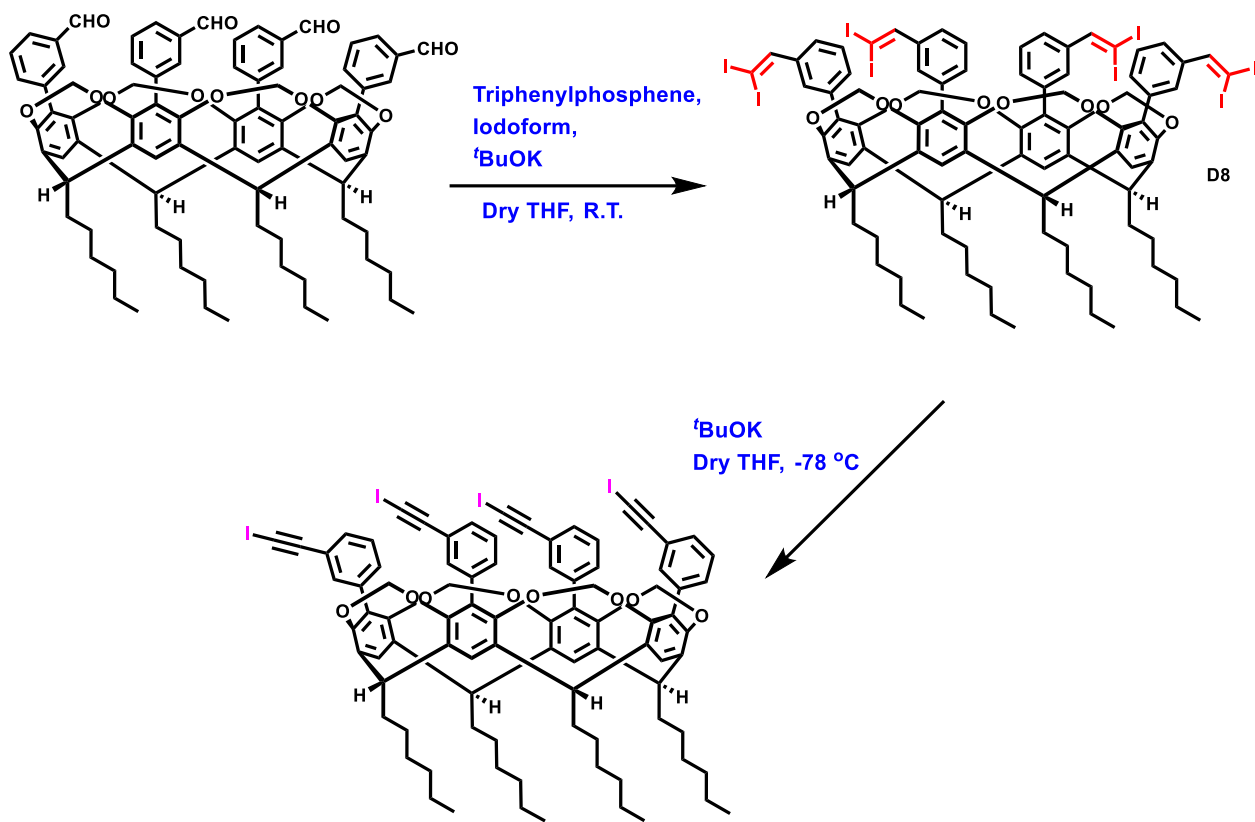
C-hexyltetra(3-phenylformyl)cavitand (0.5 g, 0.39 mmol) was placed in a 100 mL round bottom flask under a N₂ atmosphere. Compound, **1** (0.65 g, 3.12 mmol) was added to the flask with continuous stirring. The resulting slurry was stirred for 48 hrs at room temperature under a N₂ atmosphere to obtain an oil. Then 50 ml of methanol was added, and the mixture was heated under reflux for 72 hrs under a N₂ atmosphere. Upon cooling the solution to room temperature, a precipitate was obtained. The precipitate was filtered and washed with methanol to obtain the pure product. Yield 47%; M.p. >280 °C; ¹H NMR (δ H; 400 MHz, CDCl₃): 16.57 (s, 4H), 7.34 (m, 8H), 7.11-6.91(m, 12H), 5.14(d, 4H), 4.84(t, 4H), 4.26(d, 4H), 2.34 (m, 8H), 1.85(s, 24H), 1.50-1.34 (m, 32H), 0.93 (m, 12H).

4.2.2.8 Synthesis of C-hexyltetra(4-(iodoethynyl))cavitand (**D4**)



Triphenylphosphene (2.10 g, 8 mmol), iodoform (3.14 g, 7.98 mmol) and ^tBuOK (0.90 g, 8.0 mmol) were added to 100 ml of dry THF and stirred for 15 minutes under a nitrogen atmosphere. A brown suspension was formed. C-hexyltetra(4-phenylformyl)cavitand (1.0g, 0.78 mmol) was dissolved in 10 ml of dry THF and added to the brown suspension. The mixture was stirred at room temperature for 1 hr (formation of **D7**). Then the reaction mixture was cooled to -78 °C. ^tBuOK (1.71g, 15.24 mmol) was added to the reaction mixture and stirred at -78 °C for an additional hour. Then, 100 mL of NaCl was added to quench the reaction. After warming the reaction mixture to room temperature, aqueous layer was extracted with ethyl acetate (3 x 100 mL). Combined organic layer was dried with MgSO₄ and solvent was removed by rotavap to obtain the product as light brown solid. Yield 74%; M.p. >280 °C; ¹H NMR (δ H; 400 MHz, CDCl₃): 7.29 (s, 4H), 7.18 (d, 8H), 6.94 (d, 8H), 5.16 (d, 4H), 4.87(t, 4H), 4.35 (d, 4H), 2.34 (m, 8H), 1.49-1.36 (m, 32H), 0.93 (m, 12H); ¹³C NMR (δ C; 400 MHz, CDCl₃) : 152.38, 138.76, 134.77, 131.91, 129.71, 121.80, 119.68, 99.13, 94.03, 37.09, 31.88, 30.34, 29.53, 27.93, 22.67, 14.09.

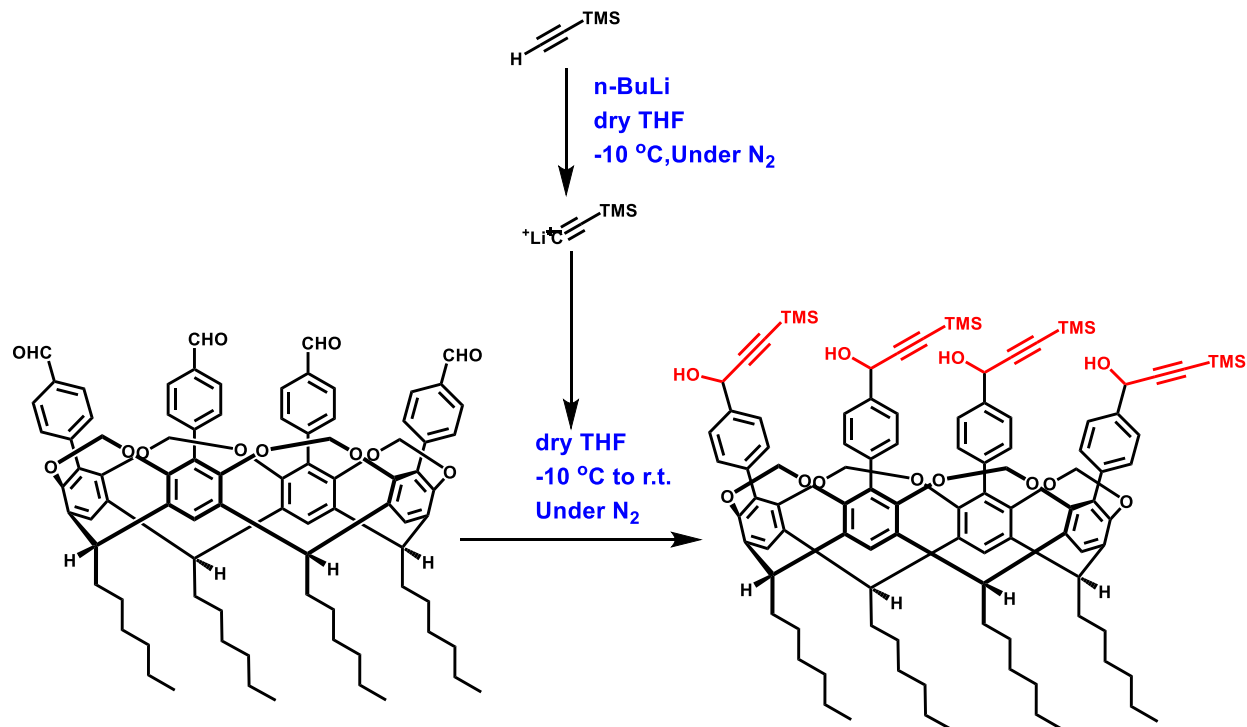
4.2.2.9 Synthesis of C-hexyltetra(3-(iodoethynyl))cavitand (**D5**)



Triphenylphosphine (2.10 g, 8 mmol), iodoform (3.14 g, 7.98 mmol) and ^tBuOK (0.90 g, 8.0 mmol) were added to 100 ml of dry THF and stirred for 15 minutes under a dinitrogen atmosphere. A brown suspension was formed. C-hexyltetra(3-phenylformyl)cavitand (1.0g, 0.78 mmol) was dissolved in 10 ml of dry THF and added to the brown suspension. The mixture was stirred at room temperature for 1 hr (formation of **D8**). Then the reaction mixture was cooled to -78 °C. ^tBuOK (1.71g, 15.24 mmol) was added to the reaction mixture and stirred at -78 °C for additional hour. Then, 100 mL of NaCl was added to quench the reaction. After warming the reaction mixture to room temperature, the aqueous layer was extracted with ethyl acetate (3 x 100 mL). Combined organic layer was dried with MgSO₄ and solvent was removed by rotavap to obtain the product as light brown solid. Yield 65%; M.p. 270 °C dec. ¹H NMR (δ H; 400 MHz, CDCl₃):

8.12 (br, 4H), 7.32 (s, 4H), 7.01 (br, 12H), 5.28 (br, 4H), 4.85(t, 4H), 4.38 (br, 4H), 2.35 (m, 8H), 1.56-1.36 (m, 32H), 0.94 (m, 12H).

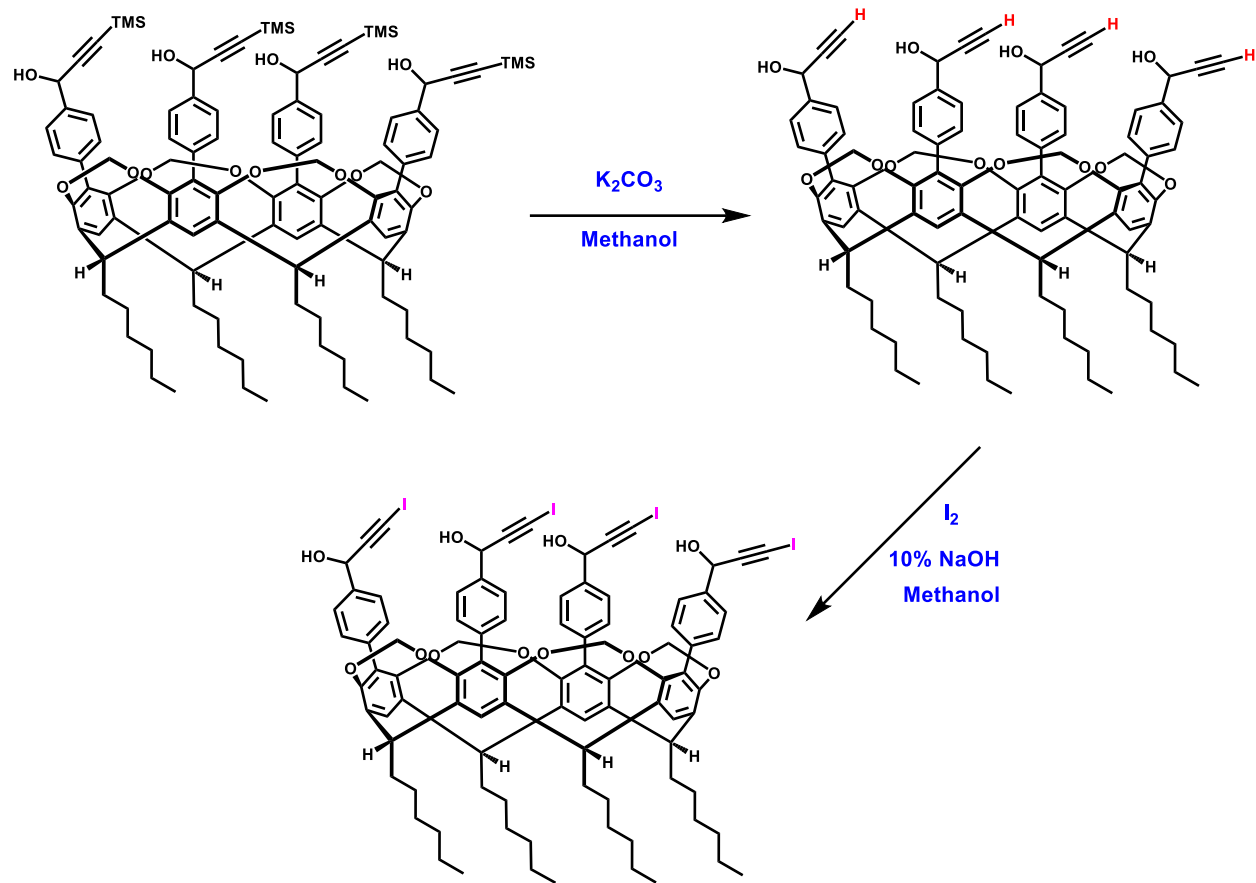
4.2.2.10 Synthesis of C-hexyltetra(4-(1-hydroxy-3-(trimethylsilyl)prop-2-yn-1-yl)cavitand



A solution of trimethylsilylacetylene (0.55 ml, 3.9 mmol) was stirred in 100 ml of dry THF and cooled to -10 °C under N₂. A solution of n-BuLi (1.55 mL, 3.9 mmol) was added slowly over 30 min. at -10 °C under N₂. The mixture was stirred for an additional hour at the same temperature. C-hexyltetra(3-phenylformyl)cavitand (1.0 g, 0.78 mmol) was dissolved in 25 ml of dry THF and added dropwise to the resulting trimethylsilyl acetylide solution under N₂ at -10 °C. The mixture was then allowed to reach room temperature and stirred for 48 hours. After completion of the reaction, 100 ml of water was added and extracted with ethyl acetate (3 × 100ml). The combined organic layers were dried over magnesium sulfate and the solution was concentrated to obtain a crude solid and purified by column chromatography (hexanes: ethyl acetate 1:1). Yield: 1.22g, 93%, M.p. >280 °C; ¹H NMR (δ H; 400 MHz, CDCl₃): 7.52 (d, 8H), 7.33 (s, 4H), 7.07 (d, 8H),

5.47(s, 2H), 5.25(q, 4H), 4.86(t, 4H), 4.23 (d, 4H), 2.36 (m, 8H), 1.52-1.36 (m, 32H), 0.93 (m, 12H), 0.21 (s, 36H); ^{13}C NMR (δC ; 400 MHz, CDCl_3) : 152.57, 138.89, 138.31, 134.09, 130.07, 128.86, 126.37, 119.94, 104.60, 100.58, 91.90, 64.69, 37.03, 31.87, 30.42, 29.48, 27.90, 22.67, 14.08, 0.17.

4.2.2.11 Synthesis of C-hexyltetra(4-(1-hydroxy-3-iodoprop-2-yn-1-yl))cavitand (D6)



C-hexyltetra(4-(1-hydroxy-3-(trimethylsilyl)prop-2-yn-1-yl))cavitand (0.750g, 0.45 mmol) and potassium carbonate (0.31 g, 2.25 mmol) were dissolved in 50ml of methanol. The reaction mixture was stirred for 3 hrs and after completion of the reaction (removal of the ethynyl proton). 50 mL of THF was added to the reaction mixture. Concentrated solution of iodine in methanol (0.91 g, 3.6 mmol) and a 10% sodium hydroxide solution was added dropwise simultaneously over 30 min, by stirring vigorously (at the beginning, the color of iodine disappears

upon adding in to the reaction mixture and with time the color tend to persist, therefore, NaOH should be added until the iodine color no longer changes upon addition of NaOH in the reaction mixture). The mixture was stirred overnight, and quenched with 100 mL water upon which a light brown color precipitate formed. The solid was filtered and washed with sodium bisulfite solution to get the product. Yield 78%; M.p. 280 °C dec.; ^1H NMR (δ H; 400 MHz, DMSO-d6): 7.80 (s, 4H), 17.39 (m, 8H), 7.06 (d, 8H), 6.06 (d, 4H), 5.43(s, 2H), 5.32 (s, 2H), 5.15 (br, 4H), 4.68 (d, 4H), 4.32 (m, 4H), 1.46-1.31 (m, 32H), 0.88 (m, 12H), 0.21 (s, 36H).

4.2.3 Metal-ligand complex, host-guest complex and co-crystal synthesis

- **L7** and **L8** (10 mg) were individually combined with divalent metal salts (Cu(II), Ni(II) and Zn (II)) in a 1:2 stoichiometric ratio in acetonitrile and left for slow evaporation.
- **D4** and **D5** (10 mg) were individually combined with each acceptor (**A1-A6**) in a 1:2 stoichiometric ratio using solvent assisted grinding (methanol as the solvent). Solvent inclusion was studied by dissolving **D4** and **D5** in solvents such as THF and dioxane.
- **D6** (10 mg) was individually combined with each acceptor (**A1-A6**) in a 1:4 stoichiometric ratio using solvent assisted grinding (methanol as the solvent).

4.2.4 UV/ Vis titrations

The UV-visible spectra of **D4** and **D4**:Cu(II) complex were recorded in spectrophotometric grade solvent, dimethyl sulfoxide (DMSO). The ligand: copper(II) stoichiometry was determined by a Job's continuous variation method involving UV-visible titrations. A series of solutions containing **D4** (0.0005 M) and Cu(II)(ClO₄)₂.6H₂O (0.0005 M) were prepared such that the sum of the total metal ion and **D4** concentration remained constant (0.0005 M). The mole fraction (X) of **D4** was varied from 0.0 to 1.0. The corrected absorbance ($A_{observed} - A_{D4} - A_{Cu(II)}$) at 420 nm and 392 nm were recorded.

4.3 Results and discussion

4.3.1 Metal-ligand complex formation

4.3.1.1 Solid state study

FTIR spectroscopy can be used to identify the metal-ligand formation between ligand **L7**-**L8** and corresponding metal ions. Figure 4.14 shows the IR spectrum of metal-ligand supramolecular complex formation between **L7** and Cu(II). Well resolved peaks in the region from $1,600\text{ cm}^{-1}$ to $1,300\text{ cm}^{-1}$ confirm the formation of the metal ligand complex between **L7** and Cu(II).

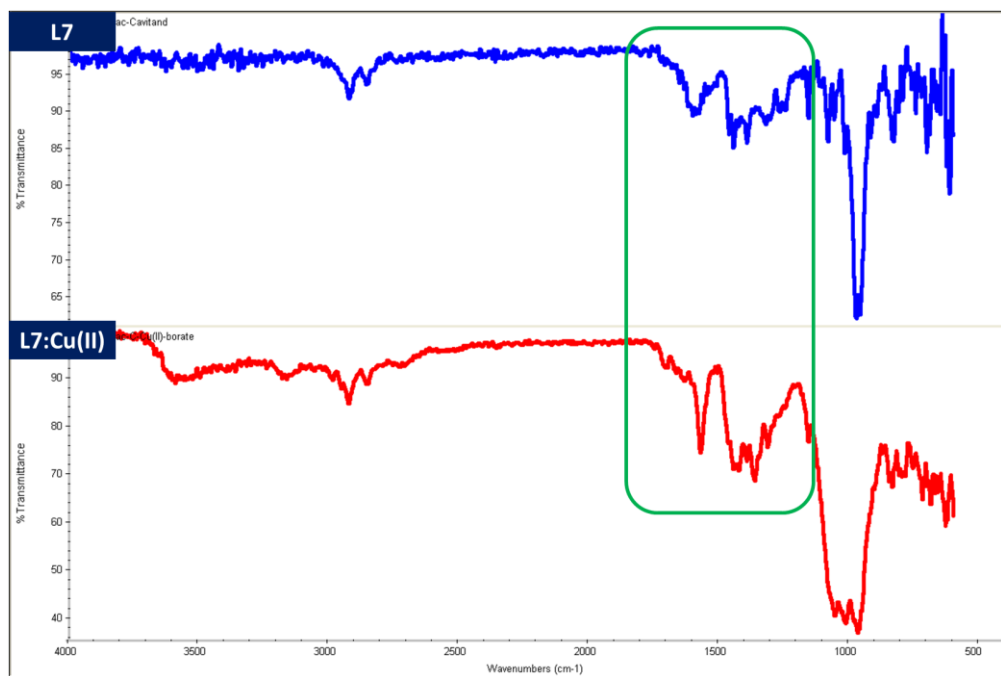


Figure 4.14 FTIR spectra of **L7** (blue) and the metal-ligand complex between **L7** and Cu(II) (red).

Similarly, **L8** also makes metal-ligand complexes with Cu(II) ion (Figure 4.15). Again, well resolved peaks in the region from $1,600\text{ cm}^{-1}$ to $1,300\text{ cm}^{-1}$ confirm the formation of the metal ligand complex between **L8** and Cu(II).

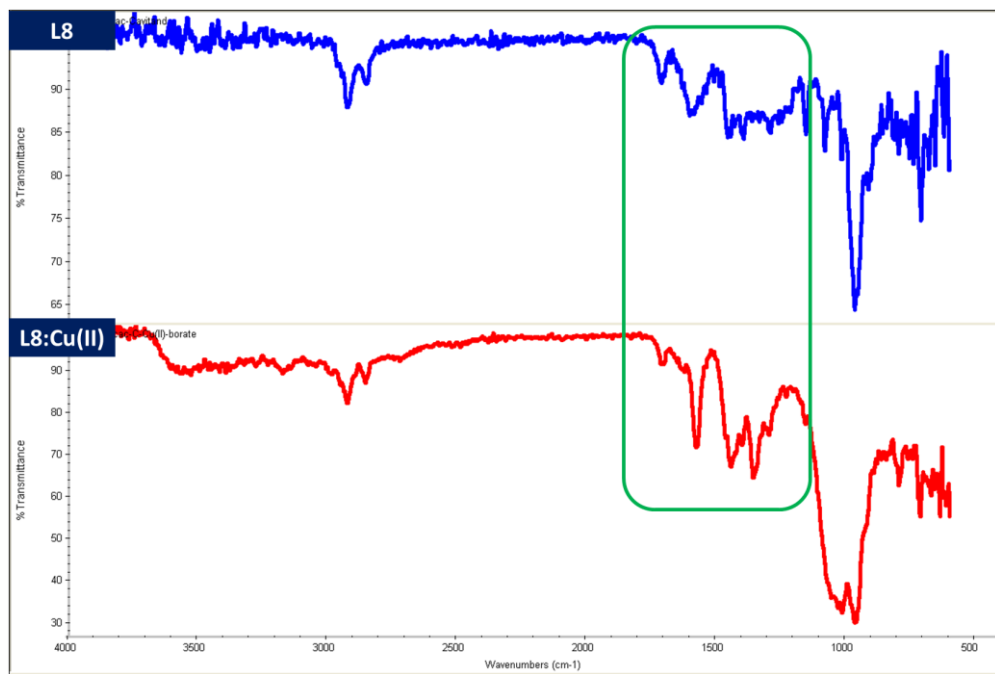


Figure 4.15 FTIR spectra of **L8** (blue) and the metal-ligand complex between **L8** and Cu(II) (red).

Similarly, evidence for formation of metal-ligand complexes with Ni(II) and Zn(II) was obtained based on IR spectroscopy.

4.3.1.2 Solution state study

The UV/Vis titration spectra for **L7:Cu(II)** are shown in the Figure 4.16. There are two notable observations from the UV-visible titrations. First, the appearance of a new absorption band at 420 nm at low metal ion concentration in the system, possibly due to discrete metal-ligand complexation. Second, the decrease in the intensity of the peak at 420 nm and subsequent new highly intense peak appearance at 283 nm. This indicates the conformational change in the metallo-supramolecular architecture with the higher concentration of metal ions.

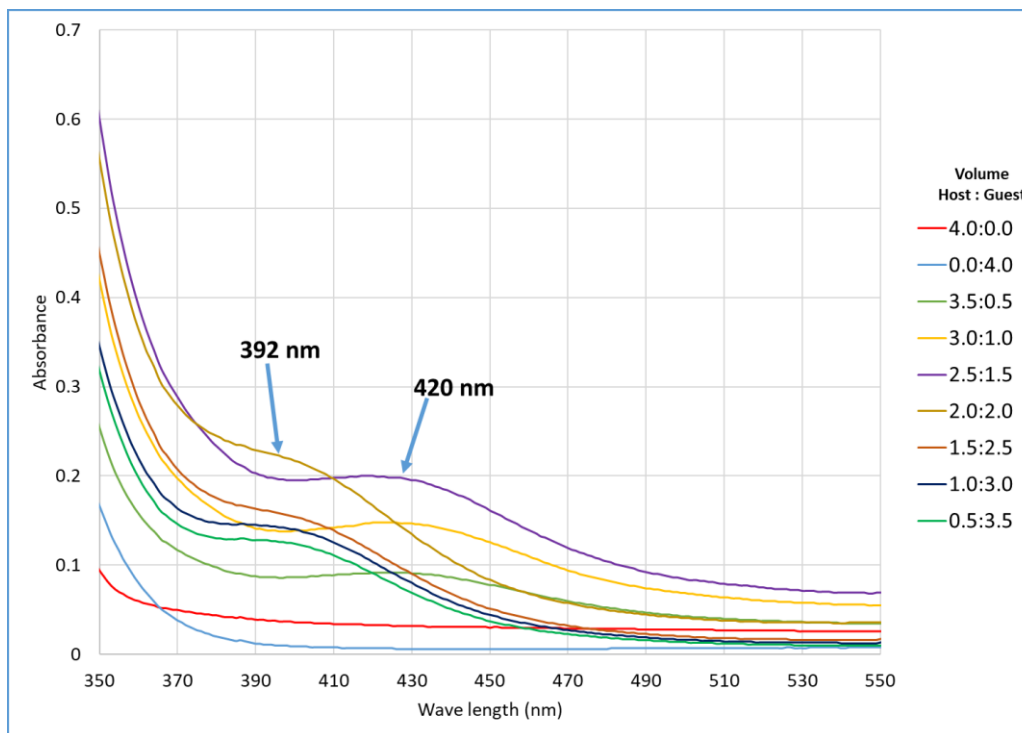


Figure 4.16 Continuous variation method using UV-visible spectroscopy (**L7**:Cu(II))

The results of UV/Vis titration performed between **L7** and **Cu(II)** perchlorate hexahydrate are tabulated in the Table 4.1 ($\lambda_{\text{max}} = 420 \text{ nm}$) and Table 4.2 ($\lambda_{\text{max}} = 392 \text{ nm}$).

Table 4.1 UV-visible data for the Job plot at $\lambda_{\text{max}} = 420 \text{ nm}$

$\lambda_{\text{max}} = 420 \text{ nm}$	Vol. Host (mL)	Vol. Guest (mL)	Absorbance (corrected)	Mole fraction of host (X)
Host	4.0	0.0	0	1
1	3.5	0.5	0.06225	0.875
2	3.0	1.0	0.12150	0.75
3	2.5	1.5	0.17675	0.625
4	2.0	2.0	0.14700	0.5
5	1.5	2.5	0.09825	0.375
6	1.0	3.0	0.08950	0.25
7	0.5	3.5	0.08075	0.125
Guest	0	4.0	0	0

Table 4.2 UV-visible data for the Job plot at $\lambda_{\max} = 392$ nm

$\lambda_{\max} = 392$ nm	Vol. Host (mL)	Vol. Guest (mL)	Absorbance (corrected)	Mole fraction of host (X)
Host	4.0	0.0	0	1
1	3.5	0.5	0.0515	0.875
2	3.0	1.0	0.0480	0.75
3	2.5	1.5	0.1715	0.625
4	2.0	2.0	0.2020	0.5
5	1.5	2.5	0.1395	0.375
6	1.0	3.0	0.1260	0.25
7	0.5	3.5	0.1135	0.125
Guest	0	4.0	0	0

Job's plots for both events were generated in order to determine the L7 to Cu(II) stoichiometry in the complex formation. Job's plot at $\lambda_{\max} = 420$ nm is shown in Figure 4.17 (a) and the 4.17 (b) shows the binding event at $\lambda_{\max} 392$ nm.

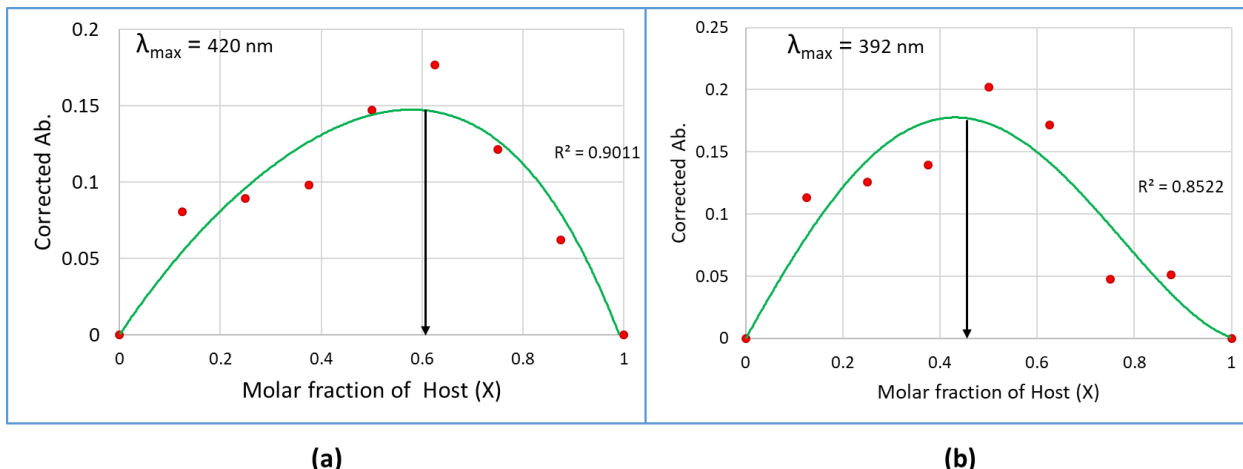


Figure 4.17 Job plot of UV/vis titration (a) at $\lambda_{\max} = 420$ nm and (b) at $\lambda_{\max} = 392$ nm

Binding event at $\lambda_{\max} = 420$ nm indicates that the stoichiometry is 3:2 L7:Cu(II) which may be due to pentameric metallo-supramolecular architecture formations (Figure 4.18). In the second binding event (at $\lambda_{\max} = 392$ nm), the stoichiometry is 1:1 ligand:metal. This may be due to a polymeric metallo-supramolecular architecture formation toward 1-D direction (Figure 4.19).

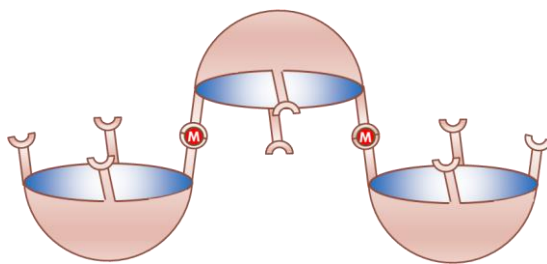


Figure 4.18 Proposed discrete metallo-supramolecular complex at $\lambda_{\max} = 420$ nm

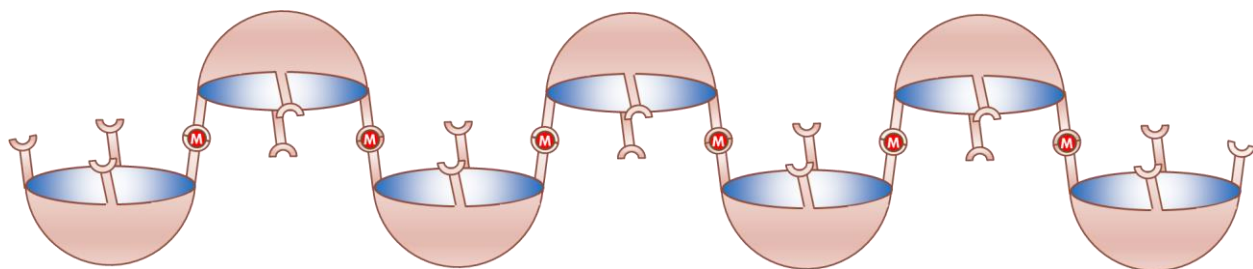


Figure 4.19 Proposed polymeric metallo-supramolecular architecture at $\lambda_{\max} = 392$ nm

4.3.1.3 Host-guest inclusion studies

Cavitands have an intrinsic cavity which can accommodate guest molecules that is suitable to fit in the cavity. In the bromo-cavitand, the inner diameter is around 8 Å and suitable for accommodate a range of small molecules (Figure 4.20).

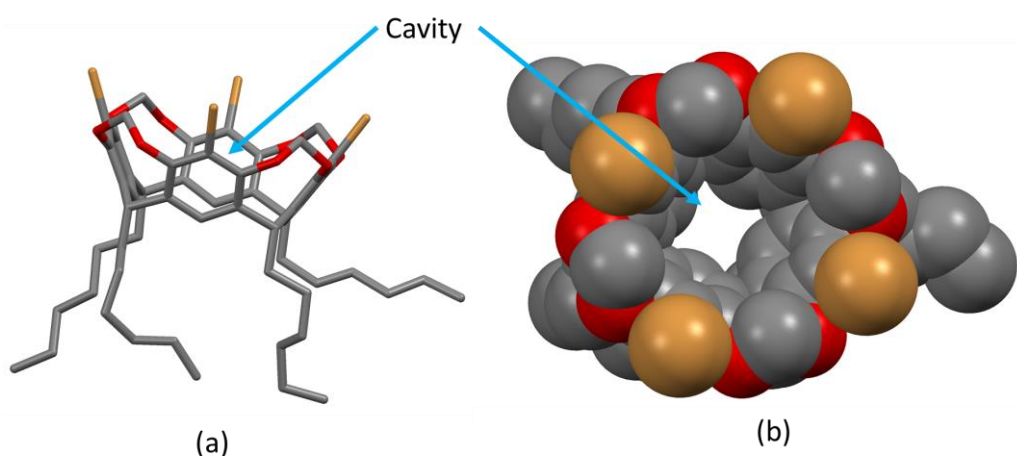


Figure 4.20 Preliminary single crystal X-ray structure (a) side view (capped stick model), (b) top view (space filling model) of C-hexyltetrabromocavitand

The functionalized cavitands also can accommodate small molecules in the cavity in addition to supramolecular interactions with the rim functionailies. **D4** and **D5** cavitands obtained from dioxane solution indicate guest inclusion based on FTIR data (Figure 4.21 and Figure 4.22).

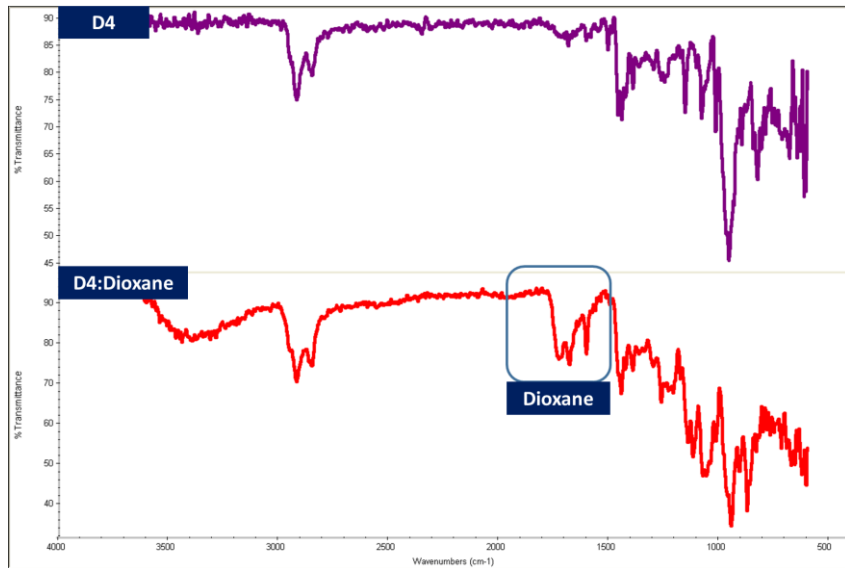


Figure 4.21(a) IR spectra of dry **D4** (violet), (b) IR spectra of **D4:Dioxane**

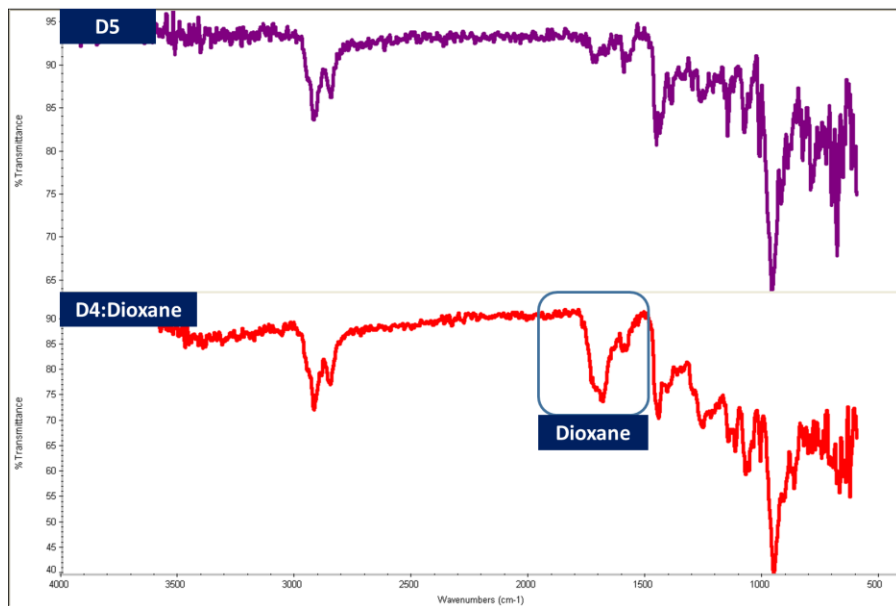


Figure 4.22(a) IR spectra of dry **D5** (violet), (b) IR spectra of **D4:Dioxane**

In addition to that, TGA traces of **D4**:Dioxane and **D5**:Dioxane provide further evidence for the guest inclusion in the cavitand (Figure 4.23).

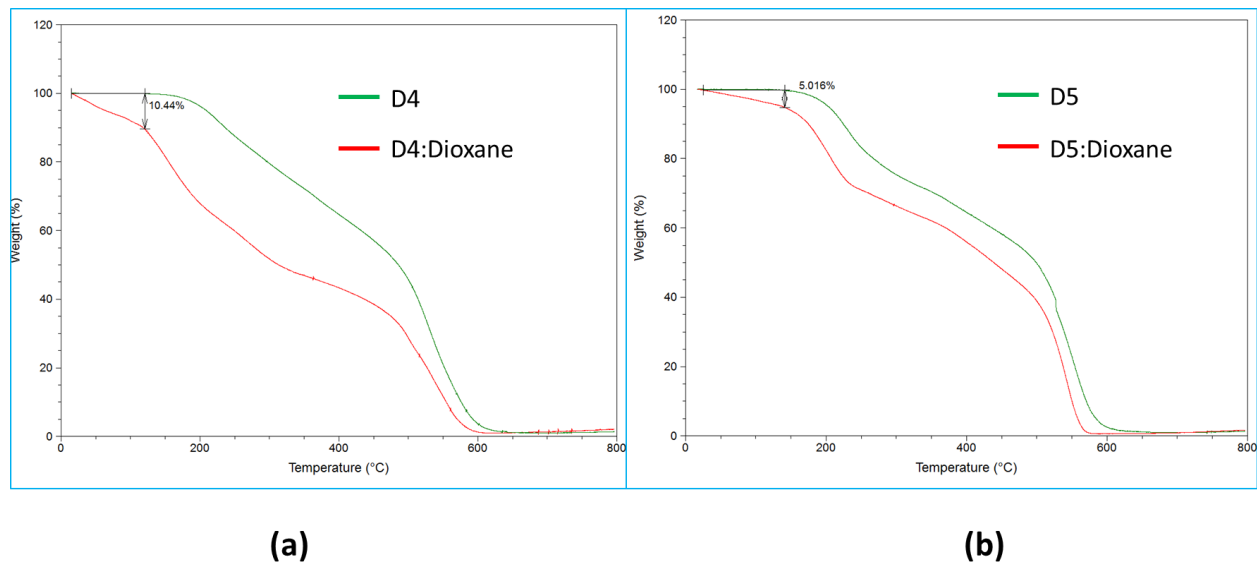


Figure 4.23(a) TGA spectra of dry **D4** (red) and **D4**:dioxane (green), **(b)** TGA spectra of dry **D5** (red) and **D5**:dioxane (green)

4.3.1.4 HB/ XB donor capability of cavitands

The ability of **D4**, **D5** and **D6** to act as XB donors or XB/HB donors were examined by IR spectroscopy of ground mixtures of donor (**D4-D6**) and acceptor (**A1-A6**) combinations (total 18 experiments were performed, Table 4.3). The IR screening shows the formation of co-crystal between cavitand and acceptors. One example for co-crystal screening (**D6:A3**) experiment is shown in Figure 4.24. The shift of most sensitive characteristic peak of acceptor can be monitored to check co-crystal formation (e.g. peak shift of **A3** from 1586 cm^{-1} to 1594 cm^{-1} in **D6:A3**)

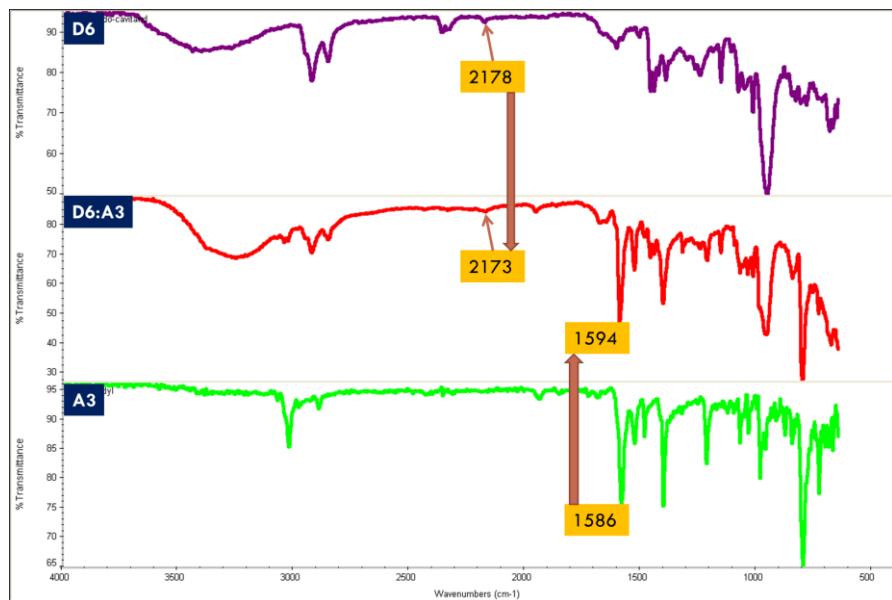


Figure 4.24 IR spectroscopy of **D6**, **A3** and ground mixture **D3:A3**

Table 4.3 IR analysis of attempted co-crystallization experiments

Combination	Characteristic peak of acceptor		Peak shift	Co-crystal
	Free (cm ⁻¹)	Bound (cm ⁻¹)		
D4:A1	1490	-	-	No
D4:A2	1437	-	-	No
D4:A3	1586	1588	+2	Yes
D4:A4	1593	1599	+7	Yes
D4:A5	1592	1594	+2	Yes
D4:A6	1603	1600	-3	Yes
D5:A1	1490	-	-	No
D5:A2	1437	-	-	No
D5:A3	1586	-	-	No
D5:A4	1593	1597	+4	Yes
D5:A5	1592	1594	+2	Yes
D5:A6	1603	1597	-6	Yes
D6:A1	1490	-	-	No
D6:A2	1437	1444	+7	Yes
D6:A3	1586	1594	+8	Yes
D6:A4	1593	1600	+7	Yes
D6:A5	1592	1595	+3	Yes
D6:A6	1603	1601	-2	Yes

Out of eighteen experiments, twelve combinations yield positive results of formation non-covalent interactions between host and the guest. Highest success rate is observed for **D6** since it contains both HB and XB donors.

There are reported studies of co-crystals between XB donor cavitand and acceptors^{34, 40} or HB co-crystals between HB donor cavitand and acceptor.³¹ However, there are no studies on multi-functional HB/ XB cavitands.

4.4 Conclusions

The synthesis and functionalization of resorcin[4]arene based bromo cavitands with metal coordinating acac groups, XB donor and HB donor were achieved. We have described the design, synthesis, and characterization of new functionalized cavitands and we also were able to achieve the functionalization of cavitands with good yields. The aldehyde functionality is a good starting point to make new cavitands (Figure 4.25).

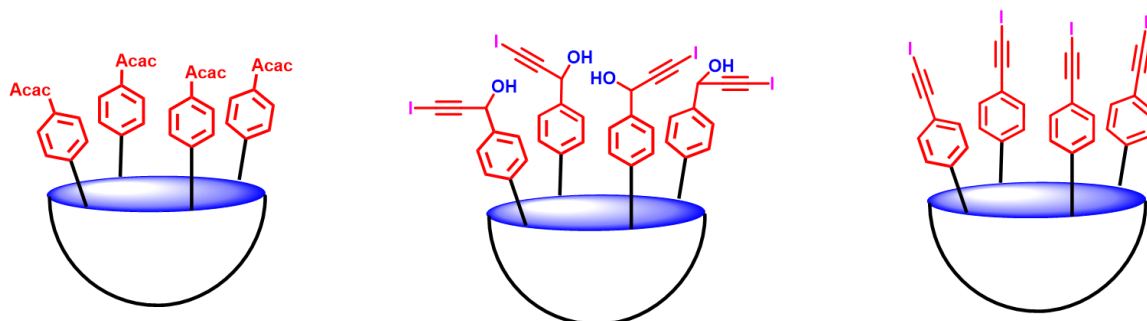


Figure 4.25 Examples for functionalized cavitands; metal-coordinating, HB/XB multi-functional and XB donor cavitands

IR spectroscopy has been used as an effective tool for identifying metal-ligand, host-guest and donor-acceptor interactions in cavitands. In addition, TGA experiments also show evidence for guest inclusion in to cavitands. UV/Vis titration was used to identify binding events and determine stoichiometry in systems such as metal-coordinating cavitands.

In conclusion, we were able to design and synthesize multi-functional functionalized cavitands which are capable of forming supramolecular architectures with suitable complementary supramolecular building blocks.

4.5 References

1. Alexov, E.; Honig, B., Chapter 2 - Structural and Energetic Basis of Molecular Recognition. In *Handbook of Cell Signaling (Second Edition)*, Bradshaw, R. A.; Dennis, E. A., Eds. Academic Press: San Diego, 2010; pp 11-13.
2. B., K., *J. prakt. Chem.* **1995**, 337 (1), 339-346.
3. Li, N.; Harrison, R. G.; Lamb, J. D., *J Incl Phenom Macrocycl Chem.* **2014**, 78 (1), 39-60.
4. El Moll, H.; Sémeril, D.; Matt, D.; Toupet, L., *Adv. Synth. Catal.* **2010**, 352 (5), 901-908.
5. Zhao, Y.; Truhlar, D. G., *J. Am. Chem. Soc.* **2007**, 129 (27), 8440-8442.
6. Krieg, E.; Weissman, H.; Shirman, E.; Shimoni, E.; Rybtchinski, B., *Nat Nanotechnol.* **2011**, 6, 141.
7. Boyd, P. D. W.; Hodgson, M. C.; Rickard, C. E. F.; Oliver, A. G.; Chaker, L.; Brothers, P. J.; Bolkskar, R. D.; Tham, F. S.; Reed, C. A., *J. Am. Chem. Soc.* **1999**, 121 (45), 10487-10495.
8. Yu, G.; Jie, K.; Huang, F., *Chem. Rev.* **2015**, 115 (15), 7240-7303.
9. Yokoyama, T.; Yokoyama, S.; Kamikado, T.; Okuno, Y.; Mashiko, S., *Nature* **2001**, 413, 619.
10. Shorthill, B. J.; Avetta, C. T.; Glass, T. E., *J. Am. Chem. Soc.* **2004**, 126 (40), 12732-12733.
11. Fujita, K.; Fujiwara, S.; Yamada, T.; Tsuchido, Y.; Hashimoto, T.; Hayashita, T., *J. Org. Chem.* **2017**, 82 (2), 976-981.
12. Gropp, C.; Quigley, B. L.; Diederich, F., *J. Am. Chem. Soc.* **2018**, 140 (8), 2705-2717.
13. Moran, J. R.; Karbach, S.; Cram, D. J., *J. Am. Chem. Soc.* **1982**, 104 (21), 5826-5828.
14. Thierry, C.; David, S.; Dominique, M.; Loïc, T., *Eur. J. Org. Chem.* **2017**, 2017 (2), 313-323.
15. Fankhauser, D.; Kolarski, D.; Grüning Wolfram, R.; Diederich, F., *Eur. J. Org. Chem.* **2014**, 2014 (17), 3575-3583.
16. Pochorovski, I.; Ebert, M.-O.; Gisselbrecht, J.-P.; Boudon, C.; Schweizer, W. B.; Diederich, F., *J. Am. Chem. Soc.* **2012**, 134 (36), 14702-14705.
17. Warmuth, R.; Makowiec, S., *J. Am. Chem. Soc.* **2007**, 129 (5), 1233-1241.
18. Liu, F.; Helgeson, R. C.; Houk, K. N., *Acc. Chem. Res.* **2014**, 47 (7), 2168-2176.
19. Kobayashi, K.; Yamanaka, M., *Chem. Soc. Rev.* **2015**, 44 (2), 449-466.
20. Tamaki, K.; Ishigami, A.; Tanaka, Y.; Yamanaka, M.; Kobayashi, K., *Chem. Eur. J.* **2015**, 21 (39), 13714-13722.
21. Sil Park, Y.; Won Kim, J.; Paek, K., *Tetrahedron Lett.* **2017**, 58 (34), 3366-3369.
22. Heidi, M.; Sara, B.; Maija, N.; Antti, Å.; Kari, R., *Chem. Eur. J.* **2006**, 12 (16), 4289-4296.
23. G., O. V.; Valentina, S.; Farhood, F.; M., R. D., *Chem. Eur. J.* **2007**, 13 (14), 4014-4023.
24. Tancini, F.; Yebeutchou Roger, M.; Pirondini, L.; De Zorzi, R.; Geremia, S.; Scherman Oren, A.; Dalcanale, E., *Chem. Eur. J.* **2011**, 16 (48), 14313-14321.
25. Hooley, R. J.; Rebek, J., *Chem. Biol.* **2009**, 16 (3), 255-264.
26. Pinalli, R.; Cristini, V.; Sottili, V.; Geremia, S.; Campagnolo, M.; Caneschi, A.; Dalcanale, E., *J. Am. Chem. Soc.* **2004**, 126 (21), 6516-6517.
27. Chavagnan, T.; Sémeril, D.; Matt, D.; Toupet, L., *Eur. J. Org. Chem.* **2016**, 2017 (2), 313-323.
28. Shamsutdinova, N. A.; Podyachev, S. N.; Sudakova, S. N.; Mustafina, A. R.; Zairov, R. R.; Burilov, V. A.; Nizameev, I. R.; Rizvanov, I. K.; Syakaev, V. V.; Gabidullin, B. M.; Katsuba, S. A.; Gubaidullin, A. T.; Safiullin, G. M.; Dehaen, W., *New J. Chem.* **2014**, 38 (9), 4130-4140.
29. Zairov, R.; Shamsutdinova, N.; Podyachev, S.; Sudakova, S.; Gimazetdinova, G.; Rizvanov, I.; Syakaev, V.; Babaev, V.; Amirov, R.; Mustafina, A., *Tetrahedron* **2016**, 72 (19), 2447-2455.

30. Ugonio, O.; Moran, J. P.; Holman, K. T., *Chem. Commun.* **2008**, (12), 1404-1406.
31. Aakeröy, C.; Schultheiss, N.; Desper, J., *CrystEngComm* **2007**, 9 (3), 211-214.
32. Kobayashi, K.; Shirasaka, T.; Yamaguchi, K.; Sakamoto, S.; Horn, E.; Furukawa, N., *Chem. Commun.* **2000**, (1), 41-42.
33. Aakeröy, C. B.; Rajbanshi, A.; Metrangolo, P.; Resnati, G.; Parisi, M. F.; Desper, J.; Pilati, T., *CrystEngComm* **2012**, 14 (20), 6366-6368.
34. Turunen, L.; Beyeh, N. K.; Pan, F.; Valkonen, A.; Rissanen, K., *Chem. Commun.* **2014**, 50 (100), 15920-15923.
35. Oliver, D.; Nils, T.; François, D., *Angew. Chem. Int. Ed.* **2015**, 54 (42), 12339-12344.
36. Turunen, L.; Pan, F.; Beyeh, N. K.; Trant, J. F.; Ras, R. H. A.; Rissanen, K., *Cryst. Growth Des.* **2018**, 18 (1), 513-520.
37. Willem M. Nissink, J.; Boerrigter, H.; Verboom, W.; N. Reinhoudt, D.; H. van der Maas, J., *J. Chem. Soc., Perkin Trans. 2* **1998**, (11), 2541-2546.
38. Sgarlata, C.; Mugridge, J. S.; Pluth, M. D.; Tiedemann, B. E. F.; Zito, V.; Arena, G.; Raymond, K. N., *J. Am. Chem. Soc.* **2010**, 132 (3), 1005-1009.
39. Beyeh, N. K.; Díez, I.; Taimoory, S. M.; Meister, D.; Feig, A. I.; Trant, J. F.; Ras, R. H. A.; Rissanen, K., *Chemical Science* **2018**, 9 (5), 1358-1367.
40. Turunen, L.; Pan, F.; Beyeh, N. K.; Cetina, M.; Trant, J. F.; Ras, R. H. A.; Rissanen, K., *CrystEngComm* **2017**, 19 (35), 5223-5229.
41. Aakeröy, C. B.; Schultheiss, N.; Desper, J., *Org. Lett.* **2006**, 8 (12), 2607-2610.
42. Gamekkanda, J.; Sinha, A.; Desper, J.; Đaković, M.; Aakeröy, C., *Crystals* **2017**, 7 (7), 226.
43. Aakeröy, C. B.; Chopade, P. D., *Org. Lett.* **2011**, 13 (1), 1-3.
44. Gamekkanda, J. C.; Sinha, A. S.; Desper, J.; Dakovic, M.; Aakeroy, C. B., *New J. Chem.* **2018**, 42 (13), 10539-10547.
45. Michel, P.; Rassat, A., *Tetrahedron Lett.* **1999**, 40 (49), 8579-8581.

Chapter 5 Crystal engineering of energetic materials: Co-crystals of nitrocarbamates with modified performance

5.1 Introduction

Energetic materials are the materials that contain a high amount of chemical energy and propellants, explosives, and pyrotechnics are the main categories of this class of materials.¹ The demand of high performance energetic materials has been increasing due to the potential applications in military, mining and construction areas.²⁻⁵ However, when the power of the materials is increased, the sensitivity towards environmental factors such as heat, impact, shock, friction, and reactivity are getting higher and the safe handling of the materials is compromised.

Common explosives which contain nitro groups and have a high nitrogen content such as: TNT, RDX, HMX, CL-20, etc., are highly sensitive and that makes them difficult to handle, store and transport.⁶ End users have to be extra careful when handling these materials to avoid accidental detonations. Therefore, designing better energetic materials that balance the power and safety is critical. When designing and synthesizing a new material, optimizing power and safety requires more time and is a costly process.⁷ The synthesis process is always risky, and the resulting product can be toxic and hazardous.⁸

In this aspect, making new materials is not always the best option and we may need alternative methods to improve the safety of existing unstable materials. A possible alternative is the use of co-crystallization which gives completely solid forms of molecules with modified properties. Co-crystallization has been used in the pharmaceutical field in order to improve properties such as thermal and physical stability, and solubility.⁹⁻¹¹ There are some examples in the literature on the use of co-crystallization in order to change the properties of the parent energetic compound.^{6, 12-15}

Nitrocarbamates are recognized as energetic materials and they can be synthesized in high yields by nitration of unsubstituted carbamates.¹⁶ Pentaerythritol tetranitrocaramate (**PETNC**) is a popular secondary explosive which is related to the well-known pentaerythritol tetranitrate (**PETN**), Figure 5.1.¹⁷

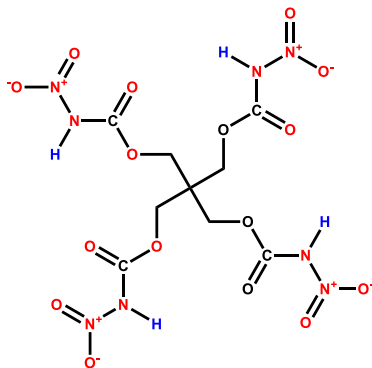


Figure 5.1 Chemical structure of **PETNC**

Most energetic nitramines show high acidity and this leads to instability and hygroscopicity.¹⁸⁻¹⁹ **PETNC (D9)** also has the same functionality and it shows high acidity and instability even though it has higher thermal, impact and friction stability. Finally, these materials can react with metal ions and can make undesirable products which can cause problems with storage and handling.

D9 in the solid state forms relatively weak hydrogen bonds between –NH (acidic proton) group and carbonyl oxygen (Figure 5.2).

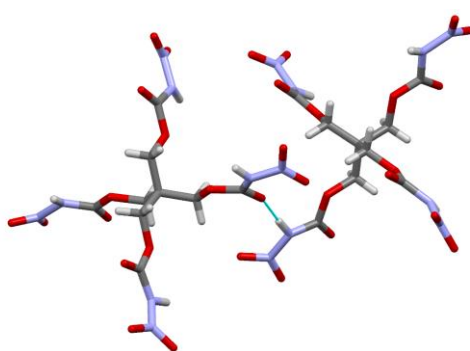


Figure 5.2 Part of crystal structure of **D9** with hydrogen bonds between acidic proton and carbonyl oxygen¹⁷

A previous report addresses the high acidity of EDNA due to the presence of nitramine group and successful use of supramolecular protecting group to suppress the acidity of the molecule by co-crystallization.²⁰ Hence, our approach here is to break these weak non-covalent interactions of **D9** by introducing strong hydrogen-bond acceptors which can produce co-crystals with modified performance compared to the parent energetic material (Figure 5.3). Since the **D9** has four –NH protons, we need to supply four acceptors to the molecule in order to balance all the interactions.

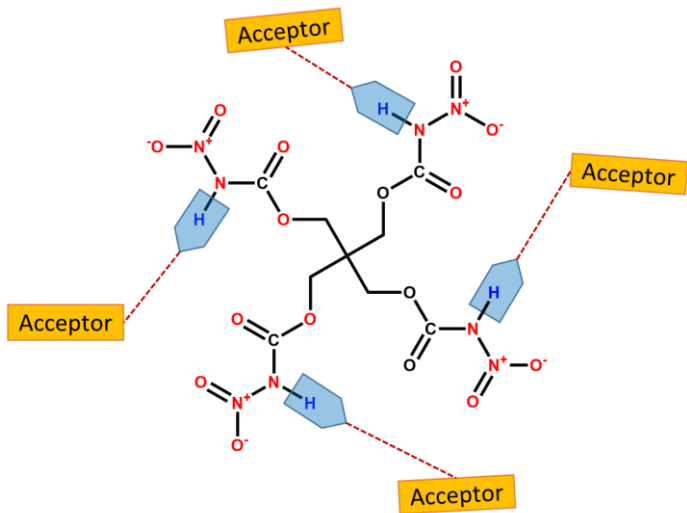


Figure 5.3 Hydrogen-bond donor sites in **D9**

In order to disrupt the weak non-covalent interactions in the **D9** molecule, several nitrogen based and oxygen based symmetric ditopic acceptors were selected (Figure 5.4). Oxygen based acceptors give an added advantage since they can increase the oxygen balance of the new material.

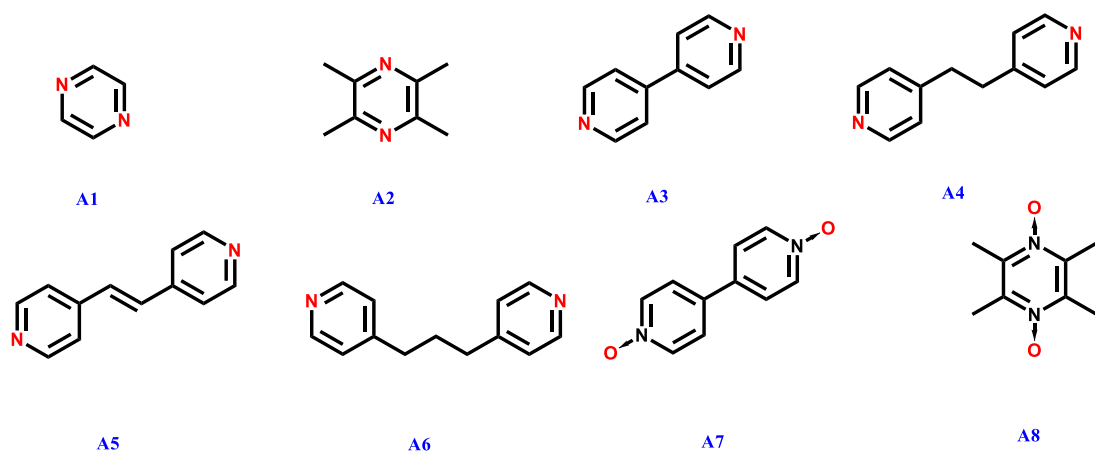


Figure 5.4 Ditopic nitrogen or oxygen based hydrogen bond acceptors (**A1-A8**)

5.1.1 Objectives of this study

This study is carried out to achieve specific goals stated below.

1. Synthesis of **PETNC (D9)** and synthesis of co-crystals thereof with suitable acceptors by using HB interaction as the non-covalent force.
2. Use of –NH proton of **D9** as potential HB donor and the driving force for the co-crystal synthesis.
3. Protection of the acidic protons of **D9** via hydrogen bonding by using suitable co-formers as supramolecular protecting groups.
4. Modification of explosive properties of **D9** in a useful manner by making co-crystals.
5. Enhance the chemical stability by reducing the reactivity of **D9** through co-crystallizations.

5.2 Experimental

5.2.1 General

All the precursors, reagents, solvents, and acceptors **A1-A7** were purchased from commercial sources and used without further purification. **A8** was synthesized using a literature reported method.²¹ ¹H NMR spectra were recorded on a Varian Unity plus 400 MHz spectrometer in CDCl₃. Infrared spectroscopy (IR) was done on a Nicolet 380 FT-IR. DSC traces were obtained on a TA Q20, using Tzero aluminum pans under N₂ (40.0 ml/min purge) and heating rate of 5 °C/min.

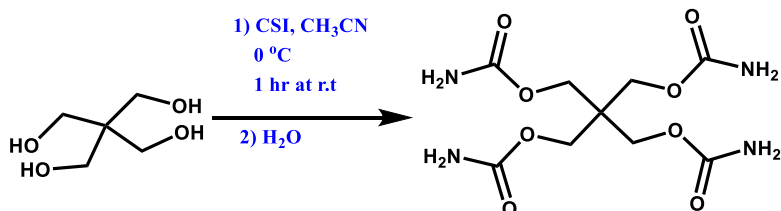
5.2.2 Safety

When handling and synthesizing energetic materials, extra precautions were taken according to the standard procedure.²² Synthesis of **D9** was done in a fume hood and non-metallic spatulas were used to avoid any mechanical stress on the energetic material. Synthesis was carried out on small scales (200-500mg at a time). **D9** was always stored in glass vials in a metal container. Kevlar gloves, safety goggles and lab coat were worn all the time when handling the compound.

5.2.3 Synthesis of energetic material

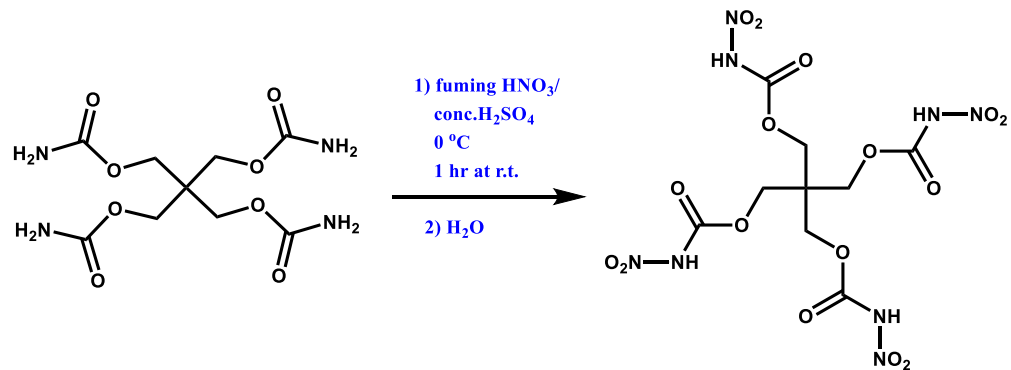
The synthesis was a two-step process and it was performed with commercially available relevant alcohol.¹⁷ The alcohol was converted to the corresponding carbamate and the resulting carbamate was nitrated in order to get the final product.

5.2.3.1 Synthesis of 2,2-bis((carbamoyloxy)methyl)propane-1,3-diyl dicarbamate



In 20mL of acetonitrile, pentaerythritol (0.50 g, 3.7 mmol) was suspended and it cooled in an ice bath. Chlorosulfonyl isocyanate (CSI) (2.55 g, 18 mmol) was added very slowly at 0 °C in to the suspension. During the addition, the alcohol was dissolved and at the end of the addition of CSI, a precipitate was observed. Then the ice bath was removed and mixture was stirred for 1 hour at room temperature. After 1 hour, the reaction mixture was cooled by placing an ice bath and 10 mL of water was added with caution. Acetonitrile was removed by rotavap and the precipitate formed was filtered and washed thoroughly with cold water and dried to obtain pure product as white color solid. Yield 1.03 g (90 %): m.p. 235 °C (DSC 5 °C/ min): ¹H NMR (δ_{H} , DMSO-d6, 400 MHz): 6.55 (8H, br), 3.92 (8H, s).

5.2.3.2 Synthesis of 2,2-bis(((nitrocarbamoyl)oxy)methyl)propane-1,3-diyl bis(nitrocarbamate) or Pentaerythritol tetranitrocaramate (D9)



At 0 °C, fuming nitric acid (99%, 4 mL) was dropped into concentrated sulfuric acid (4 mL) in an ice bath. 2,2-Bis((carbamoyloxy)methyl)propane-1,3-diyl dicarbamate (0.3 g, 0.97 mmol) was added in small portions to this mixture in the ice bath. The resulting mixture was stirred for 10 min at 0 °C and then further stirred for 1 hour at room temperature. Then the mixture was poured into ice/water (200 mL) and a precipitate was formed. The precipitate was filtered and washed three times with water, and dried to obtain the pure product as a white solid. Yield 0.4 g (84%): m.p.

215 °C) dec. (DSC 5 °C/ min: ^1H NMR (δ_{H} , DMSO-d6, 400 MHz): 4.23 (8H, s). IR -NH 3174 cm $^{-1}$, -NO₂ 1608 and 1322 cm $^{-1}$.

5.2.4 Synthesis of co-crystals

D9 (10 mg in each case) was combined with eight acceptors in stoichiometric ratio (1:2/ donor: acceptor) and dissolved in minimum amount of methanol and kept in small vials for slow evaporation in order to get X-ray quality co-crystals. Resulting crystal/ solid was analysed by IR spectroscopy and DSC to identify the formation of co-crystals.

5.2.5 Oxygen balance calculation

The oxygen balance which indicates the degree to which an explosive can be oxidized²³ was calculated using following equation for **D9** and co-crystals.

$$OB\% = \frac{-1600}{Molecular\ weight\ of\ compound} \left(2X + \left(\frac{Y}{2} \right) + M - Z \right)$$

Where,

X = number of atoms of carbon,

Y = number of atoms of hydrogen,

Z = number of atoms of oxygen, and

M = number of atoms of metal

5.2.6 Detonation velocity and pressure calculations

The detonation velocity and pressure of explosives and co-crystals were predicted with the nitrogen equivalent equations shown below.²⁴

$$V_D = (690 + 1160\rho_0)\Sigma N$$

$$P = 1.092(\rho_0\Sigma N)^2 - 0.574$$

$$\Sigma N = 100\Sigma x_i N_i/M$$

Where,

V_D = Detonation velocity

ρ_0 = Density of an explosive

ΣN = Nitrogen equivalent of the detonation products

N_i = Nitrogen equivalent index of certain detonation products

X_i = Mole number of certain detonation products produced by a mole of explosive

Nitrogen equivalent indices of detonation products are shown in the Table 5.1.

Table 5.1. Nitrogen equivalent indices of detonation products

Detonation product	H ₂ O	CO	CO ₂	N ₂	C	O ₂	H ₂
Nitrogen equivalence index	0.54	0.78	1.35	1	0.15	0.5	0.290

According to the formation of detonation products (H₂O – CO – CO₂), nitrogen equivalence (ΣN) of the detonation products were calculated.

5.2.7 Impact sensitivity test (Drop test)

Impact sensitivity of D9 and its co-crystals were measured by small-scale impact drop testing. The apparatus is designed to use small amounts of explosives in differential scanning calorimetry (DSC) pans. Freefalling 5 lbs of weight on the explosive was used to observe the detonation of the material (Figure 5.5).

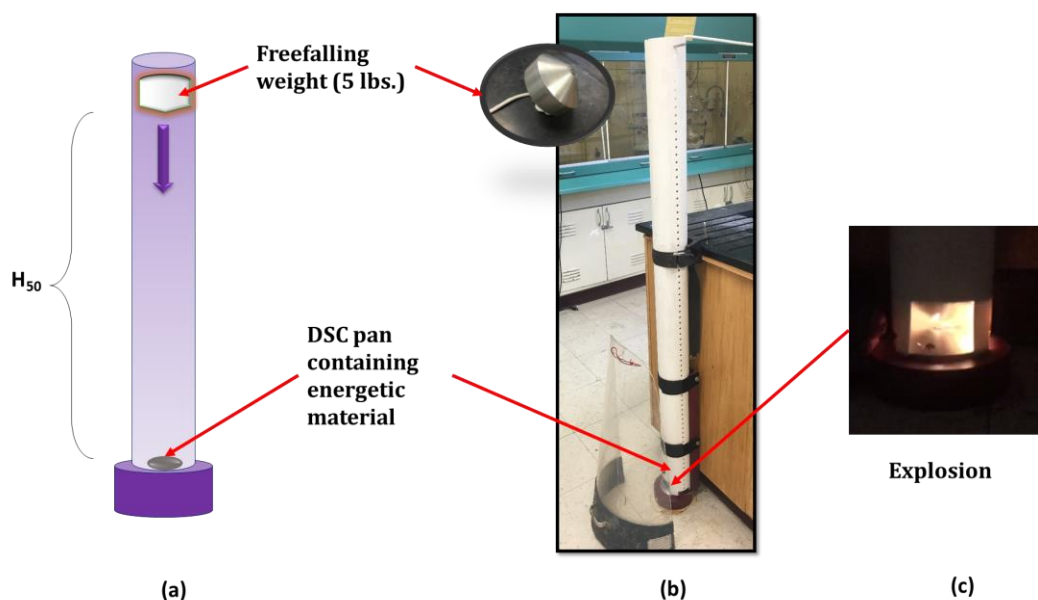


Figure 5.5 (a) Schematic diagram of impact sensitivity test apparatus, (b) Impact sensitivity test apparatus with 5 lbs weight (c) explosion of an energetic material

The freefalling weight was dropped from different heights in order to determine the H₅₀ value of the material that exhibited 50% chance of detonation. The maximum height of the apparatus was 146 cm. This equipment was used for relative comparison of the co-crystals with parent energetic material.

5.2.8 Reactivity analysis

The corrosiveness of **D9** and the newly formed co-crystals were analyzed in order to get a qualitative idea about the acidity of the materials. The effect of the energetic material on metal (Cu) was observed by placing the material (~5 mg) on a metal strip for one hour with the addition of methanol drop.

5.3 Results

5.3.1 IR analysis

The initial co-crystallization screening was carried out using IR spectroscopy for all the solids produced from attempted co-crystallization experiments. Seven of eight co-crystal attempts show the formation of co-crystals between **D9** and the acceptors (Table 5.2). The IR spectra of both starting materials were compared with resulting crystal/solid in order to identify the formation of co-crystals. A comparison between **D9**, **A8** and the co-crystal **D9:A8** is shown in Figure 5.6. The peak shift of both donor (e.g. from 3174 cm⁻¹ to 2975 cm⁻¹, from 1777 cm⁻¹ to 1780 cm⁻¹) and acceptor (e.g. from 1523 cm⁻¹ to 1510 cm⁻¹) can be observed with the formation of co-crystals. The peak shifting of the carbonyl group (C=O stretch) and the –NH bending are shown in the Table 5.2.

Table 5.2 IR analysis of attempted co-crystallization experiments

Combination	C=O stretch of D9 (cm ⁻¹)	NH bending of D9 (cm ⁻¹)	Co-crystal or not
D9	1777	1608	-
D9 : A1	1777	1609	No
D9 : A2	1775	1608	Yes
D9 : A3	1790 , 1690	1630, 1605	Yes
D9 : A4	1775, 1679	1634, 1604	Yes
D9 : A5	1676	1625	Yes
D9 : A6	1692	1635	Yes
D9 : A7	1774	1608	Yes
D9 : A8	1780	1608	Yes

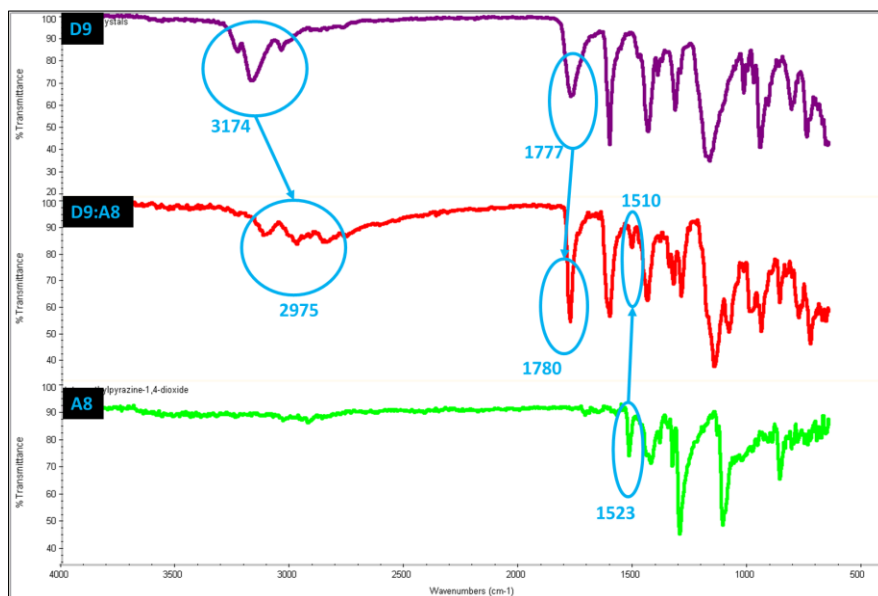


Figure 5.6 IR comparison between **D9**, **A8** and the **D9:A8**

5.3.2 Crystal structures

Three of the seven co-crystals attempts gave X-ray quality crystals (**D9:A3**, **D9:A7** and **D9:A8**). The crystal structure determination shows the formation of **D9**³⁻:**A3H**₂²⁺: **A3H**⁺ salt instead of co-crystal with the proton transfer between –NH group of **D9** and the pyriyl-N of **A3** (Figure 5.7). **D9** is tri-deprotonated while one **A3** is di-protonated and the other **A3** is singly protonated.

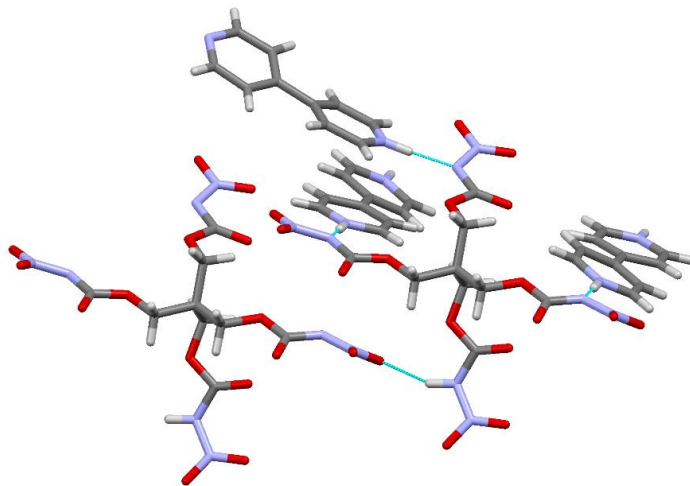


Figure 5.7 Part of the crystal structure of **D9**³⁻:**A3H**₂²⁺: **A3H**⁺ that shows the interactions originates from **D9**³⁻

There are three charge assisted HBs per **D9**³⁻ which are between **D9**³⁻ and **A3H**₂²⁺, **A3H**⁺.

The non-protonated side of **A3H**⁺ makes only short contacts to the another **A3H**₂²⁺. In addition to that, one HB interaction between -NH proton and the nitro group of another **D9**³⁻ is also present.

The three components are present in 1:1:1 ratio in the crystal packing (Figure 5.8).

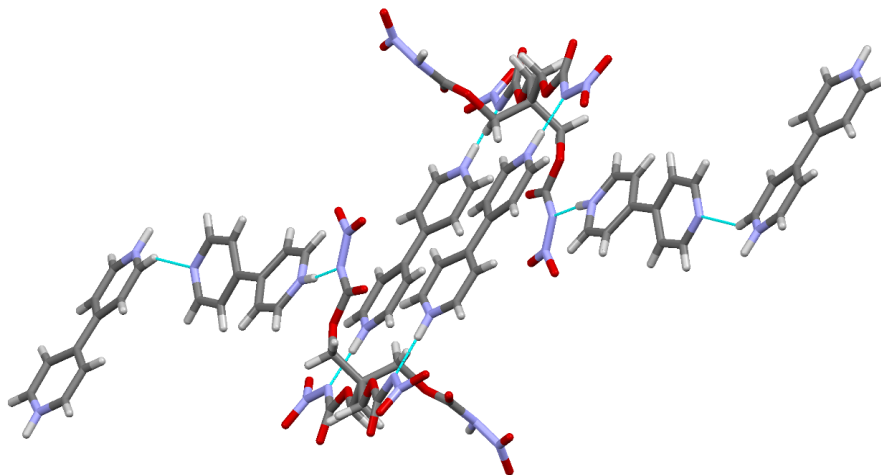


Figure 5.8 Part of the crystal structure of **D9**³⁻:**A3H**₂²⁺: **A3H**⁺ that shows additional interactions between donors and acceptors

When the oxygen based acceptor (**A7**) is introduced to the energetic material, the resulting crystal structure revealed that this time it has only neutral components (Figure 5.9). Hydrogen

bonding between –NH protons and the oxygen of acceptor were observed and no proton transfer was observed between donors and acceptors when the acceptor is oxygen. Two –NH protons interact with two different acceptor sites of two acceptor molecules and the other two –NH protons interact only with one oxygen atom of an acceptor by making bifurcated hydrogen bonding. Surprisingly, one solvent molecule (Methanol) also makes hydrogen bonding with the **D9** molecule due to interaction between the hydroxyl hydrogen of methanol and a carbonyl oxygen of **D9** molecule. The overall stoichiometry in the crystal packing is 1:2:1 for donor: acceptor: solvent (**D9:2A7:CH₃OH**).

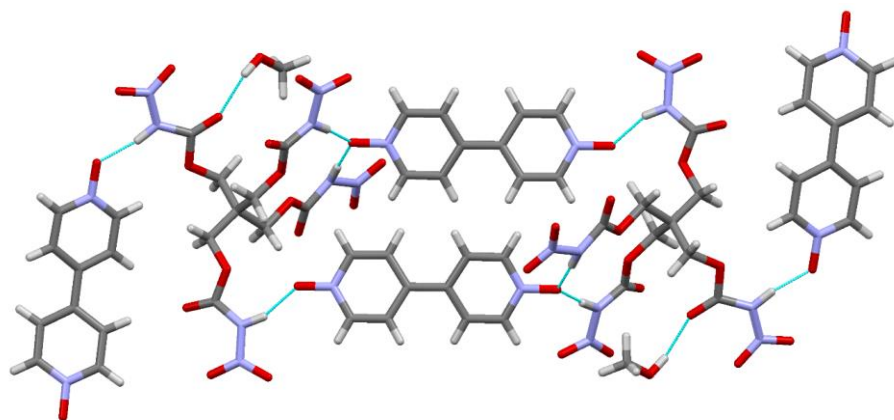


Figure 5.9 Part of the crystal structure of **D9:2A7:CH₃OH** that shows the HB interactions and stoichiometry between **D9: A7: methanol (1:2:1)**.

One **A7** molecule forms single HB interaction and bifurcated HB interactions with **D9**. Other **A7** shows two non-covalent interactions: one being HB interaction to **D9** and other being short contact between oxygen and hydrogen of phenyl of group **A7**.

The crystal structure of **D9:A8** reveals the formation of co-crystal between donor and acceptor (Figure 5.10). Again there are not any proton transfer and no solvent molecules are incorporated to the crystal structure. Bifurcated hydrogen bonds are observed on both sides of the acceptor molecule (Figure 5.11). One acceptor molecule interacts with four donors. Overall packing

indicates the formation of co-crystal with a 1:1 stoichiometry between donor and the acceptor molecules.

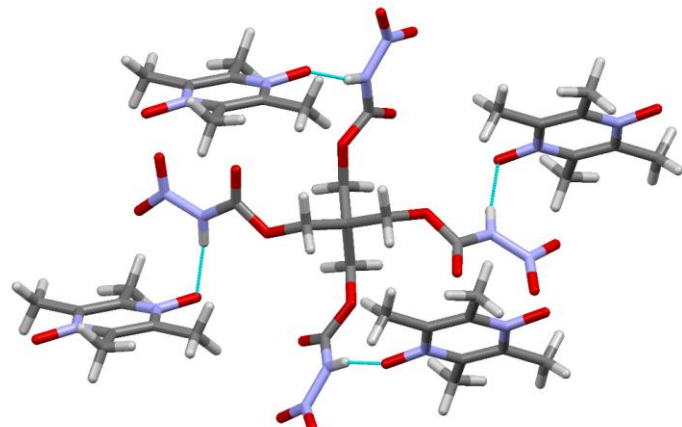


Figure 5.10 Part of the crystal structure of **D9:A8** that shows HBs originate from **D9**

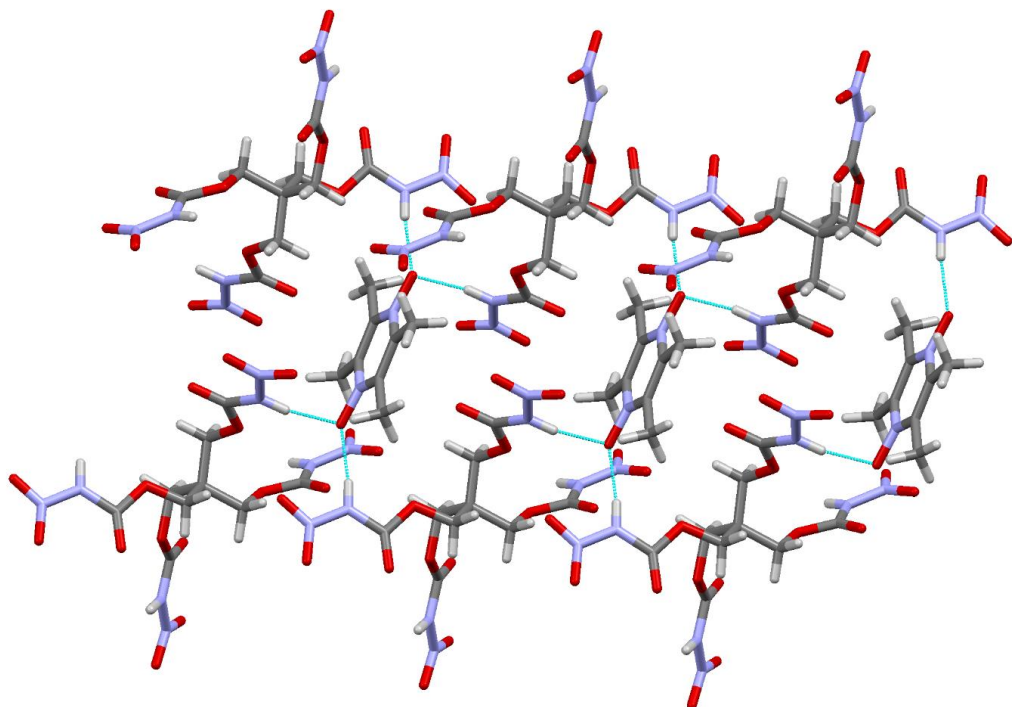


Figure 5.11 Part of the crystal structure of **D9:A8** that shows bifurcated nature of HB interactions

All the hydrogen bonding distances and angles of co-crystal, solvate and salt are shown in Table 5.3.

Table 5.3 Hydrogen bond parameters of newly formed energetic materials

Co-crystal/ solvate/ salt	D-H \cdots A	D \cdots A (Å)	D-H \cdots A($^{\circ}$)
D9$^{3-}$:A3H$_2^{2+}$: A3H$^{+}$	N30 H30 O25	3.028(3)	144(2)
	N37 H37 N22	2.746(3)	178(3)
	N43 H43 N6	2.715(3)	178(4)
	N49 H49 N14	2.771(3)	172(3)
D9:2A7:CH$_3$OH	N6 H6 O54	2.647(3)	160(3)
	N14 H14 O40	2.669(3)	170(2)
	N22 H22 O61	2.716(3)	173(2)
	N30 H30 O61	2.685(3)	175(3)
	O63 H63 O13	2.810(3)	169(5)
D9:A8	N14 H14 O21	2.772(2)	170.1(18)
	N6 H6 O21	2.767(2)	168(2)

5.3.3 Thermal properties

Thermal analysis for all the X-ray quality crystals and the **D9** were performed using DSC (Figure 5.12). Decomposition temperature and the decomposition enthalpy were determined and compared with the parent material (Table 5.4).

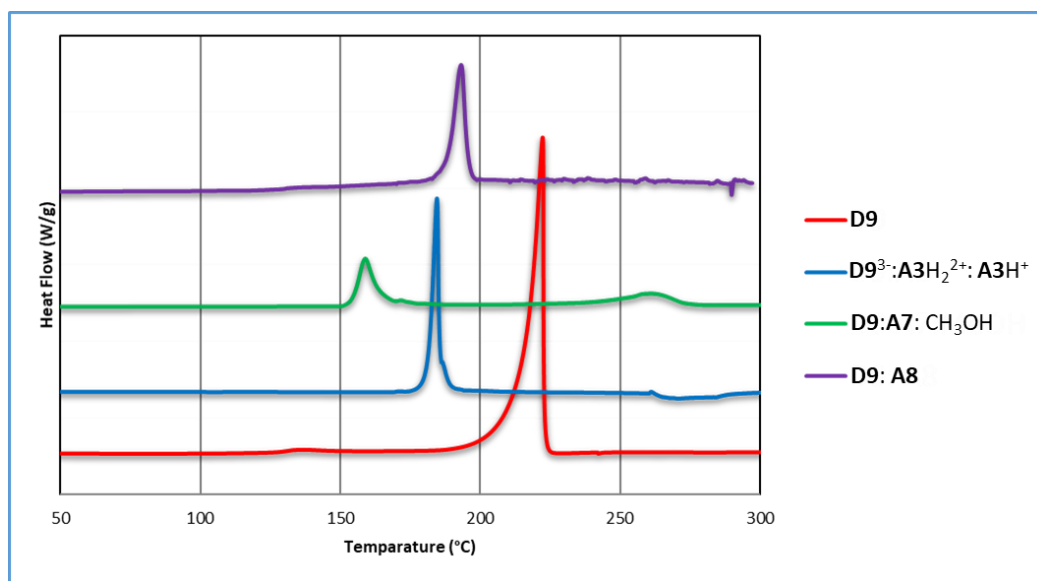


Figure 5.12 DSC traces comparison of **D9** and co-crystal/salt/solvate.

Table 5.4 Thermal properties of energetic materials

Compound/ co-crystal/ salt/ solvate	Co-former melting point (°C)	Co-crystal/ salt/ solvate	
		Decomp. point (°C) (on set)	Decomp. enthalpy (J/g)
D9	-	215	1847
D9³⁻: A3H₂²⁺: A3H⁺	109-112	181	729
D9:2A7:CH₃OH	220	154, 248	600, 400
D9: A8	224	188	616

5.3.4 Oxygen balance of the energetic materials

Oxygen balance data are summarized in Table 5.5. The parent energetic material has the most favorable oxygen balance (-26%) compared to the newly formed energetic materials. Least favorable oxygen balance is observed for **D9³⁻: A3H₂²⁺: A3H⁺** which is -112%. More negative oxygen balance indicates that there is an insufficient amount of oxygen for the complete combustion of the energetic material.

Table 5.5 Oxygen balance of energetic materials

Compound/ co-crystal/ salt/ solvate	D9	D9 ³⁻ : A3H ₂ ²⁺ : A3H ⁺	D9:2A7:CH ₃ OH	D9: A8
Oxygen balance %	-26	-112	-99	-68

5.3.5 Detonation pressure and detonation velocity

The detonation properties were calculated using the experimental density obtained from the crystal structures (Table 5.6). Detonation performance of the newly produced energetic materials are lower compared to **D9**.

Table 5.6 Detonation velocity and detonation pressure of energetic materials

Compound/ co-crystal/ salt	Density (g/cm ³)	Detonation velocity (km/s)	Detonation pressure (GPa)
D9	1.765 (100K)	8.1	29.9
D9³⁻: A3H₂²⁺: A3H⁺	1.500 (130K)	5.8	13.5
D9:2A7:CH₃OH	1.635 (130K)	6.5	18.0
D9: A8	1.616 (180K)	7.0	20.5

5.3.6 Impact sensitivity test

Impact sensitivity test was performed for **D9** and the all newly formed energetic materials. H_{50} value for the **D9** observed was 130 ± 1 cm and the salt **D9³⁻: A3H₂²⁺: A3H⁺** had lower sensitivity than the parent energetic material (144 ± 1 cm). **D9:2A7:CH₃OH** and **D9:A8** showed even lower sensitivity towards impact (H_{50} values are beyond the limit of the apparatus >146 cm).

5.3.7 Reactivity

D9 and the newly formed energetic materials were tested for the reactivity towards copper metal for 1 hour (Figure 5.13). **D9** showed the corrosion on the copper strip and the newly formed energetic materials did not show any significant corrosion after 1 hour.

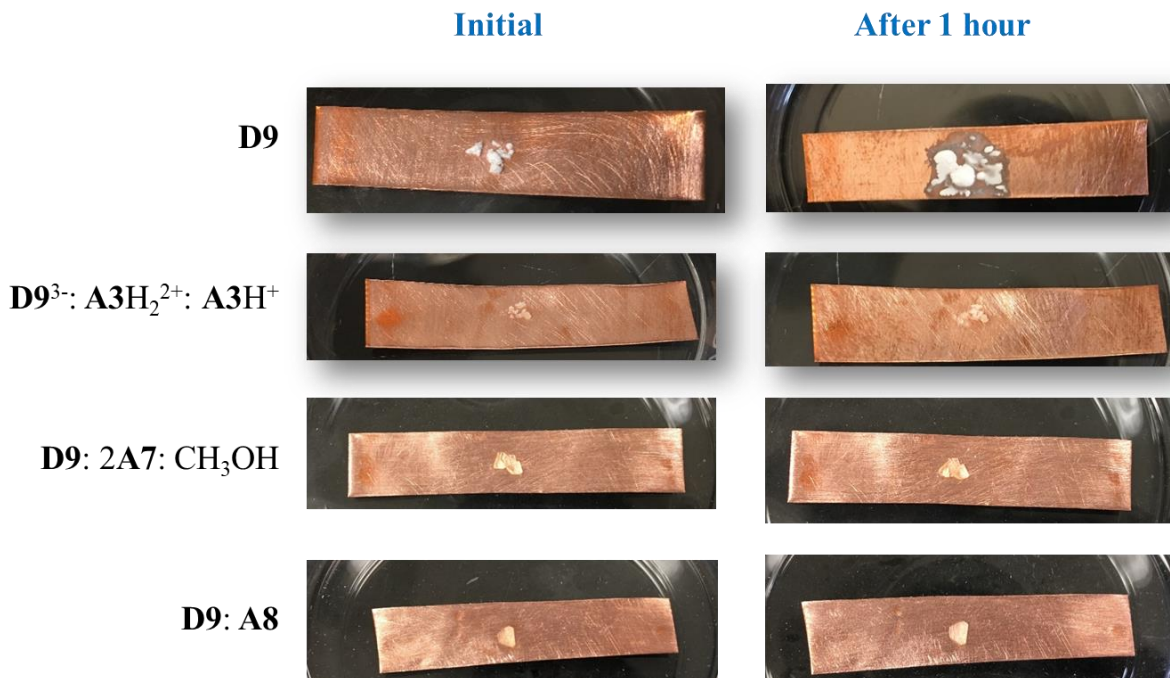


Figure 5.13 On left; **D9** and all three newly formed energetics placed on copper strip and on the right; after 1 hour with the addition of a drop of methanol

5.4 Discussion

5.4.1 IR spectroscopy analysis

The IR spectroscopy can be effectively used for screening of co-crystal formation. When a salt formation occurs between a HB donor and an acceptor such as: pyridine derivative, the large shift of characteristic IR stretch peak of pyridine derivative (shift to ca. 1640 cm^{-1}) indicates the protonation of it by a strong acid.²⁵ Since **D9** is acidic, possible salt formation can be predicted when IR peak shifts closer to 1640 cm^{-1} in a donor acceptor combination. Out of six, five possible salt formation can be expected based on IR evidence shown in Table 5.7.

Table 5.7. IR peak shift of pyridine derivatives

Combination	Characteristic pyridine derivative peak (cm^{-1})		Change (cm^{-1})	Possible salt?
	Free	Bound		
D9:A3	1586	1606, 1628	+19, +42	Yes
D9:A4	1593	1635	+42	Yes
D9: A5	1592	1626	+34	Yes
D9:A6	1603	1635	+32	Yes

5.4.2 Structural analysis

The presence of four hydrogen-bond donors enables **D9** to interact with four acceptor sites available from co-former/ **D9** in the formation of solid state structures. Hydrogen bonding between-NH protons and carbonyl hydrogen was broken with the addition of strong hydrogen bond acceptors to the **D9** molecule. In $\text{D9}^{3-}\text{: A3H}_2^{2+}\text{: A3H}^+$, proton transfer was observed from three –NH group to pyridyl-N of **A3** due to the high acidity of –NH protons by making charge assisted hydrogen bonds between donor and acceptor. Proton transfer does not happen when the remaining proton interacts with the weak acceptors such as: oxygen of nitro group. There are several reported nitro carbamates that undergo proton transfer with relatively basic HB donors. In a previous study, **D9** shows proton transfer with ammonia by making **D9** tetra-anion and

ammonium cations.¹⁷ Another energetic nitrocarbamate, 2,2,2-trinitroethyl nitrocarbamate (**NTNC**), has shown formation of an anion by proton transfer with basic reagents such as ammonium carbonate, guanidine carbonate and aminoguanidine bicarbonate.²⁶ Furthermore, **NTNC** makes charge assisted HB interactions with triazoles such as 4-amino-1,2,4-triazole and 4-amino-1,2,4-triazole.²⁶

Immediate precipitate formations were observed when **D9** reacted with nitrogen based acceptors, **A4**, **A5** and **A6**. ¹H NMR experiments were performed for resulting solids to get more information. Figure 5.14 shows the ¹H NMR spectra comparison between **D9**, **A4** and **D9:A4**. Figure 5.15 shows spectra comparison between **D9**, **A4** and **D9:A5**.

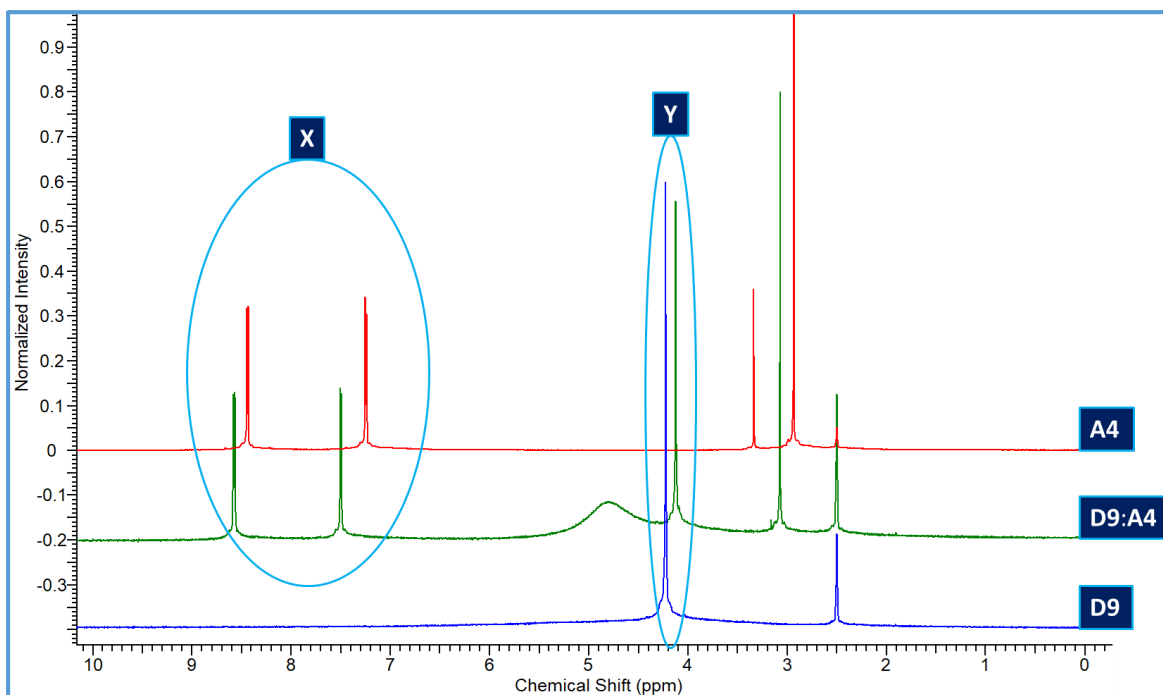


Figure 5.14. ¹H NMR spectra comparison between **D9**, **A4** and **D9:A4**

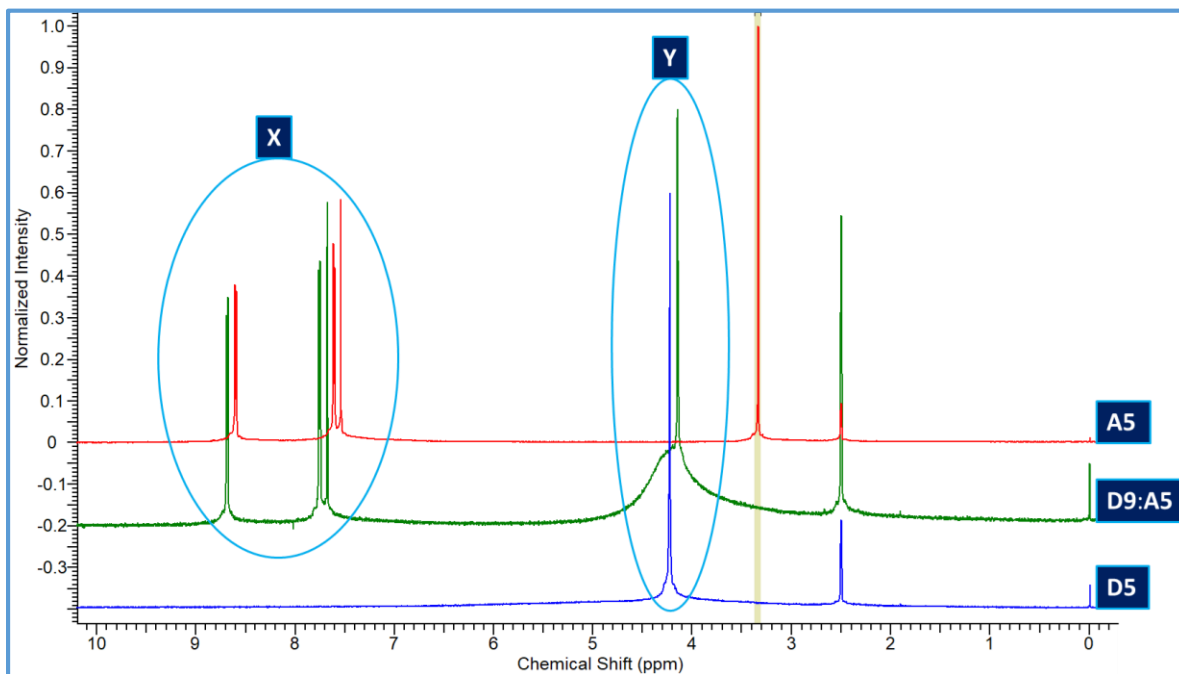


Figure 5.15. ^1H NMR spectra comparison between **D9**, **A5** and **D9:A5**

^1H NMR analysis clearly indicates the presence of both donor and acceptor in the newly formed solid and the significant ^1H NMR peak shift of acceptors in the vicinity of the nitrogen (X) clearly indicates the formation of salts.²⁷ In addition, the significant peak shift in region Y in both cases indicate the change of chemical structure of **D9**.

When less basic acceptors (**A7** and **A8**) than **A3** are introduced to the **D9**, the proton transfer from donor to acceptor is not observed. When comparatively high basic acceptors are introduced to the acidic explosive, proton transfer can be observed. In the presence of two lone pairs on oxygen acceptors, there is a trend to form bi-furcated hydrogen bonding in **D9:A7**. The ^1H NMR analysis of solvate **D9:2A7:CH₃OH** does not indicate significant change of peaks in the regions X and Y suggesting that there is no proton exchange between donor and acceptor (Figure 5.16). However, very little peak shift in the regions of X and Y shows the formation of solvate. In addition to that, the presence of methanol in the crystal is confirmed by the peak that corresponds to methyl group in the NMR spectrum.

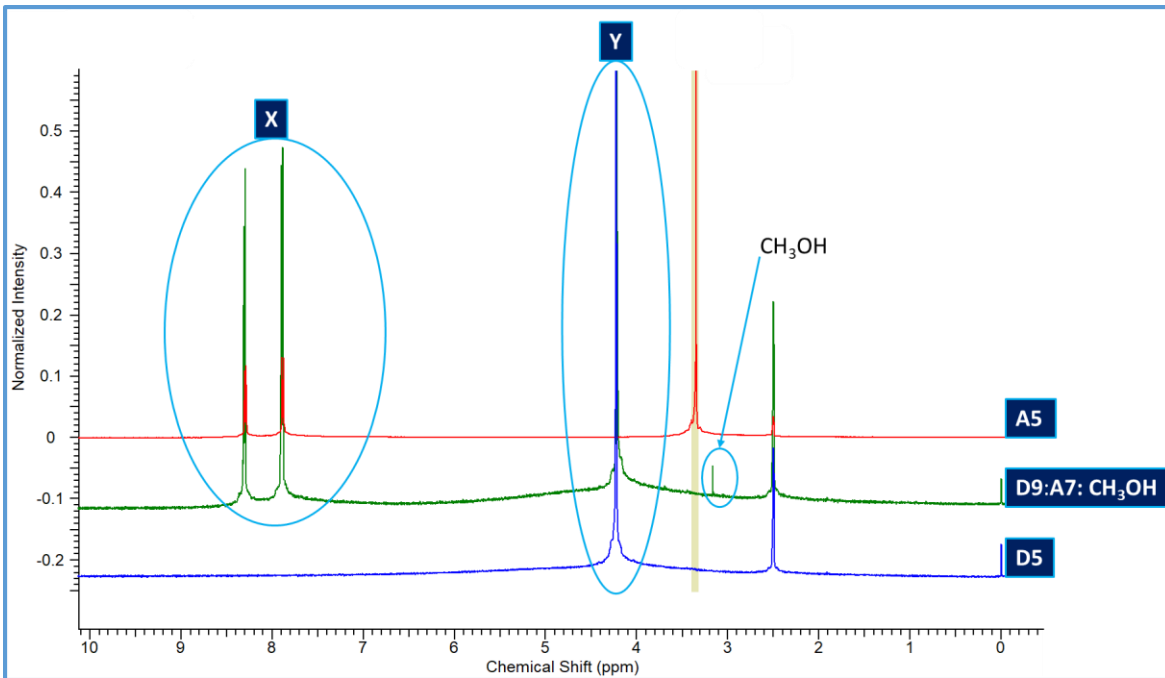


Figure 5.16. ^1H NMR spectra comparison between **D9**, **A7** and **D9:2A7:CH₃OH**

Bifurcated HB bond formation is possible when oxygen is the acceptor atom. There are several examples for bifurcated HB interactions between nitrogen of N-oxide functionality and –NH proton according to CSD data (Figure 5.17).²⁸ The most frequent HB distances (D-H…O) are around $r(\text{N} \cdots \text{O})$ 2.90 Å to 2.95 Å and the observed distances in this study are ($r_1 = 2.772(2)$ Å and $r_2 = 2.767(2)$ Å) shorter and thereby stronger than the most frequent values reported in the literature.

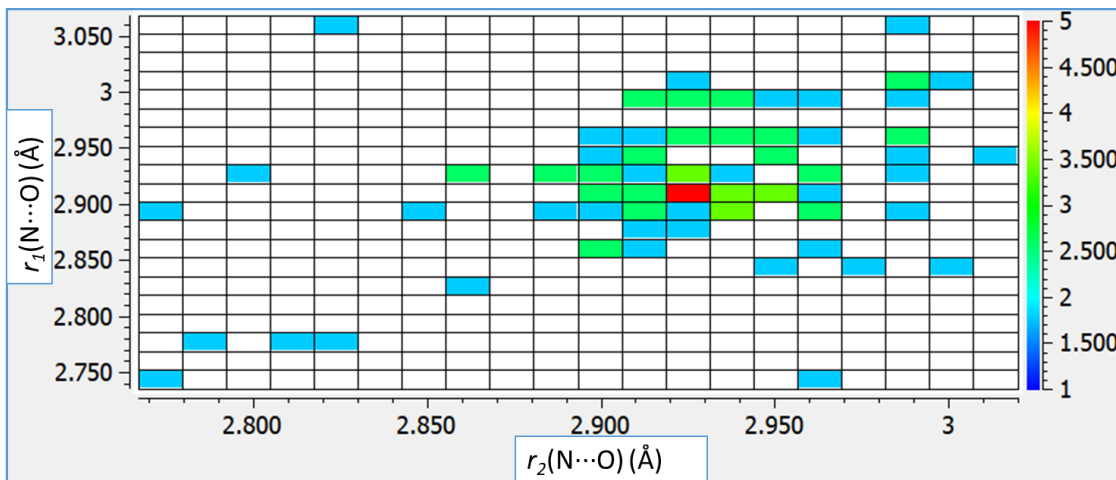


Figure 5.17. Heat plot of bifurcated HB distances between N-oxide and -NH proton²⁸

5.4.3 Thermal analysis

As expected with the introducing of the non-energetic acceptors to **D9**, reduction of decomposition enthalpy was observed. The decomposition temperatures for all the co-crystal/solvate/salt have lower value compared to **D9**, but all the values are higher than 150 °C indicating that they are relatively stable toward heat. The highest decomposition temperature was observed in the co-crystal compared to the salt and the solvate. On the other hand, the lowest decomposition was observed with the solvate. Incorporation of non-energetic solvent molecules to the crystal lattice reduces the thermal properties of the energetic material.

The removal of the solvent from the solvate **D9:2A7:CH₃OH** was not visible in DSC experiment (Figure 5.12). However, the TGA experiment shows the weight loss around 4% which indicates the loss of one methanol molecule from the crystal, at the same temperature of the decomposition of the salt (Figure 5.18). Since both solvent escape and decomposition of the energetic material occur at same temperature, the solvent escape event cannot be seen in DSC trace.

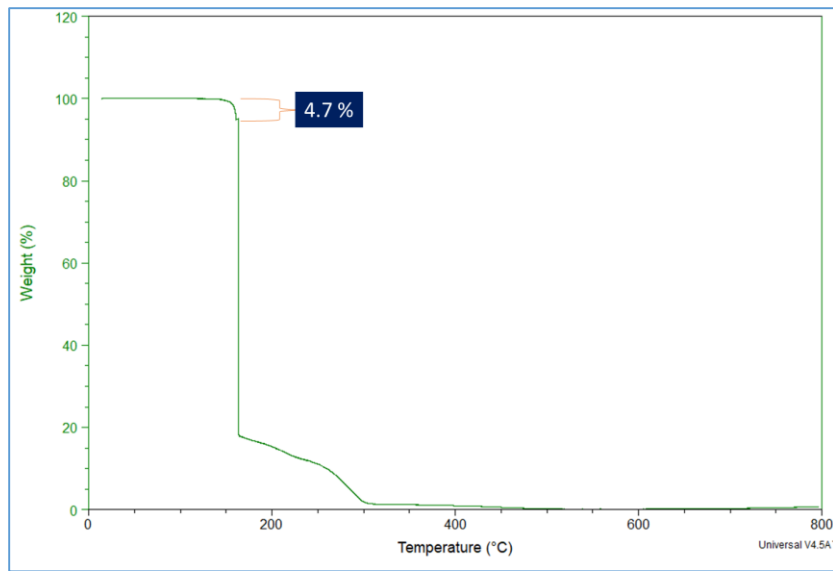


Figure 5.18. TGA trace of solvate **D9:2A7:CH₃OH**

5.4.4 Detonation performance analysis

Density and the detonation products are main factors that affect the detonation properties of the material. It was found that the high density explosives have better performance.²⁹ Newly formed compounds showed lower density compared to **D9**, hence the calculated detonation velocity and the pressure have become lower as expected.

The use of oxygen based acceptors (N-oxide) containing nitrogen and oxygen benefit the newly modified energetic material due to the increase of oxygen balance compared to nitrogen based acceptors. Compound **D9:A3** shows the least favorable oxygen balance compared to the rest due to the absence of additional oxygen in the acceptor molecule **A3**.

5.4.5 Improvement of impact sensitivity

D9 has identified as relatively low impact, and friction sensitive explosive. The impact sensitivity for the all newly formed energetic materials was tested to identify the changes of the packing of molecules. In all the cases, improved impact sensitivities were observed and the cases with **D9:A7** and **D9:A8**, the material can be considered as insensitive towards impact. The packing

and strong HB interactions of the new crystal lattice buffer the stress coming from the impact by avoiding the detonation at lower H₅₀ values.

5.4.6 Chemical reactivity/ instability modifications

The acidic protons of the **D9** explosive cause problems when stored in metal containers. Co-crystallization of **D9** blocks the reactivity of the acidic proton by making strong hydrogen bonding with chemically unstable **D9** explosive. It is clear that the corrosive nature of **D9** has changed in all three newly formed energetic materials.

5.5 Conclusions

Energetic material **PETNC (D9)** was synthesized and potential of co-crystals formation with seven out of eight acceptors was revealed by IR spectroscopy screening. A co-crystal, salt and a solvate were obtained in co-crystallization experiments with acceptor **A3**, **A7** and **A8**. The formation of salts between **D9** and **A4**, **A5** and **A6** was confirmed by NMR spectroscopy.

The –NH proton was the driving force to formation of co-crystals or salts with the acceptors. Due to the high reactivity and acidity of the proton, the formation of salts was observed instead of co-crystals. The co-crystal formation was observed via -NH···O HB interaction in the presence of oxygen based acceptors (Figure 5.19). Charge assisted HB (-N⁻···HN⁺) was observed in the presence of nitrogen based acceptors due to the high acidity of **D9** and the relatively high basicity of acceptor molecule.

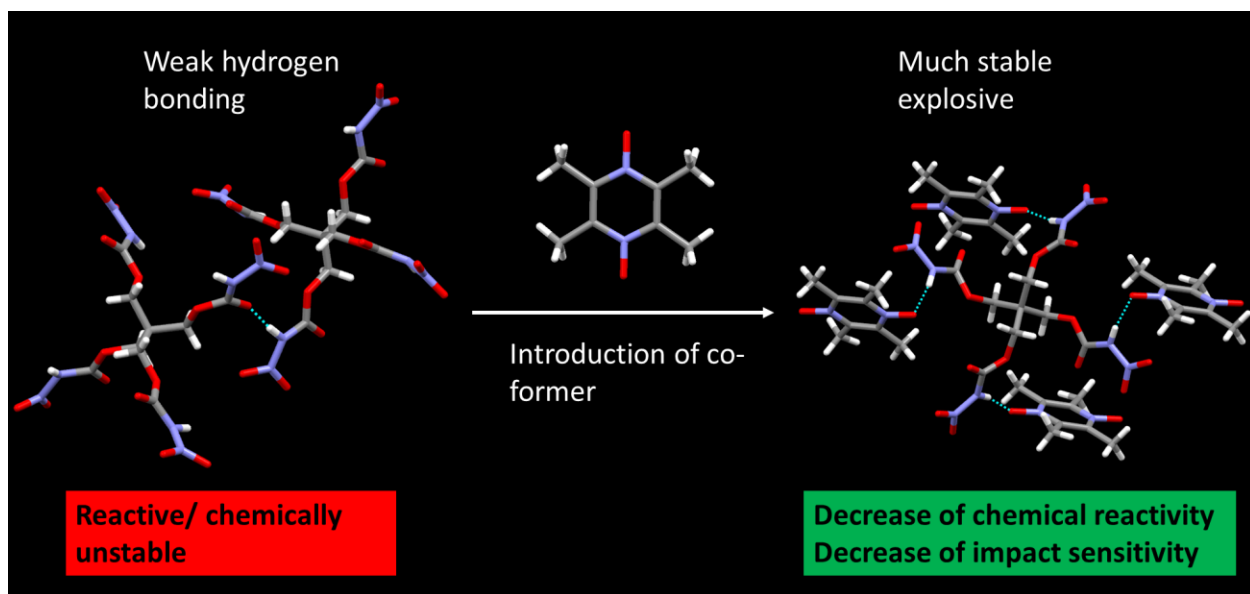


Figure 5.19. Modification of explosive properties by co-crystallization

The performance of the newly formed explosives including the oxygen balance was found better when the acceptors were oxygen based (N-oxide). Impact sensitivity of explosive **D9** was somewhat reduced with introduction of non-energetic acceptors to **D9**. Tolerance of **D9** to impact was indicated by the drop test.

The reactivity of **PETNC** drastically reduced with the introduction of co-formers which can behave as supramolecular protecting groups for the acidic proton. In conclusion, the modulation of explosive properties and enhancement of the reactivity of **PETNC** were achieved by systematic co-crystallization experiments.

5.6 References

1. Landenberger, K. B.; Bolton, O.; Matzger, A. J., *J. Am. Chem. Soc.* **2015**, *137* (15), 5074-5079.
2. Tao, J.; Jin, B.; Chu, S.; Peng, R.; Shang, Y.; Tan, B., *RSC Advances* **2018**, *8* (4), 1784-1790.
3. Gidaspov, A. A.; Bakharev, V.; Suponitsky, K. Y.; Nikitin, V. G.; Sheremetev, A. B., *RSC Advances* **2016**, *6* (106), 104325-104329.
4. Fischer, D.; Klapötke, T. M.; Stierstorfer, J., *Angew. Chem. Int. Ed.* **2015**, *54* (35), 10299-10302.
5. Dippold, A. A.; Klapötke, T. M., *J. Am. Chem. Soc.* **2013**, *135* (26), 9931-9938.
6. Landenberger, K. B.; Matzger, A. J., *Cryst. Growth Des.* **2012**, *12* (7), 3603-3609.
7. Xue, H.; Gao, Y.; Twamley, B.; Shreeve, J. n. M., *Chem. Mater.* **2005**, *17* (1), 191-198.
8. Sivaprakash, P.; Karthikeyan, L. M.; Joseph, S., *APCBEE Procedia* **2014**, *9*, 187-191.
9. Aakeröy, C. B.; Forbes, S.; Desper, J., *J. Am. Chem. Soc.* **2009**, *131* (47), 17048-17049.

10. Remenar, J. F.; Morissette, S. L.; Peterson, M. L.; Moulton, B.; MacPhee, J. M.; Guzmán, H. R.; Almarsson, Ö., *J. Am. Chem. Soc.* **2003**, 125 (28), 8456-8457.
11. Schultheiss, N.; Newman, A., *Cryst. Growth Des.* **2009**, 9 (6), 2950-2967.
12. Landenberger, K. B.; Bolton, O.; Matzger, A. J., *Angew. Chem. Int. Ed.* **2013**, 52 (25), 6468-6471.
13. Bennion, J. C.; McBain, A.; Son, S. F.; Matzger, A. J., *Cryst. Growth Des.* **2015**, 15 (5), 2545-2549.
14. Bolton, O.; Matzger, A. J., *Angew. Chem. Int. Ed.* **2011**, 50 (38), 8960-8963.
15. Bennion, J. C.; Siddiqi, Z. R.; Matzger, A. J., *Chem. Commun.* **2017**, 53 (45), 6065-6068.
16. Axthammer, Q. J.; Krumm, B.; Klapötke, T. M., *J. Org. Chem.* **2015**, 80 (12), 6329-6335.
17. Axthammer, Q. J.; Krumm, B.; Klapötke, T. M., *Eur. J. Org. Chem.* **2015**, 2015 (4), 723-729.
18. Qasim, M.; Moore, B.; Taylor, L.; Gorb, L.; Leszczynski, J.; Honea, P., *Int J Mol Sci* **2007**, 8 (12), 1234.
19. Balakrishnan, V. K.; Halasz, A.; Hawari, J., *Environ. Sci. Technol.* **2003**, 37 (9), 1838-1843.
20. Aakeröy, C. B.; Wijethunga, T. K.; Desper, J., *Chem. Eur. J.* **2015**, 21 (31), 11029-11037.
21. Aakeroy, C. B.; Wijethunga, T. K.; Desper, J., *CrystEngComm* **2014**, 16 (1), 28-31.
22. Klapötke, T. M.; Krumm, B.; Xaver Steemann, F.; Steinhauser, G., *Safety Sci.* **2010**, 48 (1), 28-34.
23. Türker, L.; Variş, S., *Defence Technology* **2017**, 13 (6), 385-391.
24. Yan, B.; Zhao, N. N.; Ma, H. X.; Song, J. R.; Zhao, F. Q.; Hu, R. Z., *S. Afr. J. Chem.* **2013**, 66, 00-00.
25. González, L.; Gimeno, N.; Tejedor, R. M.; Polo, V.; Ros, M. B.; Uriel, S.; Serrano, J. L., *Chem. Mater.* **2013**, 25 (22), 4503-4510.
26. Li, Y.; Huang, H.; Lin, X.; Pan, R.; Yang, J., *RSC Advances* **2016**, 6 (59), 54310-54317.
27. Kim, H.; Gao, J.; Burgess, D. J., *Int. J. Pharm.* **2009**, 377 (1), 105-111.
28. Groom, C. R.; Bruno, I. J.; Lightfoot, M. P.; Ward, S. C., *Acta Cryst. B* **2016**, 72 (2), 171-179.
29. Zhang, W.; Zhang, J.; Deng, M.; Qi, X.; Nie, F.; Zhang, Q., *Nat Commun.* **2017**, 8 (1), 181.

Chapter 6 Co-crystals and salts of tetrazole based energetic materials with modified performance

6.1 Introduction

High heats of formation, favorable detonation performance, good thermal stabilities, and impact and shock insensitivity are key factors that characterize an optimal explosive. Azole (imidazole, pyrazole, triazole, and tetrazole) based energetic species have shown good performance since most of these factors are present (Figure 6.1).¹ Specially, the high nitrogen content in these heterocycles may make them efficient energetic materials.²⁻⁵

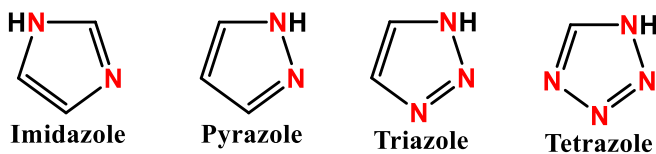


Figure 6.1 Basic structures of azoles

When it comes to tetrazoles, they have shown several applications in areas such as explosives and solid fuels due to the formation of high-density solids.⁶ Nitrated mono-aminotetrazoles, 5-(nitrimino)-1*H*-tetrazole (**D10**), 1-methyl-5-(nitrimino)-1*H*-tetrazole (**D11**), and 2-methyl-5-(nitramino)-2*H*-tetrazole (**D12**) which are rich in nitrogen, are recognized as explosive materials (Figure 6.2).⁷⁻⁸ Since the high nitrogen content backbone has been combined with an oxidizer (-NO₂), these explosives give better performance, but these are highly sensitive towards impact and friction. In addition, thermal stabilities of these are comparatively low compared to common explosives⁹ such as TNT, RDX, HMX. However, the higher sensitivity towards impact and friction along with low thermal stability make these materials problematic when it comes to storage, transportation and handling.

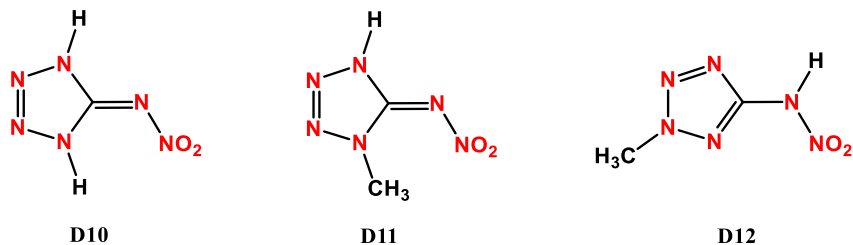


Figure 6.2 Chemical structures of some nitrated aminotetrazoles

Nitrated tetrazoles consist of several hydrogen-bond donors ($-\text{NH}$ protons) and acceptors (nitrogen atoms in the heterocycle and the aliphatic chain, oxygen of $-\text{NO}_2$) which can participate in hydrogen bonding themselves. **D10** in solid state forms HB interactions between hydrogens of $-\text{NH}$ groups and one nitrogen atom of tetrazole backbone and one nitrogen on aliphatic chain (Figure 6.3).⁸

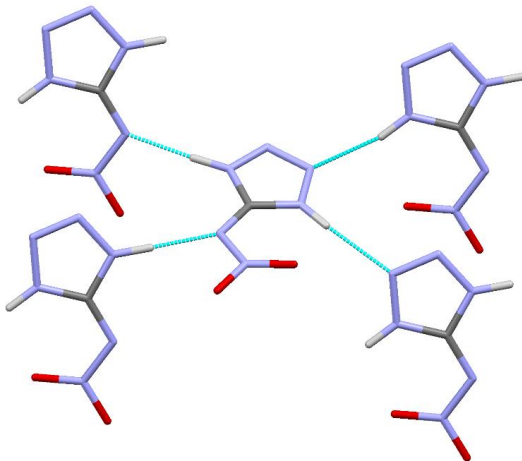


Figure 6.3 Part of the crystal structure of **D10** with hydrogen bonds between $-\text{NH}$ protons and nitrogen atoms⁸

HB interactions in **D11** can be seen between $-\text{NH}$ and the nitrogen atom of the tetrazole backbone. In addition, HB interactions can be seen between the $-\text{NH}$ proton and an oxygen atom of nitro group (Figure 6.4). **D12** also forms HB interactions between $-\text{NH}$ protons and nitrogen atoms on the tetrazole backbone (Figure 6.5). The presence of intermolecular non-covalent interactions such as hydrogen bonding and π -interactions improve the chemical and physical

stability of explosives. The non-covalent interactions that are present in **D10**, **D11** and **D12** are not strong enough to import sufficient stability.

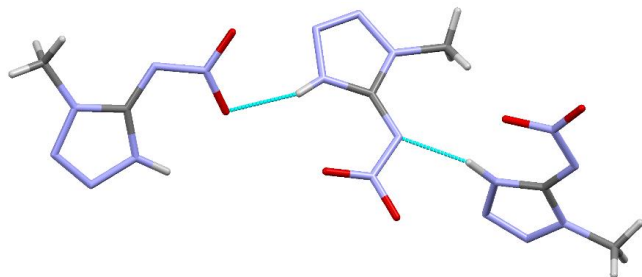


Figure 6.4 Part of the crystal structure of **D11** with hydrogen bonds between -NH protons and nitrogen and oxygen atoms⁸

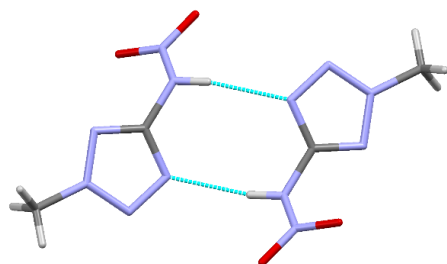


Figure 6.5 Part of the crystal structure of **D12** with hydrogen bonds between -NH protons and nitrogen atoms⁸

In order to improve the properties of **D10**, **D11** and **D12**, new molecules (co-formers) that can interact with them via non-covalent interactions need to be introduced. The best non-covalent interaction that can be observed in these crystal packing is the HB interactions. There are strong HB donors (-NH proton) in each of these molecules that can be used to pair with an incoming co-former (Figure 6.6).

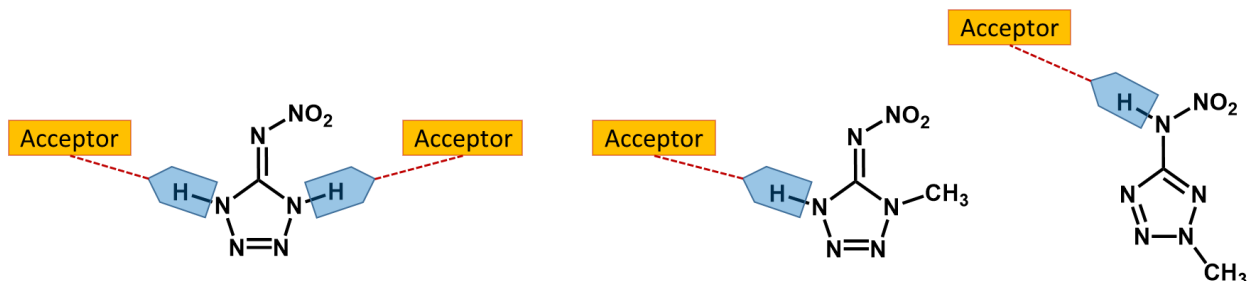


Figure 6.6 Hydrogen-bond donor sites in **D10**, **D11** and **D12**

Bis-tetrazolyl-triazenes also have high nitrogen content and they can release higher amount of energy in an explosion. Bis-tetrazolyl-triazenes, 5,5'-hydrazinebistetrazole (**HBT**), bis(1-methyltetrazolyl)triazene (**D13**) and bis(2-methyltetrazolyl)triazene (**D14**) are recognized as potential replacement for solid rocket propellants (Figure 6.7).¹⁰ These are nitrogen rich, high density, high performing compounds. Specially, **HBT** is a high performance compound comparable to known materials such as HMX and CL-20 and it has a good stability toward impact.¹¹ Compared to **HBT**, **D13** and **D14** suffer from the high sensitivity towards impact although they are high performing compounds. This instability leads to problems when handling these compounds.

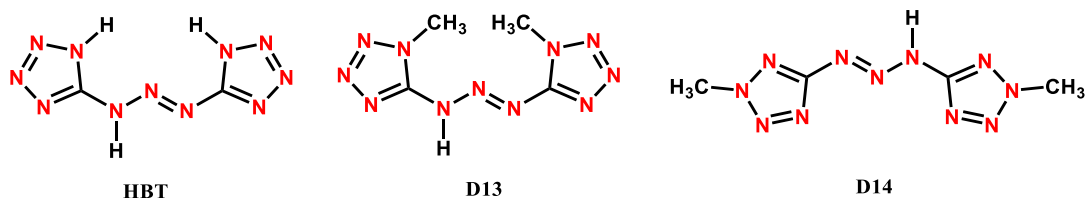


Figure 6.7 Chemical structures of bis-tetrazoles

Bis-tetrazoles also possess HB donors (-NH proton) and a number of HB acceptors in the heterocycles and the bridge of **D13** and **D14**. In the solid state, water molecules have incorporated to the crystal packing of **D13** (Figure 6.8). There are HB interactions between hydrogen atoms of –NH groups and the oxygen atom of water and hydrogen atoms of water interact with nitrogens of the tetrazole backbones.

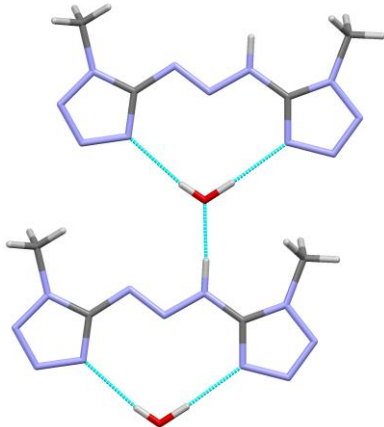


Figure 6.8 Part of the crystal structure of **D13.H₂O¹⁰**

D14 has not required any outside molecules in the crystal structure (Figure 6.9). It only shows hydrogen bonding between the –NH proton and a nitrogen atom of the tetrazole backbone.

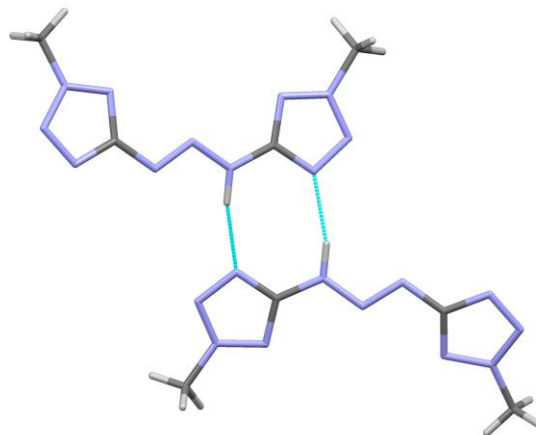


Figure 6.9 Part of the crystal structure of **D14** showing hydrogen bonding between the –NH protons and a nitrogen atom of the ring¹⁰

Since, there is a strong HB donor (-NH proton) in each of **D13** and **D14**, they can be used to pair with an incoming HB acceptor molecule (Figure 6.10).

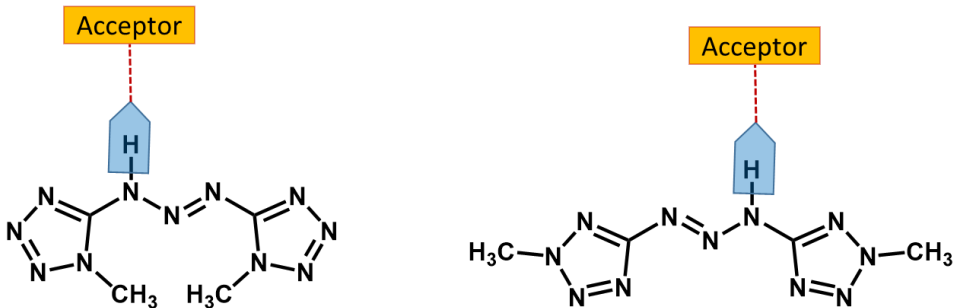


Figure 6.10 Hydrogen-bond donor sites in **D13** and **D14**

By pairing an explosive with suitable co-former, co-crystals can be obtained with different crystal packing compared to the parent packing of the explosives. This enables us to investigate and fine-tune the properties of the explosive with minimum impact on their performance.

In this study we are focused only on unstable tetrazole based energetics; **D10**, **D11**, **D3**, **D13** and **D14** since **HBT** is recognized as an insensitive high performing energetic material. In order to disrupt the non-covalent interactions in these molecule, several nitrogen based and oxygen based symmetric ditopic acceptors as co-formers were selected (Figure 6.11). Oxygen based acceptors give an added advantage since they can increase the oxygen balance of the new material.

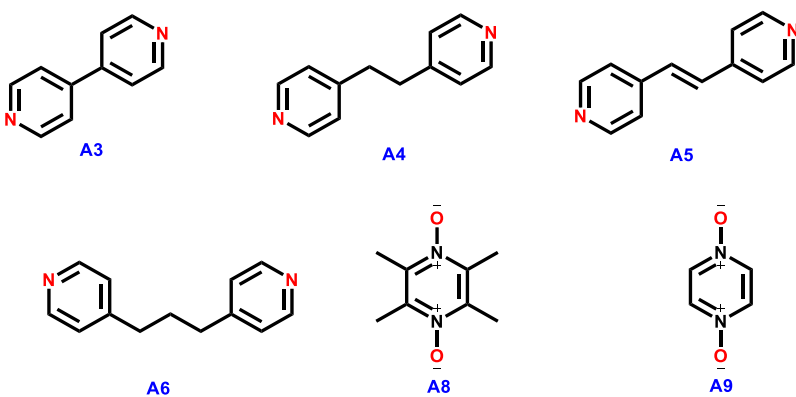


Figure 6.11 Ditopic nitrogen or oxygen based hydrogen-bond acceptors (**A1-A8**)

With the selection of co-formers, co-crystallization experiments were performed to obtain new crystalline materials. The newly formed solids were further studied structurally. Thermal

analysis and impact sensitivity tests were performed in order to characterize new properties of the materials.

6.1.1 Objectives of this study

This study is carried out to achieve specific goals stated below.

1. Synthesis of energetic materials, **D10**, **D11**, **D12**, **D13**, and **D14** and synthesis of co-crystal thereof with suitable acceptors by using HB interaction as the non-covalent force.
2. Use of –NH proton of energetic materials as potential HB donor and the driving force for the co-crystal synthesis.
3. Modification of explosive properties of energetic materials in a useful manner by making co-crystals.
4. Enhance the thermal stability and improve impact sensitivity of energetic materials through co-crystallizations.

6.2 Experimental

6.2.1 General

All the precursors, reagents, solvents, acceptors **A3-A6** were purchased from commercial sources and used without further purification. Acceptor **A8** and **A9** were synthesized by using literature reported methods.¹² ¹H NMR spectra were recorded on a Varian Unity plus 400 MHz spectrometer in DMSO-d6. Infrared spectroscopy (IR) of the compounds were obtained on a Nicolet 380 FT-IR. DSC traces were obtained on a TA Q20, using Tzero aluminum pans under N₂ (40.0 ml/min purge) and the heating rate of 5 °C/ min.

6.2.2 Safety

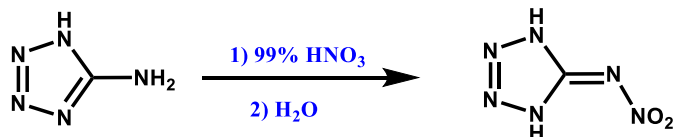
Handling and synthesis of energetic materials were carried out according to the standard procedures.¹³ Synthesis of **D10**, **D11**, **D12**, **D13** and **D14** were done in a fume hood and non-

metallic spatulas were used when applying any mechanical stress on the energetic material. Synthesis has been carried out in small scales (ranging from 200 mg to 900mg at a time). Energetic materials were always stored in glass vials in a metal container. Kevlar gloves, safety goggles and lab coat were worn all the time when handling the compounds.

6.2.3 Synthesis of energetic material

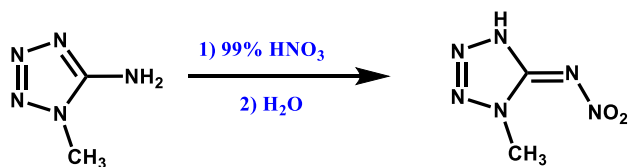
The synthesis was proceeded with commercially available relevant amino tetrazoles and by following literature reported methods.^{8,11} Corresponding amino tetrazoles were nitrated by fuming nitric acid in order to obtain **D10**, **D11** and **D12**. Bis-tetrazolyl-triazenes, **D13** and **D14** were obtained by diazotation reactions by using corresponding amino tetrazoles.

6.2.3.1 Synthesis of 5-(nitrimino)-1*H*-tetrazole (**D10**)⁸



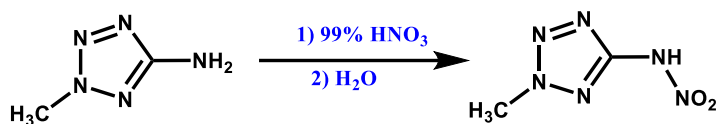
5-Amino-1*H*-tetrazole (0.30 g, 3.5 mmol) was added slowly in small portions to 4 ml of ice-cooled fuming HNO₃ (99 %). After two hours, the ice-bath was removed, and the mixture was stirred for further 24 hours in an open vessel. Then the reaction was quenched with 4 ml of cold water. HNO₃ was reduced in volume under vacuum until the colorless product started to precipitate. The precipitate was filtered and washed with cold water to obtain the product. Yield 0.43 g (94 %): m.p. dec. 122 °C (DSC 5 °C/ min): ¹H NMR (δ_{H} , DMSO-d6, 400 MHz): 6.43 (2H, s).

6.2.3.2 Synthesis of 1-methyl-5-(nitrimino)-1*H*-tetrazole (**D11**)⁸



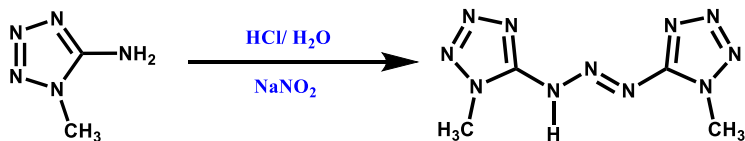
5-Amino-1-methyl-1H-tetrazole (0.3 g, 3.0 mmol) was added slowly in small portions to 3 ml of ice-cooled HNO₃ (99 %). After 2 hours, the ice-bath was removed, and the mixture was stirred for further for 24 hours. Then the reaction was quenched with 3 ml of cold water, and the HNO₃ was removed using vacuum until the product started to precipitate. The precipitate was filtered and washed with cold water to obtain the product. Yield 0.4 g (92 %): m.p. 125 °C dec. (DSC 5 °C/ min): ¹H NMR (δ_{H} , DMSO-d6, 400 MHz): 5.95 (1H, s), 4.07 (3H, s).

6.2.3.3 Synthesis of 2-methyl-5-(nitramino)-2*H*-tetrazole (D12)⁸



5-Amino-2-methyl-1H-tetrazole (0.3 g, 3.0 mmol) was added slowly in small portions to 3 ml of ice-cooled HNO₃ (99 %). After two hours, the ice-bath was removed, and the mixture was stirred for further for 24 hours. Then the reaction was quenched with 3 ml of cold water, and the HNO₃ was removed using vacuum until the product started to precipitate. The precipitate was filtered and washed with cold water to obtain the product. Yield 0.38 g (88 %): m.p. 120-122 °C 123 °C dec. (DSC 5 °C/ min): ¹H NMR (δ_{H} , DMSO-d6, 400 MHz): 6.63 (1H, s), 3.69 (3H, s).

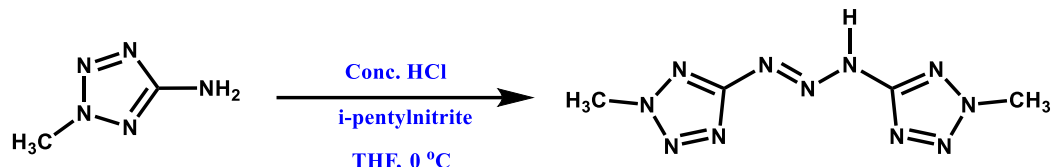
6.2.3.4 Synthesis of bis(1-methyltetrazolyl)triazene (D13)¹¹



5-Amino-1-methyl-1H-tetrazole (0.5 g, 5.0 mmol) was elutriated in 5 mL water and cooled to 0 °C. 1-methyl-5-aminotetrazole was dissolved completely by adding concentrated HCl (0.58 g, 5.0 mmol). A solution of NaNO₂ (0.02 g, 0.25 mmol) in 2 ml water was added drop wise within 20 min. After that the solution was stirred for 24 hours and the resulting solid was separated by

filtration and washed with cold water. Yield 0.6 g (57 %): m.p. 181-183 °C, 183°C dec. (DSC 5 °C/ min): ^1H NMR (δ_{H} , DMSO-d6, 400 MHz): 4.08 (6H, s).

6.2.3.5 Synthesis of bis(2-methyltetrazolyl)triazene (D14)¹¹



2-Methyl-5-amino-1H-tetrazole (0.5g, 5.0 mmol) was dissolved in 5ml THF and cooled to 0 °C. After adding concentrated HCl (0.29 g, 2.5 mmol), the formation of a colorless solid could be observed. Within 30 min i-pentylnitrite (0.29 g, 2.5 mmol) were added drop wise, the suspension turned into light yellow and was stirred for 24 h at room temperature afterwards. The resulted solid was filtered and washed with cold water to obtain the product. Yield 0.9 g (86 %): m.p. 207-208 °C, 209 °C dec. (DSC 5 °C/ min): ^1H NMR (δ_{H} , DMSO-d6, 400 MHz): 4.37 (6H, s).

6.2.4 Synthesis of co-crystals

D10, D11, D12, D13 and D14 (10 mg in each case) were individually combined with six acceptors in stoichiometric ratios and dissolved in a minimum amount of methanol or methanol/dichloromethane mixture and kept in small vials for slow evaporation in order to get X-ray quality co-crystals. Resulting crystals/ solids were analysed by IR spectroscopy and DSC to identify the formation of co-crystals.

6.2.5 Energy optimization

Since **D10, D11** and **D12** can exist as two isomeric forms, geometry optimization was performed to identify most stable isomers. In addition, molecular electrostatic potential surfaces of all energetic materials were determined in order to rank the hydrogen bond donors. Geometry

optimization of **D10**, **D11**, **D12**, **D13** and **D14** were carried out by using B3LYP functional and 6-311++G* basis set under vacuum in Spartan'14 software. MEPs surfaces were generated for the optimized structures on the electron isodensity surface of the 0.002 electrons/au³.

6.2.6 Explosive properties determination

Oxygen balance calculation, detonation velocity and pressure calculations and impact sensitivity determination were determined by method listed in sections 5.2.5, 5.2.6 and 5.2.7 respectively.

6.3 Results

6.3.1 Geometry optimizations

Since there are multiple possible constitutional isomers for each nitrated tetrazole, geometry optimizations were carried out in order to identify the most stable isomer (Figure 6.12).

The energy difference between isomers were indicated relative to the most stable structure.

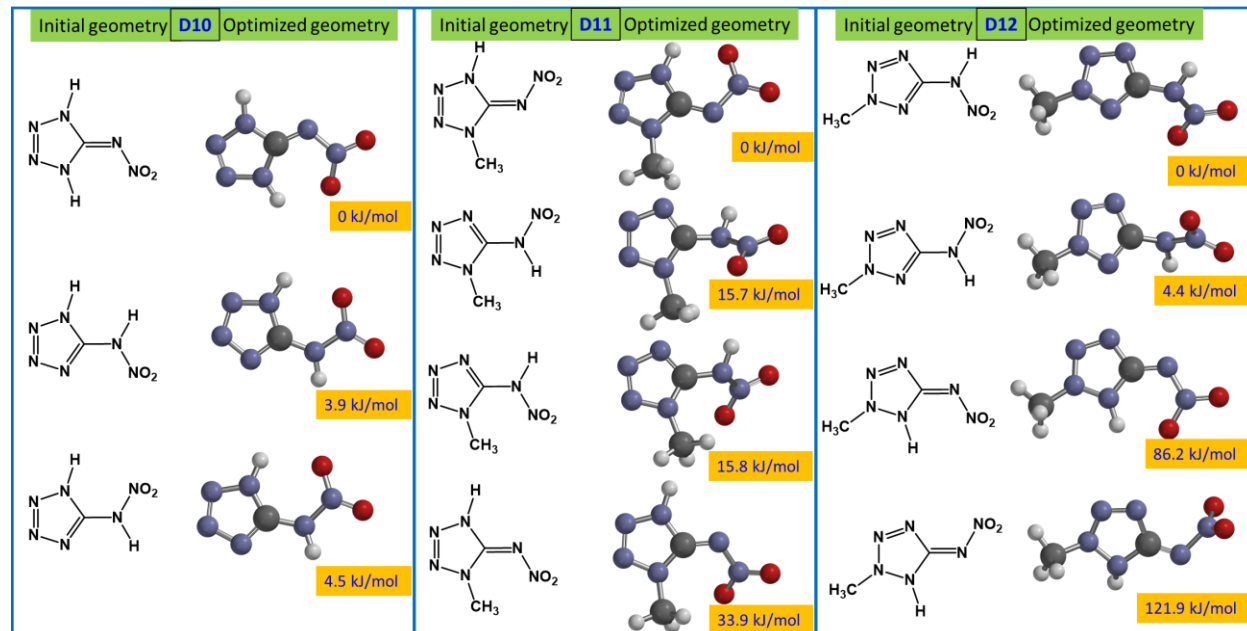


Figure 6.12 Geometry optimized structures and energy differences of different constitutional isomers of each tetrazole.

In order to identify the strongest hydrogen-bond donor site of the explosives, calculated MEPs surfaces of the most stable isomer of **D10**, **D11**, **D12**, **D13** and **D14** have been obtained (Figure 6.13).

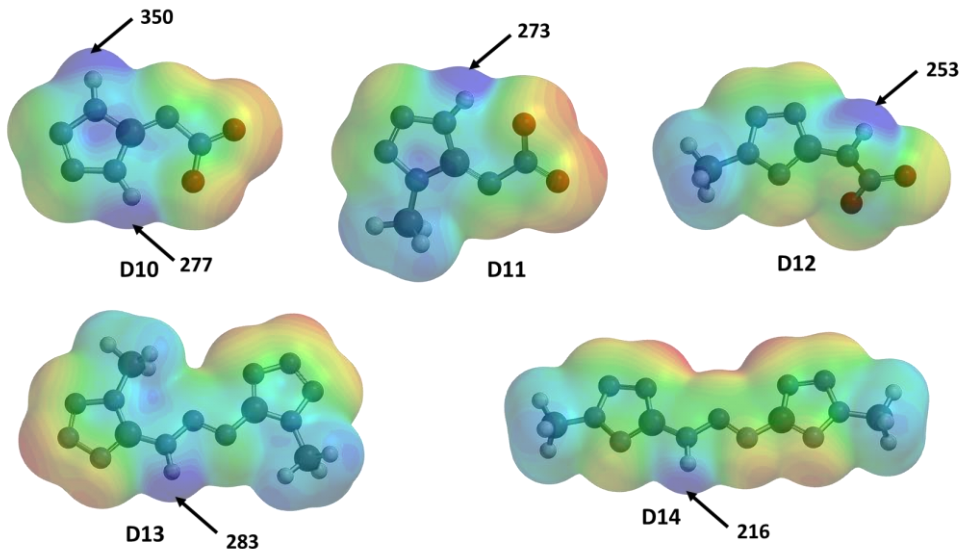


Figure 6.13 MEPs surfaces of **D10**, **D11**, **D12**, **D13**, and **D14** showing highest positive points of MEPs (All values are in kJ/mol)

6.3.2 IR analysis

The co-crystallization screening was carried out by using IR spectroscopy on all the solids produced from attempted co-crystallization experiments. Seventeen of eighteen co-crystallization attempts show the formation of co-crystals between **D10**, **D11**, **D12** and the acceptors (Table 6.1). The IR spectra of both starting materials (donor and acceptor) were compared with the resulting crystal/solid in order to identify the formation of co-crystals. Eleven of twelve co-crystal attempts show the formation of co-crystals between **D13**, **D14** and the acceptors. An example of IR spectroscopy comparison between **D12**, **A3** and the co-crystal **D12:A3** is shown in Figure 6.14. The peak shift of both donor (e.g. from 1602 cm^{-1} to 1628 cm^{-1}) and acceptor (e.g. from 1586 cm^{-1} to 1596 cm^{-1}) molecules can be observed with the interaction between donor and acceptor (Table 6.1).

Table 6.1. IR analysis of attempted co-crystallization experiments

Combination	Donor peak: N-H bend (cm ⁻¹)		Characteristic acceptor peak (cm ⁻¹)		Co-crystal
	Free	bound	Free	bound	
D10 : A3	1582	1627	1586	1596	Yes
D10 : A4	1582	1633	1593	1605	Yes
D10 : A5	1582	1634	1592	1611	Yes
D10 : A6	1582	1634	1603	1520	Yes
D10 : A8	1582	1593	1523	1506	Yes
D10 : A9	1582	1608	1436	1478	Yes
D11 : A3	1583	1628	1586	1596	Yes
D11 : A4	1583	1632	1593	1596	Yes
D11 : A5	1583	1625	1592	1509	Yes
D11 : A6	1583	1632	1603	1594	Yes
D11 : A8	1583	1573	1523	1486	Yes
D11 : A9	1583	1577	1436	1492	Yes
D12 : A3	1602	1628	1586	1596	Yes
D12 : A4	1602	1633	1593	1532	Yes
D12 : A5	1602	1624	1592	1624	Yes
D12 : A6	1602	1633	1603	1614	Yes
D12 : A8	1602	1595	1523	1513	Yes
D12 : A9	1602	No	1436	1436	No
D13 : A3	1627	1630	1586	1588	Yes
D13 : A4	1627	1625	1593	1596	Yes
D13 : A5	1627	1622	1592	1595	Yes
D13 : A6	1627	1637	1603	1600	Yes
D13 : A8	1627	1629	1523	1525	Yes
D13 : A9	1627	1627	1436	No	No
D14 : A3	1592	1595	1586	1595	Yes
D14 : A4	1592	1604	1593	1604	Yes
D14 : A5	1592	1597	1592	1597	Yes
D14 : A6	1592	1596	1603	1596	Yes
D14 : A8	1592	1520	1523	1429	Yes
D14 : A9	1592	1590	1436	1448	Yes

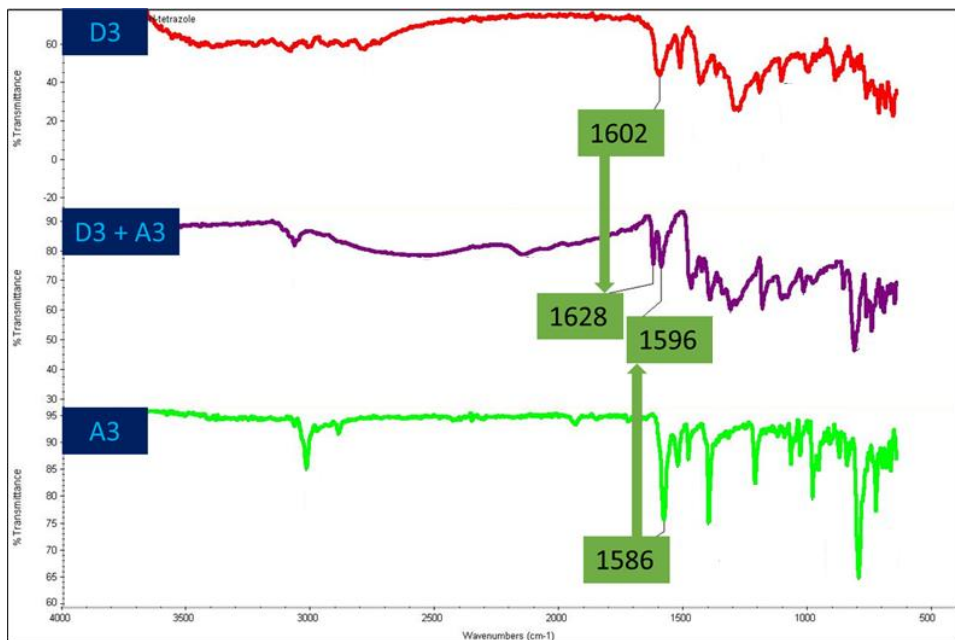


Figure 6.14 IR spectroscopy comparison between **D12**, **A3** and the **D12:A3**

6.3.3 Crystal structures

Out of twenty-eight possible co-crystal formations, nine of co-crystals were obtained as X-ray quality crystals (combinations: **D10:A8**, **D10:A9**, **D11:A3**, **D11:A8**, **D11:A9**, **D12:A3**, **D12:A4**, **D12:A6**, and **D12:A8**).

The **D10:A8** co-crystal is formed as a result of N-H···O hydrogen-bonds between –NH proton of **D10** and the oxygen of N-oxide **A8** (Figure 6.15). The two components are present in 1:1 ratio and **D10:A8** forms a 1-D network. The other noticeable change in this crystal packing is the presence of a less stable constitutional isomer of **D10**.

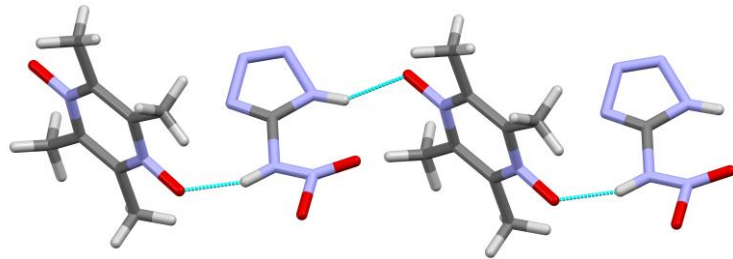


Figure 6.15 Part of the crystal structure of **D10:A8** showing main HB interactions and 1-D network

When acceptor **A9** which is also N-oxide is introduced to the energetic material **D10**, the resulting crystal structure again shows 1:1 stoichiometry between **D10** and **A9** with 1-D network formation via N-H \cdots O, HB interactions between –NH protons of **D10** and oxygen of N-oxide group of **A9** (Figure 6.16). There is no isomer change of **D10** upon co-crystallization.

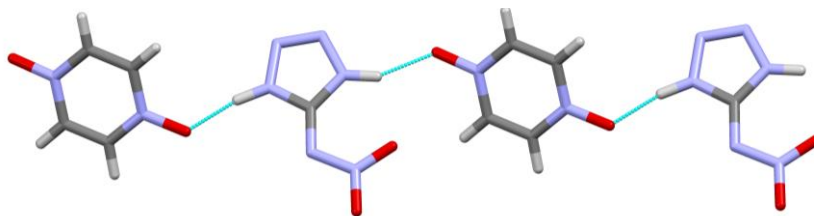


Figure 6.16 Part of the crystal structure of **D10:A9** showing primary HB interactions and 1-D network

Formation of trimeric salt 2(**D11** $^-$):A3H $_2^{2+}$ is observed instead of co-crystal when **A3** is introduced (Figure 6.17). A proton transfer from donor (-NH) to the acceptor (N) is observed with a charge assisted hydrogen-bond (-NH $^+$ \cdots N $^-$) formation.

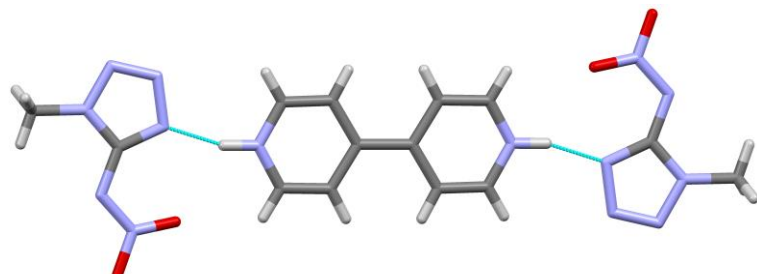


Figure 6.17 Crystal structure of trimeric salt, 2(**D11** $^-$):A3H $_2^{2+}$ showing charge assisted HB interactions

A co-crystal (**2(D11):A8**) formation is observed via N-H \cdots O, HB interactions between –NH protons **D11** and oxygen of N-oxide group of **A8** (Figure 6.18). Acceptor **A9** also behaves similarly to **A8** by co-crystal formation (**2(D11):A9**) via HB interactions (N-H \cdots O) between –NH protons of **D11** and oxygen of N-oxide group of **A9** (Figure 6.19). Both co-crystal are trimeric architectures.

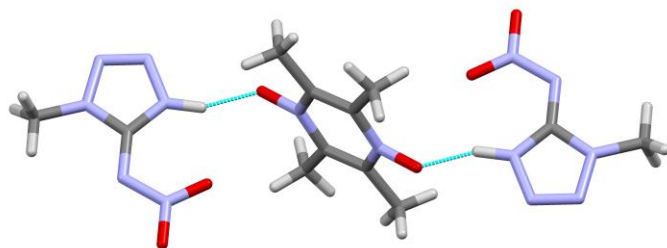


Figure 6.18. Crystal structure of **2(D11):A8** showing primary HB interactions

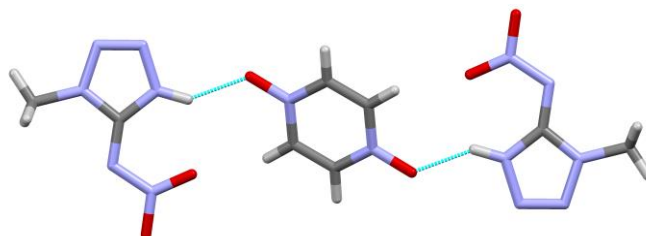


Figure 6.19. Crystal structure of **2(D11):A9** showing main HB interactions

A salt formation (**2(D12 $^-$):A3H $_2^{2+}$**) was observed between **D12 $^-$** and **A3H $_2^+$** due to the proton transfer between donor and the acceptor (Figure 6.20). There are two types of HB interactions in this solid state trimeric architecture. First, charge assisted hydrogen bonding (–NH $^+\cdots$ N $^-$) between a nitrogen of **D12 $^-$** and the proton attached to the **A3H $_2^+$** . Second, a weak HB interaction between hydrogen attached to the nitrogen of **A3H $_2^+$** and the one of oxygen of the nitro group of **D12 $^-$** .

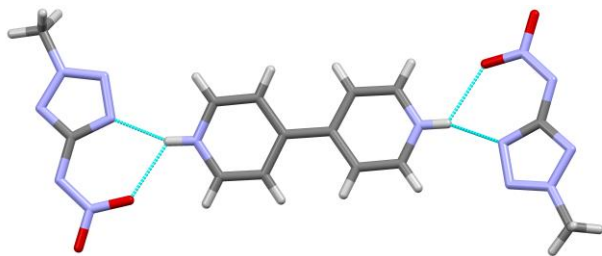


Figure 6.20 Crystal structure of 2(**D12⁻**):A3H₂²⁺ showing main HB interactions

The salt 2(**D12⁻**):A4H₂²⁺ shows only one type of HB interaction (charge assisted HB, - NH⁺⋯⋯N⁻) between a nitrogen of **D12⁻** and the proton attached to the A4H₂²⁺ (Figure 6.21). In addition, **D12⁻** has adopted a different geometrical isomeric form compared to the isomer present in the salt, 2(**D12⁻**):A3H₂²⁺.

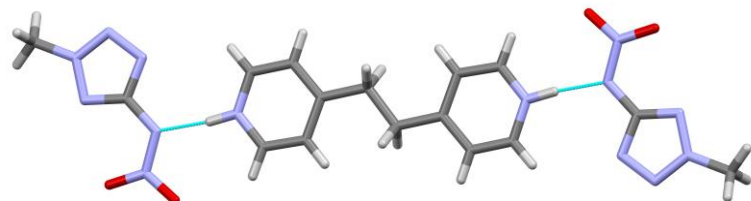


Figure 6.21 Part of the crystal structure of 2(**D12⁻**):A4H₂²⁺ showing main HB interactions

In the salt, 2(**D12⁻**):A6H₂²⁺, both geometrical isomers of **D12⁻** can be observed (Figure 6.22). In this case three different HB interactions are observed; first, a charge assisted HB interaction between hydrogen attached to nitrogen of A6H₂²⁺ and a nitrogen of tetrazole backbone. Second, the interaction between hydrogen attached to nitrogen of A6H₂²⁺ and the nitrogen of aliphatic branch of **D12⁻**. The third one is the HB interaction between hydrogen attached to nitrogen of A6H₂²⁺ and the oxygen of nitro group of **D12⁻**. These HB interactions are mirrored in 2(**D12⁻**):A3H₂²⁺ and 2(**D12⁻**):A4H₂²⁺.

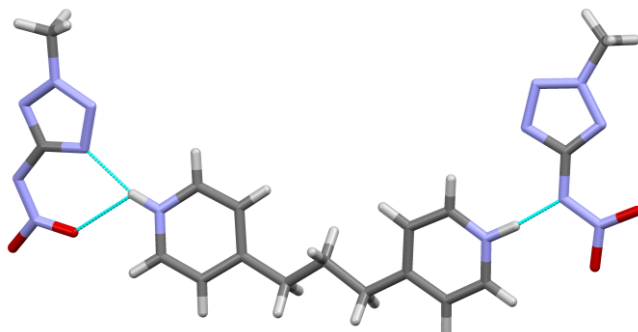


Figure 6.22 Part of the crystal structure of $2(\mathbf{D12}^-):\mathbf{A6H}_2^{2+}$ showing main HB interactions

A co-crystal ($2(\mathbf{D12}^-):\mathbf{A8}$) was obtained via HB interaction ($\text{N-H}\cdots\text{O}$) between $-\text{NH}$ protons and the oxygen of N-oxide group (Figure 6.23). Again, formation of trimeric architecture was observed.

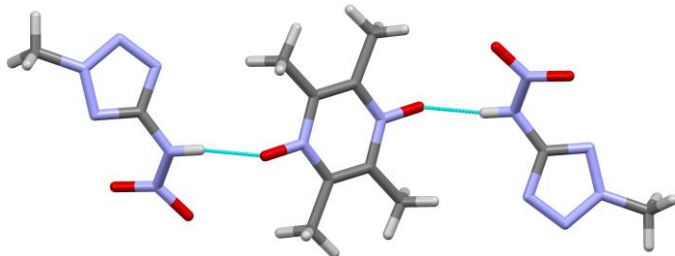


Figure 6.23. Part of the crystal structure of $2(\mathbf{D12}^-):\mathbf{A8}$

All the hydrogen bonding parameters (distances and angles) are tabulated in the table 6.2.

Table 6.2. Hydrogen bond parameters of co-crystals and salts

Co-crystal/ salt	D-H \cdots A	D \cdots A (Å)	D-H \cdots A(°)
D10:A8	N4 H4 O19	2.614(10)	138.6
	N6 H6 O16	2.656(11)	161(7)
D10:A9	N1 H1 O17	2.666(3)	168(3)
	N4 H4 O16	2.689(3)	154(3)
2(D11⁻):A3H₂²⁺	N14 H14 N4	2.722(3)	163(2)
2(D11⁻):A8	N4 H4 O11	2.604(2)	157(2)
2(D11⁻):A9	N4 H4 O11	2.676(3)	144(3)
2(D12⁻):A3H₂²⁺	N30 H30 N14	2.7715(18)	156.2(18)
2(D12⁻):A4H₂²⁺	N15 H15 N7	2.704(9)	174(7)
2(D12⁻):A6H₂²⁺	N33 H33 N7	2.694(2)	174(2)
2(D12⁻):A8	N27 H27 N14	2.838(2)	166.9(19)

6.3.4 Thermal properties

Thermal analysis for all the X-ray quality crystals and the **D10**, **D11** and **D12** were done using DSC. Decomposition temperature and the decomposition enthalpy were determined and compared with parent energetic material. DSC traces are shown in Figure 6.24 (for **D10** and co-crystals), Figure 6.25 (for **D11** and salts/ co-crystals) and Figure 6.26 (for **D12** and salts/ co-crystals). The thermal data, melting point, decomposition point and decomposition enthalpy are summarized in the table 6.3.

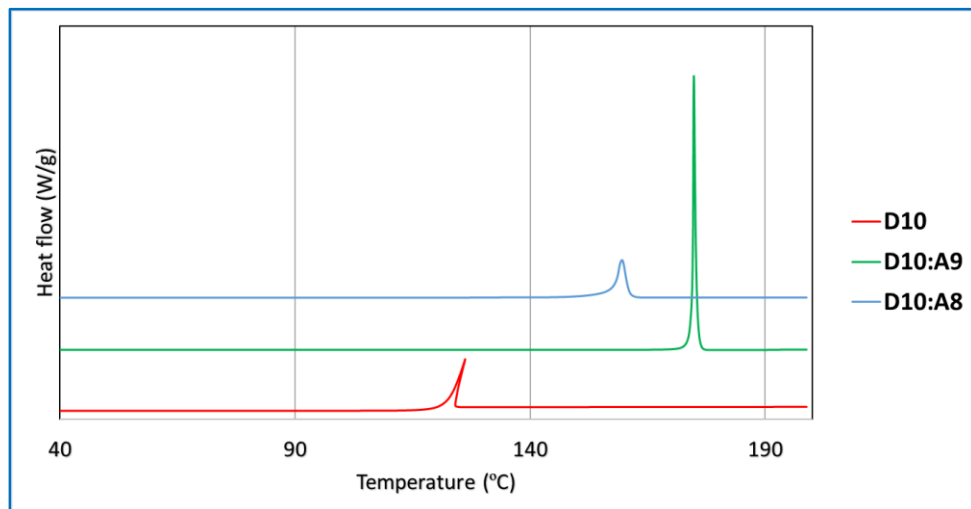


Figure 6.24. DSC traces comparison of **D10** and co-crystals.

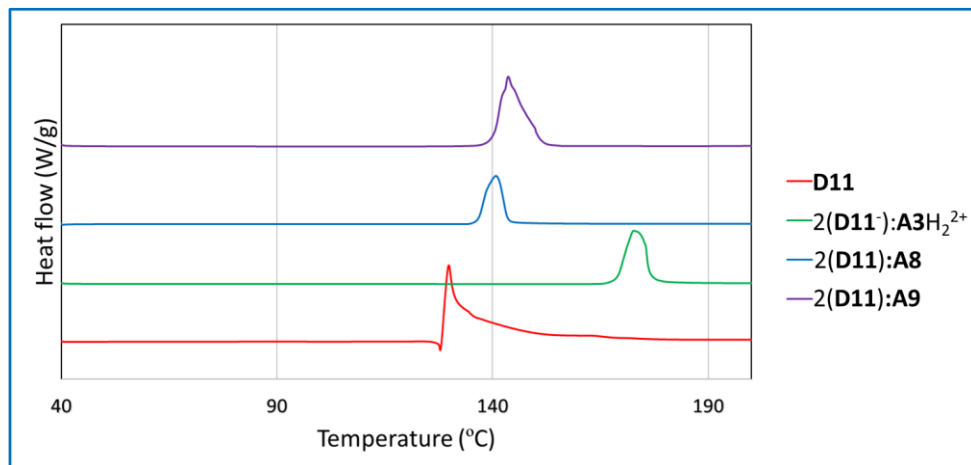


Figure 6.25. DSC traces comparison of **D11** and co-crystals/salt.

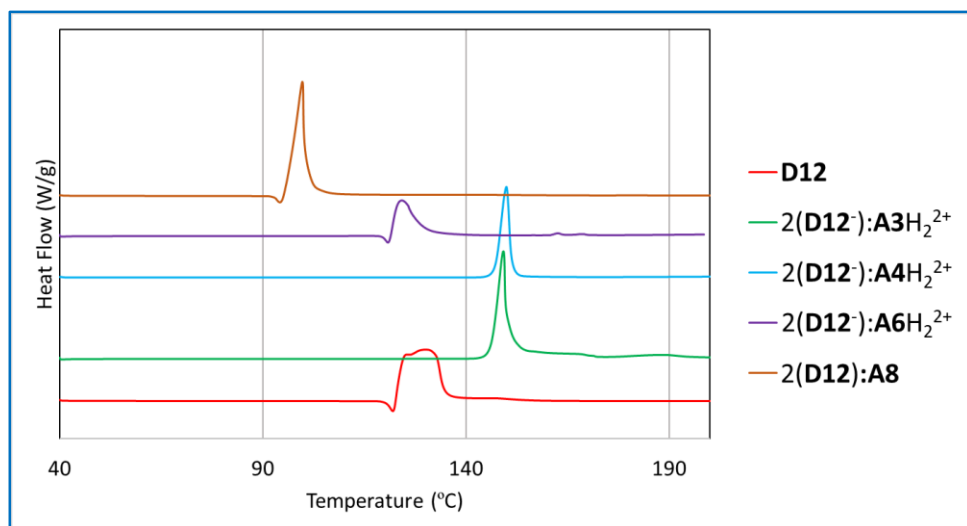


Figure 6.26. DSC traces comparison of **D12** and co-crystal/salts.

Table 6.3. Thermal properties of **D10**, **D11**, **D12** and their co-crystals/ salts.

Compound/ co-crystal/ salt	Co-former melting point (°C)	Co-crystal/ salt/ solvate	
		Decomp. point (°C) (on set)	Decomp. enthalpy (J/g)
D10	-	122	2475
D10:A8	220-222	175	2280
D10:A9	>300	181	2206
D11	-	125	2437
2(D11⁻):A3H₂²⁺	109-112	169	1851
2(D11⁻):A8	220-222	140	1948
2(D11⁻):A9	>300	138	1599
D12	-	123	2452
2(D12⁻):A3H₂²⁺	109-112	146	1079
2(D12⁻):A4H₂²⁺	110-112	147	958
2(D12⁻):A6H₂²⁺	57-60	121	1009
2(D12⁻): A8	220-222	96	1375

6.3.5 Oxygen balance, detonation pressure and detonation velocity of the energetic materials

Oxygen balance, detonation pressure and detonation velocity data for parent energetic materials (**D10**, **D11** and **D12**) and their co-crystals / salts were summarized in the table 6.4. Parent energetic materials show the most favorable oxygen balance compared to the newly formed

energetic materials except in the case of **D10:A9**. Detonation performances of the newly produced energetic materials are lower compared to the parent energetic materials.

Table 6.4. Oxygen balance, detonation velocity and detonation pressure of energetic materials

Compound/ co-crystal/ salt	Density (g/cm ³)	Oxygen balance (%)	Detonation velocity (km/s)	Detonation pressure (GPa)
D10	1.867(200K)	-12.0	9.1	37.9
D10:A8	1.478(200K)	-112.7	6.8	18.3
D10:A9	1.707(298-303K)	-7.1	7.6	25.4
D11	1.755 (200K)	-44.4	8.3	30.5
2(D11 ⁻):A3H ₂ ²⁺	1.449(298-303K)	-115.2	6.6	17.3
2(D11 ⁻):A8	1.521(298-303K)	-98.2	7.1	20.6
2(D11 ⁻):A9	1.610(298-303K)	-64.0	7.3	22.5
D12	1.667(200K)	-44.4	8.0	27.5
2(D12 ⁻):A3H ₂ ²⁺	1.568(130K)	-115.2	7.0	20.4
2(D12 ⁻):A4H ₂ ²⁺	1.538(130K)	-128.7	7.0	19.9
2(D12 ⁻):A6H ₂ ²⁺	1.504(130K)	-134.9	6.9	19.1
2(D12 ⁻): A8	1.557(130K)	-98.2	7.2	21.4

6.3.6 Impact sensitivity test

Impact sensitivity test was performed for the **D10**, **D11**, **D12** and the selected newly formed energetic materials. H₅₀ value for the **D10** observed as 32 ±1cm which is the highest sensitive material while **D11** and **D12** showed 94 ±1cm and 88 ±1cm respectively being relatively stable towards impact. Newly formed co-crystals and salts show much lower sensitivity towards impact compared to the parent energetic materials (Table 6.5).

Table 6.5. H₅₀ values of energetic materials

Compound/ co-crystal/ salt	D10	D11	D12	D10:A8	D10:A9	2(D11 ⁻):A3H ₂ ²⁺	2(D11 ⁻):A8	2(D11 ⁻):A9	2(D12 ⁻):A3H ₂ ²⁺	2(D12 ⁻):A4H ₂ ²⁺	2(D12 ⁻):A6H ₂ ²⁺
Impact sensitivity H ₅₀ ±1(cm)	32	94	88	98	144	110	140	138	>146	>146	>146

6.4 Discussion

6.4.1 Geometry optimization

The geometry optimized structures of **D10** indicates that there is very small energy barrier between two constitutional isomers. Due to this small energy barrier between two isomers, small variations of local environment could promote one isomer over the other. For the **D11** and **D12**, the differences are relatively larger, and the conversion of one isomer to other is difficult. The lowest energy isomers obtained by energy optimizing are match with the solid state crystal packing of all three materials.

6.4.2 IR spectroscopy analysis

The weak hydrogen bond interactions among donors in all cases were able to break by the newly introduced co-formers due to the presence of strong acceptors in co-formers compared to the acceptor atoms in donor molecules. The IR spectroscopy shows strong evidence for the above statement by supporting the characteristic peak shifts on both donor and acceptor molecules when they are together. Notably, peak changes were observed for -NH stretch and bending for all the donors **D10**, **D11**, **D12**, **D13** and **D14** and additionally the asym-NO₂ stretch for **D10**, **D11** and **D12**.

6.4.3 Structural analysis

Due to the presence of two HB donors in **D10**, co-crystals that propagate in the 1-D direction with both ditopic acceptors **A8** and **A9**. Both less stable constitutional isomer and more stable constitutional isomer of **D10** can be seen in **D10:A8** and **D10:A9** respectively. Most stable constitutional isomer has been reported three times in solid state in the crystal packing of anhydrous **D10**⁸, hydrated **D10**⁷ and **D10:2-aminotetrazole**¹⁴. There is only one evidence that shows **D10** adopts less stable constitutional isomer which is in the crystal packing of **D10:2-**

methyl-5-aminotetrazole⁷. There is no evidence for constitutional isomer formation for the **D11** and **D12** in the literature. This may be due to the relatively larger energy differences between more stable and the less stable isomers of them. There are only two reports showing that the more stable isomer of **D11**⁷⁻⁸ (anhydrous **D11** and hydrated **D11**) and two reports for the stable isomer of **D12**^{8, 15}.

In addition, HB interactions ($\text{-NH}\cdots\text{N}$) and charge assisted HB interactions ($\text{-NH}^+\cdots\text{N}^-$), there are significant contributions from $-\text{NO}_2$ groups in the crystal packing by formation of short HB interactions. Specially, when the $-\text{NH}^+$ group interacts with the nitrogen of the aromatic ring of tetrazole, a significant contribution for the HB interaction can be observed from $-\text{NO}_2$ group. On the other hand, there are several $-\text{CH}\cdots\text{N}$ short HB interactions in the crystal packing of newly formed solids.

6.4.4 Acidity of energetics

Most of the nitrogen based acceptors react quickly with the energetics **D10**, **D11** and **D12** and make immediate precipitates. Oxygen based acceptors with **D10**, **D11** and **D12** tend to yield crystals all of the times. All of the crystals that are formed are the salts when nitrogen based acceptors are introduced due to acidic nature of the $-\text{NH}$ protons of energetics. High basicity of nitrogen based acceptors compared to the oxygen based acceptors enables proton transfer from donor to acceptor. When a basic reagent such as ammonia is introduced to these energetics, easy formation of corresponding energetic anion and the ammonium salt further indicated the acidic nature of $-\text{NH}$ protons (Figure 6.27)¹⁶.

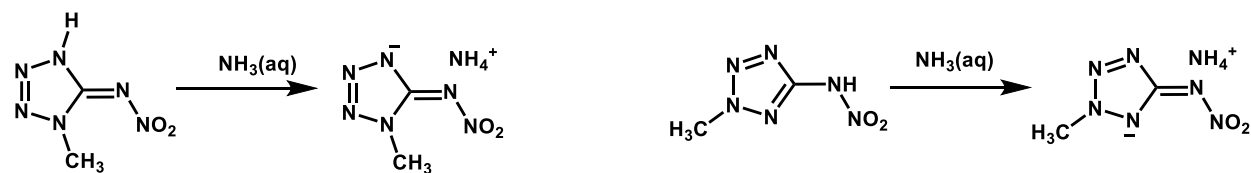


Figure 6.27 Salts formation of **D11** and **D12** with aqueous ammonia¹⁶

6.4.5 Thermal stability analysis

The presence of strong hydrogen bonds and number of strong HB interactions can improve the thermal stability of a compound¹⁷. When compared all the co-crystals that have HB interactions, **D10:A9** which has two hydrogen HB interactions shows the highest thermal stability. The lowest thermal stability is observed for **2(D12):A8** which has one HB interaction. In addition, the HB distance between donor atom and acceptor (N27 H27 N14) of **2(D12):A8** shorter than the other similar interactions in rest of the co-crystals. All the co-crystals show decomposition points in between the melting/ decomposition points of donor and the acceptor except the case of **2(D12):A8** (Figure 6.28).

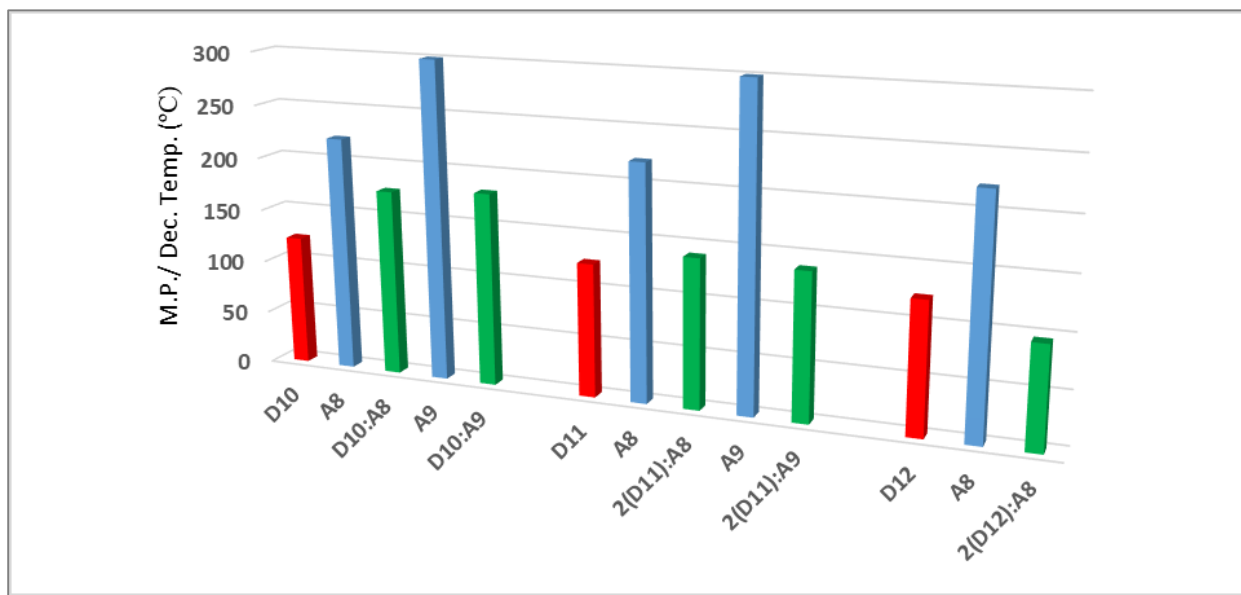


Figure 6.28 Melting point/ decomposition temperature comparison of explosives, co-formers and co-crystals

6.4.6 Detonation property analysis

As expected, reduction of decomposition enthalpy, detonation velocity and detonation pressure were witnessed due to introduction of non-energetic materials in to the explosive materials. Significant retention of these properties can be seen with minimal negative effect on the performance of the explosives. Oxygen balance is also decreased in the co-crystals and salts due

to the absence of enough oxygen in co-formers. When the co-former is an N-oxide, favorable oxygen balance can be observed compared to the other formed salts, due to presence of two additional oxygen atoms per that particular co-former compared to nitrogen based acceptors.

6.4.7 Impact sensitivity analysis

In all the tested cases, a significant improvement of stability towards impact in both salts and co-crystals were observed. The most impact sensitive explosive **D10** has gained much improved impact sensitivity with the formation of co-crystals. With the formation of salts with acceptors, **D12** gets higher H_{50} values (much lower impact sensitivity) that go beyond the testing limit (146 cm) of the instrument. The Figure 6.29 shows the comparison of H_{50} values for all explosives and newly formed co-crystals and salts. Co-crystal 2(**D12**):**A8** was not further tested for the impact sensitivity due to the low thermal stability.

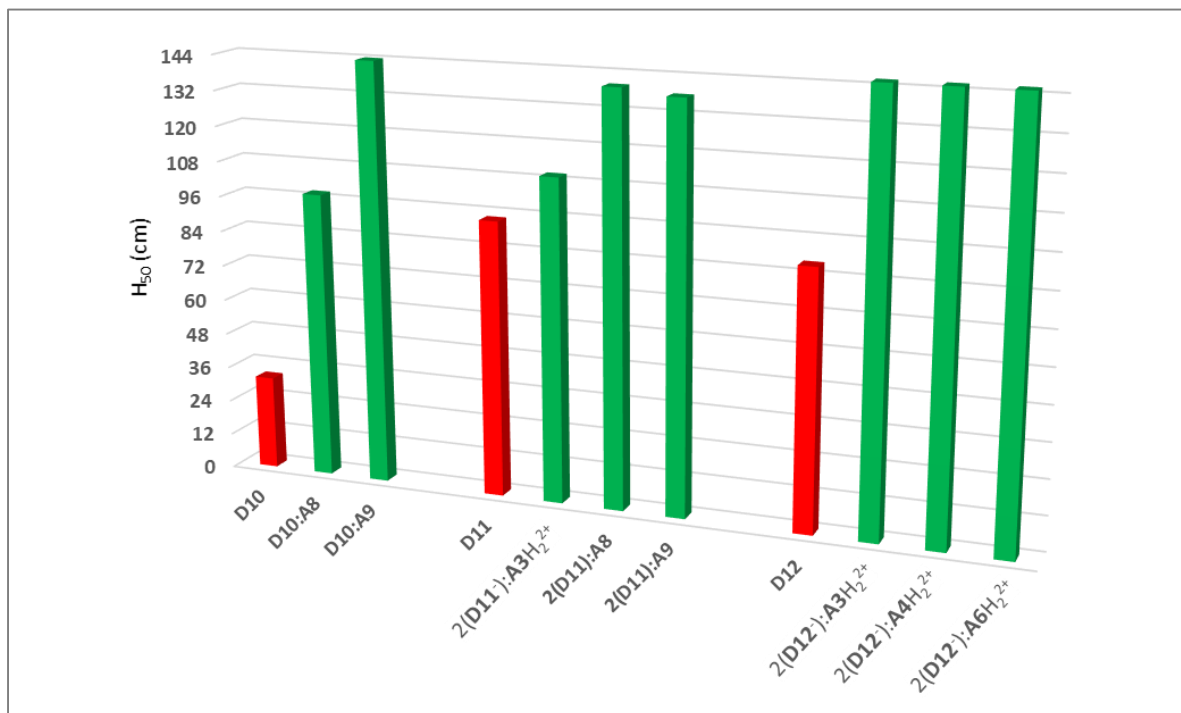


Figure 6.29 H_{50} values comparison for the explosives and their salts/ co-crystals

It has been found that the presence of strong intermolecular HB interactions¹⁸ and π interaction aided sliding layered packing¹⁹ in the crystal improve the impact sensitivity of explosives. When HB interactions of **D12** compared to co-crystal 2(**D12**⁻):A3H₂²⁺, it can be recognized that having stronger HB interactions and additional several short HB interactions support the crystal propagation on the same layer (Figure 6.30). In addition, the hydrophobic methyl groups are held closer in the crystal packing to take advantage of hydrophobic interactions.

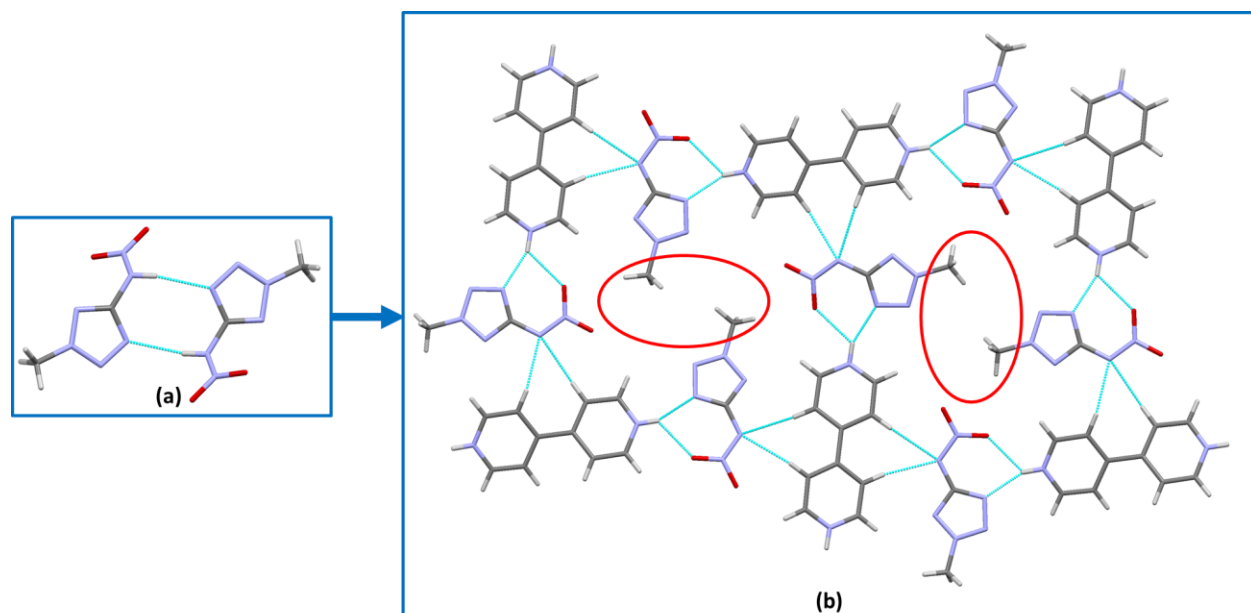


Figure 6.30 (a) HB interactions in **D12**, (b) HB interactions and short non-covalent interactions in **D12:A3**

In the packing of **D12**, the molecules are arranged perpendicular to each other and there is lack of layered architecture which leads to highly sensitive towards impact. In the 2(**D12**⁻):A3H₂²⁺, the packing has improved by more planar crystal arrangement and a wave like layer arrangement is also observed (Figure 6.31).

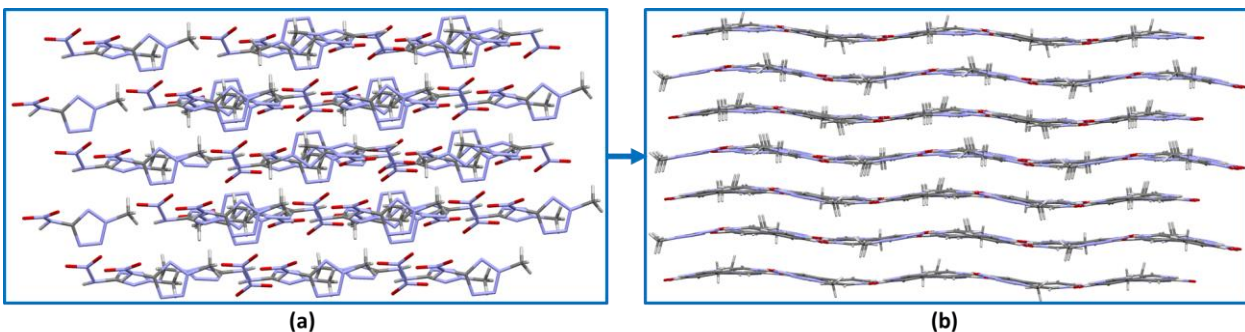


Figure 6.31 (a) Packing of D10, (b) layered packing of salt

These kind of π -stacked packing arrangements can easily buffer sliding and compressions by an external stimulus (Figure 6.32).²⁰ The mechanical energy supplied outside is converted into intermolecular interaction energy and it disperses all over the π -stacked layers²¹. It minimizes the local molecular vibration and it makes the material insensitive to external impact.

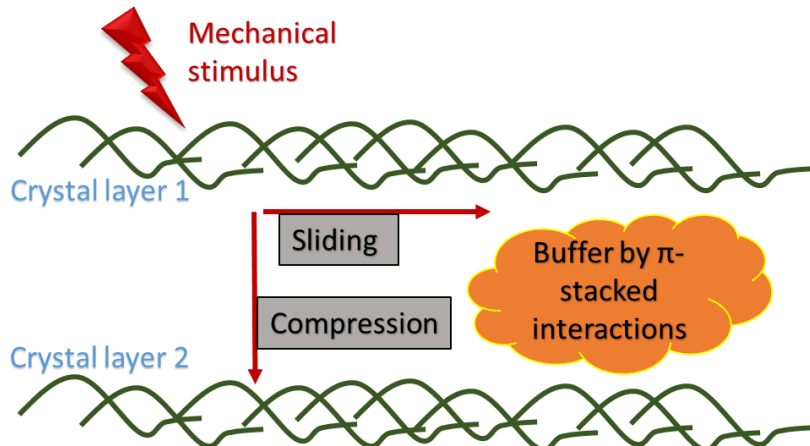


Figure 6.32 π -stacked interactions in a crystal buffer against external mechanical stimuli

6.5 Conclusions

The co-crystallization of energetics **D10**, **D11** and **D12** has revealed that the energetic properties of explosives can be manipulated by selecting suitable hydrogen bond acceptors. Five co-crystals and four salts that are produced in the experiments show N-H \cdots O and N-H $^+$ \cdots N $^-$ HB interactions which makes supramolecular motifs. In addition, several short hydrogen bond interactions such as N-H \cdots O₂N and C-H \cdots N was observed in these supramolecular settings. it is

also shown that the changing one constitutional isomer to another by small change of environment around the molecule is possible when the energy difference between them is small.

The thermal stability of energetics was altered with the formation of non-covalent interactions with co-formers. When strong HB interactions are present in the crystal packing, improvement of thermal stability was observed. The best improvement of thermal stability was observed for the co-crystal **D10:A9**. Out from nine co-crystal/ salt formations, improvement of thermal stability of the material was observed for seven co-crystals/ salts.

Improvement of impact sensitivity of explosives was observed when energetic co-crystals were formed due to the presence of strong non-covalent interactions such as hydrogen bonding and several other short interactions such as short HB interactions and π interactions. Highest impact sensitivity improvement (112 cm increment of H_{50} for the **D10:A9** co-crystal) was observed for **A9** which was the highest impact sensitive explosive (Figure 6.33).

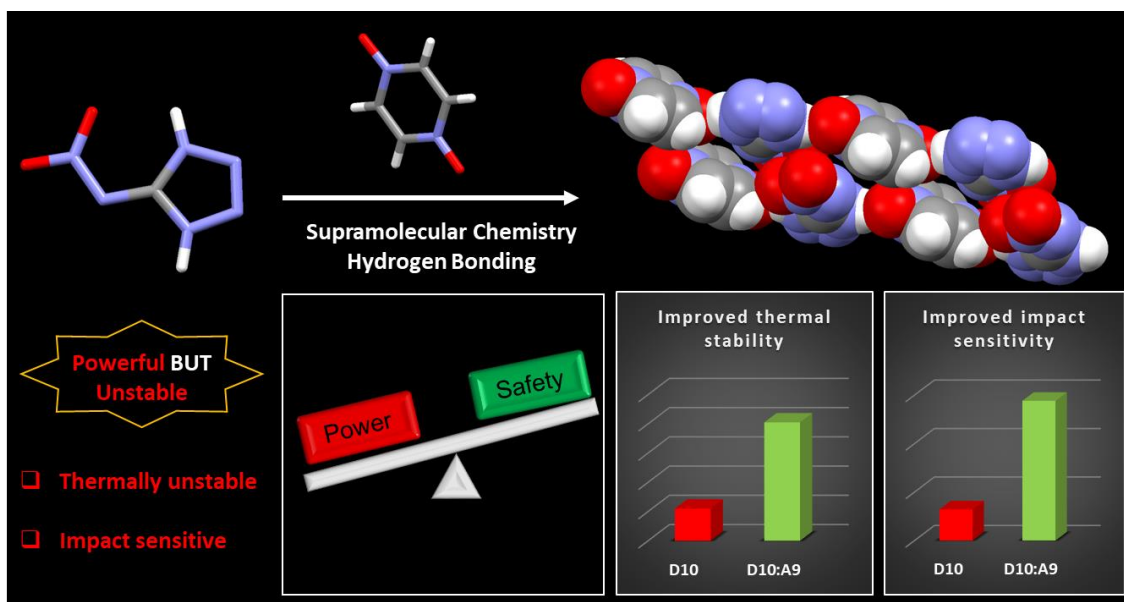


Figure 6.33 Use of supramolecular chemistry and crystal engineering to balance the power and safety of explosives

Even though less favorable oxygen balance was observed for most cases, it is possible to make compounds that has more favorable oxygen balance by selecting co-formers that contain oxygen

atoms. The introduction of non-energetic materials may effect negatively on the performance of the explosives. Making of safer materials should be the priority in the settings of presence of relatively unstable materials.

This study suggests that systematic co-crystallizations permit to balance the power and the stability of explosives. By fine tuning the properties that are important for storage, handling, and transport with minimal negative impact on explosive behavior of the targeted energetic material, a better explosive can be engineered with co-crystallization.

6.6 References

1. Yu, Z.; Bernstein, E. R., *J. Phys. Chem. A* **2013**, *117* (42), 10889-10902.
2. Sinditskii, V. P.; Egorshev, V. Y.; Rudakov, G. F.; Filatov, S. A.; Burzhava, A. V., High-Nitrogen Energetic Materials of 1,2,4,5-Tetrazine Family: Thermal and Combustion Behaviors. In *Chemical Rocket Propulsion: A Comprehensive Survey of Energetic Materials*, De Luca, L. T.; Shimada, T.; Sinditskii, V. P.; Calabro, M., Eds. Springer International Publishing: Cham, 2017; pp 89-125.
3. Talawar, M. B.; Sivabalan, R.; Mukundan, T.; Muthurajan, H.; Sikder, A. K.; Gandhe, B. R.; Rao, A. S., *J. Hazard. Mater.* **2009**, *161* (2), 589-607.
4. Yin, P.; Zhang, Q.; Shreeve, J. n. M., *Acc. Chem. Res.* **2016**, *49* (1), 4-16.
5. Li, Z.-m.; Xie, S.-h.; Zhang, J.-g.; Feng, J.-l.; Wang, K.; Zhang, T.-l., *J. Chem. Eng. Data* **2012**, *57* (3), 729-736.
6. da Silva, G.; Bozzelli, J. W., *J. Org. Chem.* **2008**, *73* (4), 1343-1353.
7. Niko, F.; M., K. T.; Jörg, S., *Z. Anorg. Allg. Chem.* **2009**, *635* (2), 271-281.
8. M., K. T.; Jörg, S., *Helv. Chim. Acta* **2007**, *90* (11), 2132-2150.
9. Chatterjee, S.; Deb, U.; Datta, S.; Walther, C.; Gupta, D. K., *Chemosphere* **2017**, *184*, 438-451.
10. Klapötke, T. M.; Minar, N. K.; Stierstorfer, J., *Polyhedron* **2009**, *28* (1), 13-26.
11. Klapötke, T. M.; Sabaté, C. M., *Chem. Mater.* **2008**, *20* (11), 3629-3637.
12. Aakeroy, C. B.; Wijethunga, T. K.; Desper, J., *CrystEngComm* **2014**, *16* (1), 28-31.
13. Klapötke, T. M.; Krumm, B.; Xaver Steemann, F.; Steinhauser, G., *Safety Sci.* **2010**, *48* (1), 28-34.
14. Klapotke, T. M.; Piercy, D. G.; Stierstorfer, J., *Dalton Trans.* **2012**, *41* (31), 9451-9459.
15. Fendt, T.; Fischer, N.; Klapötke, T. M.; Stierstorfer, J., *Inorg. Chem.* **2011**, *50* (4), 1447-1458.
16. M., K. T.; A., L. H.; Jörg, S., *Propellants Explos. Pyrotech* **2008**, *33* (6), 421-430.
17. Nayak, A.; Pedireddi, V. R., *Cryst. Growth Des.* **2016**, *16* (10), 5966-5975.
18. Ma, Y.; Zhang, A.; Xue, X.; Jiang, D.; Zhu, Y.; Zhang, C., *Cryst. Growth Des.* **2014**, *14* (11), 6101-6114.
19. Tian, B.; Xiong, Y.; Chen, L.; Zhang, C., *CrystEngComm* **2018**, *20* (6), 837-848.
20. Zhang, C.; Wang, X.; Huang, H., *J. Am. Chem. Soc.* **2008**, *130* (26), 8359-8365.
21. Kent, R. V.; Wiscons, R. A.; Sharon, P.; Grinstein, D.; Frimer, A. A.; Matzger, A. J., *Cryst. Growth Des.* **2018**, *18* (1), 219-224.

Chapter 7 Summary

The chemistry beyond the molecule has opened new avenues to make predictable supramolecular assemblies and functional materials using non-covalent interactions. Hydrogen bonding, halogen bonding, metal-ligand coordination, and π interactions play a major role in assembling supramolecular architectures. Since the supramolecular synthesis is one pot process, the identification of correct synthons and supramolecular forces in order to build desired architecture has to be done carefully and systematic manner. In this thesis, we have discussed how to efficiently manipulate several supramolecular synthons and non-covalent interactions in order to make advanced supramolecular assemblies and materials.

7.1 Manipulation of halogen bonding and metal-ligand coordination in supramolecular chemistry

As the first step, we have selected halogen bonding and metal-ligand coordination in order to make predictable supramolecular architectures. A library of ligands containing acac functionality and halogen bond donor functionality (1,4-substituted and 1,3-substituted) has been designed and synthesized. The acac moiety has been used as metal coordinating site and halogen bond donors have utilized to make non-covalent interactions with the acceptor sites present in ligand/ metal-ligand complexes. As expected metal-coordination site has coordinated with the copper metal ion successfully without any interferences from counter anions or coordinating solvents. In the presence of solvents (acetonitrile and ethyl acetate) that can act as halogen bond acceptors, the halogen bond donor sites of 1,4-substituted metal-ligand complexes have interacted with the solvent. In the presence of poor halogen bond acceptor such as nitromethane, halogen bond driven supramolecular architecture was observed and no interactions were formed between metal-ligand complex and the solvent. With the 1,3-substituted ligand, halogen bonded

supramolecular architecture was observed even in the presence of acetonitrile as the solvent. When forming supramolecular architectures, halogen bond donor sites and several acceptor sites of the metal-ligand complexes have been utilized by the non-covalent interactions such as halogen bonding and halogen $\cdots\pi$ interactions (Figure 7.1).

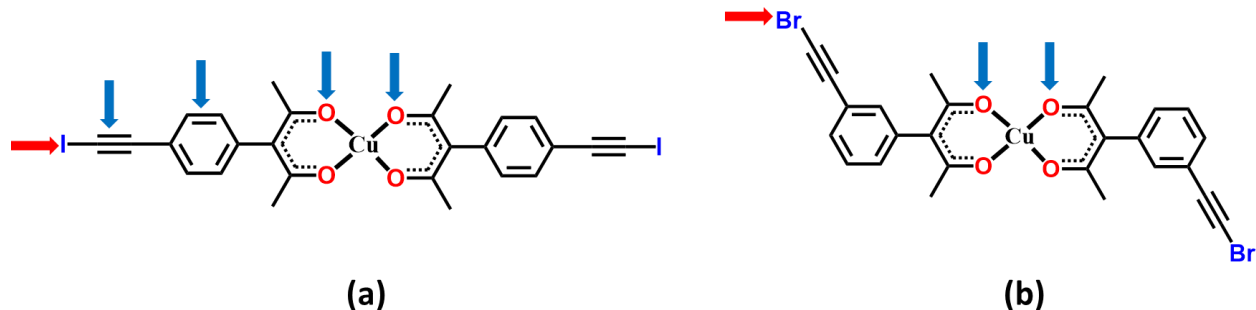


Figure 7.1 Donor (red arrows) and acceptor (blue arrows) sites utilized by non-covalent interactions (a) in a 1,4-substituted metal ligand complex, (b) in a 1,3-substituted metal ligand complex¹

7.2 Finding alternative supramolecular forces

Next, we have investigated competition of halogen bonding Vs. hydrogen bonding by designing and synthesizing tetra-functionalized HB and XB donor molecules. The donor molecules were equipped with two halogen-bond donors ($C\equiv C-I$) and two hydrogen bond donors ($O-H$). Several nitrogen based acceptors were introduced to the donors in order study the competition between HB and XB interactions. Based on the interactions that are observed in the co-crystals, both interaction types are equally competitive to behave similarly (Figure 7.2).

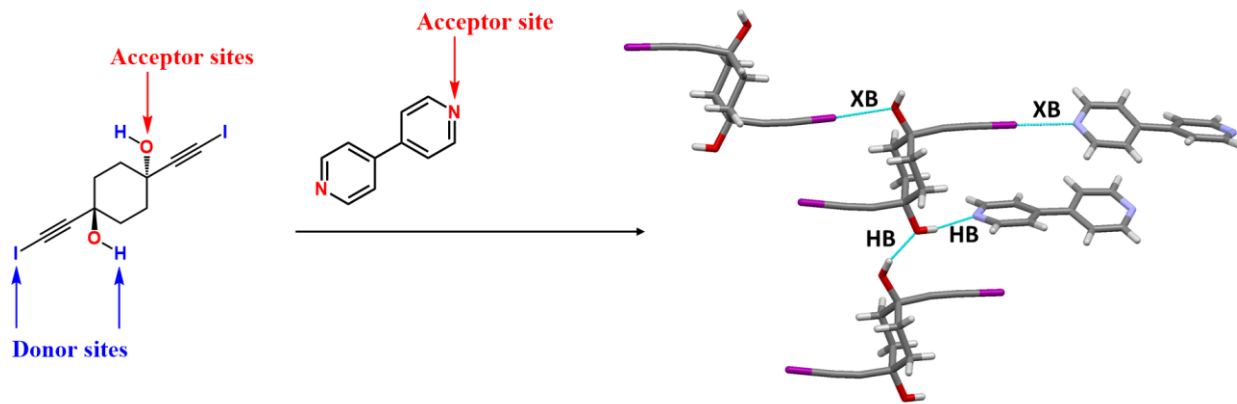


Figure 7.2 Formation of equal number of HB and XB interactions between a donor and an acceptor molecules²

7.3 Host-guest chemistry in supramolecular chemistry

In order to study the host-guest chemistry involved in cavitands, we have synthesized several cavitands molecules. These cavitands were further functionalized with several functionalitites such as acac, XB donor and HB/XB donor functionalities in order to make advanced supramolecular architectures driven by non-covalent interactions. Formation of supramolecular architectures based on metal-ligand interactions were observed between acac functionalized cavitands and Cu(II) metal ions in solid state and solution state as well (Figure 7.3 (a)). XB donor cavitands and HB/XB donor were able to form non-covalent interactions with nitrogen based acceptors in solid state (Figure 7.3 (b)).

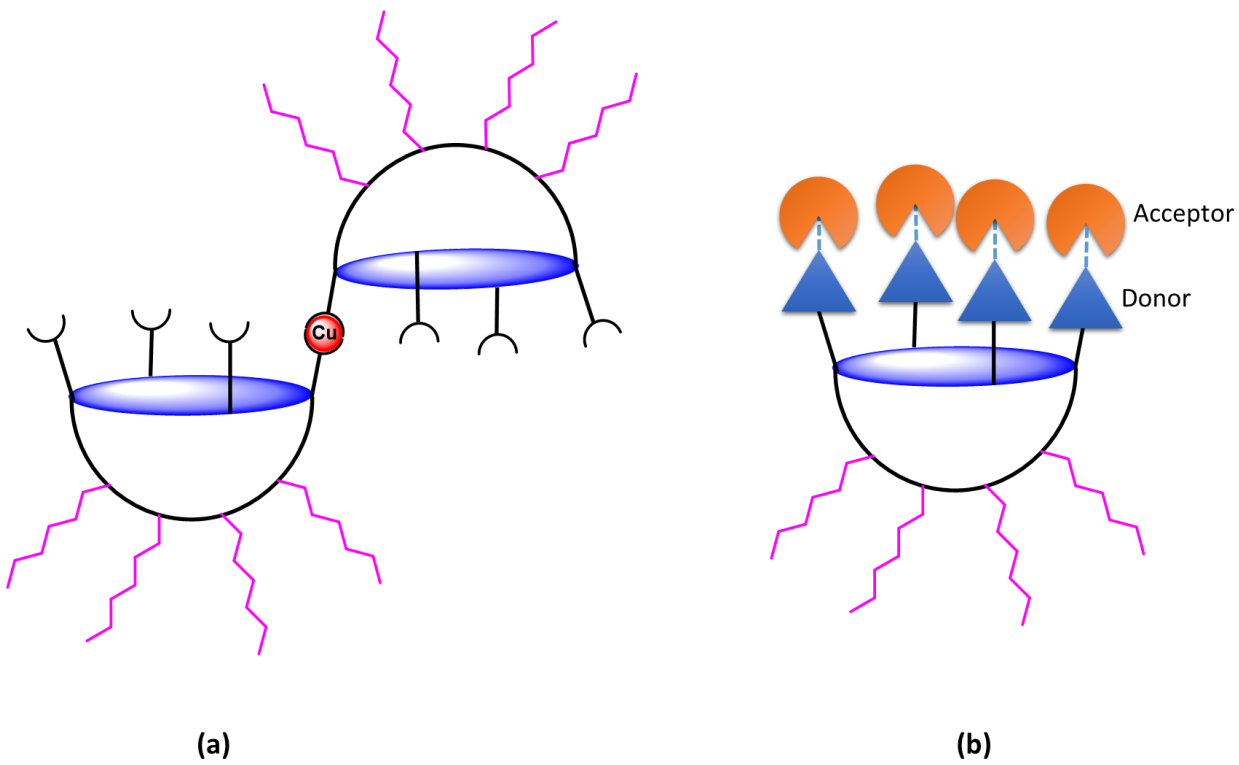


Figure 7.3 Schematic representation of (a) metal-ligand coordination and (b) HB/XB interactions in cavitands

7.4 Applications of supramolecular chemistry

The knowledge of supramolecular interactions and crystal engineering were applied to modify the properties of materials. An energetic material, **PETNC** which suffers from high chemical reactivity due to the presence of acidic protons was combined with potential nitrogen and oxygen based acceptors via hydrogen bonding. Several nitrated tetrazole based explosives suffer from high impact sensitivity and low thermal stability were also subjected co-crystallization with potential nitrogen and oxygen based acceptors. In addition to that potential propellants based on bis-tetrazoles also subjected to the co-crystallization. The co-crystallization approach was successful in improving the stability of the energetics/ explosives by modifying the chemical and physical properties such as reactivity, thermal stability and impact sensitivity while retaining energetic properties (Figure 7.4).

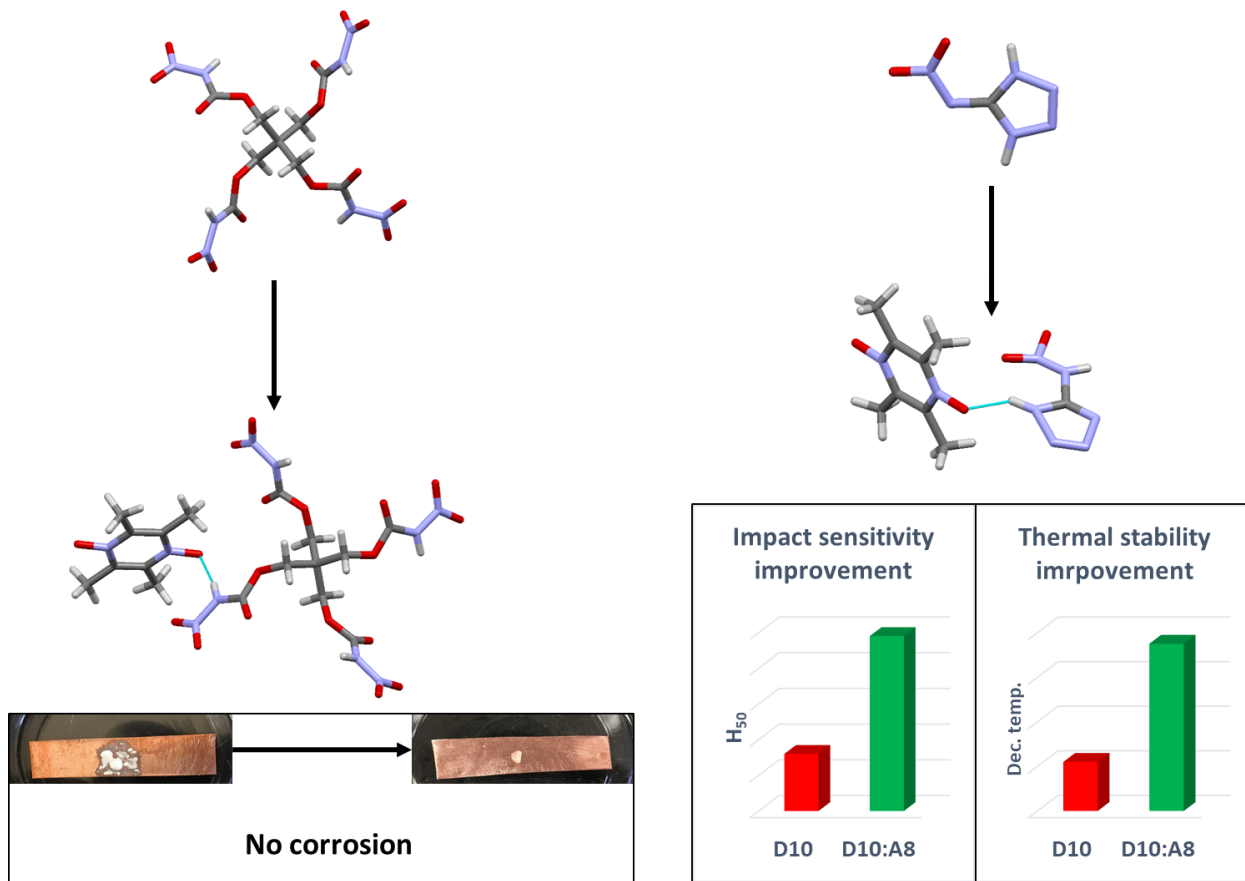


Figure 7.4 Use of co-crystallization to improve chemical, thermal stability and impact sensitivity of explosives

7.5 Future works

The work presented in this thesis provides the fundamental understanding and application of supramolecular chemistry. However, some of these systems can be extended to the next level as described below.

The metal-ligand complexed that were formed between ligands **L1-L6** and metal ions can be further extended by introducing potential halogen-bond acceptors to the system (Figure 7.5). The formation of XB interactions can be expected between halogen atoms and the acceptors such as nitrogen or oxygen by forming complex supramolecular architectures.

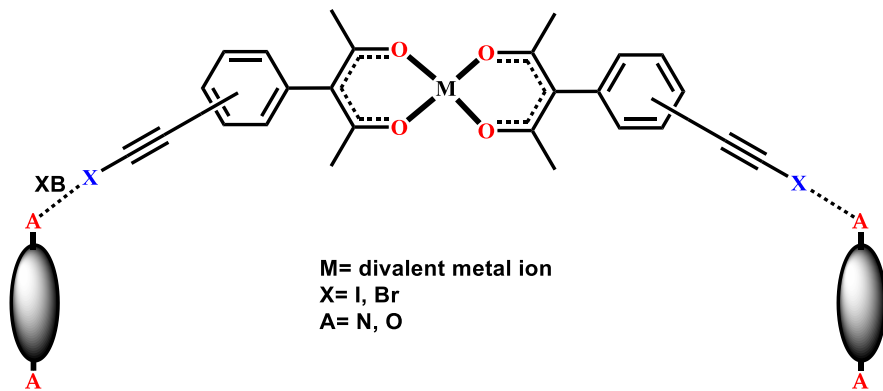


Figure 7.5 Formation of XB interactions between metal-ligand complex and acceptors

The formation of molecular capsules can be expected by introducing suitable ditopic acceptors to the XB donor cavitands. Furthermore, introduction of cavitands that are functionalized with XB acceptors is an alternative way of making capsules.³⁻⁴ (Figure 7.6)

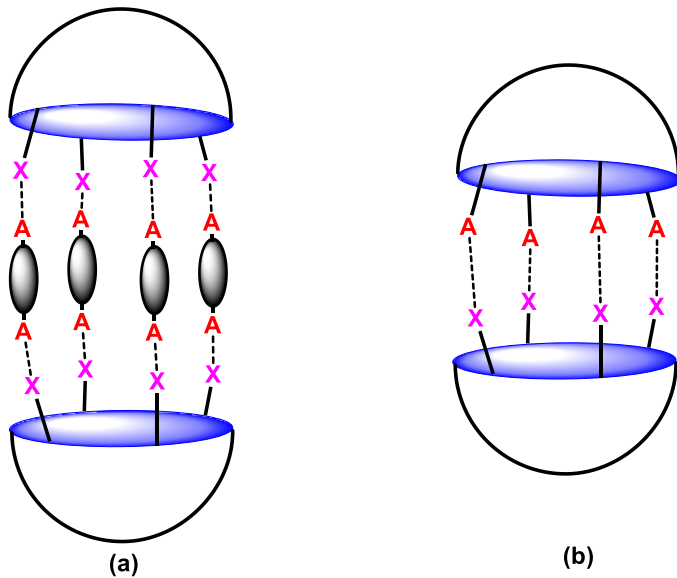


Figure 7.6 Capsule formation between (a) XB donor cavitands and ditopic acceptors (b) XB donor cavitand and XB acceptor cavitand

Energetic-energetic co-crystals formation may give a co-crystal with better performance compared to the energetic-non energetic co-crystals due to the presence of more oxidizers and fuels in the system.⁵⁻⁶ At the same time stabilization of unstable explosives can be achieved with the formation of co-crystals with minimum effect to the explosive properties of both materials. In

order to do that, we have to select one energetic material contains HB donors and the other contains HB acceptors (Figure 7.8).

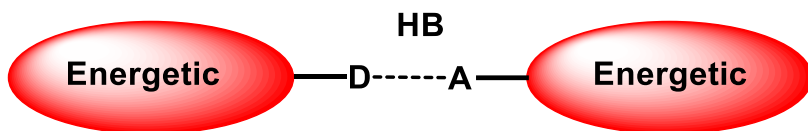
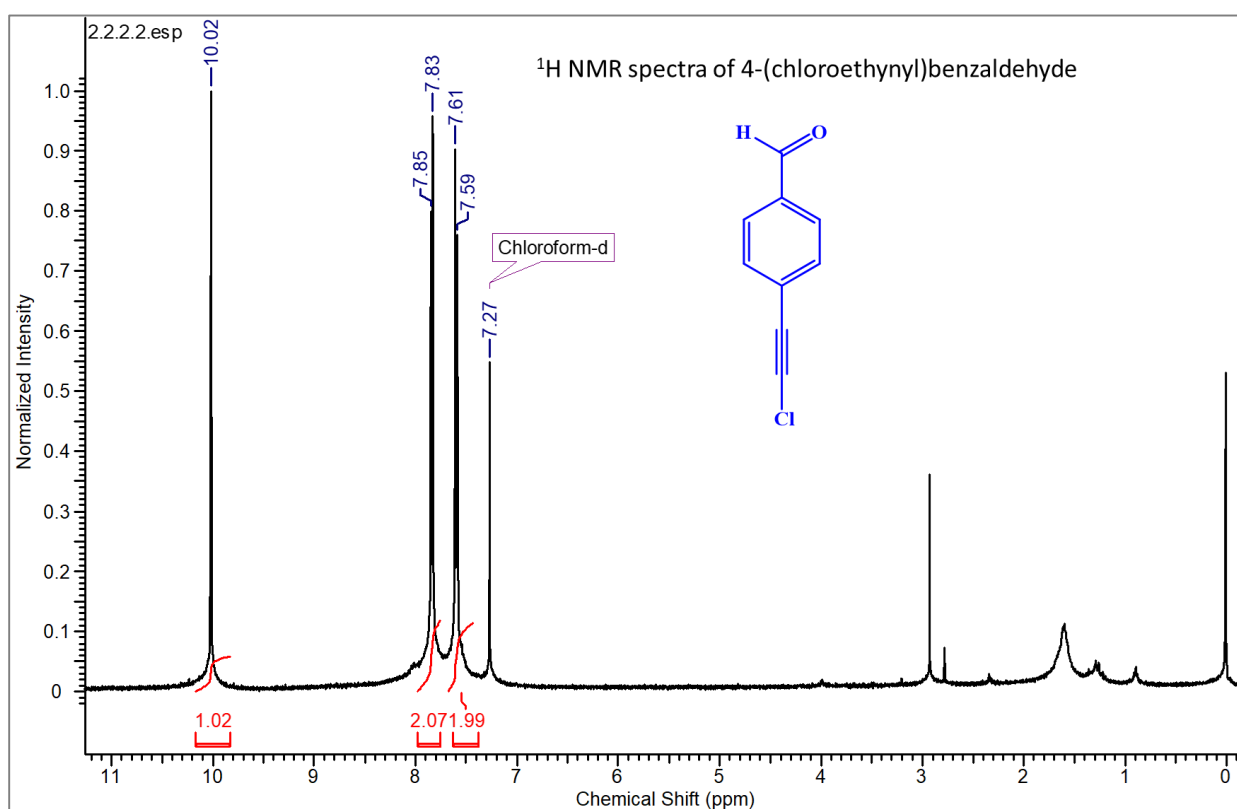
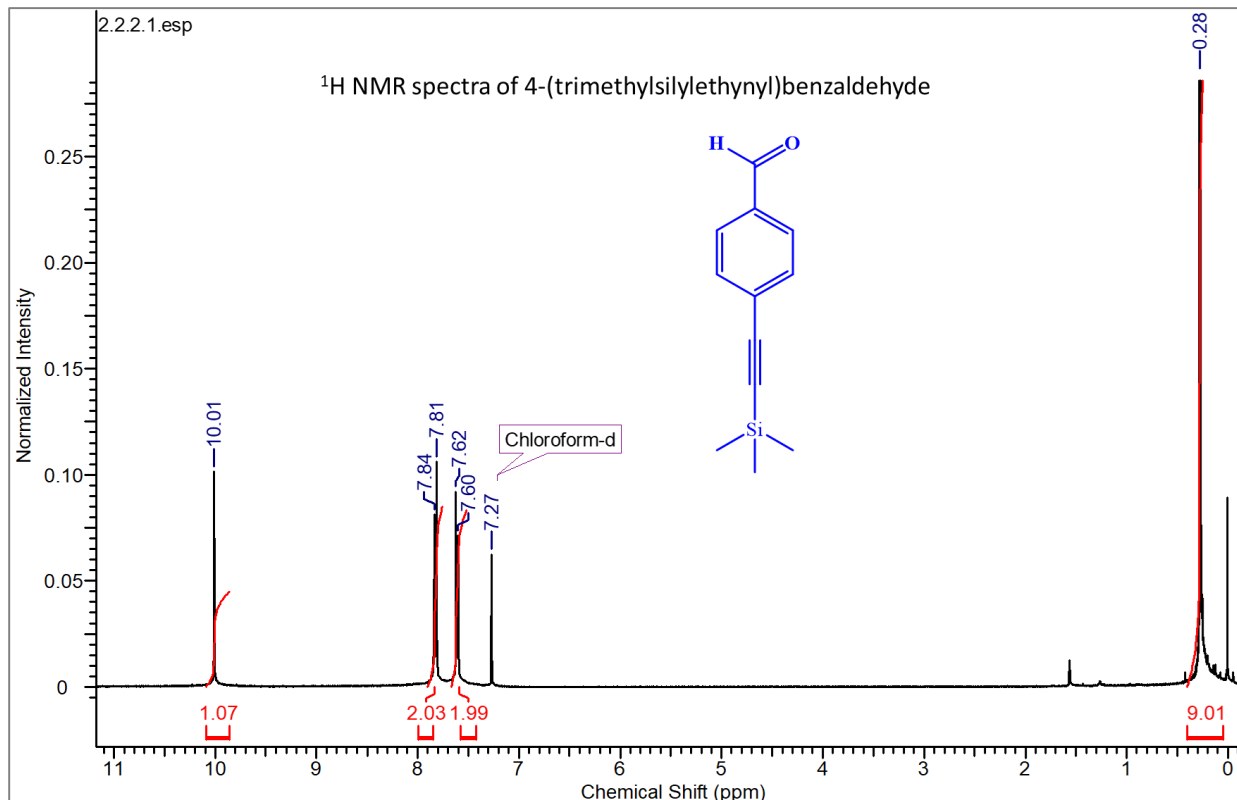


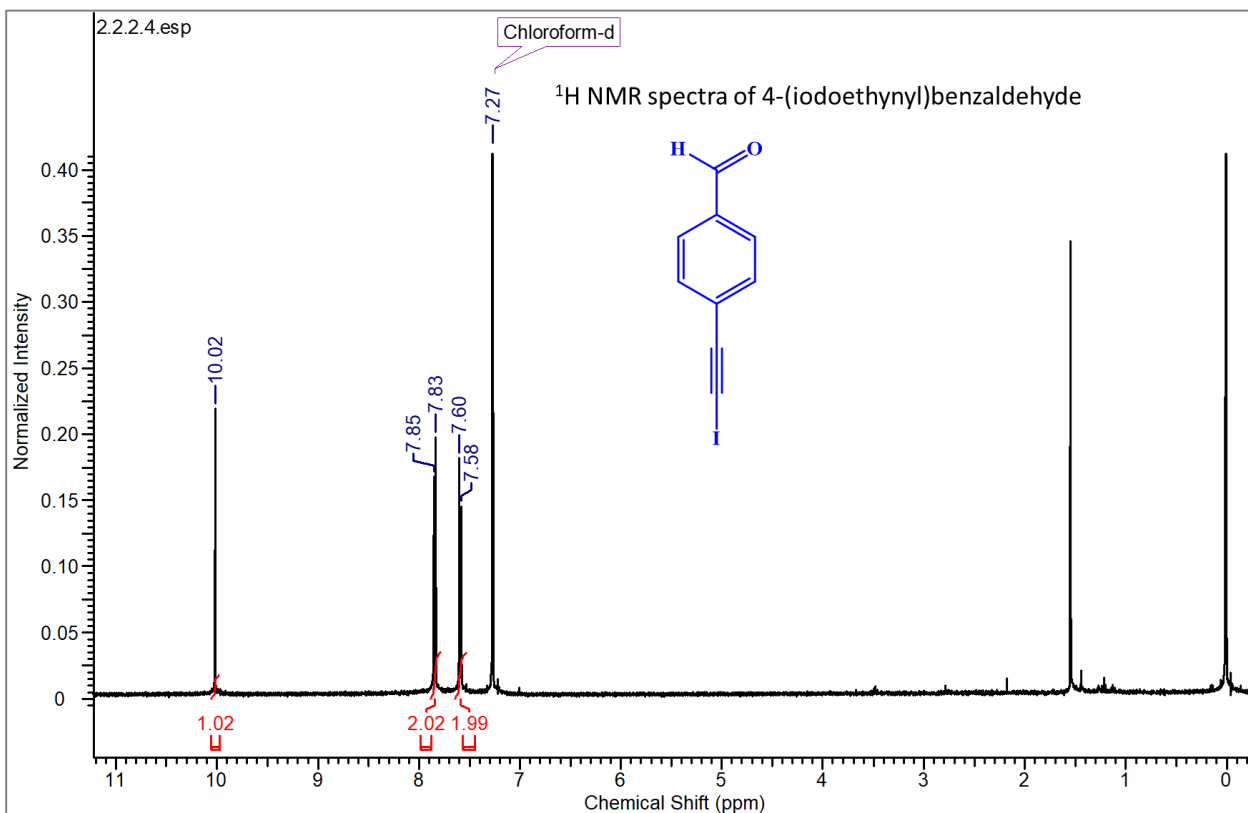
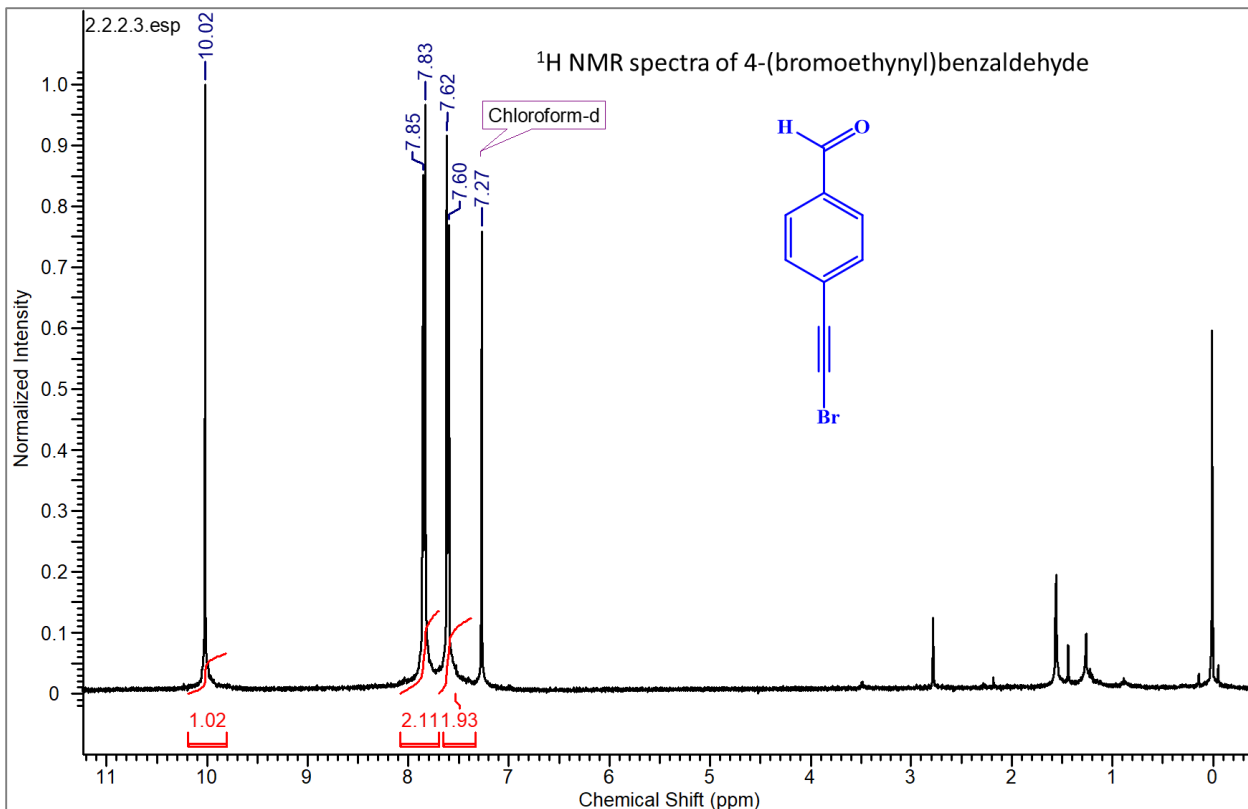
Figure 7.7 Formation of HB interaction driven co-crystal between two energetic materials

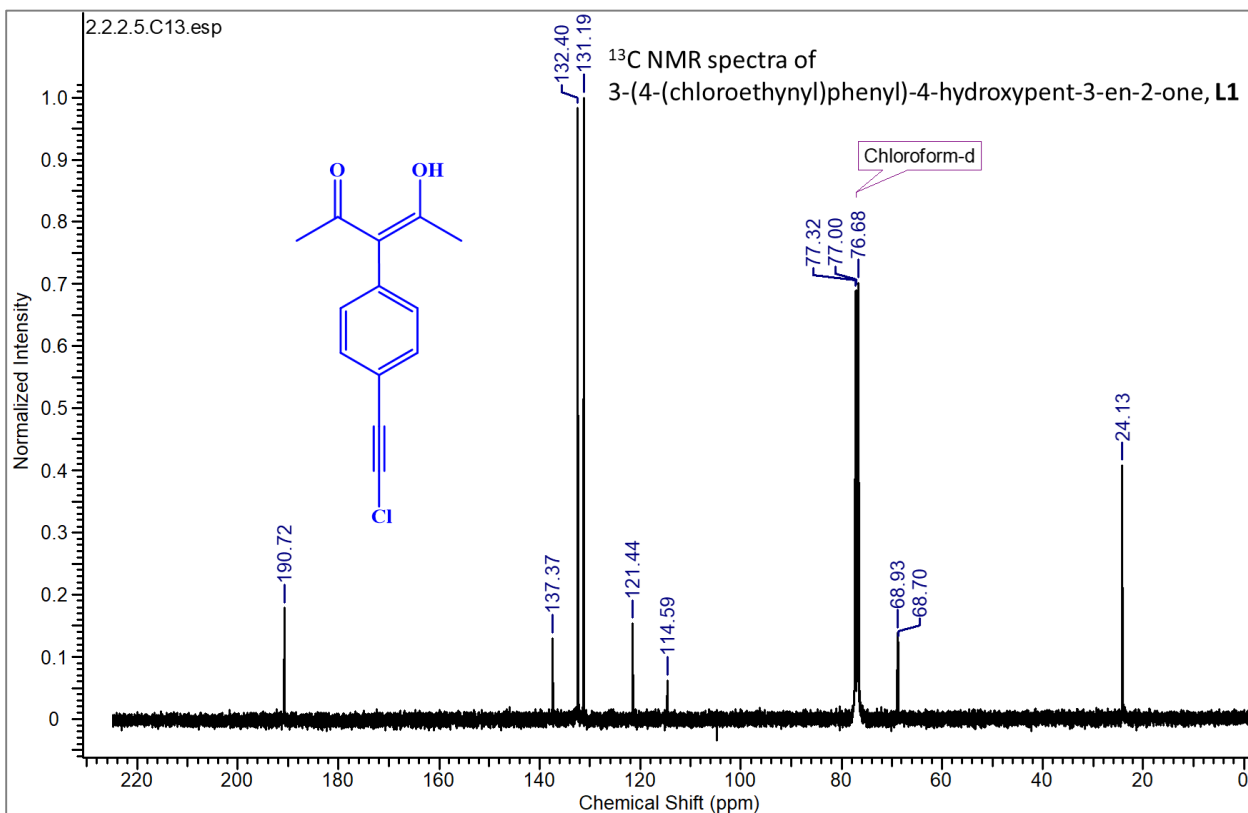
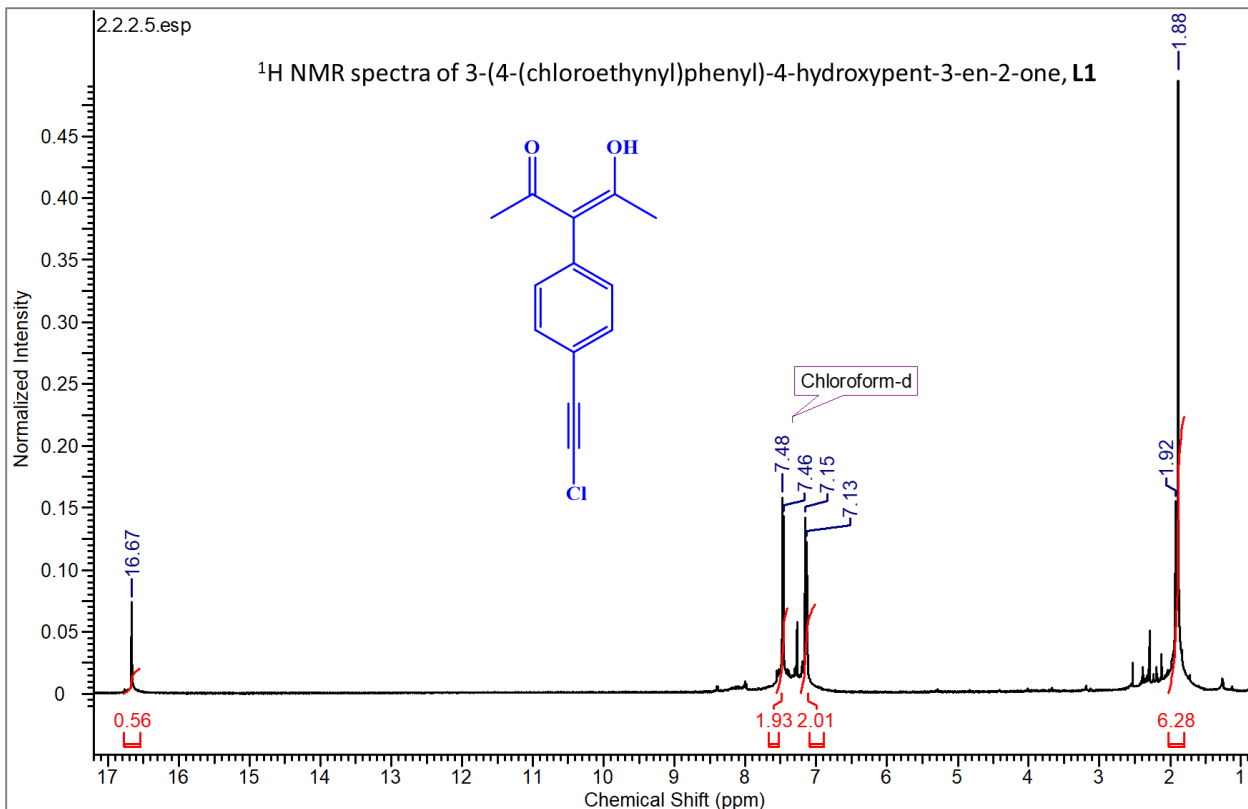
7.6 References

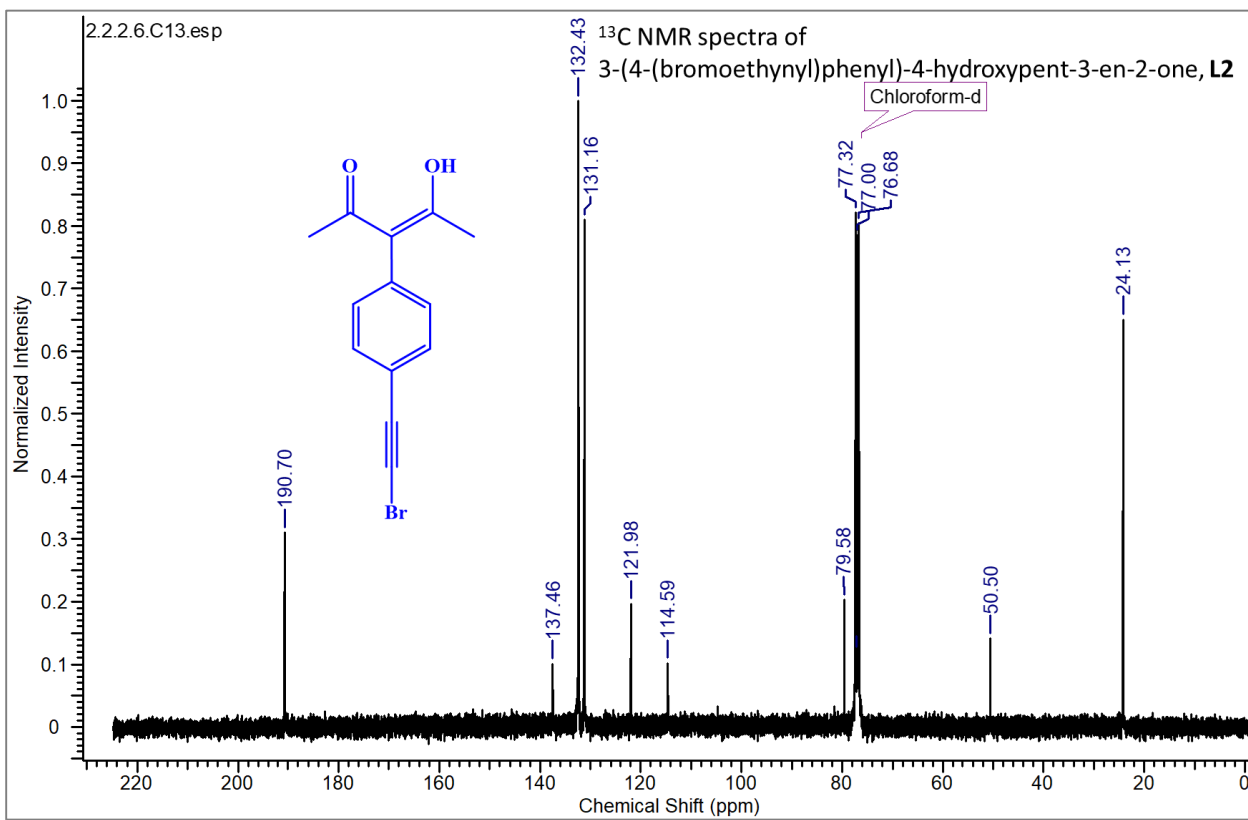
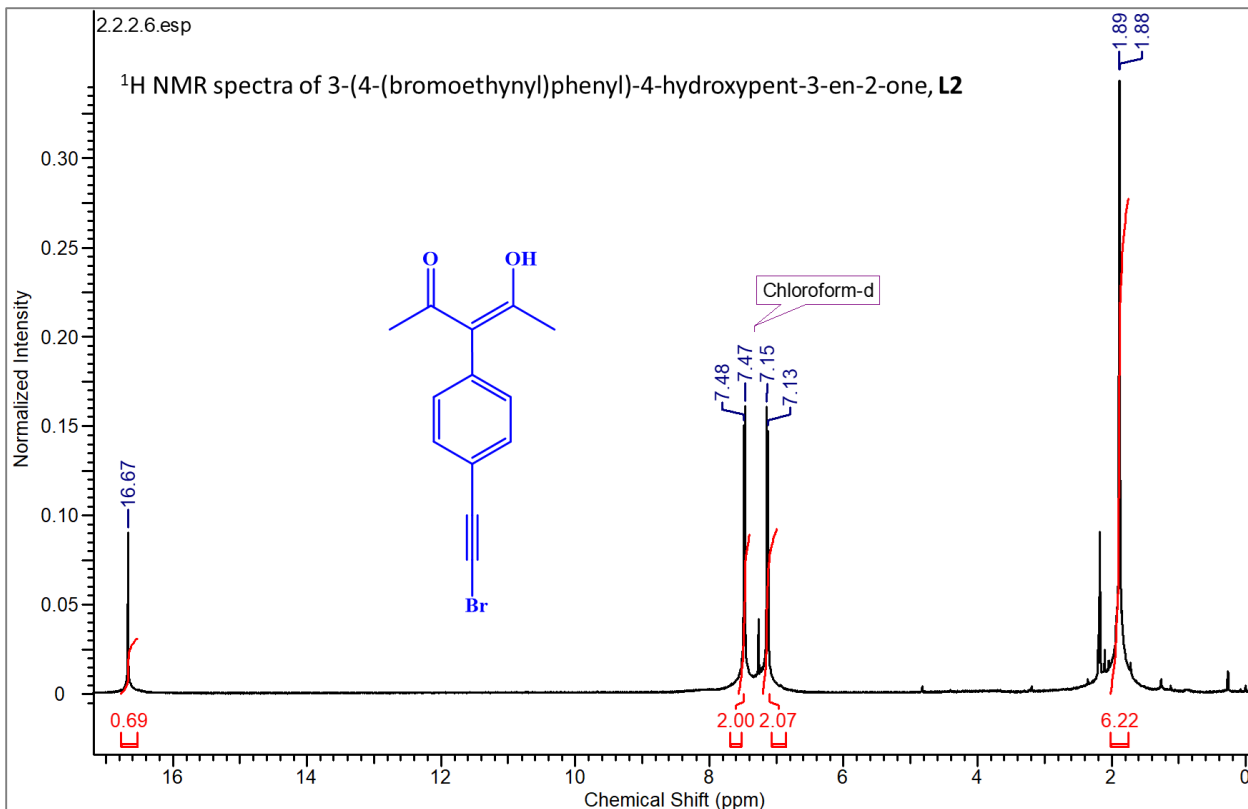
1. Gamekkanda, J.; Sinha, A.; Desper, J.; Đaković, M.; Aakeröy, C., *Crystals* **2017**, 7 (7), 226.
2. Gamekkanda, J. C.; Sinha, A. S.; Desper, J.; Dakovic, M.; Aakeroy, C. B., *New J. Chem.* **2018**, 42 (13), 10539-10547.
3. Groppe, C.; Quigley, B. L.; Diederich, F., *J. Am. Chem. Soc.* **2018**, 140 (8), 2705-2717.
4. Oliver, D.; Nils, T.; François, D., *Angew. Chem. Int. Ed.* **2015**, 54 (42), 12339-12344.
5. Landenberger, K. B.; Bolton, O.; Matzger, A. J., *J. Am. Chem. Soc.* **2015**, 137 (15), 5074-5079.
6. Yang, Z.; Li, H.; Zhou, X.; Zhang, C.; Huang, H.; Li, J.; Nie, F., *Cryst. Growth Des.* **2012**, 12 (11), 5155-5158.

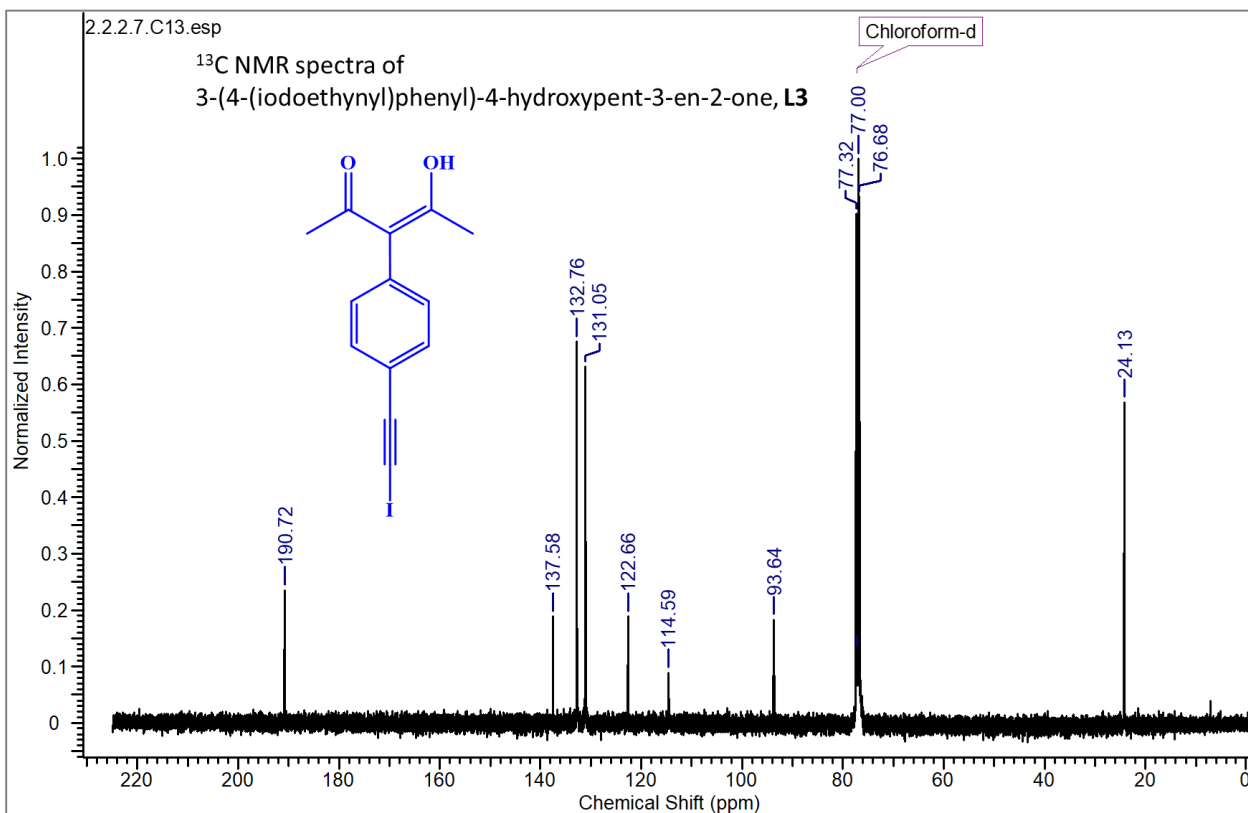
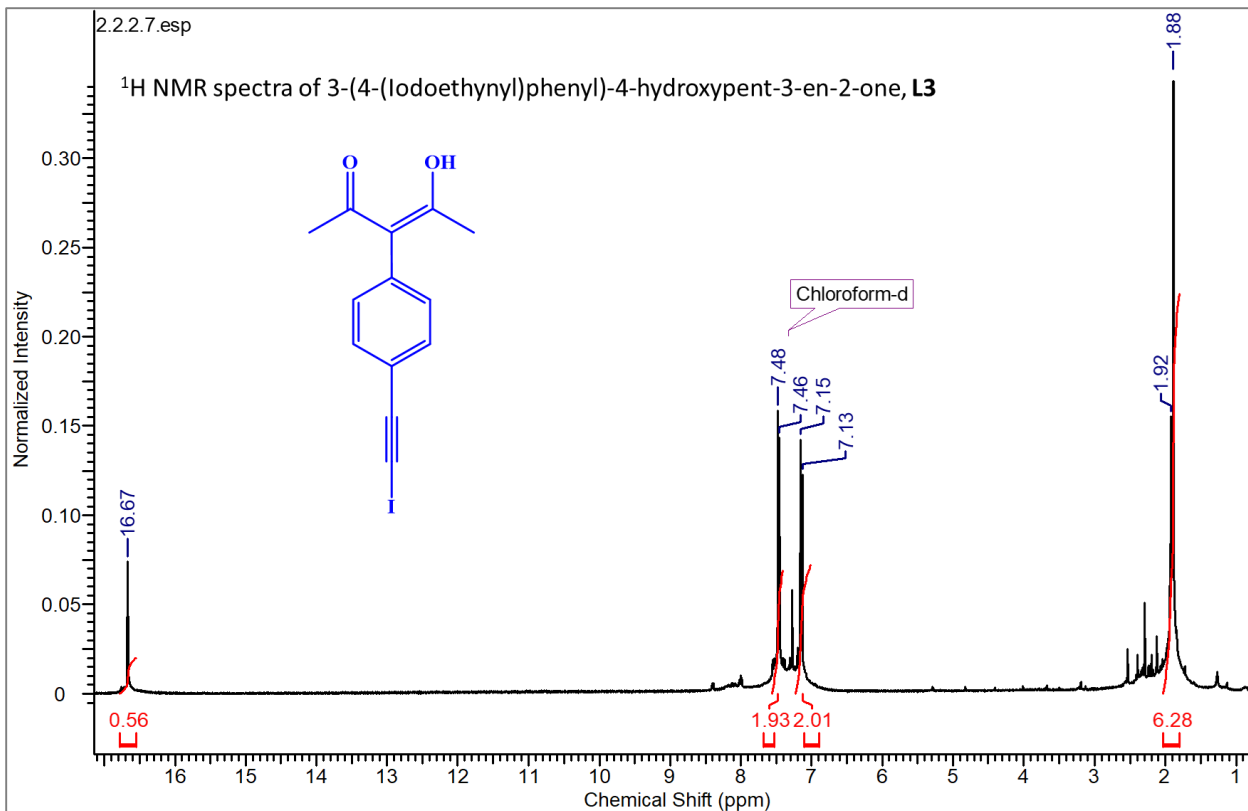
Appendix A – NMR spectra

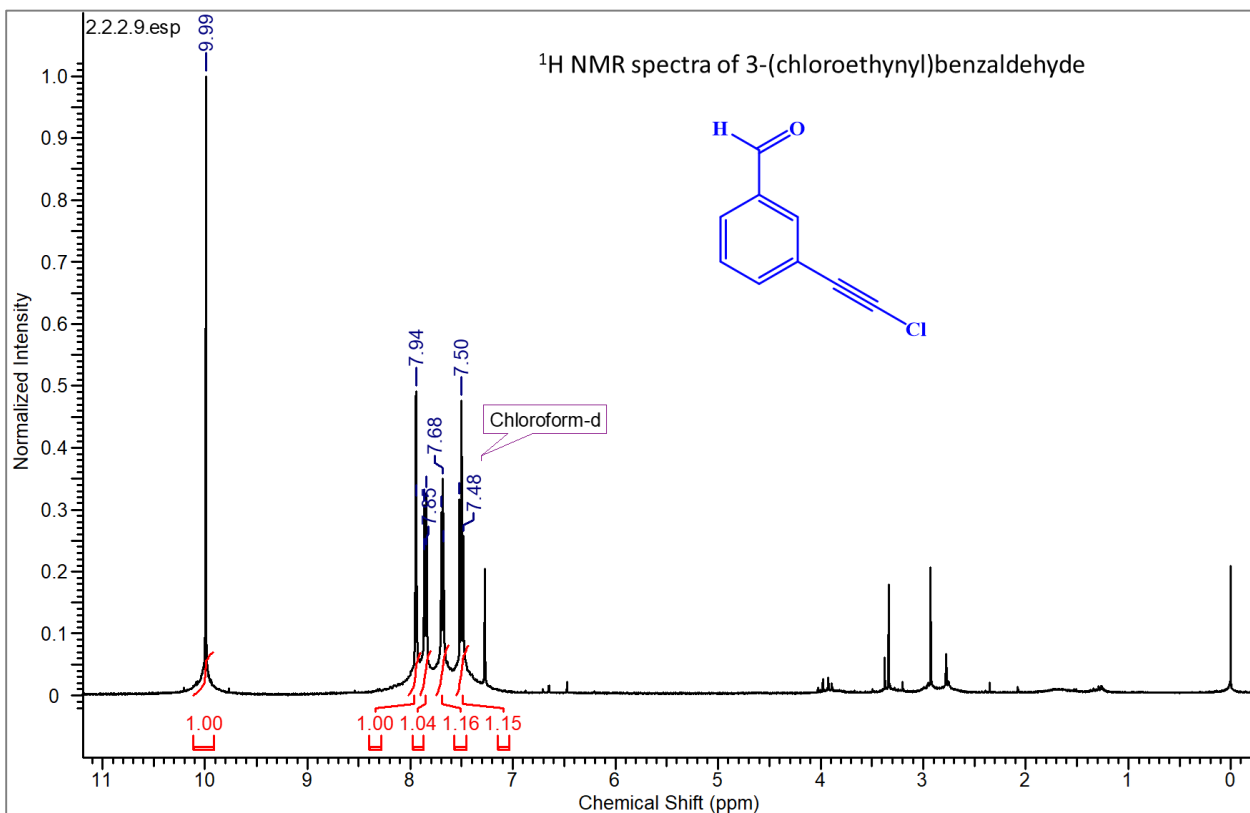
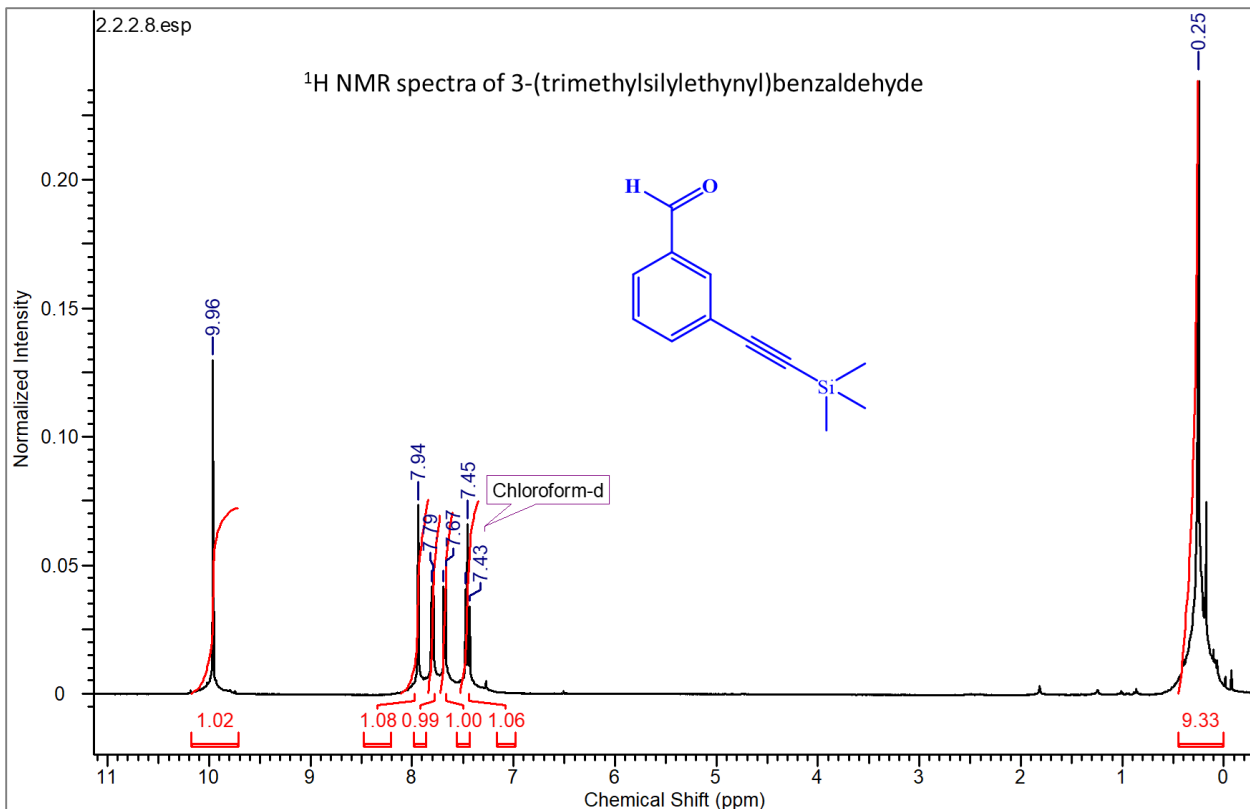


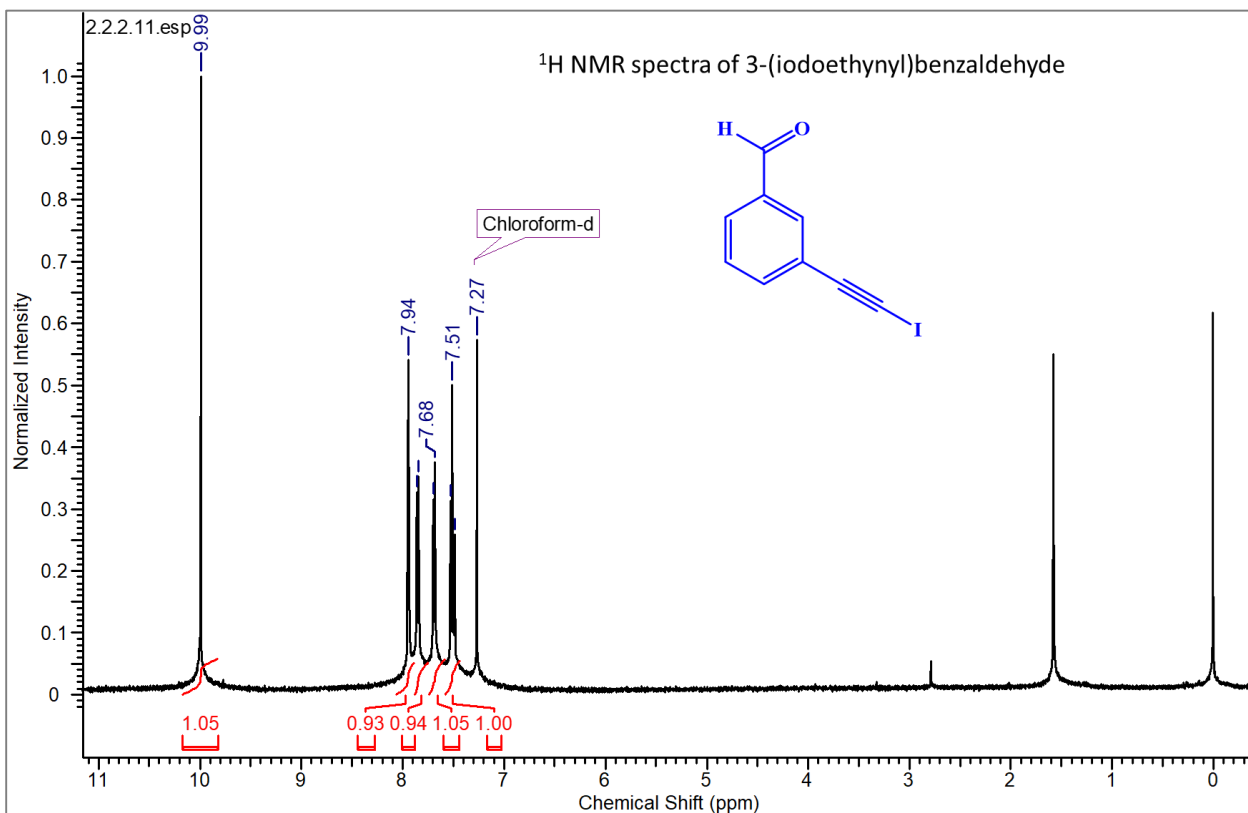
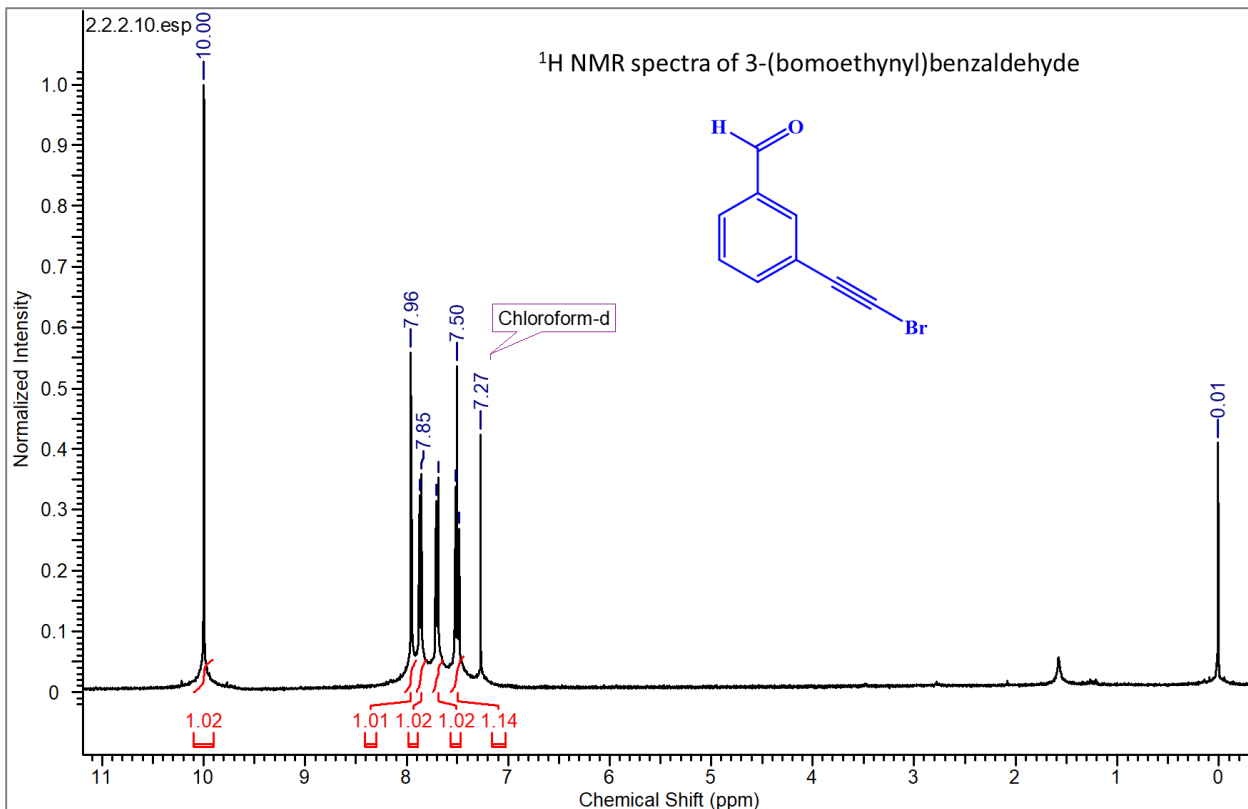


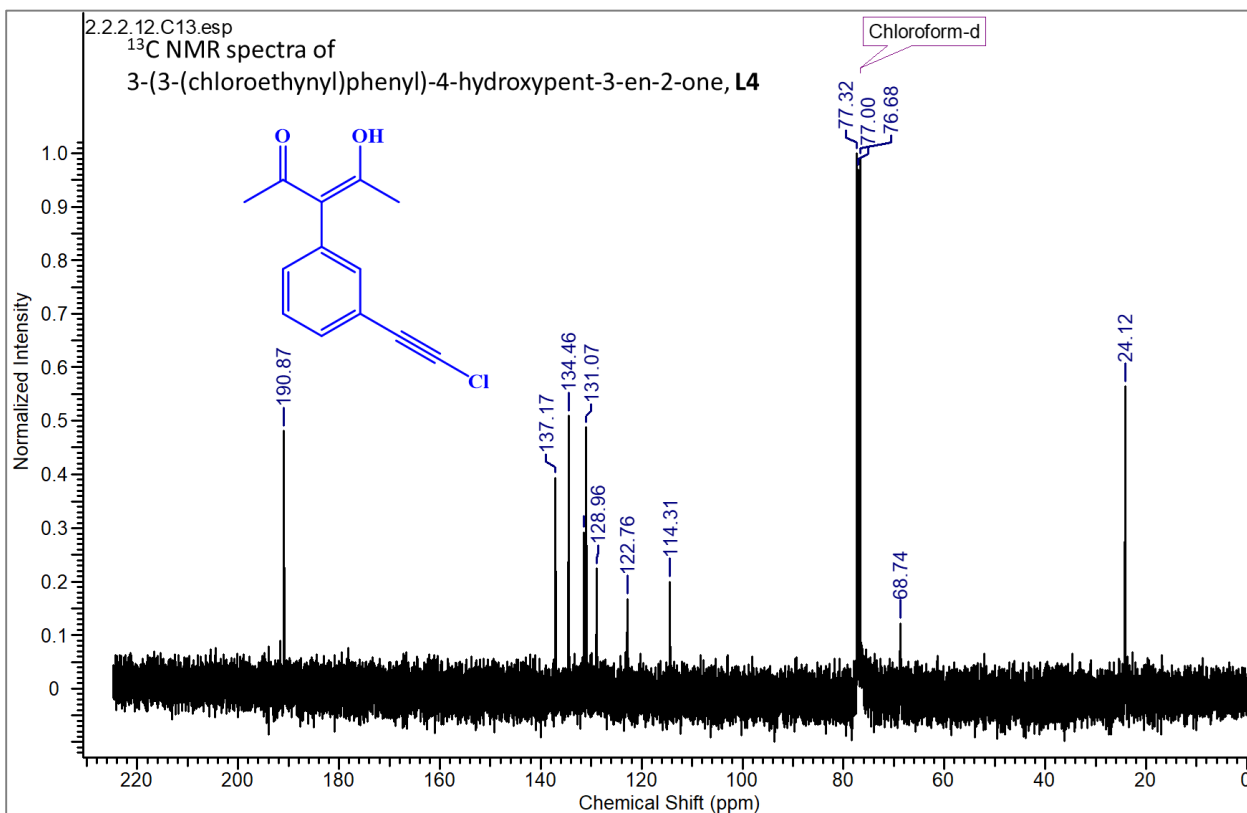
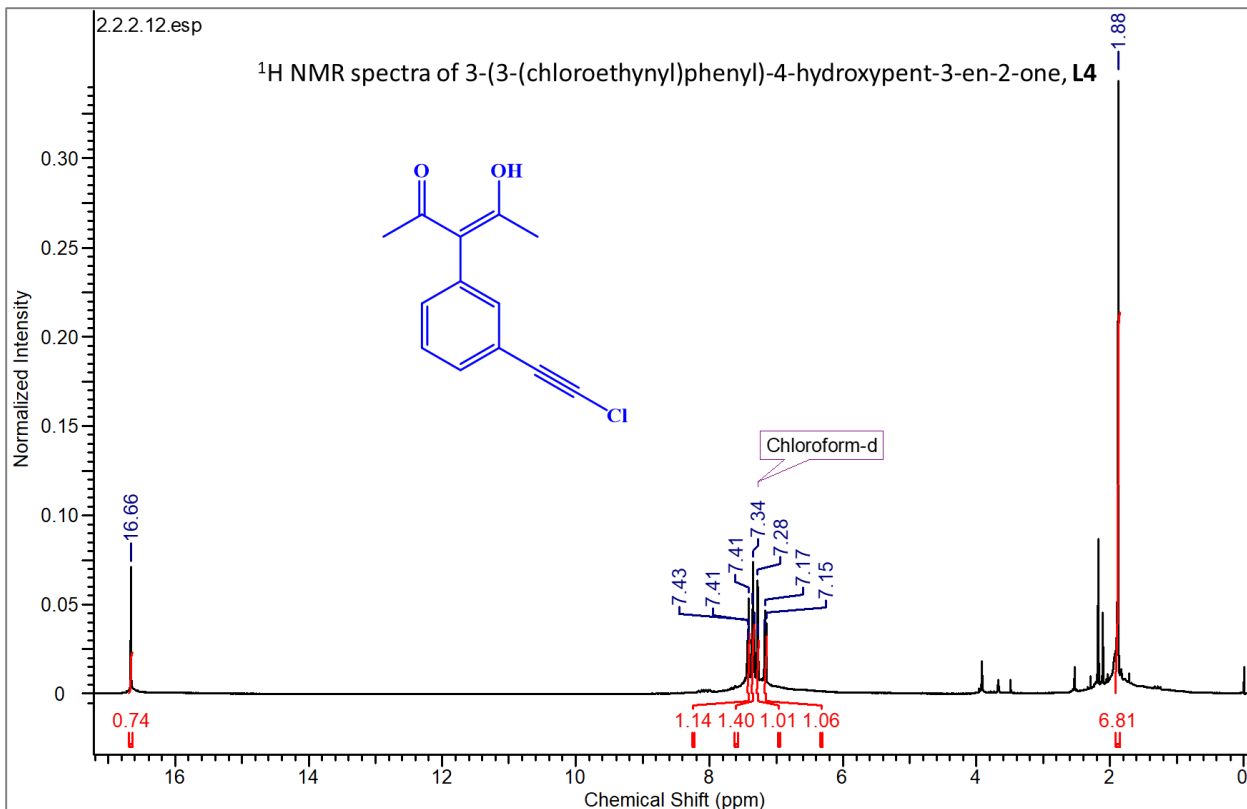


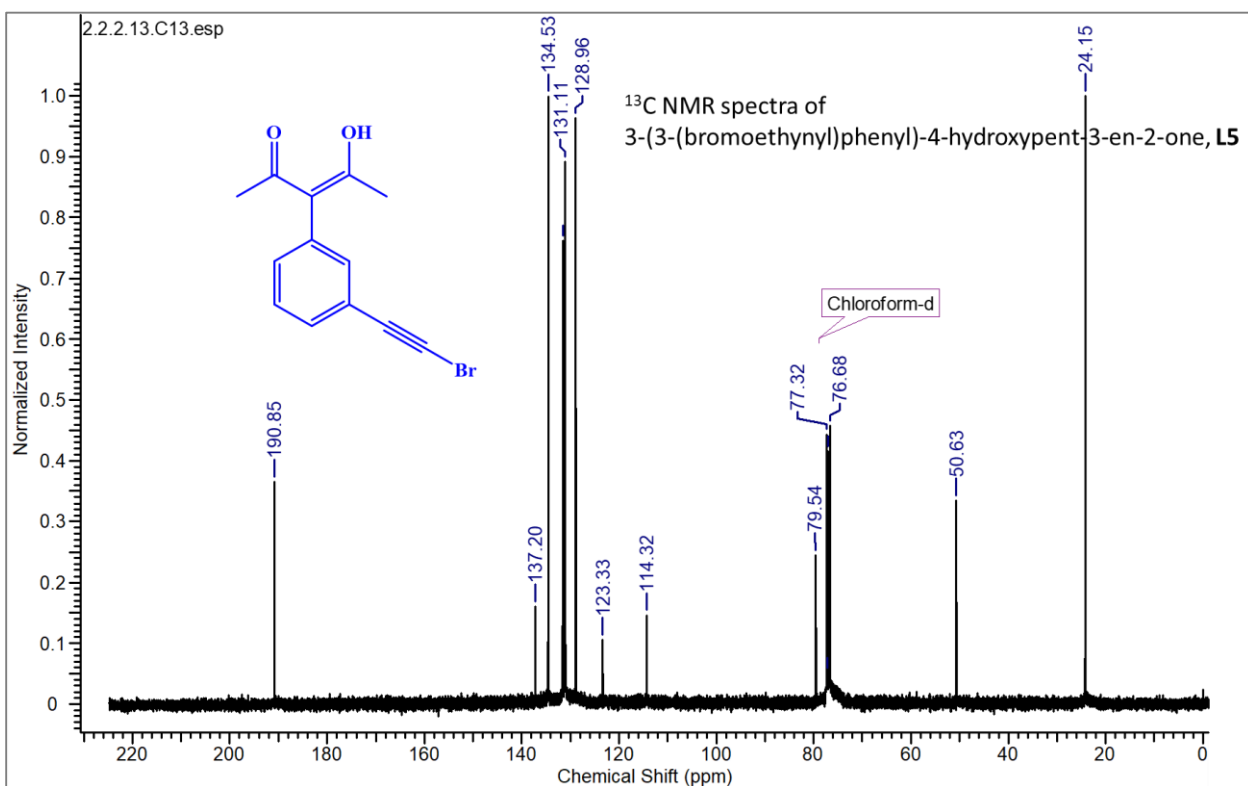
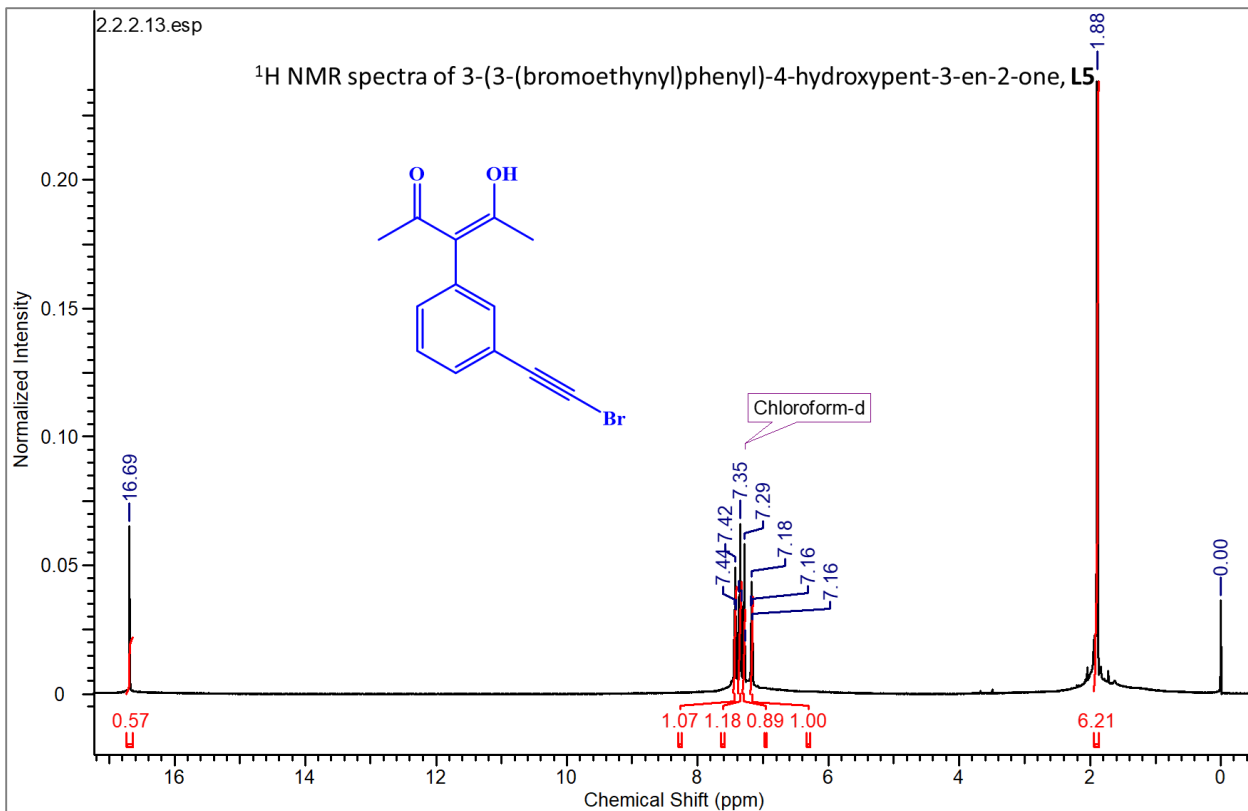


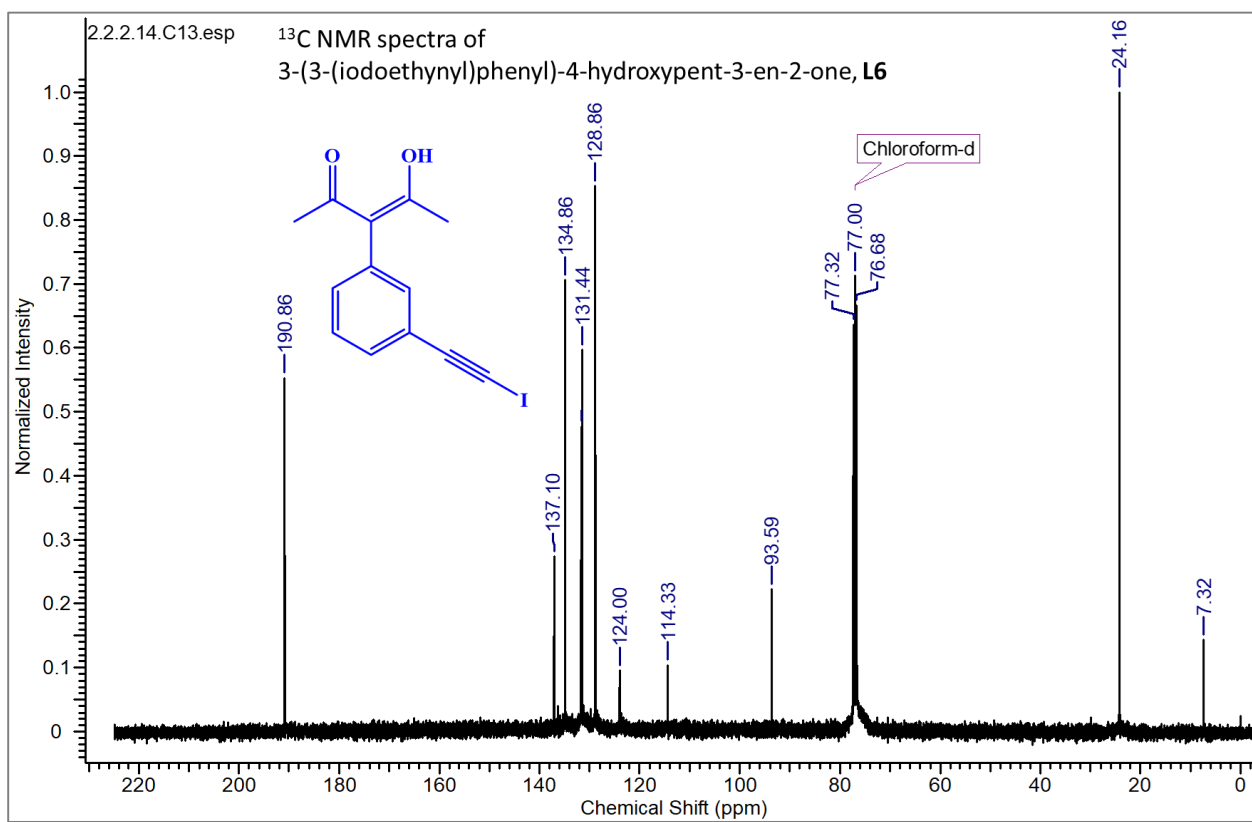
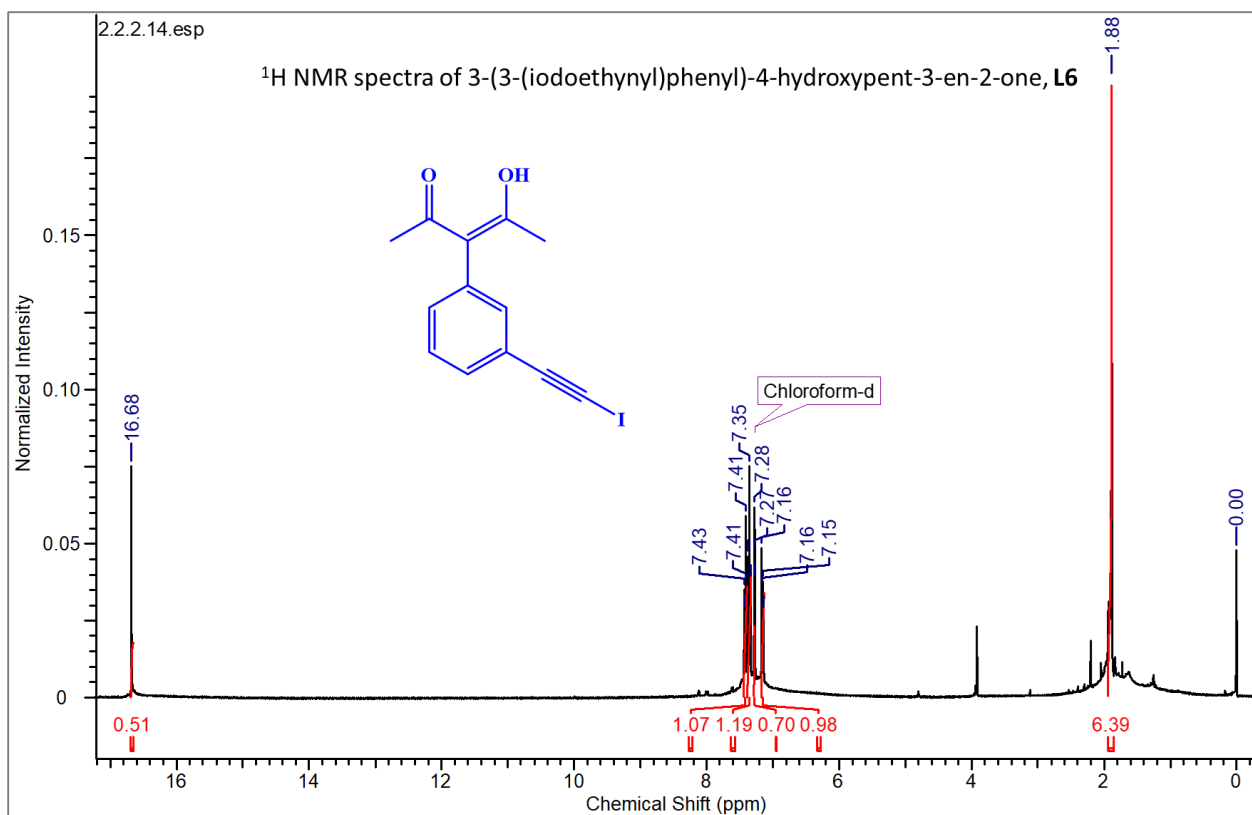


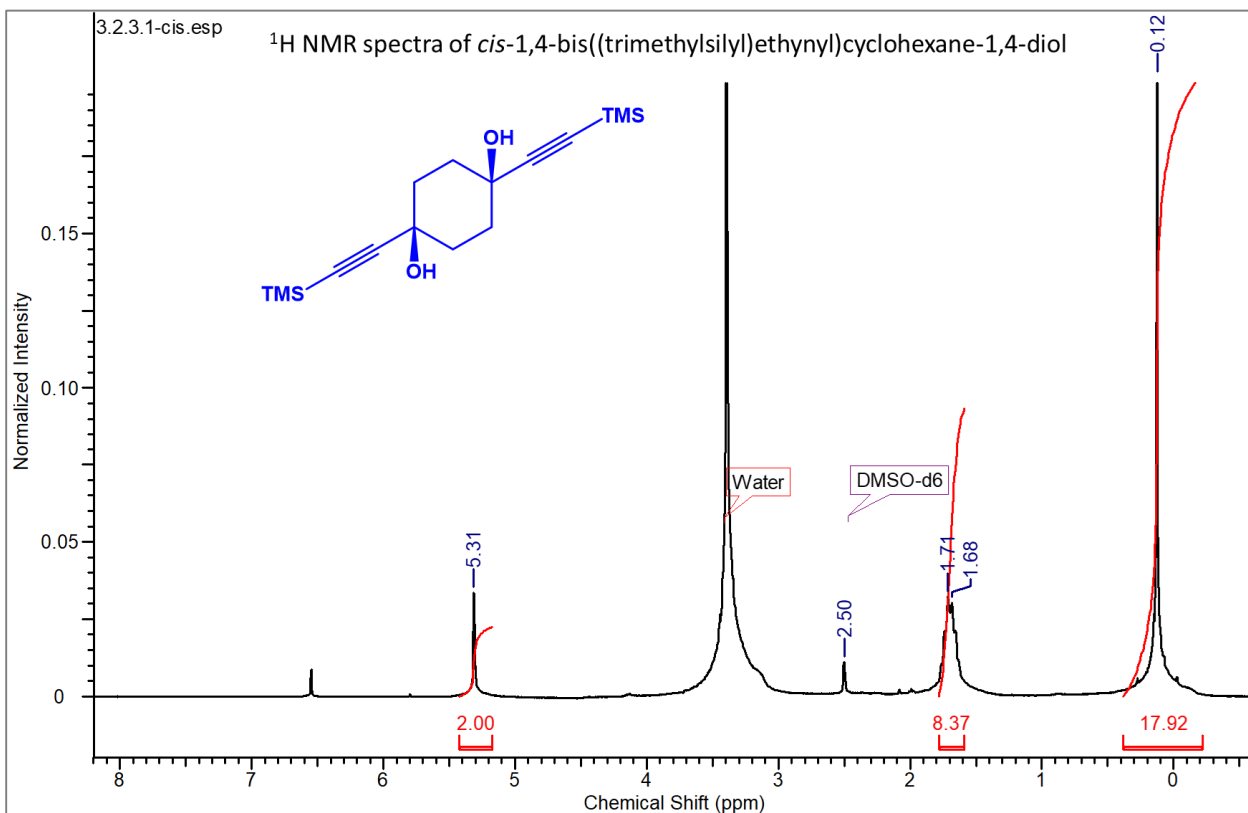
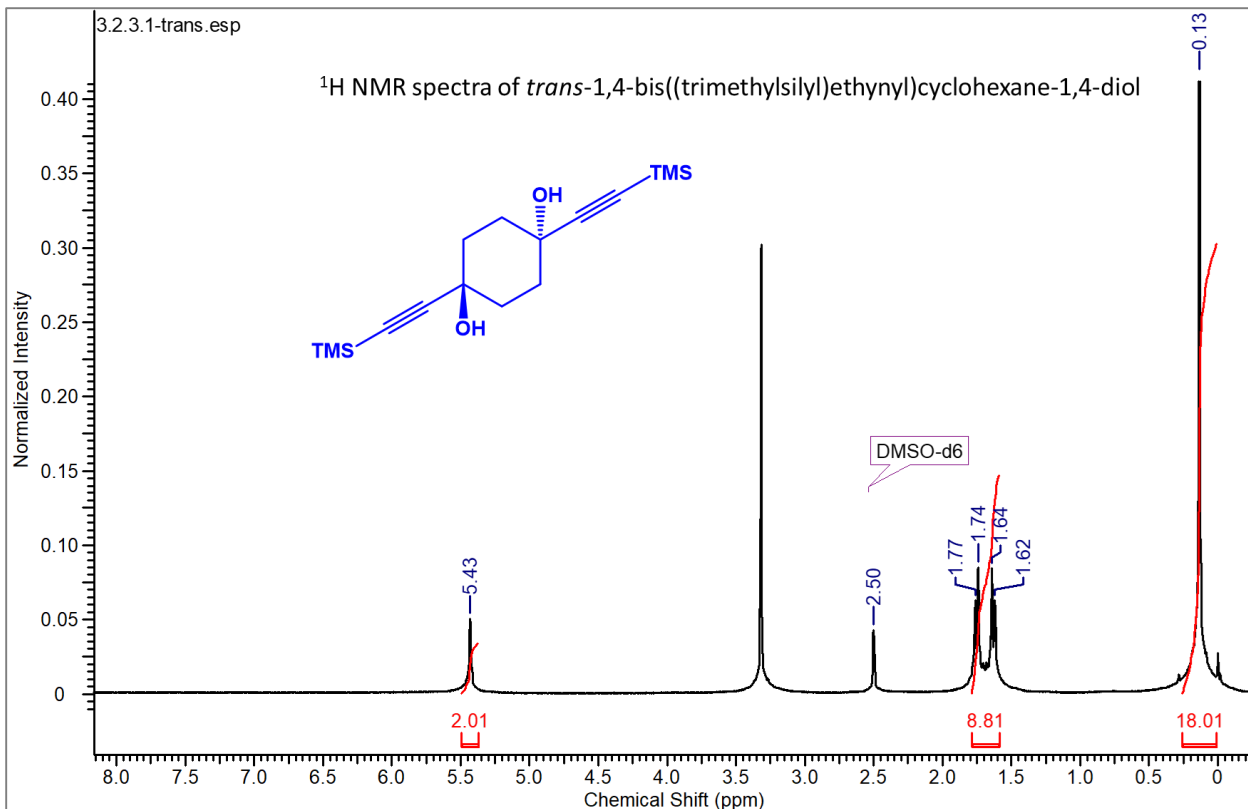


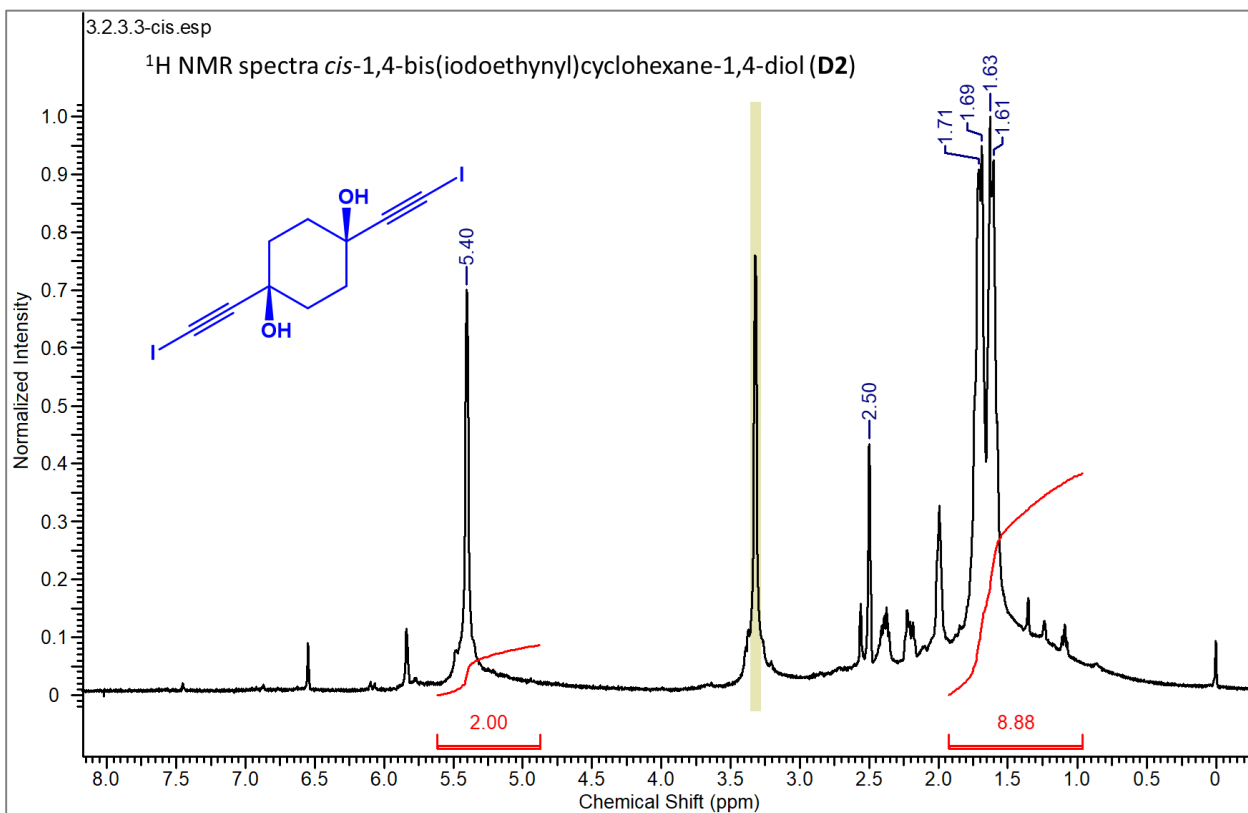
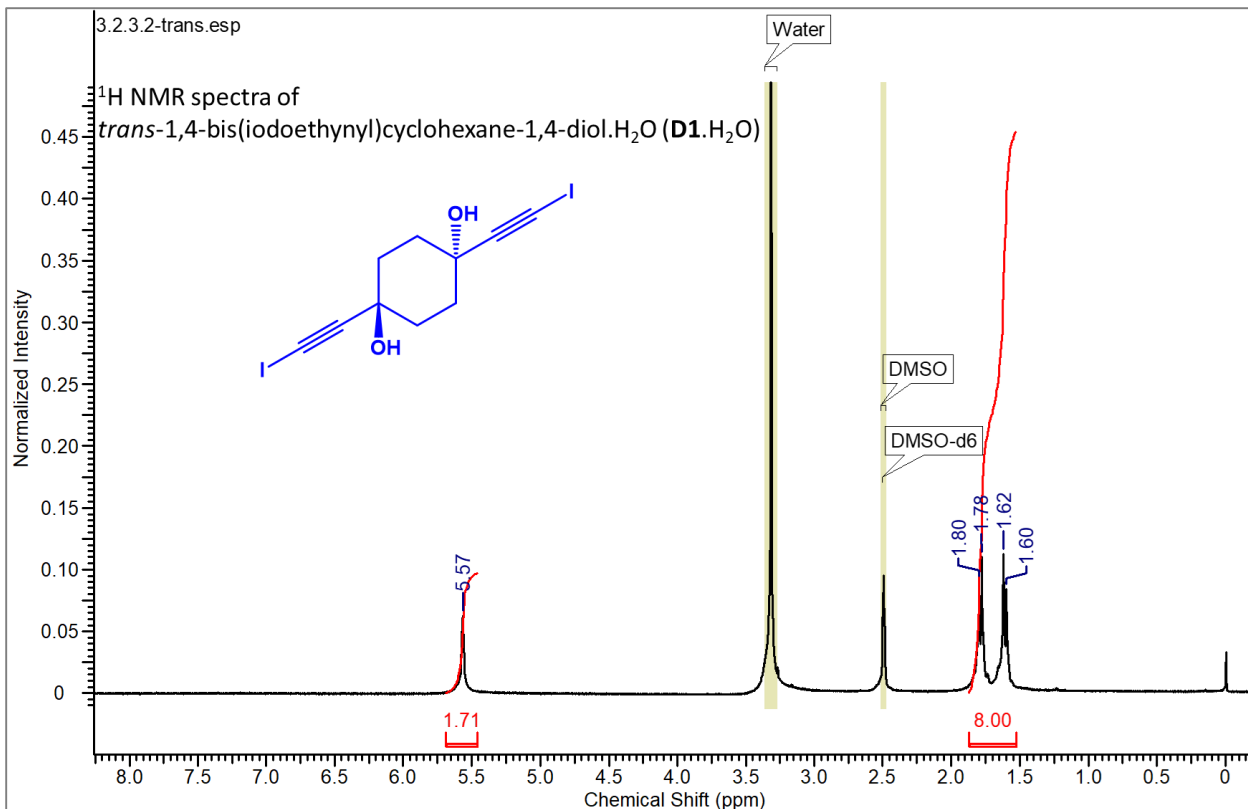


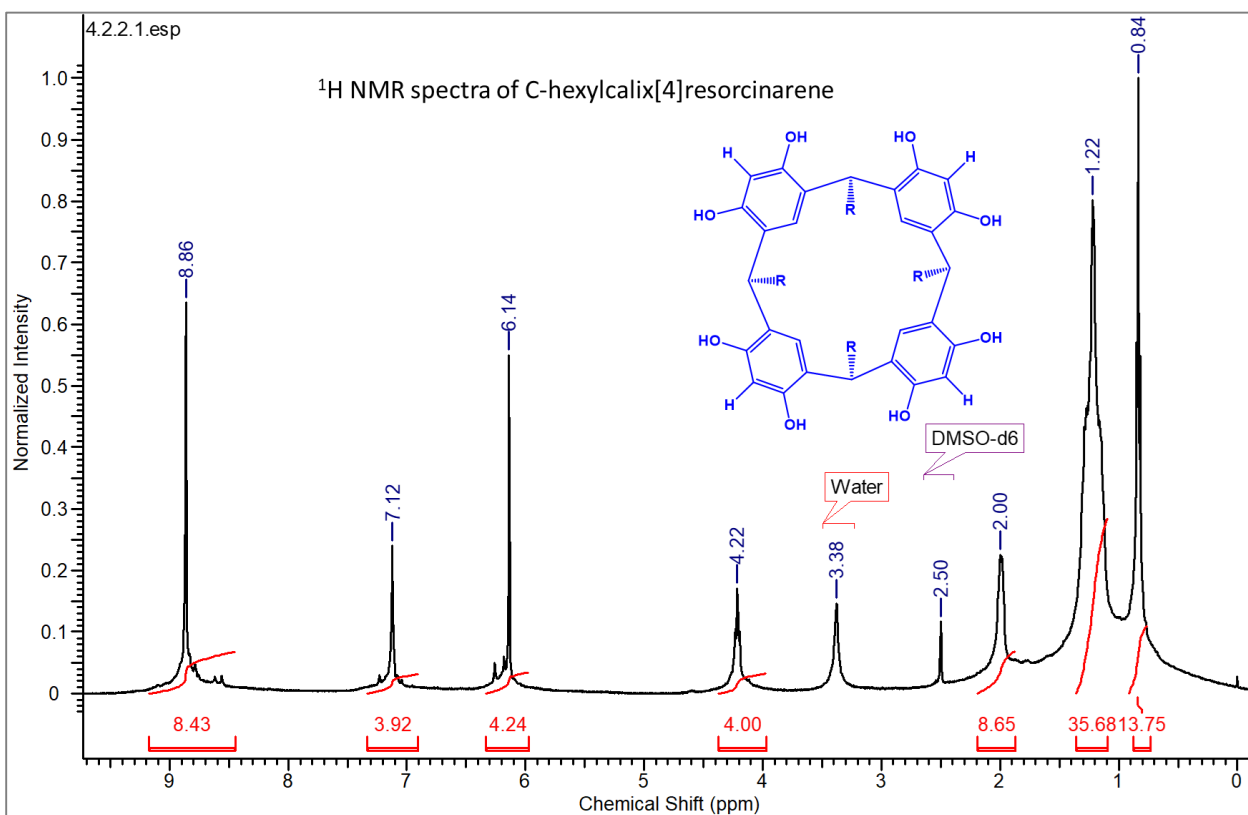
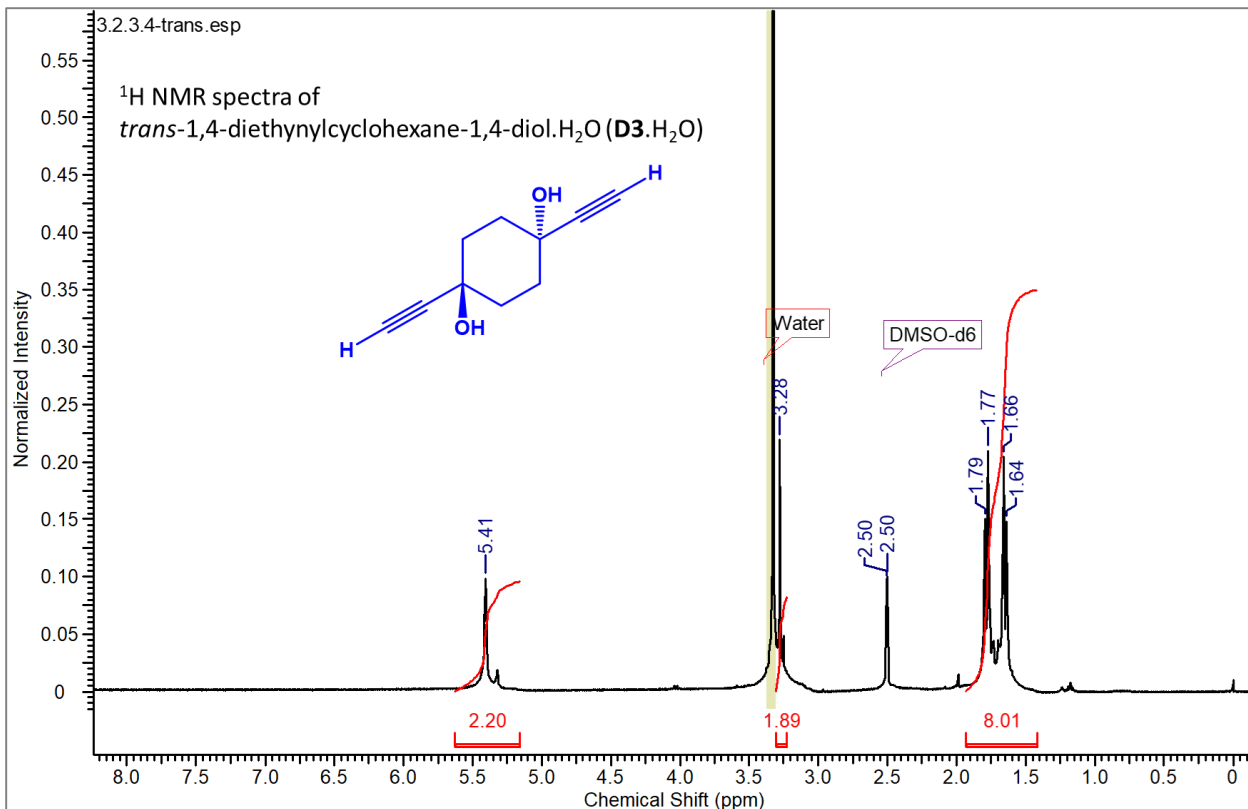


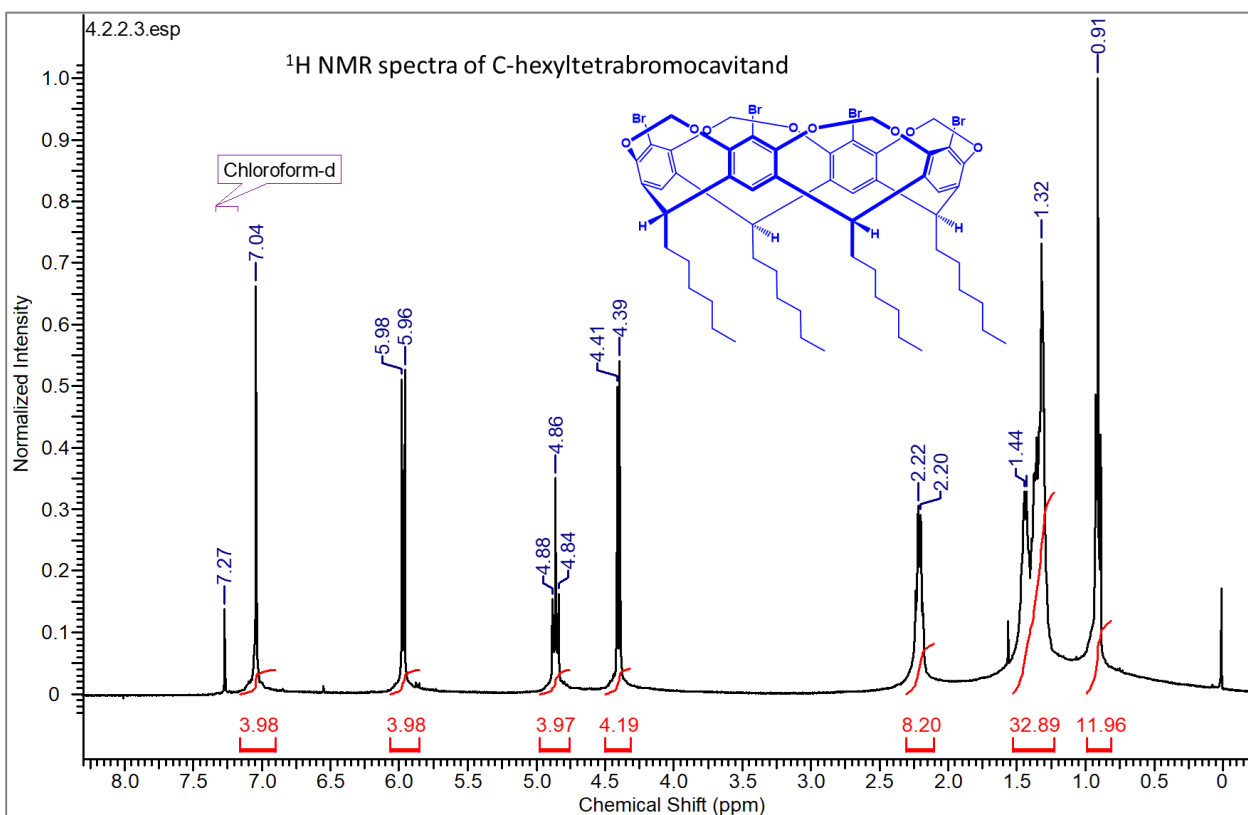
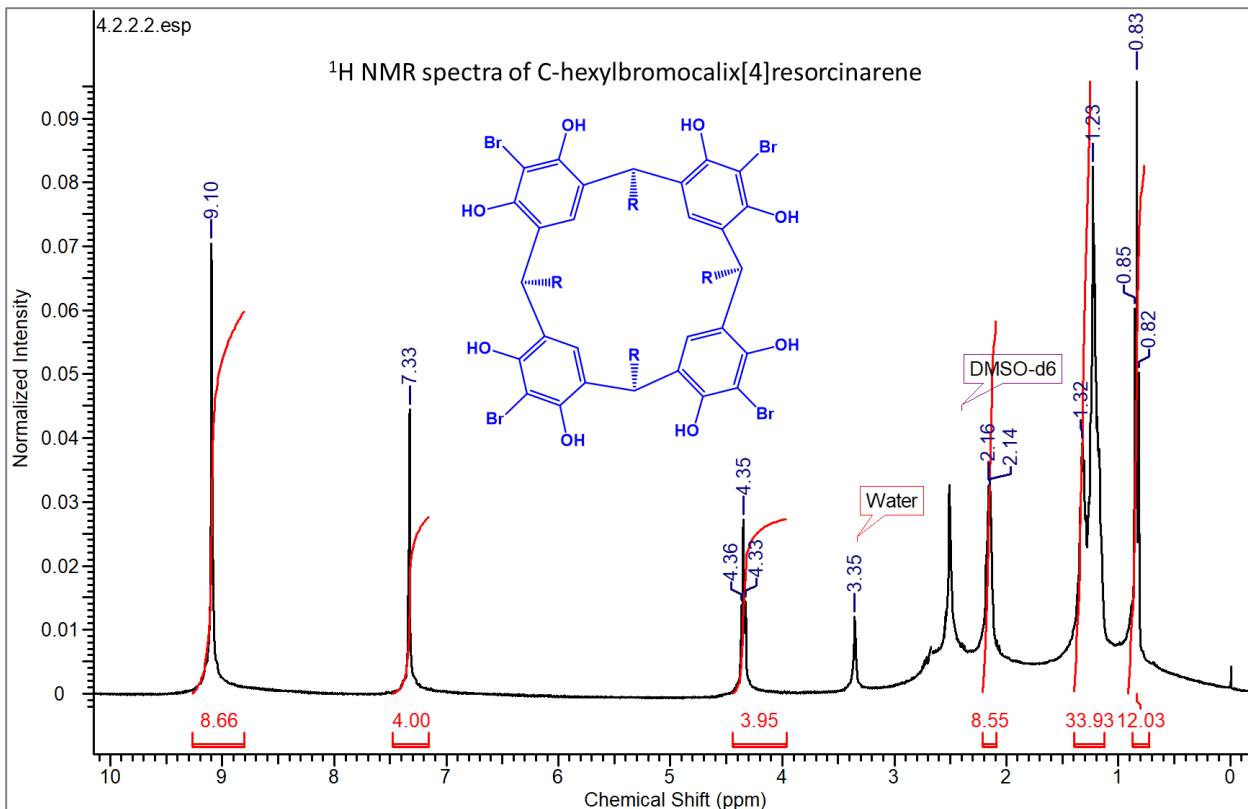


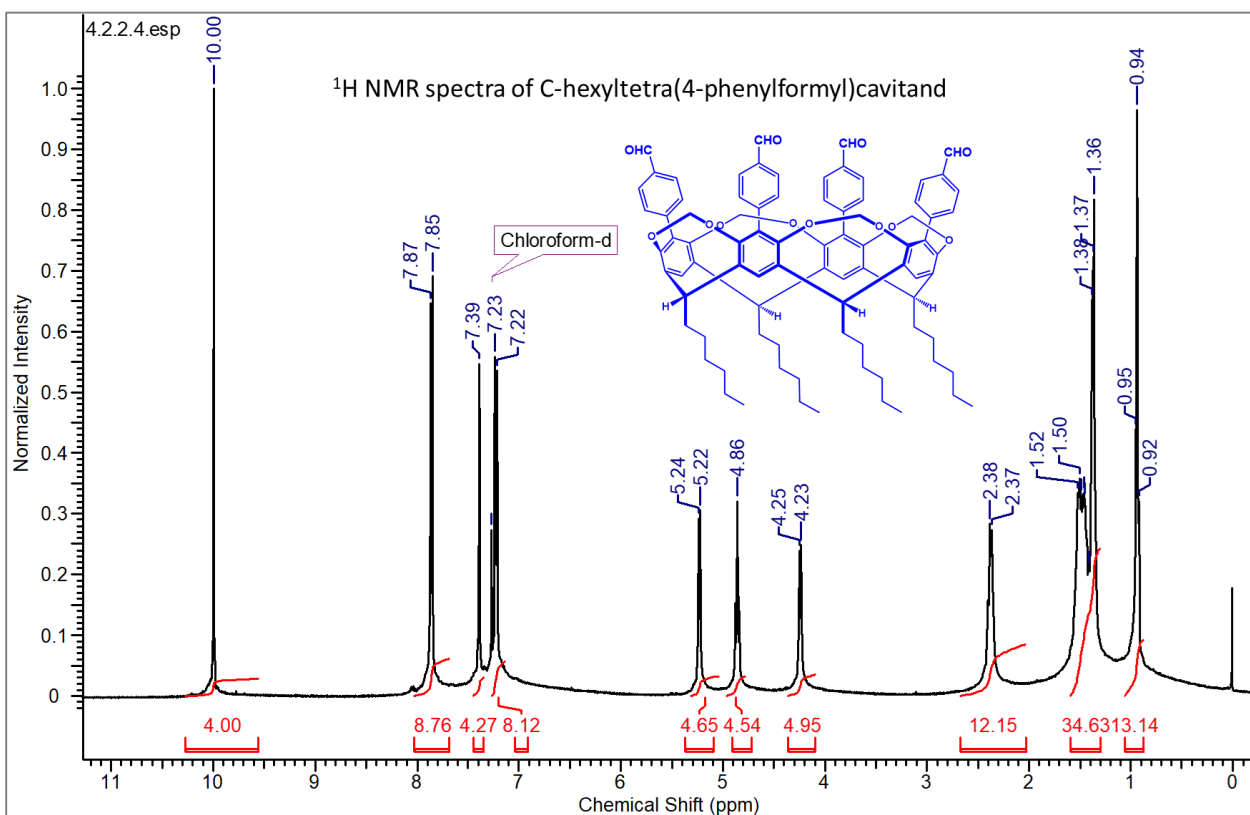
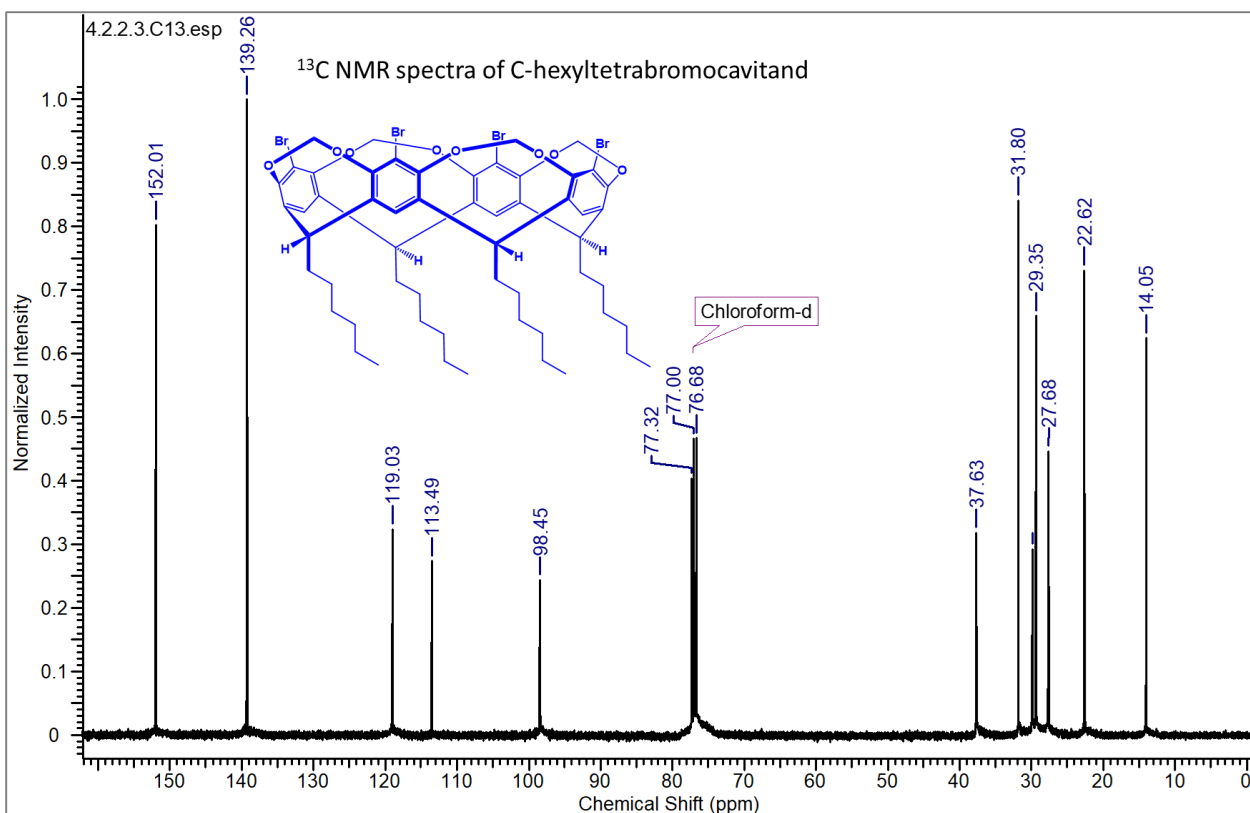


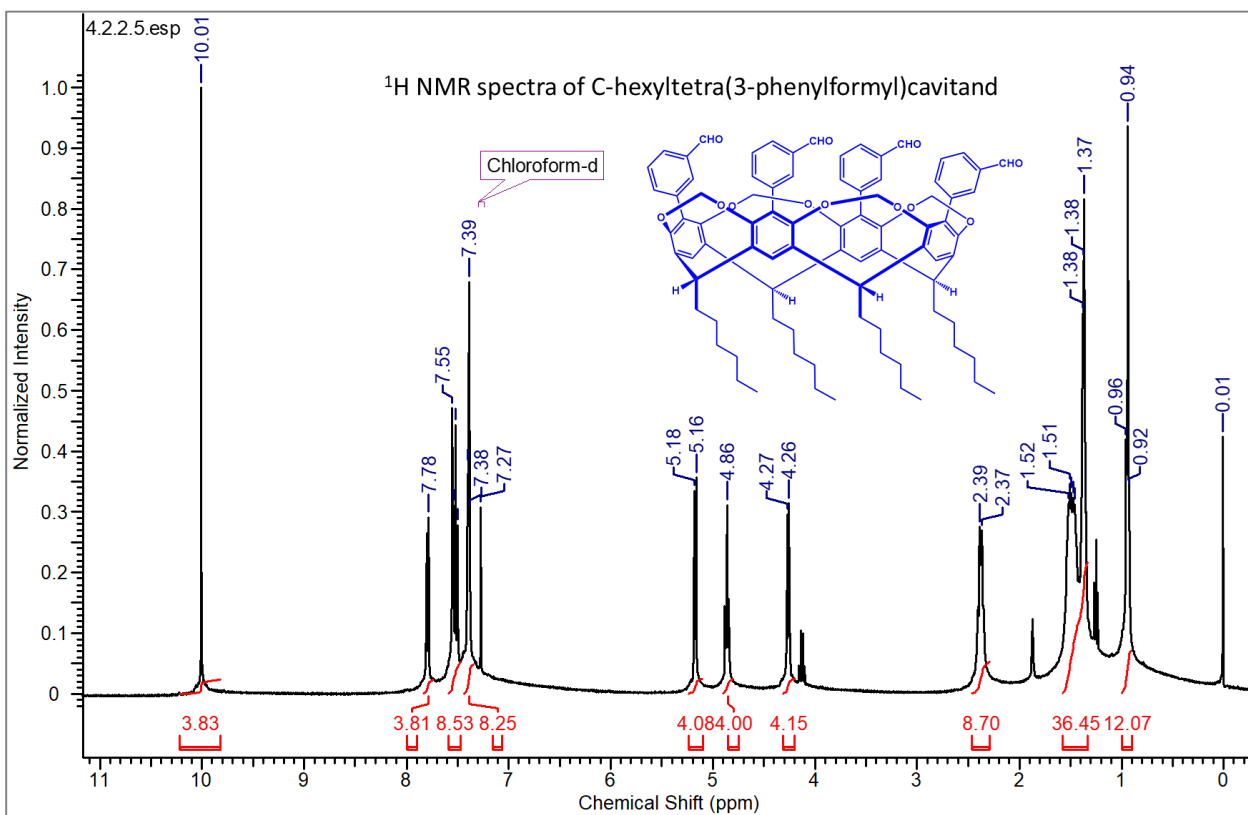
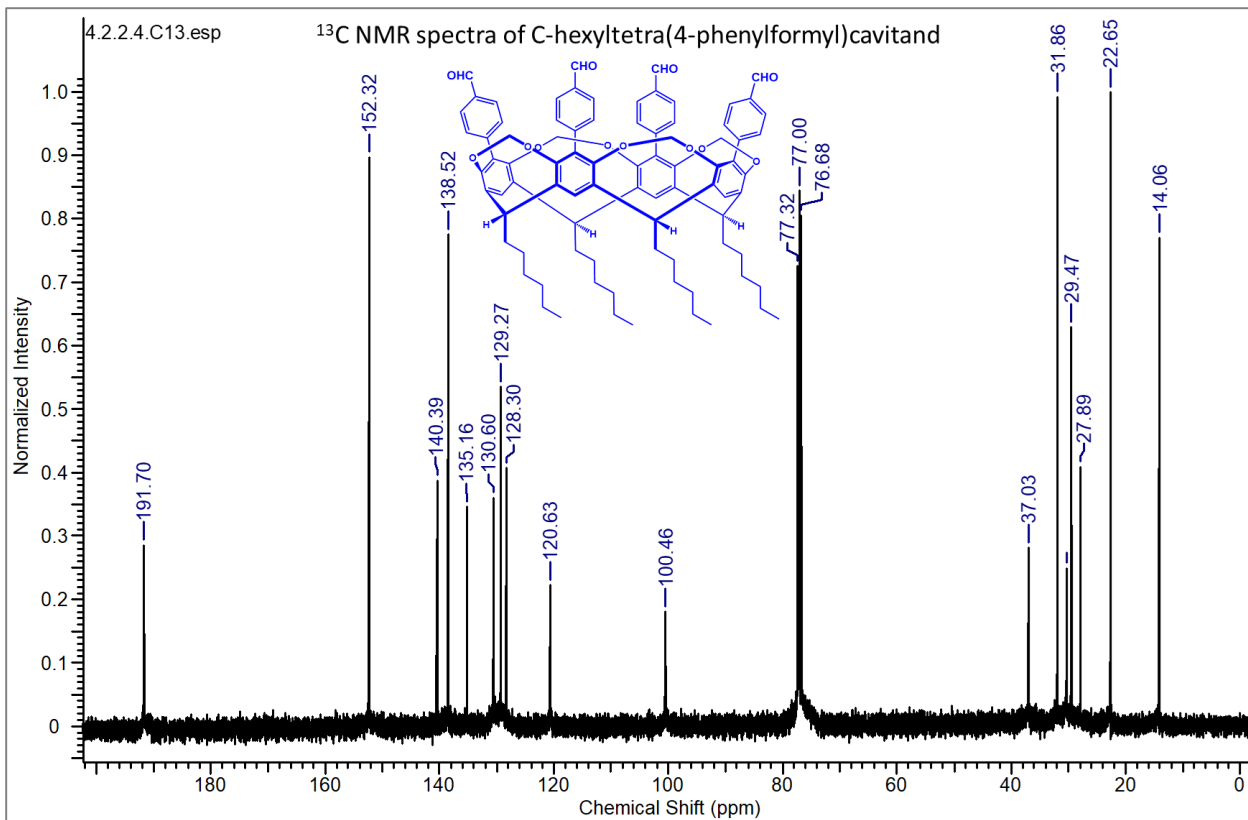


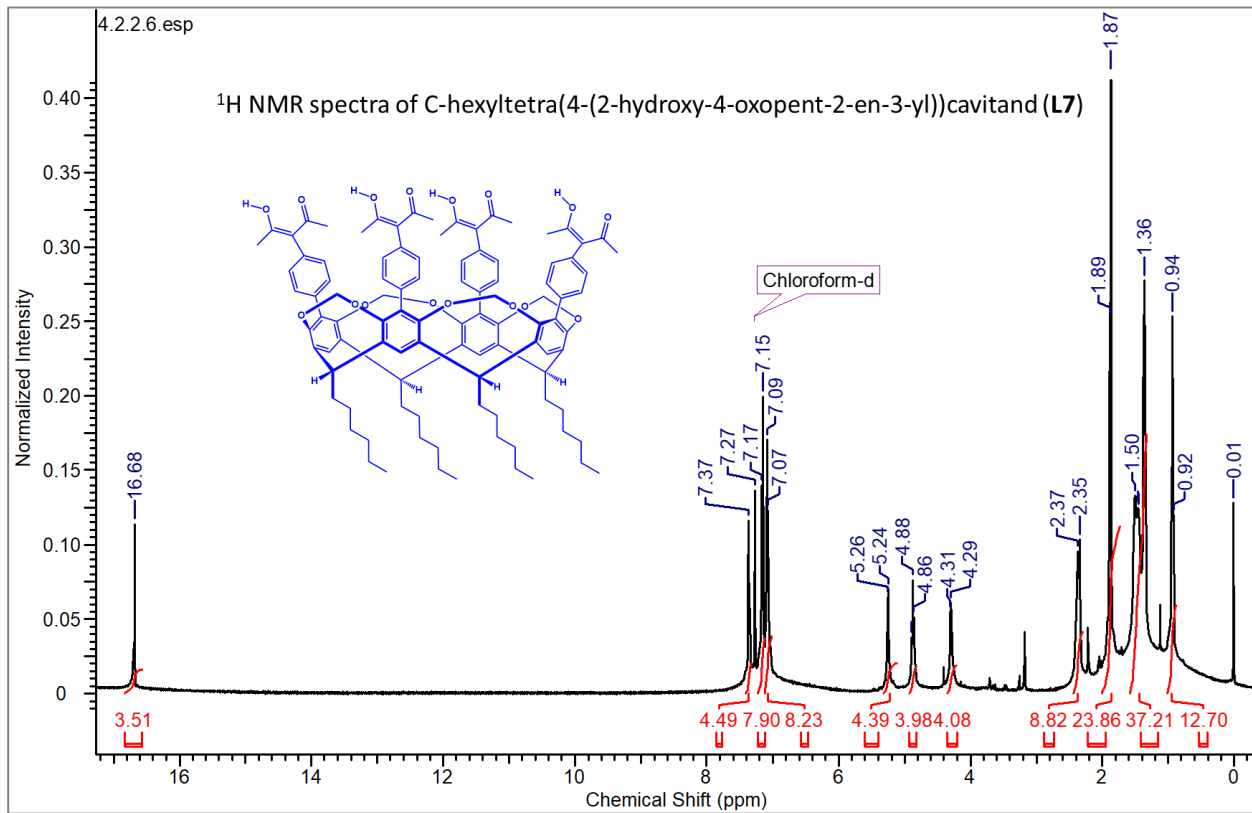
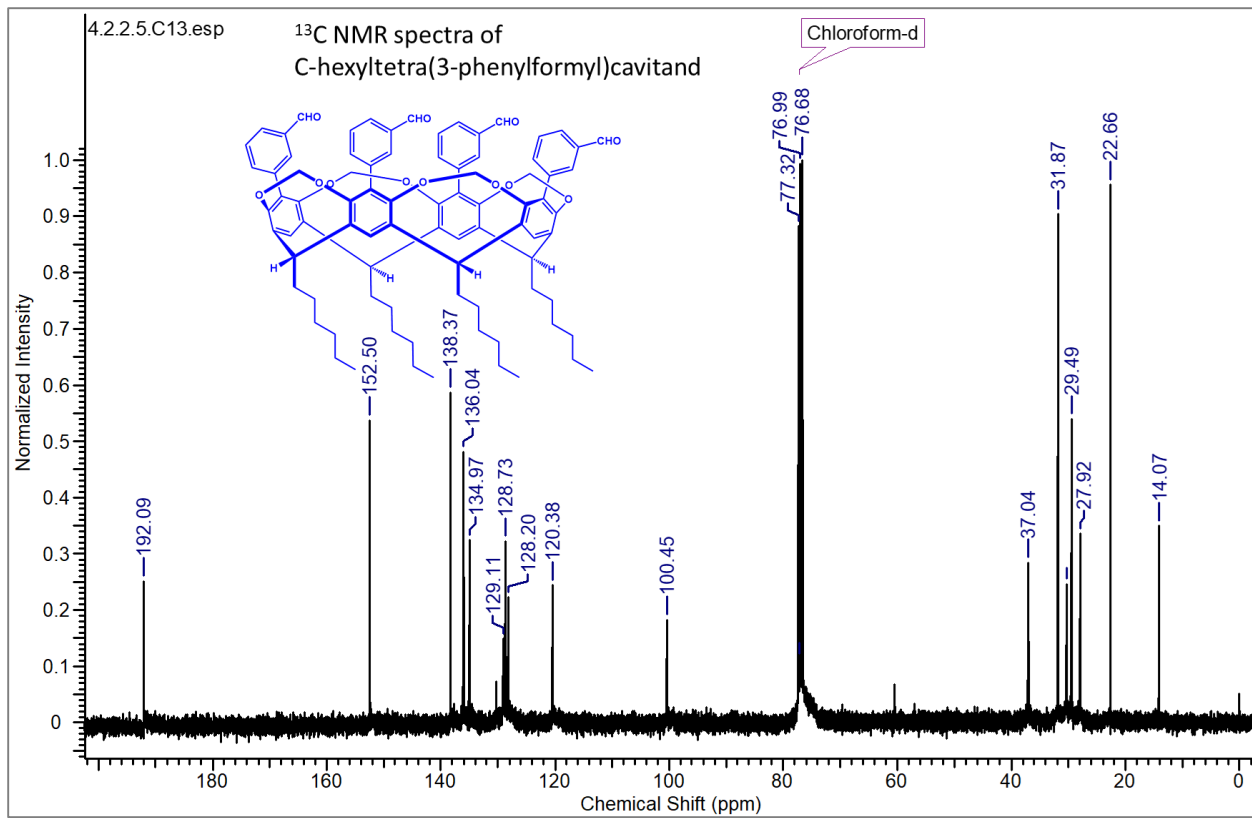


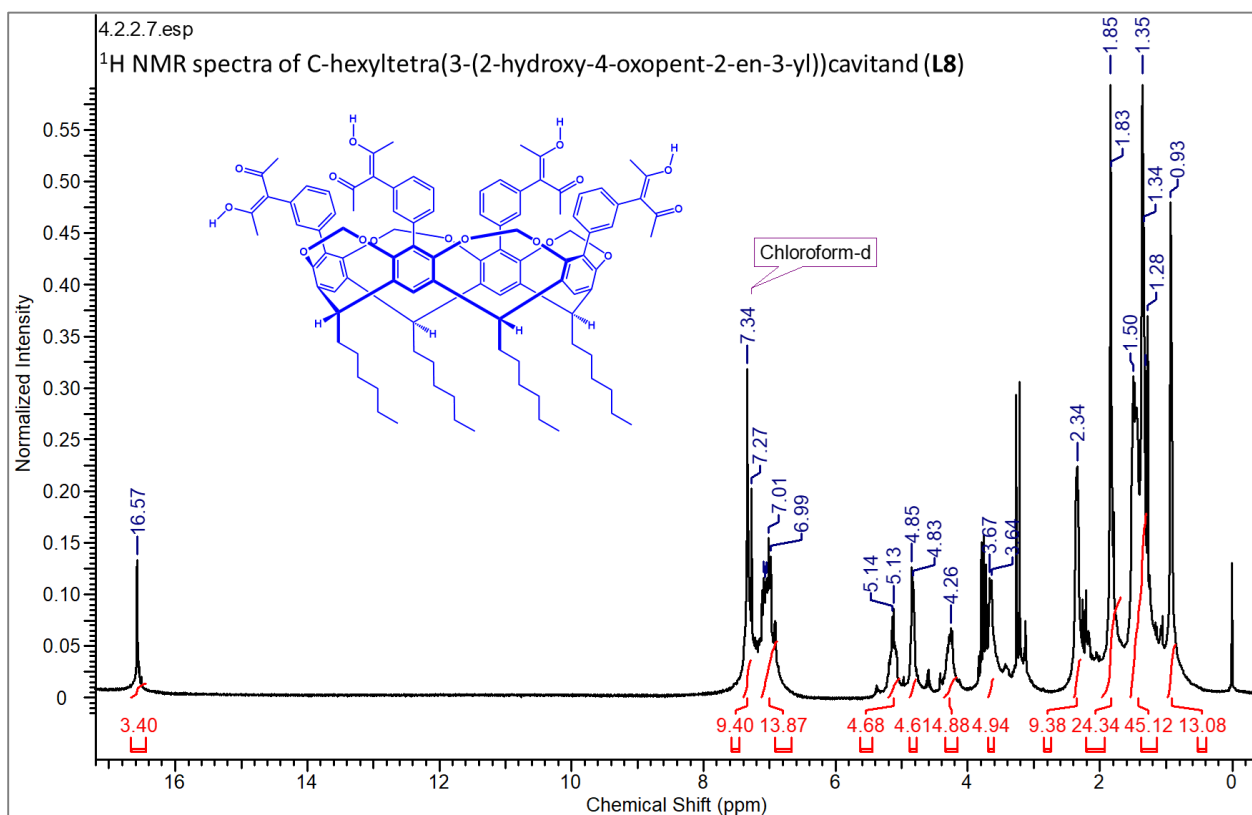
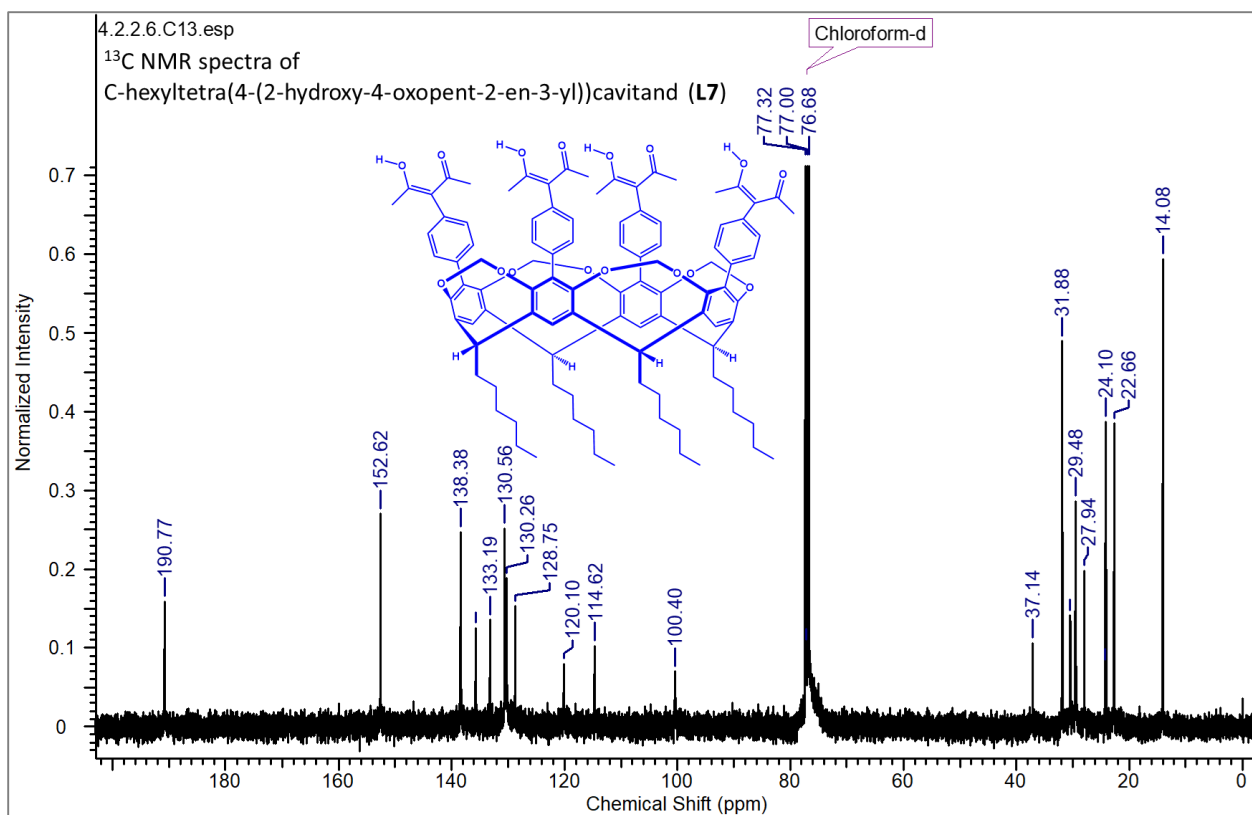


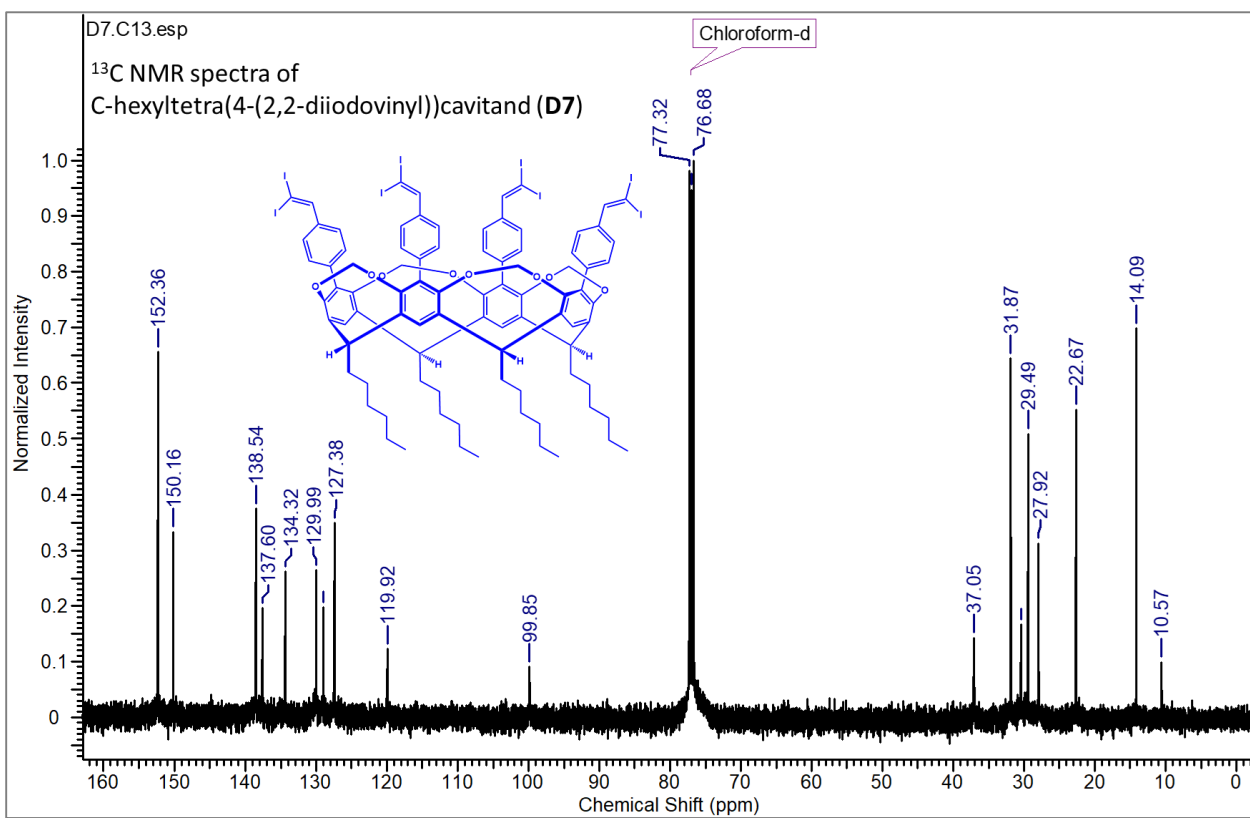
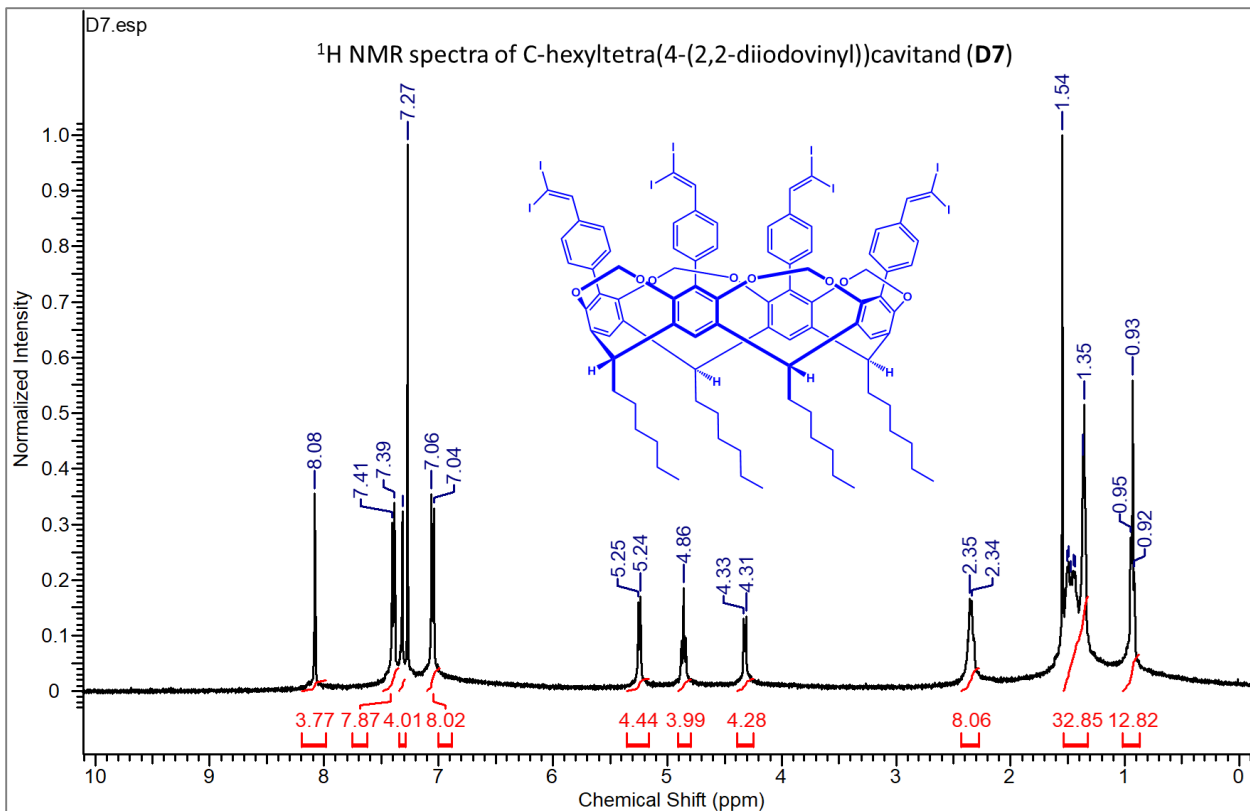


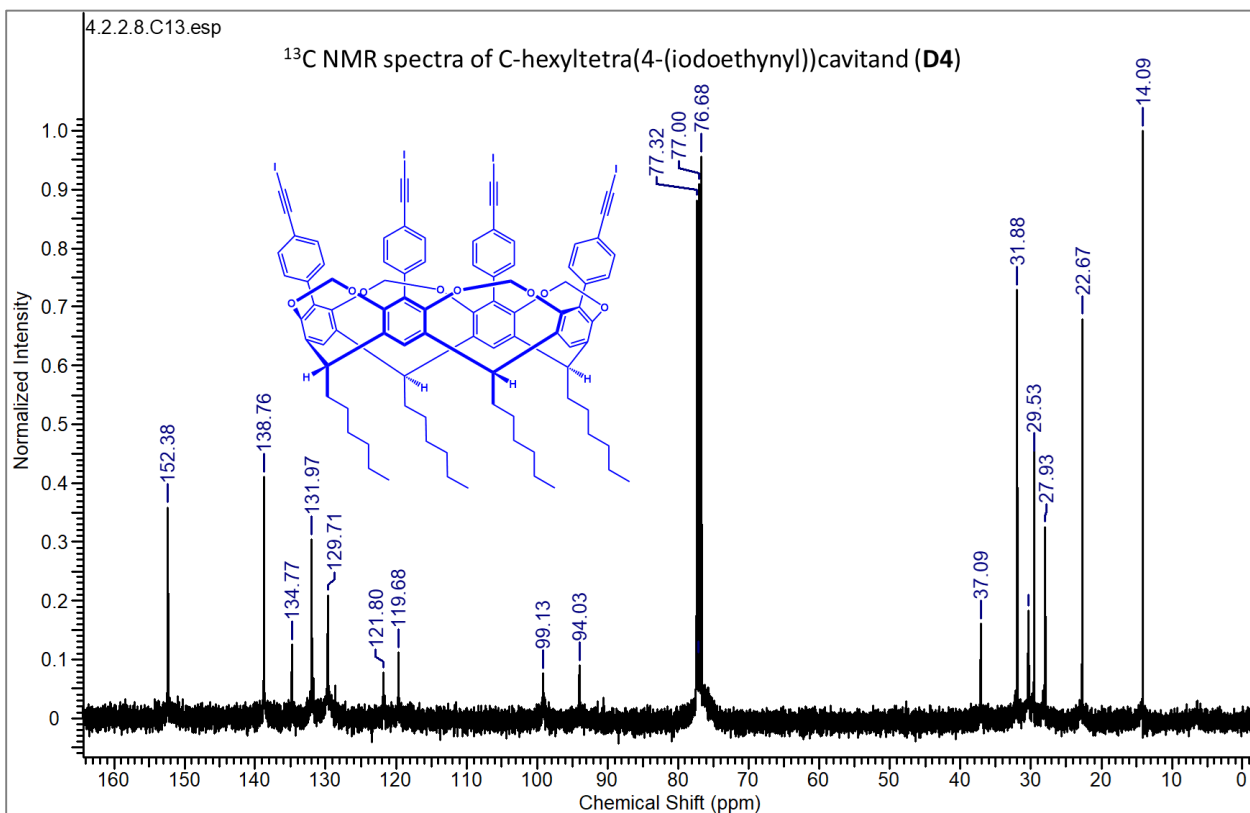
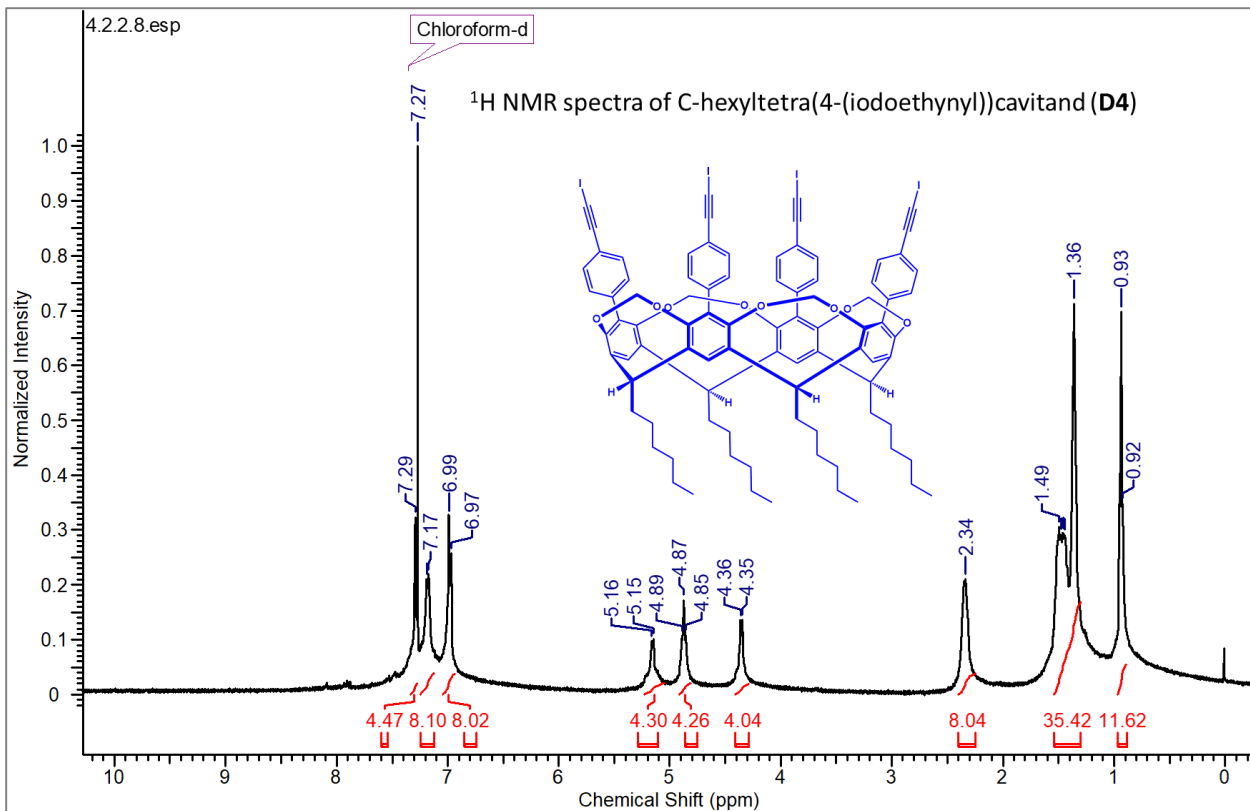


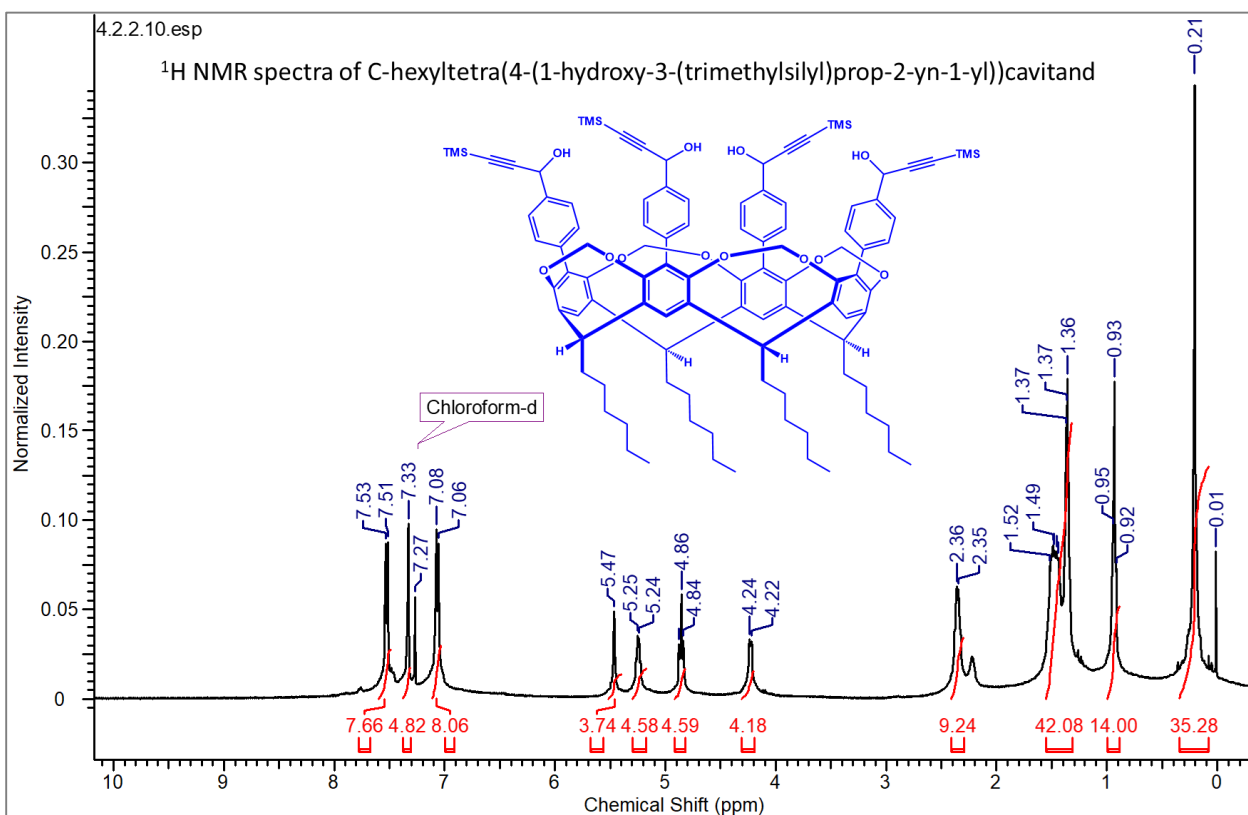
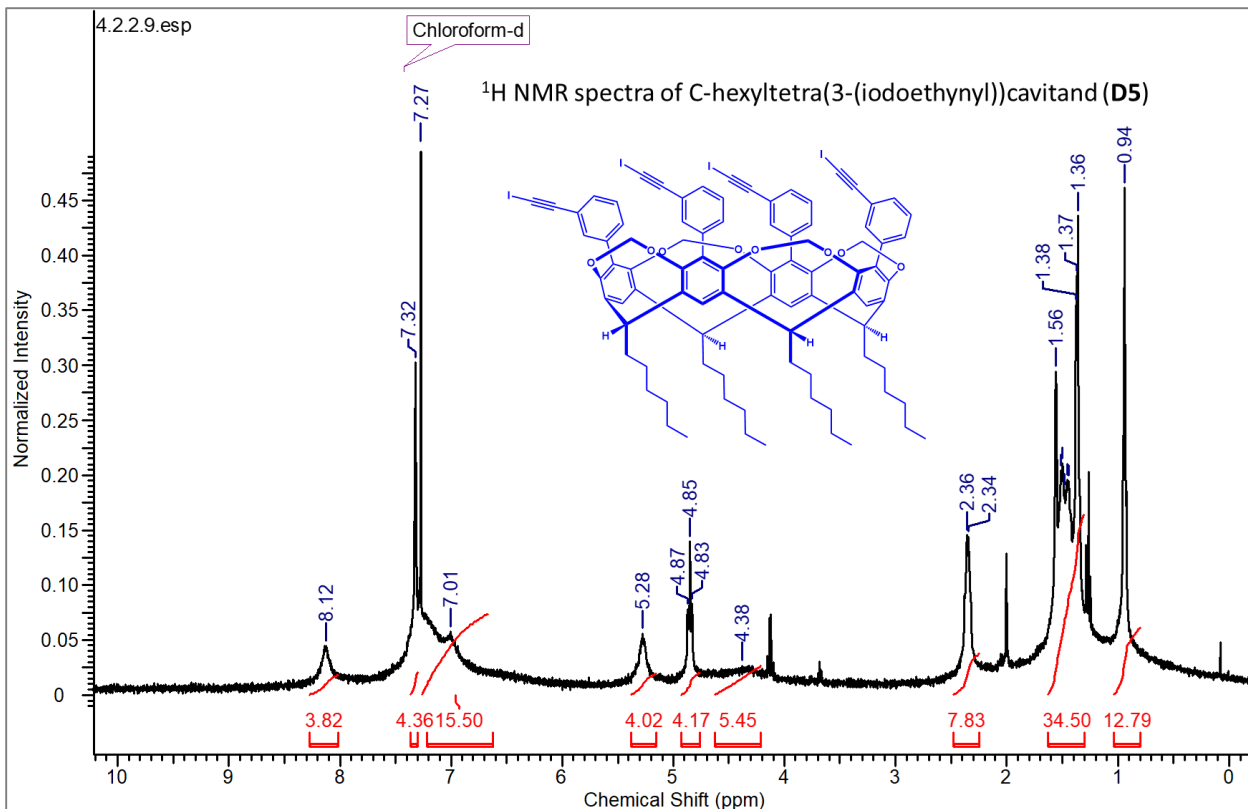


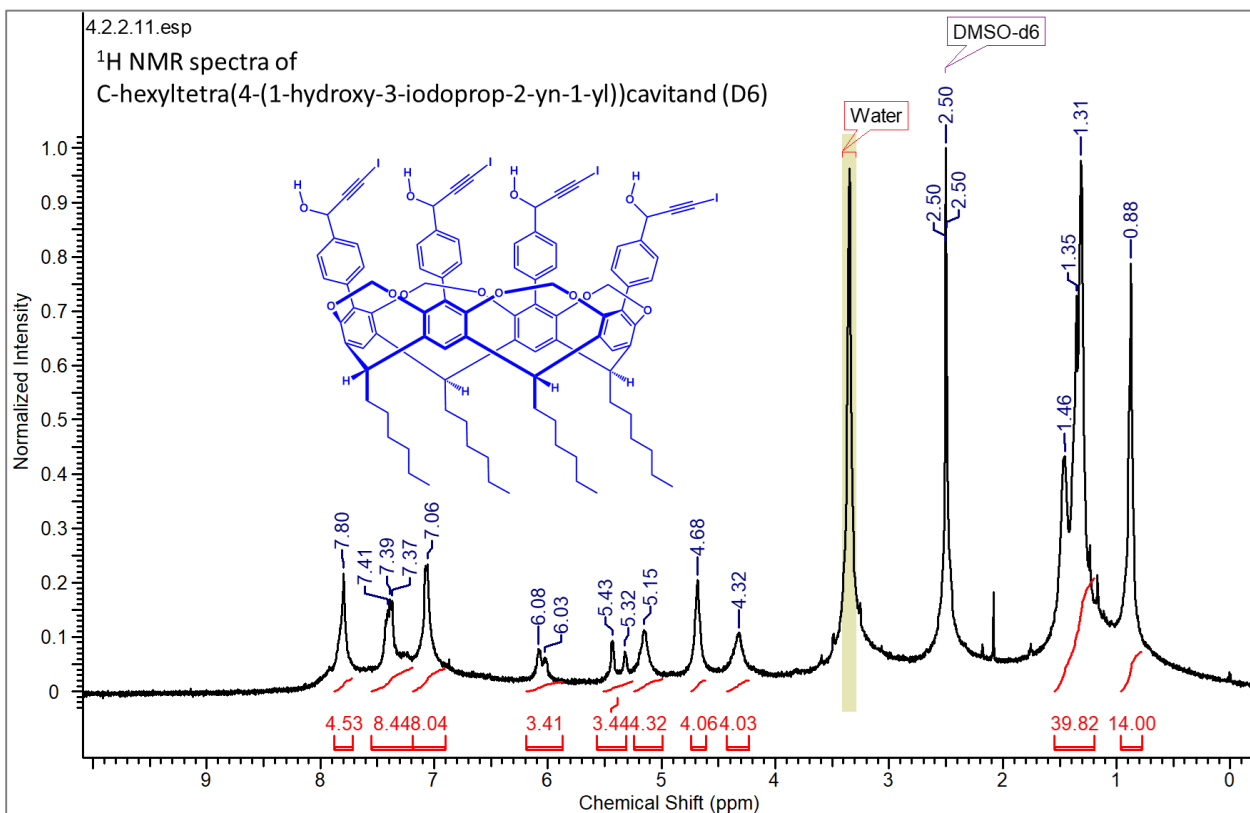
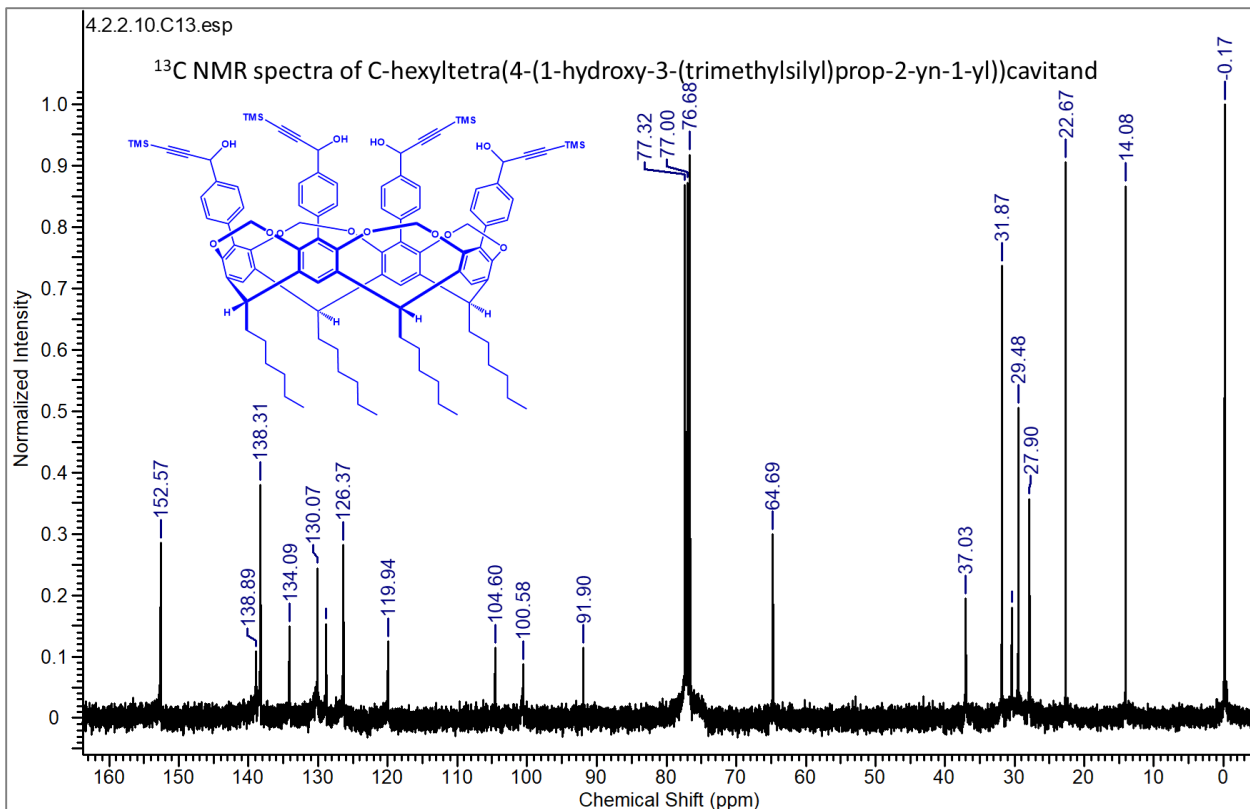












Appendix B – Crystallographic data

Datasets were collected on a Bruker Kappa APEX II system using MoK α radiation (**L1**; **L2**; [Cu(**L1**)₂]; [Cu(**L2**)₂].2CH₃CN; [Cu(**L2**)₂].2C₄H₈O₂; [Cu(**L2**)₂].2CH₃NO₂; [Cu(**L3**)₂].4CH₃CN; [Cu(**L3**)₂].2C₄H₈O₂; [Cu(**L3**)₂]). Data were collected using APEX2 software¹. Initial cell constants were found by small widely separated “matrix” runs. Data collection strategies were determined using COSMO². Scan speed and scan widths were chosen based on scattering power and peak rocking curves. Datasets were collected at -143 °C ([Cu(**L1**)₂]; [Cu(**L3**)₂].2C₄H₈O₂; [Cu(**L3**)₂]), and at -153 °C (**L1**; **L2**; [Cu(**L2**)₂].2CH₃CN; [Cu(**L2**)₂].2C₄H₈O₂; [Cu(**L2**)₂].2CH₃NO₂; [Cu(**L3**)₂].4CH₃CN) using an Oxford Cryostream low-temperature device.

For the above datasets, unit cell constants and orientation matrix were improved by least-squares refinement of reflections thresholded from the entire dataset. Integration was performed with SAINT³, using this improved unit cell as a starting point. Precise unit cell constants were calculated in SAINT from the final merged dataset. Lorenz and polarization corrections were applied. Multi-scan absorption corrections were performed with SADABS⁴.

For the above datasets, data were reduced with SHELXTL⁵. The structures were solved in all cases by direct methods without incident. Except as noted, hydrogen atoms were located in idealized positions and were treated with a riding model. All non-hydrogen atoms were assigned anisotropic thermal parameters. Refinements continued to convergence, using the recommended weighting schemes.

Also, the dataset for **L3** was collected on an Oxford Diffraction Xcalibur four-circle kappa geometry single-crystal diffractometer with Sapphire 3 CCD detector, using a graphite monochromated MoK α radiation, and applying the CrysAlisPro Software system⁶ at 23 °C.

Data reduction, including Lorentz and polarization corrections as well as absorption correction, was done by CrysAlis RED program⁷. The structures were solved by direct methods implemented in the SHELXS-2013 program⁸. The coordinates and the anisotropic displacement parameters for all non-hydrogen atoms were refined by full-matrix least-squares methods based on F^2 using the SHELXL-2013 program⁸. Except as noted, hydrogen atoms were located in idealized positions and were treated with a riding model.

[Cu(**L3**)₂].4CH₃CN – The asymmetric unit contains two molecules of the iodoethynyl ligand complexed with a Cu(II) atom and four acetonitrile solvent molecules. One of the acetonitrile solvent molecule is disordered over two closely related positions, thus representing different orientations. Relative populations were allowed to refine. Thermal parameters for closely located atoms were pairwise constrained using EADP commands. Geometry of the acetonitrile solvent molecule was restrained using the SAME command.

[Cu(**L2**)₂].2CH₃NO₂ – The asymmetric unit contains two molecules of the bromoethynyl ligand complexed with a Cu(II) atom and two molecules of nitromethane solvent. One of the methyl groups on the acetylacetone moiety is disordered over two closely related positions, thus representing different orientations. Relative positions were allowed to refine. Thermal parameters for closely located methyl carbon atoms were pairwise constrained using EADP command.

Also, one of the nitromethane solvent molecule is disordered over two closely related positions, thus representing different orientations. Relative populations were allowed to refine. Thermal parameters for closely located atoms were pairwise constrained using EADP commands. Geometry of the nitromethane solvent molecule was restrained using the SAME command. Also, all atoms of the nitromethane solvent molecule were restrained to lie in a common plane using the FLAT command.

L1 – Coordinates of the acetylacetone moiety proton H12 was allowed to refine.

L3 – Coordinates of the acetylacetone moiety proton H1O was allowed to refine.

Datasets were collected on a Bruker Kappa APEX II system using MoK α radiation (**D1:A5**; **D2**), or on a Bruker SMART APEX II system using MoK α radiation (**D3**; **D1:A3**; **D1:A4**; **D3:A5**). Data were collected using APEX2 software.ⁱ Initial cell constants were found by small widely separated “matrix” runs. Data collection strategies were determined using COSMO.ⁱⁱ Scan speed and scan widths were chosen based on scattering power and peak rocking curves. Datasets were collected at -45 °C (**D3**; **D1:A3**; **D1:A4**; **D3:A5**), -143 °C(**D2**), and -153 °C (**D1:A5**) using an Oxford Cryostream low-temperature device.

For the above datasets, unit cell constants and orientation matrix were improved by least-squares refinement of reflections thresholded from the entire dataset. Integration was performed with SAINT,ⁱⁱⁱ using this improved unit cell as a starting point.

Precise unit cell constants were calculated in SAINT from the final merged dataset. Lorenz and polarization corrections were applied. Multi-scan absorption corrections were performed with SADABS.^{iv}

For the above datasets, data were reduced with SHELXTL.^v The structures were solved in all cases by direct methods without incident. Except as noted, hydrogen atoms were located in idealized positions and were treated with a riding model. All non-hydrogen atoms were assigned anisotropic thermal parameters. Refinements continued to convergence, using the recommended weighting schemes.

Also, datasets for **D1**, **D2:A3**, and **D3:A3** were collected on an Oxford Diffraction Xcalibur four-circle kappa geometry single-crystal diffractometer with Sapphire 3 CCD detector, using a graphite monochromated MoK α radiation, and applying the CrysAlisPro Software system^{vi} at 23 °C.

Data reduction, including Lorentz and polarization corrections as well as absorption correction, was done by CrysAlisPro program.^{vi} The structures were solved by direct methods implemented in the SHELXS-2014/7 program.^{vii} The coordinates and the anisotropic displacement parameters for all non-hydrogen atoms were refined by full-matrix least-squares methods based on F^2 using the SHELXS-2014/7 program.^{vii} Except as noted, hydrogen atoms were located in idealized positions and were treated with a riding model.

D1 – Coordinates of the hydroxy proton H10, and the water proton H20 were allowed to refine.

D2 – Coordinates of the hydroxy protons H10 and H14 were allowed to refine.

D3 – Coordinates of the hydroxy protons H4 and H10, and the water protons H13A and H13B were allowed to refine.

D1:A3 – Coordinates of the hydroxy protons H7, H11 and H21 were allowed to refine.

D1:A4 – Coordinates of the hydroxy protons H7 and H11 were allowed to refine.

D1:A5 – The asymmetric unit contains one molecule each of the iodoethynyl-based target molecule and the pyridine-based co-former. The entire pyridine-based co-former is disordered over two closely related positions, thus representing different orientations. Relative populations were allowed to refine. Thermal parameters were pairwise constrained using EADP commands. Geometry of the aromatic ring was restrained using the SAME command. The bond distances were fixed to idealized distances using the DFIX command.

D2:A3 – Coordinates of the hydroxy protons H10 and H20 were allowed to refine.

D3:A3 – Coordinates of the hydroxy protons H10 and H20 were allowed to refine.

D3:A5 – Coordinates of the hydroxy proton H13 was allowed to refine.

Code	L1	L2	L3	[Cu(L1) ₂]	[Cu(L2) ₂ .2CH ₃ CN
Formula moiety	C ₁₃ H ₁₁ ClO ₂	C ₁₃ H ₁₁ BrO ₂	C ₁₃ H ₁₁ IO ₂	(C ₁₃ H ₁₀ ClO ₂) ₂ , Cu	(C ₁₃ H ₁₀ BrO ₂) ₂ , Cu, (C ₂ H ₃ N) ₂
Empirical formula	C ₁₃ H ₁₁ ClO ₂	C ₁₃ H ₁₁ BrO ₂	C ₁₃ H ₁₁ IO ₂	C ₂₆ H ₂₀ Cl ₂ CuO ₄	C ₃₀ H ₂₆ Br ₂ CuN ₂ O ₄
Molecular weight	234.67	279.13	326.12	530.87	701.89
Color, Habit	Colorless, Prism	Brown, Prism	Yellow, Plate	Green, Needles	Green, Plate
Crystal system	Monoclinic	Monoclinic	Orthorhombic	Monoclinic	Triclinic
Space group, Z	C ₂ /c, 4	P2(1)/n, 4	Pnma, 4	P2(1)/c, 2	Pī, 1
a, Å	9.704(5)	7.0148(7)	12.5746(13)	12.112(4)	8.0843(8)
b, Å	13.620(6)	12.2169(12)	7.2883(9)	12.704(4)	9.2352(10)
c, Å	8.810(5)	13.5874(13)	13.9188(7)	7.622(3)	10.8870(12)
α, °	90	90	90	90	92.144(4)
β, °	99.138(12)	91.691(4)	90	100.46(2)	99.260(3)
γ, °	90	90	90	90	100.990(3)
Volume, Å ³	1149.6(10)	1163.9(2)	1275.6(2)	1153.3(6)	785.57(14)
Density, g/cm ³	1.356	1.593	1.698	1.529	1.484
T, °K	120(2)	120(2)	296(2)	130(2)	120(2)
Crystal size, min x mid x max	0.120 x 0.220 x 0.380	0.160 x 0.440 x 0.480	0.100 x 0.330 x 0.590	0.048 x 0.242 x 0.368	0.060 x 0.320 x 0.400
X-ray wavelength, Å	0.71073	0.71073	0.71073	0.71073	0.71073
μ, mm ⁻¹	0.313	3.513	2.493	1.210	3.273
Trans min / max	0.89 / 0.96	0.28 / 0.60	0.54 / 1.00	0.66 / 0.94	0.35 / 0.83
θ _{min} , °	2.99	2.24	4.36	1.71	1.90
θ _{max} , °	32.16	31.00	26.99	25.55	32.55
Reflections					
collected	5953	24368	5677	31884	19718
independent	1770	3637	1482	2127	5127
observed	1306	2859	1085	1743	2577
R _{int}	0.0399	0.0516	0.0288	0.0730	0.0488
Threshold expression	> 2σ(I)	> 2σ(I)	> 2σ(I)	> 2σ(I)	> 2σ(I)
No. parameters	80	145	94	153	180
No. restraints	0	0	0	0	0
R ₁ (observed)	0.0496	0.0748	0.0418	0.0310	0.0519
wR ₂ (all)	0.1492	0.2238	0.0891	0.0872	0.1584
Goodness of fit (all)	1.093	1.068	1.074	1.072	0.932
ρ _{max} , ρ _{min} , e Å ⁻³	0.374, -0.250	4.819, -0.768	0.529, -0.450	0.340, -0.378	0.718, -0.945
Completeness to 2θ limit	0.972	0.981	0.994	0.985	0.900

Code	[Cu(L2)2].2C4H8O2	[Cu(L2)2].2CH3NO2	[Cu(L3)2].4CH3CN	[Cu(L3)2].2C4H8O2	[Cu(L3)2]
Formula moiety	(C ₁₃ H ₁₀ BrO ₂) ₂ , Cu, (C ₄ H ₈ O ₂) ₂	(C ₁₃ H ₁₀ BrO ₂) ₂ , Cu, (CH ₃ NO ₂) ₂	(C ₁₃ H ₁₀ IO ₂) ₂ , Cu, (C ₂ H ₃ N) ₄	(C ₁₃ H ₁₀ IO ₂) ₂ , Cu, (C ₄ H ₈ O ₂) ₂	(C ₁₃ H ₁₀ IO ₂) ₂ , Cu
Empirical formula	C ₃₄ H ₃₆ Br ₂ CuO ₈	C ₂₈ H ₂₆ Br ₂ CuN ₂ O ₈	C ₃₄ H ₃₂ CuI ₂ N ₄ O ₄	C ₃₄ H ₃₆ CuI ₂ O ₈	C ₂₆ H ₂₀ CuI ₂ O ₄
Molecular weight	795.99	741.87	877.98	889.98	713.77
Color, Habit	Blue, Prism	Green, Plate	Blue, Plate	Green, Needles	Green, Plates
Crystal system	Monoclinic	Triclinic	Triclinic	Monoclinic	Monoclinic
Space group, Z	P2(1)/c, 2	P̄1, 1	P̄1, 1	P2(1)/c, 2	P2(1)/n, 6
a, Å	8.0238(9)	7.9062(13)	8.2630(4)	8.242(2)	21.351(4)
b, Å	13.8635(15)	8.9753(15)	10.6819(6)	14.206(4)	7.2561(13)
c, Å	15.3770(16)	11.2457(19)	11.4576(6)	15.472(4)	25.317(5)
α, °	90	85.197(7)	92.134(3)	90	90
β, °	102.274(4)	80.067(6)	104.211(2)	102.722(12)	112.809(10)
γ, °	90	76.761(6)	107.705(3)	90	90
Volume, Å ³	1671.4(3)	764.3(2)	927.04(8)	1767.1(8)	3615.5(12)
Density, g/cm ³	1.582	1.612	1.573	1.673	1.967
T, °K	120(2)	120(2)	120(2)	130(2)	130(2)
Crystal size, min x mid x max	0.320 x 0.400 x 0.440	0.100 x 0.320 x 0.440	0.060 x 0.320 x 0.400	0.122 x 0.356 x 0.578	0.055 x 0.232 x 0.356
X-ray wavelength, Å	0.71073	0.71073	0.71073	0.71073	0.71073
μ, mm ⁻¹	3.094	3.378	2.293	2.412	3.499
Trans min / max	0.34 / 0.44	0.32 / 0.73	0.46 / 0.87	0.34 / 0.76	0.37 / 0.83
θ _{min} , °	2.00	1.84	1.85	1.97	1.06
θ _{max} , °	32.60	33.02	32.61	25.71	25.34
Reflections					
collected	22675	27759	19909	49520	35365
independent	5919	5266	6249	3335	6499
observed	5026	3837	3322	3037	4692
R _{int}	0.0264	0.0364	0.0527	0.0607	0.0647
Threshold expression	> 2σ(I)	> 2σ(I)	> 2σ(I)	> 2σ(I)	> 2σ(I)
No. parameters	209	192	202	209	454
No. restraints	0	15	9	0	0
R ₁ (observed)	0.0279	0.0576	0.0506	0.0232	0.0438
wR ₂ (all)	0.0699	0.1744	0.1425	0.0564	0.1344
Goodness of fit (all)	1.031	1.090	1.055	1.048	1.083
ρ _{max} , ρ _{min} , e Å ⁻³	0.532, -0.365	1.640, -1.156	0.840, -0.790	0.381, -0.401	1.765, -1.133
Completeness to 2θ limit	0.976	0.987	0.921	0.994	0.982

Code	L5	[Cu(L5) ₂]
Formula moiety	C ₁₃ H ₁₁ BrO ₂	(C ₁₃ H ₁₀ BrO ₂) ₂ , Cu
Empirical formula	C ₁₃ H ₁₁ BrO ₂	C ₂₆ H ₂₀ Br ₂ CuO ₄
Molecular weight	279.13	619.78
Color, Habit	Colorless, Blocks	Blue, Prism
Crystal system	Triclinic	Monoclinic
Space group, Z	P $\bar{1}$, 4	C2/c, 4
a, Å	7.377(3)	25.8092(16)
b, Å	12.052(4)	7.4193(5)
c, Å	13.560(5)	13.7881(9)
α , °	93.358(16)	90
β , °	93.198(12)	113.652(2)
γ , °	103.160(11)	90
Volume, Å ³	1168.9(7)	2418.4(3)
Density, g/cm ³	1.586	1.702
T, °K	180(2)	120(2)
Crystal size, min x mid x max	0.122 x 0.298 x 0.349	0.120 x 0.280 x 0.400
X-ray wavelength, Å	0.71073	0.71073
μ , mm ⁻¹	3.497	4.238
Trans min / max	0.38 / 0.68	0.28 / 0.63
ϑ_{min} , °	1.74	1.72
ϑ_{max} , °	25.52	32.57
Reflections		
collected	14981	25220
independent	4288	4169
observed	3157	3388
R _{int}	0.0467	0.0315
Threshold expression	> 2σ(I)	> 2σ(I)
No. parameters	301	153
No. restraints	2	0
R ₁ (observed)	0.0370	0.0293
wR ₂ (all)	0.0847	0.0737
Goodness of fit (all)	1.030	1.024
ρ_{max}, ρ_{min} , e Å ⁻³	0.459, -0.531	0.762, -0.645
Completeness to 2θ limit	0.983	0.992

Code	D1	D2	D3	D1:A3	D1:A4
Formula moiety	C ₁₀ H ₁₀ I ₂ O ₂ , H ₂ O	C ₁₀ H ₁₀ I ₂ O ₂	C ₁₀ H ₁₂ O ₂ , H ₂ O	C ₁₀ H ₁₀ I ₂ O ₂ , C ₁₀ H ₈ N ₂	C ₁₀ H ₁₀ I ₂ O ₂ , C ₁₂ H ₁₀ N ₂
Empirical formula	C ₁₀ H ₁₂ I ₂ O ₃	C ₁₀ H ₁₀ I ₂ O ₂	C ₁₀ H ₁₄ O ₃	C ₂₀ H ₁₈ I ₂ N ₂ O ₂	C ₂₂ H ₂₀ I ₂ N ₂ O ₂
Molecular weight	434.00	415.98	182.21	572.16	598.20
Color, Habit	Pale yellow, Prism	Colorless, Needle	Colorless, Rectangular	Colorless, Irregular	Colorless, Rectangular
Crystal system	Tetragonal	Monoclinic	Monoclinic	Triclinic	Triclinic
Space group, Z	P4(2)/m, 2	P2(1)/c, 4	P2(1)/c, 4	P $\bar{1}$, 4	P $\bar{1}$, 2
a, Å	8.5167(5)	11.1961(17)	9.9472(12)	7.7674(8)	7.8373(7)
b, Å	8.5167(5)	11.5073(18)	6.1399(8)	10.0010(10)	11.6273(11)
c, Å	8.8404(9)	9.2386(15)	16.775(2)	26.238(3)	12.6853(12)
α , °	90	90	90	81.2340(10)	93.5792(12)
β , °	90	100.613(4)	104.248(2)	89.2680(10)	96.5739(11)
γ , °	90	90	90	85.8440(10)	107.2327(11)
Volume, Å ³	641.23(10)	1169.9(3)	993.0(2)	2009.1(3)	1091.15(18)
Density, g/cm ³	2.243	2.362	1.219	1.892	1.821
T, °K	296(2)	130(2)	228(2)	228(2)	228(2)
Crystal size, min x mid x max	0.210 x 0.230 x 0.520	0.110 x 0.188 x 0.370	0.230 x 0.260 x 0.480	0.180 x 0.220 x 0.390	0.140 x 0.290 x 0.370
X-ray wavelength, Å	0.71073	0.71073	0.71073	0.71073	0.71073
μ , mm ⁻¹	4.891	5.350	0.089	3.147	2.901
Trans min / max	0.27 / 1.00	0.24 / 0.59	0.96 / 0.98	0.37 / 0.60	0.41 / 0.69
ϑ_{min} , °	4.61	2.86	2.50	2.07	2.33
ϑ_{max} , °	32.65	29.58	33.54	33.46	33.33
Reflections					
collected	5381	22544	13268	27960	15152
independent	1152	3266	3686	14217	7687
observed	891	3030	2678	10970	6045
Threshold expression	> 2σ(I)	> 2σ(I)	> 2σ(I)	> 2σ(I)	> 2σ(I)
R ₁ (observed)	0.0294	0.0203	0.0455	0.0473	0.0289
wR ₂ (all)	0.0741	0.0443	0.1308	0.1070	0.0659
Goodness of fit (all)	1.078	1.091	1.032	1.149	1.034
ρ_{max} , ρ_{min} , e Å ⁻³	0.947, -1.114	1.085, -1.799	0.355, -0.226	1.433, -1.219	1.070, -1.031
Completeness to 2θ limit	0.994	0.994	0.940	0.905	0.910

Code	D1:A5	D2:A3	D3:A3	D3:A5
Formula moiety	C ₁₀ H ₁₀ I ₂ O ₂ , C ₁₂ H ₁₂ N ₂	C ₁₀ H ₁₀ I ₂ O ₂ , C ₁₀ H ₈ N ₂	C ₁₀ H ₁₂ O ₂ , C ₁₀ H ₈ N ₂	C ₁₀ H ₁₂ O ₂ , C ₁₂ H ₁₂ N ₂
Empirical formula	C ₂₂ H ₂₂ I ₂ N ₂ O ₂	C ₂₀ H ₁₈ I ₂ N ₂ O ₂	C ₂₀ H ₂₀ N ₂ O ₂	C ₂₂ H ₂₄ N ₂ O ₂
Molecular weight	600.21	572.16	320.38	348.43
Color, Habit	Colorless, Plate	Pale yellow, block	Pale yellow, plate	Colorless, Irregular
Crystal system	Triclinic	Monoclinic	Triclinic	Monoclinic
Space group, Z	P $\bar{1}$, 2	P2(1)/c, 4	P $\bar{1}$, 2	P2(1)/n, 2
a, Å	7.8440(14)	9.5108(4)	5.9239(5)	11.5202(15)
b, Å	11.568(2)	10.5838(6)	12.3895(9)	7.7849(10)
c, Å	12.755(2)	22.0298(8)	13.2181(8)	11.8577(16)
α , °	92.124(6)	90	110.998(6)	90
β , °	97.154(6)	100.451(4)	96.684(6)	114.559(2)
γ , °	109.722(6)	90	99.359(6)	90
Volume, Å ³	1077.1(3)	2180.74(18)	877.44(12)	967.2(2)
Density, g/cm ³	1.851	1.743	1.213	1.196
T, °K	120(2)	296(2)	296(2)	228(2)
Crystal size, min x mid x max	0.080 x 0.380 x 0.440	0.27 x 0.55 x 0.59	0.16 x 0.54 x 0.59	0.160 x 0.280 x 0.380
X-ray wavelength, Å	0.71073	0.71073	0.71073	0.71073
μ , mm ⁻¹	2.939	2.899	0.078	0.077
Trans min / max	0.36 / 0.80	0.458 / 1.000	0.817 / 1.000	0.97 / 0.99
ϑ_{min} , °	1.62	4.36	4.39	3.23
ϑ_{max} , °	30.59	27.00	26.99	28.28
Reflections				
collected	22664	14205	9747	9913
independent	6403	4769	3841	2395
observed	5625	3558	2595	1878
Threshold expression	> 2σ(I)	> 2σ(I)	> 2σ(I)	> 2σ(I)
R ₁ (observed)	0.0297	0.0564	0.0518	0.0457
wR ₂ (all)	0.0734	0.1540	0.1109	0.1210
Goodness of fit (all)	1.037	1.042	1.012	1.039
ρ_{max} , ρ_{min} , e Å ⁻³	1.735, -1.034	2.259, -1.564	0.173, -0.169	0.313, -0.280
Completeness to 2θ limit	0.966	0.996	0.995	0.998

Code	D9³⁻:A3H₂²⁺: A3H⁺	D9:A8	2(D12⁻):A4H₂²⁺	2(D12⁻):A3H₂²⁺	D9:2A7:CH₃OH
Formula moiety	C ₉ H ₉ N ₈ O ₁₆ , C ₁₀ H ₁₀ N ₂ , C ₁₀ H ₉ N ₂	C ₉ H ₁₂ N ₈ O ₁₆ , C ₈ H ₁₂ N ₂ O ₂	C ₁₂ H ₁₄ N ₂ , (C ₂ H ₃ N ₆ O ₂) ₂	C ₁₀ H ₁₀ N ₂ , (C ₂ H ₃ N ₆ O ₂) ₂	C ₉ H ₁₂ N ₈ O ₁₆ , (C ₁₀ H ₈ N ₂ O ₂) ₂ , CH ₄ O
Empirical formula	C ₂₉ H ₂₈ N ₁₂ O ₁₆	C ₁₇ H ₂₄ N ₁₀ O ₁₈	C ₁₆ H ₂₀ N ₁₄ O ₄	C ₁₄ H ₁₆ N ₁₄ O ₄	C ₃₀ H ₃₂ N ₁₂ O ₂₁
Molecular weight	800.63	656.46	472.46	444.41	896.67
Color, Habit	Colorless, Plates	Colorless, Blocks	Colorless, Blocks	Yellow, Blocks	Colorless, Plates
Crystal system	Triclinic	Monoclinic	Monoclinic	Monoclinic	Triclinic
Space group, Z	P $\bar{1}$, 2	C2/c, 4	P2(1)/n, 2	P2(1)/c, 4	P $\bar{1}$, 2
a, Å	10.099(5)	14.718(4)	11.349(3)	15.251(4)	7.2297(15)
b, Å	10.666(5)	9.254(2)	6.714(2)	16.309(4)	14.486(3)
c, Å	17.332(8)	20.890(5)	13.947(4)	7.6465(19)	17.705(4)
α , °	101.39(3)	90	90	90	97.269(13)
β , °	103.93(3)	108.553(10)	105.847(17)	98.110(14)	96.333(12)
γ , °	90.53(2)	90	90	90	93.935(12)
Volume, Å ³	1773.2(15)	2697.4(11)	1022.3(5)	1882.9(8)	1821.7(7)
Density, g/cm ³	1.500	1.616	1.535	1.568	1.635
T, °K	130(2)	280(2)	130(2)	130(2)	130(2)
Crystal size, min x mid x max	0.168 x 0.224 x 0.328	0.126 x 0.182 x 0.357	0.112 x 0.234 x 0.488	0.174 x 0.268 x 0.344	0.098 x 0.384 x 0.436
X-ray wavelength, Å	0.71073	0.71073	0.71073	0.71073	0.71073
μ , mm ⁻¹	0.125	0.147	0.118	0.122	0.141
Trans min / max	0.96 / 0.98	0.95 / 0.98	0.94 / 0.99	0.96 / 0.98	0.94 / 0.99
ϑ_{min} , °	1.24	2.64	2.06	1.35	1.17
ϑ_{max} , °	25.89	24.93	26.23	25.49	25.76
Reflections					
collected	26219	20958	26418	36308	15081
independent	6186	2297	2024	3491	6695
observed	4549	1984	1815	2992	5077
R _{int}	0.0536	0.0415	0.0554	0.0427	0.0329
Threshold expression	> 2σ(I)	> 2σ(I)	> 2σ(I)	> 2σ(I)	> 2σ(I)
No. parameters	530	214	159	300	589
No. restraints	2	1	1	0	0
R ₁ (observed)	0.0472	0.0335	0.0364	0.0330	0.0440
wR ₂ (all)	0.1294	0.0808	0.0972	0.0910	0.1248
Goodness of fit (all)	1.068	1.054	1.051	1.028	1.072
ρ_{max}, ρ_{min} , e Å ⁻³	0.348, -0.289	0.244, -0.183	0.215, -0.263	0.213, -0.189	0.411, -0.320
Completeness to 2θ limit	0.899	0.972	0.982	0.996	0.959

Code	2(D12 ⁻):A6H ₂ ²⁺	2(D12):A8	D10:A9	2(D11):A9	2(D11):A8
Formula moiety	C ₁₃ H ₁₆ N ₂ , (C ₂ H ₃ N ₆ O ₂) ₂	C ₈ H ₁₂ N ₂ O ₂ , (C ₂ H ₄ N ₆ O ₂) ₂	CH ₂ N ₆ O ₂ , C ₄ H ₄ N ₂ O ₂	C ₂ H ₄ N ₆ O ₂ , 0.5(C ₄ H ₄ N ₂ O ₂)	C ₈ H ₁₂ N ₂ O ₂ , (C ₂ H ₄ N ₆ O ₂) ₂
Empirical formula	C ₁₇ H ₂₂ N ₁₄ O ₄	C ₁₂ H ₂₀ N ₁₄ O ₆	C ₅ H ₆ N ₈ O ₄	C ₄ H ₆ N ₇ O ₃	C ₁₂ H ₂₀ N ₁₄ O ₆
Molecular weight	486.48	456.42	242.18	200.16	456.42
Color, Habit	Yellow, Blocks	Colorless, Blocks	Colorless, Plates	Colorless, Plates	Colorless, Blocks
Crystal system	Monoclinic	Monoclinic	Monoclinic	Monoclinic	Monoclinic
Space group, Z	P2(1)/c, 4	I2/a, 4	P2(1)/n, 4	P2(1)/c, 4	C2/c, 4
a, Å	13.069(4)	17.193(5)	9.880(4)	16.291(9)	29.886(8)
b, Å	13.769(4)	3.8138(10)	6.529(3)	5.224(3)	4.5914(12)
c, Å	12.854(3)	29.689(10)	15.060(6)	9.844(5)	16.515(6)
α, °	90	90	90	90	90
β, °	111.761(14)	90.255(13)	104.01(3)	99.76(4)	118.41(3)
γ, °	90	90	90	90	90
Volume, Å ³	2148.2(10)	1946.7(10)	942.6(7)	825.6(8)	1993.2(11)
Density, g/cm ³	1.504	1.557	1.707	1.610	1.521
T, °K	130(2)	130(2)	296(2)	296(2)	296(2)
Crystal size, min x mid x max	0.168 x 0.355 x 0.394	0.094 x 0.192 x 0.388	0.035 x 0.158 x 0.242	0.032 x 0.245 x 0.322	0.125 x 0.238 x 0.318
X-ray wavelength, Å	0.71073	0.71073	0.71073	0.71073	0.71073
μ, mm ⁻¹	0.114	0.127	0.148	0.138	0.124
Trans min / max	0.96 / 0.98	0.95 / 0.99	0.96 / 1.00	0.96 / 1.00	0.96 / 0.98
θ _{min} , °	1.68	1.37	2.24	1.27	1.55
θ _{max} , °	25.04	25.55	25.22	25.40	25.89
Reflections					
collected	46042	17545	16735	12664	24897
independent	3776	1822	1689	1523	1930
observed	3055	1586	1081	950	1508
R _{int}	0.0551	0.0461	0.0962	0.0947	0.0537
Threshold expression	> 2σ(I)	> 2σ(I)	> 2σ(I)	> 2σ(I)	> 2σ(I)
No. parameters	326	152	163	133	153
No. restraints	1	0	1	0	1
R ₁ (observed)	0.0371	0.0356	0.0492	0.0518	0.0380
wR ₂ (all)	0.1004	0.0965	0.1306	0.1497	0.1283
Goodness of fit (all)	1.039	1.122	1.040	1.073	1.087
ρ _{max} , ρ _{min} , e Å ⁻³	0.165, -0.286	0.216, -0.247	0.201, -0.237	0.186, -0.215	0.233, -0.215
Completeness to 2θ limit	0.989	0.996	0.995	0.999	0.994

-
- i APEX2 v2013.10-0, © 2013, Bruker Analytical X-ray Systems, Madison, WI.
 - ii COSMO v1.61, © 1999 - 2009, Bruker Analytical X-ray Systems, Madison, WI.
 - iii SAINT v8.34a, © 1997 - 2013, Bruker Analytical X-ray Systems, Madison, WI.
 - iv SADABS v2012/1, © 2012, Bruker Analytical X-ray Systems, Madison, WI.
 - v SHELXTL v2008/4, © 2008, Bruker Analytical X-ray Systems, Madison, WI.
 - vi Oxford Diffraction, Xcalibur CCD System, CrysAlis Software System, Version 1.171.37, Oxford Diffraction Ltd., 2014.
 - vii (a) Sheldrick, G. M. (2014). SHELX-2014. University of Göttingen, Germany.
(b) Sheldrick, G. M. *Acta Crystallogr., Sect. A: Found. Crystallogr.* **2008**, A64, 112–122.